

学位論文
核子対あたり重心系エネルギー 5.02 TeV 陽子-陽子及び鉛-鉛
原子核衝突における中性中間子と直接光子測定

Measurement of neutral mesons and direct photons
in pp and Pb-Pb collisions at $\sqrt{s_{NN}} = 5.02$ TeV

2019年1月博士(理学)申請

関畑 大貴 (D150900)
広島大学大学院 理学研究科 物理科学専攻
クォーク物理学研究室
January 31, 2019

Ph.D Thesis
Measurement of neutral mesons and direct photons
in pp and Pb–Pb collisions at $\sqrt{s_{\text{NN}}} = 5.02$ TeV

Daiki Sekihata (D150900)
Graduate School of Science in Hiroshima University
Department of Physical Science
Experimental Quark Physics Laboratory
January 31, 2019

Abstract

The new state of matter, called quark-gluon plasma (QGP), created by the high-energy heavy-ion collision has been studied for more than 40 years. Partons originating from initial hard scatterings lose their energy in the hot and dense QCD medium, which results in suppression of hadron production at high transverse momentum (p_T), compared to pp collisions at the same center-of-mass energy $\sqrt{s_{NN}}$. Light flavor particles are excellent probes to study the suppression in a wide p_T range with high precision. Especially, neutral mesons such as π^0 and η mesons that decay into two photons can be reconstructed and identified by a fine-segmented electro-magnetic calorimeter in a wide p_T range.

In this thesis, the suppression of π^0 and η mesons in Pb–Pb collisions at the highest energy $\sqrt{s_{NN}} = 5.02$ TeV is reported. By increasing the collision energy, p_T spectra of π^0 meson become harder than that at $\sqrt{s_{NN}} = 2.76$ TeV in both pp and Pb–Pb collisions. Nevertheless, the suppression of π^0 meson in Pb–Pb collisions compared to pp collisions is the same level, which is by a factor of up to 8. This indicates the larger energy-loss at the higher collision energy. Comparing light and heavy flavor hadrons, namely π^0 and D mesons, the suppression of D mesons at low p_T is weaker than that of π^0 meson. This is interpreted as the smaller energy-loss for charm quarks than for up, down quarks. The suppression pattern of η meson seems to be similar to K^\pm meson consisting of a strange quark, though uncertainties for the η meson measurement is large.

Direct photons that are defined as photons not originating from hadron decays are also discussed in this thesis. Direct photons are unique probes to study the space-time evolution of the QGP, since they are not involved in strong interaction and can carry information when they are produced. When focusing on direct photons, π^0 and η mesons contribute as huge backgrounds. To subtract decay photon yields, the cocktail simulation where p_T spectra of neutral mesons are inputs has been performed. Direct photon spectra or upper limits at the 90% of confidence level have been extracted. Finally, R_{AA} of direct photons has been determined and is consistent with unity at high p_T which justifies the measurement. On the other hand, the excess beyond the pQCD calculation is observed at low p_T by a factor of up to 4 in central Pb–Pb collisions. This indicates thermal photon emissions from the hot and dense QCD medium. The obtained effective temperature T_{eff} is 345 ± 222 (total unc.) MeV in Pb–Pb collisions at $\sqrt{s_{NN}} = 5.02$ TeV for centrality 0-10%. This is the first measurement and setting upper limits on direct photons in pp and Pb–Pb collisions at $\sqrt{s_{NN}} = 5.02$ TeV.

 33 **Contents**

34	1 Introduction	1
35	1.1 Quantum Chromo-Dynamics (QCD)	1
36	1.2 Quark-gluon plasma (QGP)	1
37	1.3 High-energy heavy-ion collisions	3
38	1.4 Suppression of high p_T hadrons	4
39	1.4.1 Particle production in hadron colliders at high p_T	5
40	1.4.2 Nuclear modification factor R_{AA}	5
41	1.4.3 Cold nuclear matter effects	6
42	1.4.4 Parton energy-loss	7
43	1.5 Direct photons production	8
44	1.5.1 Pioneers of the direct photon measurement	9
45	1.5.2 Direct photon puzzle	9
46	1.6 Organization of this thesis	12
47	2 The LHC and the ALICE apparatus	13
48	2.1 The Large Hadron Collider (LHC)	13
49	2.2 ALICE apparatus	14
50	2.2.1 Overview of ALICE apparatus	14
51	2.2.2 Basic kinematic variables in ALICE coordinate	14
52	2.2.3 Trigger detectors	16
53	2.2.4 Central Tracking System	18
54	2.2.5 Electro-magnetic calorimeters	20
55	2.2.6 Other detectors	21
56	3 Data sets	22
57	3.1 Data sets in pp collisions at $\sqrt{s} = 5.02$ TeV	22
58	3.1.1 Quality assessment of MB data	23
59	3.1.2 Quality assessment of PHOS triggered data	26
60	3.2 Data sets in Pb–Pb collisions at $\sqrt{s_{NN}} = 5.02$ TeV	30
61	3.2.1 Quality assessment of MB data	31
62	3.2.2 Quality assessment of PHOS triggered data	31
63	4 Analyses of neutral mesons	39
64	4.1 Analysis strategy	39
65	4.2 Photon identification	40
66	4.2.1 CPV cut	40
67	4.2.2 Dispersion cut	40
68	4.3 Analyses in pp collisions at $\sqrt{s} = 5.02$ TeV	41
69	4.3.1 Raw yield extraction	41
70	4.3.2 Acceptance \times reconstruction efficiency	42
71	4.3.3 Timing cut	43
72	4.3.4 Trigger efficiency	44
73	4.3.5 Feed down correction from strange hadrons	45
74	4.4 Analyses in Pb–Pb collisions at $\sqrt{s_{NN}} = 5.02$ TeV	46
75	4.4.1 Raw yield extraction	46
76	4.4.2 Acceptance \times reconstruction efficiency	51
77	4.4.3 Timing cut	56
78	4.4.4 Trigger efficiency	56

79	4.4.5	Feed down correction from strange hadrons	57
80	4.5	Combining MB and PHOS triggered data	57
81	5	Systematic uncertainties for neutral mesons	60
82	5.1	Yield extraction	60
83	5.2	Global energy scale	60
84	5.3	Non-linearity of energy measurement in simulation	61
85	5.4	Trigger efficiency	61
86	5.5	Timing cut efficiency	61
87	5.6	PID cut efficiency	61
88	5.7	Feed down from strange hadrons	62
89	5.8	Acceptance of PHOS detector	64
90	5.9	Material budget	64
91	5.10	Summary of systematic uncertainties	65
92	5.10.1	Summary of systematic uncertainties in pp collisions at $\sqrt{s} = 5.02$ TeV .	65
93	5.10.2	Summary of systematic uncertainties in Pb–Pb collisions at $\sqrt{s_{NN}} = 5.02$	
94		TeV	65
95	6	Results and discussions for neutral mesons	70
96	6.1	Invariant cross section of particles	70
97	6.2	Particle ratio	74
98	6.3	Nuclear modification factors R_{AA} of neutral mesons	75
99	6.3.1	Collision energy $\sqrt{s_{NN}}$ dependence	75
100	6.3.2	Comparison to theoretical models	77
101	6.3.3	Hadron species dependence	77
102	6.3.4	Comparison of R_{AA} and R_{pA} at $\sqrt{s_{NN}} = 5.02$ TeV	80
103	7	Analyses for direct photon	81
104	7.1	Analysis strategy	81
105	7.2	Raw yields of clusters	82
106	7.3	Acceptance \times reconstruction efficiency	83
107	7.4	TOF cut efficiency	83
108	7.5	Trigger efficiency	83
109	7.6	Feed down correction for $K_S^0 \rightarrow \pi^0 \pi^0 \rightarrow 4\gamma$	83
110	7.7	Photon purity	84
111	7.7.1	Data driven approach for photon purity estimation	84
112	7.7.2	Photon purity in pp collisions at $\sqrt{s} = 5.02$ TeV	85
113	7.7.3	Photon purity in Pb–Pb collisions at $\sqrt{s_{NN}} = 5.02$ TeV	89
114	7.8	Photon cocktail simulation	99
115	7.8.1	Cocktail simulation in pp at $\sqrt{s} = 5.02$ TeV	99
116	7.8.2	Cocktail simulation in Pb–Pb at $\sqrt{s_{NN}} = 5.02$ TeV	99
117	8	Systematic uncertainties for photon measurements	103
118	8.1	Photon purity	103
119	8.1.1	Data Driven approach method itself	103
120	8.1.2	Different assumption of particle composition	103
121	8.2	Cocktail simulation	103
122	8.2.1	Shape of input π^0 spectrum	104
123	8.2.2	Particle ratios	104
124	8.3	Summary of systematic uncertainties for inclusive photons γ^{inc}	105

125	8.3.1	Summary of systematic uncertainties for γ^{inc} in pp collisions at $\sqrt{s} = 5.02$	
126		TeV	105
127	8.3.2	Summary of systematic uncertainties for γ^{inc} in Pb–Pb collisions at $\sqrt{s_{\text{NN}}}$	
128		$= 5.02$ TeV	106
129	9	Results and discussions for photons	108
130	9.1	Results on inclusive photons γ^{inc}	108
131	9.2	Results on direct photons γ^{dir}	108
132	9.2.1	$\gamma^{\text{inc}}/\pi^0$ ratio	108
133	9.2.2	Direct photon excess ratio R_γ	110
134	9.2.3	Direct photon spectra	111
135	9.2.4	R_{AA} of direct photons	112
136	9.2.5	Effective temperature T_{eff} extraction	113
137	10	Conclusion	114
138	A	Zero Suppression study in Run2	116
139	B	pp collisions at $\sqrt{s} = 5.02$ TeV in 2015	117
140	B.1	Date sets and QA	117
141	B.1.1	Date sets in pp collisions at $\sqrt{s} = 5.02$ TeV	117
142	B.1.2	event selection	118
143	B.1.3	minimal cluster selection	118
144	B.1.4	π^0 peak parameters vs. run numbers	118
145	B.2	Trigger QA	119
146	B.2.1	Distance between fired TRU channels and clusters	119
147	B.2.2	Energy distribution of matched clusters	119
148	B.3	Raw yield extraction	119
149	B.4	Acceptance \times reconstruction efficiency	119
150	B.5	Trigger efficiency	119
151	B.6	Timing cut	124
152	B.7	Feed down from strange hadrons	124
153	B.8	Systematic uncertainties in pp collisions at $\sqrt{s} = 5.02$ TeV in LHC15n	124
154	B.8.1	Yield extraction of neutral mesons	124
155	B.8.2	PID cut	124
156	B.8.3	TOF cut	125
157	B.8.4	Feed-down correction	125
158	B.8.5	Global energy scale	125
159	B.8.6	Non-linearity of energy response	125
160	B.8.7	Acceptance of detector	126
161	B.8.8	Material budget	126
162	B.8.9	Summary of systematic uncertainties	126
163	B.9	Invariant differential cross section of π^0	126

164 List of Figures

165	1	The energy density ε divided by 4th power of the temperature T^4 predicted by	
166		lattice QCD	2
167	2	A schematic phase diagram of QCD matter	2
168	3	A schematic view of collision geometry in high-energy heavy-ion collisions	3

169	4	A schematic view of space-time evolution of the matter in high-energy heavy-ion collisions	4
170			
171	5	The production cross section of charged hadrons in pp collisions at CERN-ISR	5
172	6	A schematic diagram $a + b \rightarrow c + d$, where hadron X represents anything else.	6
173	7	Power parameter α vs. p_T	6
174	8	The ratio of structure function in heavy nuclei to one in Carbon.	7
175	9	Feynman diagrams for direct photon productions	9
176	10	Results from WA80	10
177	11	Results from WA98	10
178	12	Direct photon yields and flow in 20-40 % Au–Au collisions at $\sqrt{s_{NN}} = 0.2$ TeV with PHENIX	11
179			
180	13	Direct photon yields and v_2 in 20-40% Pb–Pb collisions at $\sqrt{s_{NN}} = 5.02$ TeV with ALICE	11
181			
182	14	CERN accelerator complex [44].	13
183	15	Overview of ALICE detectors in Run2	14
184	16	Sketches of V0A and V0C arrays [48].	16
185	17	Position of VZERO (A-C) arrays and ITS around the beam pipe [48].	16
186	18	V0 (V0A + V0C) amplitude distribution [46].	17
187	19	Correlation between the sum and the difference of hit timing of V0A and V0C [46].	17
188	20	Positions of T0A and T0C [49].	18
189	21	The layout of ITS [50].	18
190	23	The layout of TPC [52, 53].	18
191	22	dE/dx measured in ITS standalone as a function momentum of charged particle [46].	19
192	24	dE/dx measured in TPC as a function momentum of charged particle [46].	19
193	25	Elements of the PHOS detector.	20
194	26	The integrated luminosity in pp collisions at $\sqrt{s} = 5.02$ TeV taken in 2017.	22
195	27	The average cluster energy and number of hits in each run on PHOS in LHC17p pass1.	24
196			
197	28	The average cluster energy and number of hits in each run on PHOS in LHC17q pass1.	24
198			
199	29	π^0 yield, peak position and sigma in each run in LHC17p pass1.	25
200	30	π^0 yield, peak position and sigma in each run in LHC17q pass1.	25
201	31	The distance between fired TRU channels and cluster position in different module for $E_{cluster} > 4$ GeV in LHC17pq.	27
202			
203	32	Energy distribution of all clusters and triggered clusters and ratios in LHC17pq.	28
204	33	The rejection factor of PHOS L0 trigger (run-by-run) in pp collisions at $\sqrt{s} = 5.02$ TeV	29
205			
206	34	The integrated luminosity in Pb–Pb collisions at $\sqrt{s_{NN}} = 5.02$ TeV taken in 2015.	30
207	35	The average cluster energy and number of hits in each run on PHOS in LHC15o pass1.	32
208			
209	36	The average cluster energy and number of hits in each run on PHOS in LHC15o pass1_pidfix.	32
210			
211	37	The average cluster energy and number of hits in each run on PHOS in LHC15o lowIR pass5.	33
212			
213	38	π^0 yield, peak position and sigma in each run in LHC15o pass1.	33
214	39	π^0 yield, peak position and sigma in each run in LHC15o pass1_pidfix.	34
215	40	π^0 yield, peak position and sigma in each run in LHC15o lowIR pass5.	34
216	41	The distance between fired TRU channels and cluster position on different modules for LIH at $E_{cluster} > 8$ GeV in Pb–Pb collisions at $\sqrt{s_{NN}} = 5.02$ TeV	35
217			

218	42	The distance between fired TRU channels and cluster position on different modules for L1M at $E_{\text{cluster}} > 4$ GeV in Pb–Pb collisions at $\sqrt{s_{\text{NN}}} = 5.02$ TeV	36
219			
220	43	Energy distribution of all clusters and triggered clusters and ratios on different modules for L1H in Pb–Pb collisions at $\sqrt{s_{\text{NN}}} = 5.02$ TeV	37
221			
222	44	Energy distribution of all clusters and triggered clusters and ratios on different modules for L1M in Pb–Pb collisions at $\sqrt{s_{\text{NN}}} = 5.02$ TeV	38
223			
224	45	The rejection factor of PHOS L1 trigger (run-by-run) in Pb–Pb collisions at $\sqrt{s_{\text{NN}}} = 5.02$ TeV	38
225			
226	46	Invariant mass distributions in pp collisions at $\sqrt{s} = 5.02$ TeV (INT7)	41
227	47	Invariant mass distributions in pp collisions at $\sqrt{s} = 5.02$ TeV (PHI7)	41
228	48	Raw yields of neutral mesons in pp collisions at $\sqrt{s} = 5.02$ TeV	42
229	49	π^0 peak parameters in pp collisions at $\sqrt{s} = 5.02$ TeV	42
230	50	η peak parameters in pp collisions at $\sqrt{s} = 5.02$ TeV	43
231	51	acceptance \times reconstruction efficiency of neutral mesons in pp collisions at $\sqrt{s} = 5.02$ TeV with PHOS	43
232			
233	52	The cluster timing distribution and TOF cut efficiency	44
234	53	PHOS L0 trigger efficiency in pp collisions at $\sqrt{s} = 5.02$ TeV	44
235	54	Feed down factor for π^0 from K_S^0 in pp collisions at $\sqrt{s} = 5.02$ TeV	45
236	55	K^\pm/π^\pm ratio in PYTHIA8	45
237	56	Centrality V0M distributions in Pb–Pb collisions at $\sqrt{s_{\text{NN}}} = 5.02$ TeV (2015)	46
238	57	Invariant mass distributions in Pb–Pb collisions at $\sqrt{s_{\text{NN}}} = 5.02$ TeV (INT7)	47
239	58	Invariant mass distributions in Pb–Pb collisions at $\sqrt{s_{\text{NN}}} = 5.02$ TeV (PHI7)	48
240	59	Raw yields of π^0 in Pb–Pb collisions at $\sqrt{s_{\text{NN}}} = 5.02$ TeV	49
241	60	Raw yields of η in Pb–Pb collisions at $\sqrt{s_{\text{NN}}} = 5.02$ TeV	50
242	61	acceptance \times reconstruction efficiency of neutral mesons in Pb–Pb collisions at $\sqrt{s_{\text{NN}}} = 5.02$ TeV with PHOS	51
243			
244	62	π^0 peak position in Pb–Pb collisions at $\sqrt{s_{\text{NN}}} = 5.02$ TeV for different centrality classes	52
245			
246	63	π^0 peak width in Pb–Pb collisions at $\sqrt{s_{\text{NN}}} = 5.02$ TeV for different centrality classes	53
247			
248	64	η peak position in Pb–Pb collisions at $\sqrt{s_{\text{NN}}} = 5.02$ TeV for different centrality classes	54
249			
250	65	η peak width in Pb–Pb collisions at $\sqrt{s_{\text{NN}}} = 5.02$ TeV for different centrality classes	55
251	66	Timing distribution of clusters and TOF cut efficiency	56
252	67	PHOS L1 triggers performance in Pb–Pb collisions at $\sqrt{s_{\text{NN}}} = 5.02$ TeV	56
253	68	Feed down factor for π^0 from K_S^0 in Pb–Pb collisions at $\sqrt{s_{\text{NN}}} = 5.02$ TeV	57
254	69	K^\pm/π^\pm ratio in M.C. before re-weighting.	58
255	70	K^\pm/π^\pm ratio in M.C. after re-weighting.	59
256	71	E/p of e^\pm and the uncertainty of particle yield by the energy scale in pp collisions at $\sqrt{s} = 5.02$ TeV.	60
257			
258	72	The ratio of π^0 raw yields in high intensity runs to those in low intensity runs.	61
259	73	PID cut efficiency as a function of photon energy in pp collisions at $\sqrt{s} = 5.02$ TeV.	62
260	74	PID cut efficiency as a function of photon energy in Pb–Pb collisions at $\sqrt{s_{\text{NN}}} = 5.02$ TeV centrality 0-10%.	62
261			
262	75	PID cut efficiency as a function of photon energy in Pb–Pb collisions at $\sqrt{s_{\text{NN}}} = 5.02$ TeV centrality 10-20%.	62
263			
264	76	PID cut efficiency as a function of photon energy in Pb–Pb collisions at $\sqrt{s_{\text{NN}}} = 5.02$ TeV centrality 20-40%.	63
265			

266	77	PID cut efficiency as a function of photon energy in Pb–Pb collisions at $\sqrt{s_{NN}} = 5.02$ TeV centrality 40-60%.	63
267			
268	78	PID cut efficiency as a function of photon energy in Pb–Pb collisions at $\sqrt{s_{NN}} = 5.02$ TeV centrality 60-80%.	63
269			
270	79	top : ratio of π^0 yields at $B = 0.5$ T to those at $B = 0.0$ T in data and M.C..	
271		bottom : Double ratio of π^0 yields	64
272	80	The summary of systematic uncertainties of the π^0 measurement in pp collisions at $\sqrt{s} = 5.02$ TeV	65
273			
274	81	The summary of systematic uncertainties of the η measurement in pp collisions at $\sqrt{s} = 5.02$ TeV	65
275			
276	82	The summary of systematic uncertainties of the π^0 measurement in Pb–Pb collisions at $\sqrt{s_{NN}} = 5.02$ TeV (0-5 %)	66
277			
278	83	The summary of systematic uncertainties of the π^0 measurement in Pb–Pb collisions at $\sqrt{s_{NN}} = 5.02$ TeV (5-10 %)	66
279			
280	84	The summary of systematic uncertainties of the π^0 measurement in Pb–Pb collisions at $\sqrt{s_{NN}} = 5.02$ TeV (10-20 %)	66
281			
282	85	The summary of systematic uncertainties of the π^0 measurement in Pb–Pb collisions at $\sqrt{s_{NN}} = 5.02$ TeV (20-40 %)	67
283			
284	86	The summary of systematic uncertainties of the π^0 measurement in Pb–Pb collisions at $\sqrt{s_{NN}} = 5.02$ TeV (40-60 %)	67
285			
286	87	The summary of systematic uncertainties of the π^0 measurement in Pb–Pb collisions at $\sqrt{s_{NN}} = 5.02$ TeV (60-80 %)	67
287			
288	88	The summary of systematic uncertainties of the η measurement in Pb–Pb collisions at $\sqrt{s_{NN}} = 5.02$ TeV (0-10 %)	68
289			
290	89	The summary of systematic uncertainties of the η measurement in Pb–Pb collisions at $\sqrt{s_{NN}} = 5.02$ TeV (10-20 %)	68
291			
292	90	The summary of systematic uncertainties of the η measurement in Pb–Pb collisions at $\sqrt{s_{NN}} = 5.02$ TeV (20-40 %)	68
293			
294	91	The summary of systematic uncertainties of the η measurement in Pb–Pb collisions at $\sqrt{s_{NN}} = 5.02$ TeV (40-60 %)	69
295			
296	92	The summary of systematic uncertainties of the η measurement in Pb–Pb collisions at $\sqrt{s_{NN}} = 5.02$ TeV (60-80 %)	69
297			
298	93	Production cross sections of neutral mesons in pp collisions at $\sqrt{s} = 5.02$ TeV	70
299	94	Invariant yields of neutral mesons in Pb–Pb collisions at $\sqrt{s_{NN}} = 5.02$ TeV	71
300	95	Comparison of p_T spectra for π^0 between $\sqrt{s_{NN}} = 5.02$ and 2.76 TeV in Pb–Pb collisions	73
301			
302	96	The η/π^0 ratio in pp collisions at $\sqrt{s} = 5.02$ TeV	74
303	97	η/π^0 ratios in Pb–Pb collisions at $\sqrt{s_{NN}} = 5.02$ TeV	74
304	98	R_{AA} of π^0 in Pb–Pb collisions at $\sqrt{s_{NN}} = 5.02$ and 2.76 TeV	75
305	99	Comparison of the ratio of p_T spectrum and R_{AA} in Pb–Pb collisions at $\sqrt{s_{NN}} = 5.02$ and 2.76 TeV (2011 sample)	76
306			
307	100	Comparison of R_{AA} with theoretical models in Pb–Pb collisions at $\sqrt{s_{NN}} = 5.02$ TeV	78
308			
309	101	Comparison of R_{AA} between π^0 and η in Pb–Pb collisions at $\sqrt{s_{NN}} = 5.02$ TeV for different centrality classes.	79
310			
311	102	R_{AA} of π^0 , η , π^\pm , K^\pm , D and B^\pm mesons in central (0-10%) Pb–Pb collisions at $\sqrt{s_{NN}} = 5.02$ TeV	79
312			
313	103	R_{AA} , R_{pA} of π^0 and η mesons	80
314	104	Raw yields of clusters $\frac{1}{N_{ev}} \frac{dN}{dp_T}$ in pp and Pb–Pb collisions at $\sqrt{s_{NN}} = 5.02$ TeV	82

315	105	Acceptance \times reconstruction efficiencies in pp and Pb–Pb collisions at $\sqrt{s_{\text{NN}}} = 5.02$ TeV	83
316			
317	106	Feed down corrections from K_S^0 in pp and Pb–Pb collisions at $\sqrt{s_{\text{NN}}} = 5.02$ TeV	84
318	107	The distance between a cluster on PHOS and a charged particle in pp collisions at $\sqrt{s} = 5.02$ TeV.	85
319			
320	108	Measured particle ratios on PHOS in pp collisions at $\sqrt{s} = 5.02$ TeV.	86
321	109	PID cut efficiency for identified charged particles in pp collisions at $\sqrt{s} = 5.02$ TeV	86
322	110	The summary of particle abundance on PHOS in pp collisions at $\sqrt{s} = 5.02$ TeV for $C_{\text{nh}} = 0$	87
323			
324	111	The summary of particle abundance on PHOS in pp collisions at $\sqrt{s} = 5.02$ TeV for $C_{\text{nh}} = 0.5 \times K^\pm/\pi^\pm + p/\pi^\pm$	88
325			
326	112	The summary of particle abundance on PHOS in 0-10% Pb–Pb collisions at $\sqrt{s_{\text{NN}}} = 5.02$ TeV for $C_{\text{nh}} = 0$	89
327			
328	113	The summary of particle abundance on PHOS in 0-10% Pb–Pb collisions at $\sqrt{s_{\text{NN}}} = 5.02$ TeV for $C_{\text{nh}} = 0.5 \times K^\pm/\pi^\pm + p/\pi^\pm$	90
329			
330	114	The summary of particle abundance on PHOS in 10-20% Pb–Pb collisions at $\sqrt{s_{\text{NN}}} = 5.02$ TeV for $C_{\text{nh}} = 0$	91
331			
332	115	The summary of particle abundance on PHOS in 10-20% Pb–Pb collisions at $\sqrt{s_{\text{NN}}} = 5.02$ TeV for $C_{\text{nh}} = 0.5 \times K^\pm/\pi^\pm + p/\pi^\pm$	92
333			
334	116	The summary of particle abundance on PHOS in 20-40% Pb–Pb collisions at $\sqrt{s_{\text{NN}}} = 5.02$ TeV for $C_{\text{nh}} = 0$	93
335			
336	117	The summary of particle abundance on PHOS in 20-40% Pb–Pb collisions at $\sqrt{s_{\text{NN}}} = 5.02$ TeV for $C_{\text{nh}} = 0.5 \times K^\pm/\pi^\pm + p/\pi^\pm$	94
337			
338	118	The summary of particle abundance on PHOS in 40-60% Pb–Pb collisions at $\sqrt{s_{\text{NN}}} = 5.02$ TeV for $C_{\text{nh}} = 0$	95
339			
340	119	The summary of particle abundance on PHOS in 40-60% Pb–Pb collisions at $\sqrt{s_{\text{NN}}} = 5.02$ TeV for $C_{\text{nh}} = 0.5 \times K^\pm/\pi^\pm + p/\pi^\pm$	96
341			
342	120	The summary of particle abundance on PHOS in 60-80% Pb–Pb collisions at $\sqrt{s_{\text{NN}}} = 5.02$ TeV for $C_{\text{nh}} = 0$	97
343			
344	121	The summary of particle abundance on PHOS in 60-80% Pb–Pb collisions at $\sqrt{s_{\text{NN}}} = 5.02$ TeV for $C_{\text{nh}} = 0.5 \times K^\pm/\pi^\pm + p/\pi^\pm$	98
345			
346	122	The decay photon cocktail in pp collisions at $\sqrt{s} = 5.02$ TeV	100
347	123	The decay photon cocktail in Pb–Pb collisions at $\sqrt{s} = 5.02$ TeV centrality 0-10 %	100
348	124	The decay photon cocktail in Pb–Pb collisions at $\sqrt{s} = 5.02$ TeV centrality 10-20 %	101
349	125	The decay photon cocktail in Pb–Pb collisions at $\sqrt{s} = 5.02$ TeV centrality 20-40 %	101
350	126	The decay photon cocktail in Pb–Pb collisions at $\sqrt{s} = 5.02$ TeV centrality 40-60 %	102
351	127	The decay photon cocktail in Pb–Pb collisions at $\sqrt{s} = 5.02$ TeV centrality 60-80 %	102
352	128	Systematic uncertainties of the DDA method itself.	103
353	129	Systematic uncertainties due to particle ratios in the cocktail simulation	105
354	130	Systematic uncertainties for γ^{inc} in pp collisions at $\sqrt{s} = 5.02$ TeV.	105
355	131	Systematic uncertainties for γ^{inc} in Pb–Pb collisions at $\sqrt{s_{\text{NN}}} = 5.02$ TeV for centrality 0-10%.	106
356			
357	132	Systematic uncertainties for γ^{inc} in Pb–Pb collisions at $\sqrt{s_{\text{NN}}} = 5.02$ TeV for centrality 10-20%.	106
358			
359	133	Systematic uncertainties for γ^{inc} in Pb–Pb collisions at $\sqrt{s_{\text{NN}}} = 5.02$ TeV for centrality 20-40%.	107
360			
361	134	Systematic uncertainties for γ^{inc} in Pb–Pb collisions at $\sqrt{s_{\text{NN}}} = 5.02$ TeV for centrality 40-60%.	107
362			

363	135	Systematic uncertainties for γ^{inc} in Pb–Pb collisions at $\sqrt{s_{\text{NN}}} = 5.02$ TeV for	
364		centrality 60-80%.	107
365	136	Inclusive photons spectra in pp and Pb–Pb collisions at $\sqrt{s_{\text{NN}}} = 5.02$ TeV.	108
366	137	$\gamma^{\text{inc}}/\pi^0$ ratios in pp and Pb–Pb collisions at $\sqrt{s_{\text{NN}}} = 5.02$ TeV.	109
367	138	R_γ in pp and Pb–Pb collisions at $\sqrt{s_{\text{NN}}} = 5.02$ TeV.	110
368	139	Direct photon spectra in pp and Pb–Pb collisions at $\sqrt{s_{\text{NN}}} = 5.02$ TeV.	111
369	140	R_{AA} of direct photons in Pb–Pb collisions at $\sqrt{s_{\text{NN}}} = 5.02$ TeV for centrality 0-10%.	112
370	141	The p_{T} spectrum of direct photons in Pb–Pb collisions at $\sqrt{s_{\text{NN}}} = 5.02$ TeV for	
371		centrality 0-10% and the TCM fit to data.	113
372	142	standard cluster cut efficiency as a function of photon energy. (12.5 MeV is default	
373		value in M.C.) Note these cuts are not apply in my analysis.	116
374	143	γ -ID cut efficiency as a function of photon energy. (12.5 MeV is default value in	
375		M.C.)	116
376	144	Integrated luminosity in pp collisions at $\sqrt{s} = 5.02$ TeV in 2015.	117
377	145	average cluster energy and number of hits in each run on PHOS in LHC15n.	118
378	146	π^0 yield, peak position and sigma in each run in LHC15n.	119
379	147	The distance between fired TRU channels and cluster position in different module	
380		for $E_{\text{cluster}} > 3$ GeV in LHC15n. Note that M4 is excluded from my analysis from	
381		the very beginning.	120
382	148	Energy distribution of all clusters and triggered clusters and ratios in LHC15n.	
383		Note that M4 is excluded from my analysis from the very beginning.	121
384	149	π^0 peak in kINT7 and kPHI7. An energy threshold of PHOS L0 trigger was 3	
385		GeV in 2015	122
386	150	Raw yields of π^0 in LHC15n.	122
387	151	peak parameters of π^0 in data and M.C. as a function of p_{T}	123
388	152	The acceptance \times reconstruction efficiency of π^0	123
389	153	The rejection factor and trigger efficiency of PHOS L0 trigger in LHC15n data.	123
390	154	TOF cut efficiency as a function of photon energy in LHC15n data sample.	124
391	155	The ratio of π^0 yield in BS = 25 ns to one in BS = 1000 ns triggered by kINT7	
392		in pp collisions at $\sqrt{s} = 5.02$ TeV.	125
393	156	χ^2/ndf of fitting to the ratio of π^0 peak position in data to that in M.C. at	
394		different parameters a,b.	126
395	157	π^0 peak parameters in different NL.	127
396	158	The ratio of corrected yield in different distance cut.	127
397	159	Summary of systematic uncertainties of π^0 measurement	128
398	160	The invariant differential cross section of π^0	128

399 List of Tables

400	1	Fitting parameters of TCM function in pp collisions at $\sqrt{s} = 5.02$ TeV	72
401	2	Fitting parameters of Hagedorn function in pp collisions at $\sqrt{s} = 5.02$ TeV	72
402	3	Fitting parameters of TCM function for π^0 in Pb–Pb collisions at $\sqrt{s_{\text{NN}}} = 5.02$	
403		TeV	72
404	4	Fitting parameters of TCM function for η in Pb–Pb collisions at $\sqrt{s_{\text{NN}}} = 5.02$ TeV	72
405	5	Geometrical parameters in Pb–Pb collisions at $\sqrt{s_{\text{NN}}} = 5.02$ TeV [79]	75
406	6	Particles which decay into photons	99

1 Introduction

Our main goal in high-energy heavy-ion collisions is to understand properties, such as energy density, temperature, transport coefficient, order of the phase transition e.t.c., of the quark-gluon plasma (QGP), which is the state of deconfined quarks and gluons from hadrons. These research for the QGP will provide phenomenological knowledge of fundamental Quantum Chromo-Dynamics (QCD).

1.1 Quantum Chromo-Dynamics (QCD)

The Quantum Chromo-Dynamics is a fundamental non-Abelian SU(3) gauge theory to describe strong interaction. The strong interaction is mediated by gluons between elementary particles which have color charge (red, blue and green). As gluon also has color, self-interaction among gluons can be induced. On the other hand, in Quantum Electro-Dynamics (QED), photon is neutral gauge boson and mediates electric charge with coupling constant $\alpha_{\text{QED}} = 1/137$. Hence, photons do not interact themselves. This is a main difference between QCD and QED. One of the most important point of QCD is that the strong interaction among quarks and gluons becomes weaker at high energy (i.e. large momentum transfer Q^2). This behavior is called “asymptotic freedom”. The strong coupling constant α_s at large Q^2 can be approximated as :

$$\alpha_s(Q^2) \approx \frac{12\pi}{(33 - 2N_f) \ln(Q^2/\lambda_{\text{QCD}}^2)}, \quad (1)$$

where N_f is the number of quark flavors ($N_f \leq 6$), λ_{QCD} is called QCD scale, which is typically 200 MeV. Therefore, $\alpha_s(Q^2)$ becomes smaller and perturbative calculation is applicable at large Q^2 . The confinement can be also expressed by a following phenomenological potential:

$$V(r) = -\frac{4}{3} \frac{\alpha_s}{r} + kr, \quad (2)$$

where $1/r$ term is dominant at small distance which is similar to Coulomb potential and kr is related to the confinement of quarks in hadrons. When one wants to separate two quarks, the potential energy kr increases and tends to produce a new $q\bar{q}$ pair. This results in two shorter strings. Finally, extracting single quark is not possible and new colorless hadrons will be produced.

1.2 Quark-gluon plasma (QGP)

The confined state of quarks and gluons in hadrons can be broken at the extremely high temperature or high density of many body systems of hadrons. This leads a transition from hadronic phase to the deconfined state of partons. The deconfined state of partons is called “quark-gluon plasma (QGP)” proposed by Bjorken [1]. Numerical calculations based on the lattice QCD are performed. Step-like behavior of ε/T^4 at $T = T_C$ is clearly seen in Figure 1. This is interpreted as the transition from the hadronic phase to the QGP at the critical temperature $T_C = 150 \sim 200$ MeV due to increase of degrees of freedom related to deconfined quarks and gluons from hadrons. In addition, recent lattice QCD calculations also predict crossover transition [2, 3].

Figure 2 shows a schematic phase diagram of QCD matter. The horizontal axis represents the net baryon density normalized to the normal nucleus, the vertical axis indicates the temperature. It is thought that the QGP has existed in the early universe at a few micro seconds after Big-Bang.

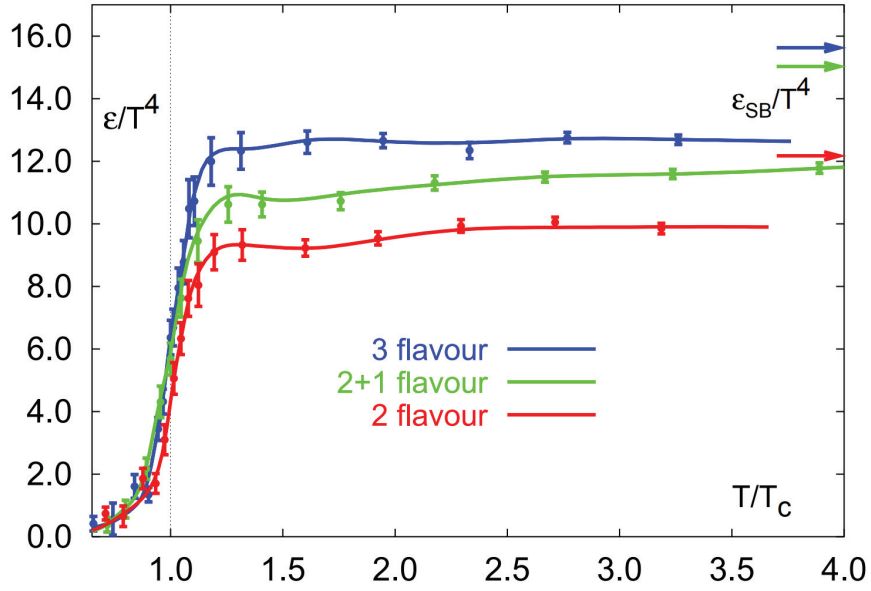


Figure 1: The energy density ε divided by 4th power of the temperature T^4 predicted by lattice QCD [4].

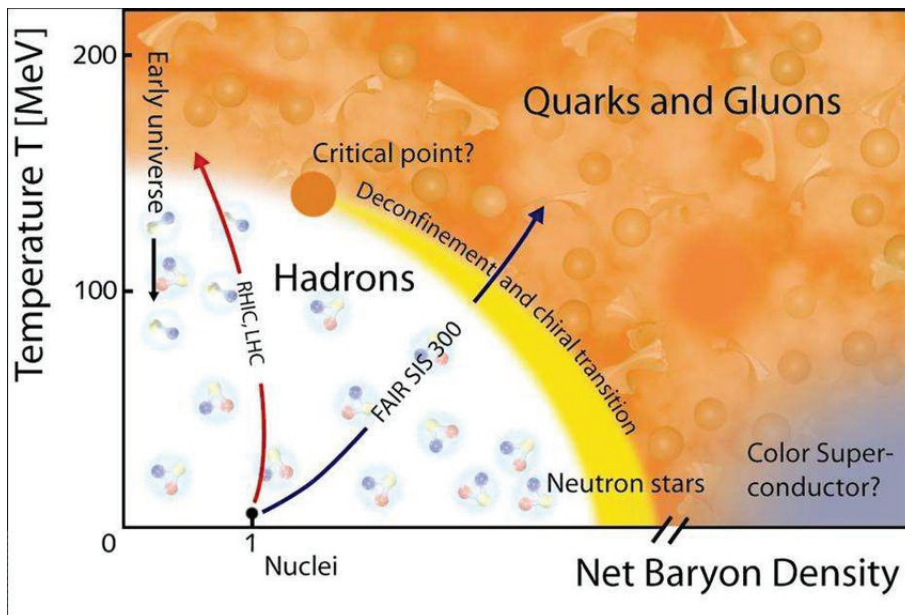


Figure 2: A schematic phase diagram of QCD matter [5].

1.3 High-energy heavy-ion collisions

High-energy heavy-ion collisions provide an unique opportunity to study strongly interacting matter, namely the QGP. In high-energy heavy-ion collisions, two Lorentz-contracted nuclei interact at the geometrical overlap region (Figure 3). A distance between the center of each nuclei is called “impact parameter” b . Nucleons participating the interaction are “participants” and the others are “spectators”. The impact parameter b is not directly measured, but can be simulated by the Glauber model calculation [6]. Then it provides the number of participant N_{part} and the number of binary nucleon-nucleon collisions N_{coll} . N_{part} is related to the volume of the interaction region. The number of particles produced at the later stage of collisions is roughly scaled by N_{part} . On the other hand, the number of particles produced by initial hard scatterings is basically scaled by N_{coll} .

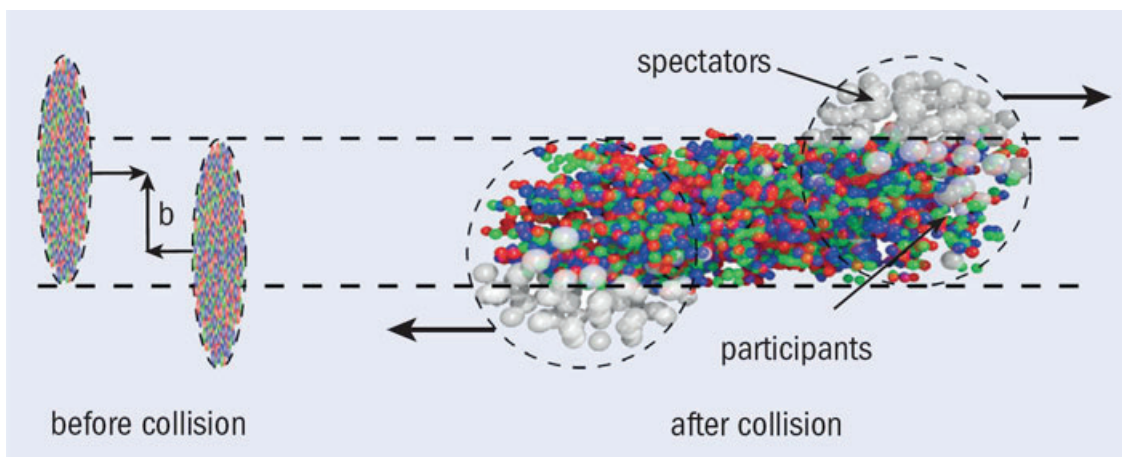


Figure 3: A schematic view of collision geometry in high-energy heavy-ion collisions [7].

As shown by Figure 4, the space-time evolution of the QCD matter created by heavy-ion collisions pass through various phases.

1. Pre-equilibrium ($0 < t < \tau_0$)

Two accelerated nuclei collide with each other at $t = 0$ and high energy is released in a tiny volume. Multiple parton scatterings lead local equilibrium of the hot and dense matter.

2. QGP phase ($\tau_0 < t < \tau_C$)

The QGP phase is formed at $t = \tau_0$, if energy density is higher than a value necessary for the transition ($\varepsilon > 1 \text{ GeV}/\text{fm}^3$). Its evolution can be described by hydrodynamics and the temperature becomes cooler.

3. Mixed phase between QGP and hadron gas ($\tau_C < t < \tau_H$)

The mixed phase consisting of quarks, gluons and hadrons can exist only if the phase transition is at first order. When the temperature reaches the transition temperature T_C , hadronization will start. Eventually, inelastic scattering of hadrons stops. This temperature is called “chemical freeze-out temperature”.

4. Hadron gas ($\tau_H < t < \tau_F$)

Hadronization processes finishes here, but still keep interaction as momentum exchange by elastic scatterings. At the end, elastic scattering ceases, too. This temperature is called “kinetic freeze-out temperature”. After the kinetic freeze-out, hadrons fly to our detectors.

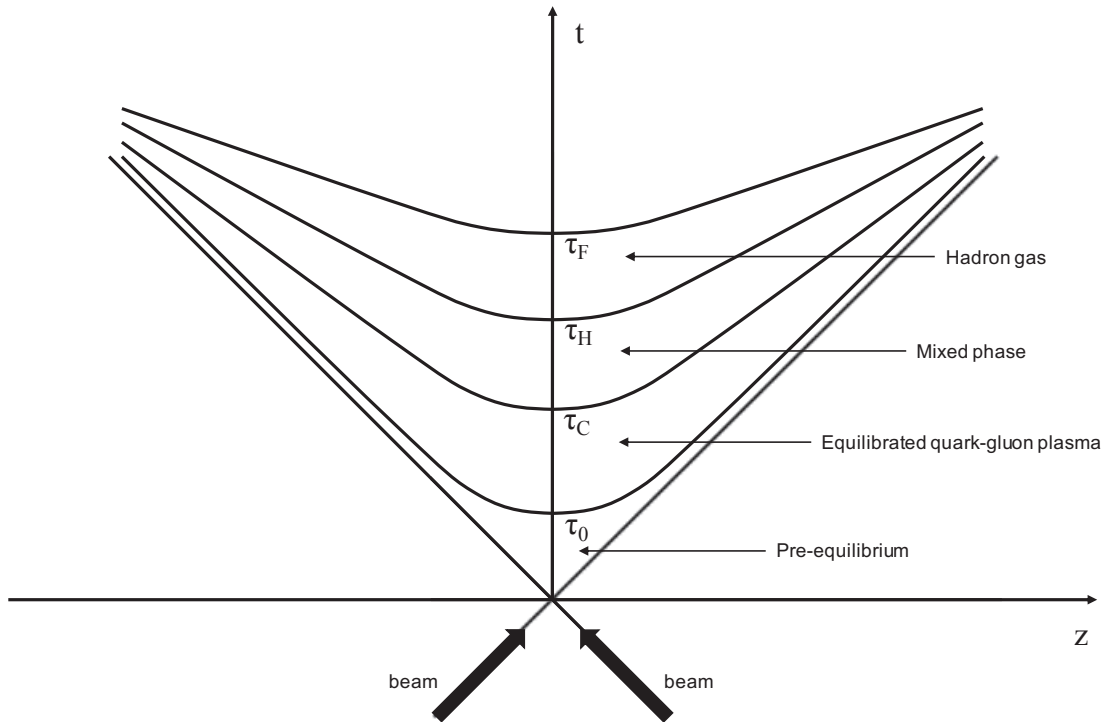


Figure 4: A schematic view of space-time evolution of the matter in high-energy heavy-ion collisions

473 1.4 Suppression of high p_T hadrons

474 Partons originating from initial hard scatterings lose their energy in the hot and dense medium,
 475 which results in modification of p_T spectra of hadrons. Light flavor hadrons are excellent probes
 476 to study the hadron suppression with high precision, because their statistics is large. It has
 477 been reported that the suppression of hadron yields compared to those in pp collisions scaled
 478 by N_{coll} , quantified by the nuclear modification factor R_{AA} (Eq. 4), is up to by a factor of 5
 479 in Au–Au collisions at $\sqrt{s_{NN}} = 0.2$ TeV at RHIC [8, 9]. It is by a factor of up to 8 in Pb–Pb
 480 collisions at $\sqrt{s_{NN}} = 2.76$ TeV in LHC Run1 (2009–2013) [10, 11, 12]. At the latest during
 481 LHC Run2 (2015–2018), the LHC provided Pb–Pb collisions at $\sqrt{s_{NN}} = 5.02$ TeV, which is
 482 the highest collision energy in the world. In this thesis, neutral meson (π^0 and η mesons) are
 483 focused on. Its advantage is that π^0 and η mesons can be reconstructed via their 2γ decays
 484 with a fine-segmented electro-magnetic calorimeter in a wide transverse momentum (p_T) range.
 485 In addition, photons decayed from neutral mesons are huge backgrounds, which have to be
 486 subtracted from inclusive photons, for the direct photons measurement described in section 1.5
 487 later.

488 1.4.1 Particle production in hadron colliders at high p_T

489 First of all, the particle production at high p_T
 490 was measured by CERN-ISR in pp collisions
 491 at different energies (23, 45 and 62 GeV) [14].
 492 Figure 5 shows the production cross section of
 493 charged hadrons in pp collisions at 23, 53,
 494 546 and $p\bar{p}$ collisions at $\sqrt{s} = 1800$ GeV. The
 495 invariant differential cross section of charged
 496 hadrons is described by an exponential func-
 497 tion $\exp(-a \cdot p_T)$ at low p_T region, while a
 498 power-law behavior p_T^{-n} is seen at high p_T .
 499 Moreover, the power-law parameter n is lower
 500 at higher collision energies, resulting in harder
 501 slope of p_T spectra at high p_T .

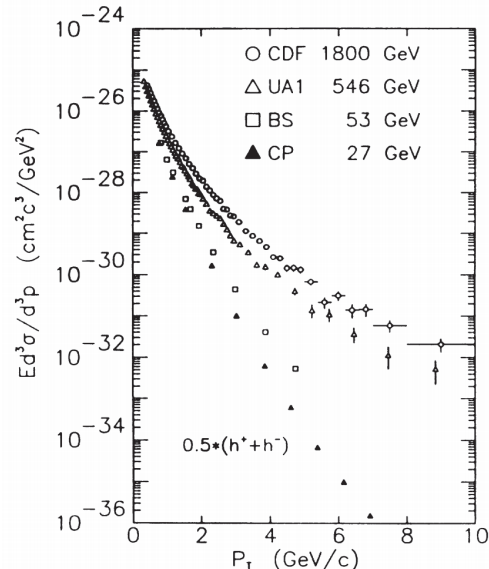


Figure 5: The production cross section of charged hadrons in pp collisions [13].

502 The hard scattering occurs in the initial stage of pp and heavy-ion collisions and can be calcu-
 503 lated by perturbative QCD (pQCD) based on factorization theorem. Figure 6 shows a schematic
 504 diagram of parton interaction $a + b \rightarrow c + x$ in hadronic collisions. The production cross section
 505 is defined as :

$$d\sigma^{pp \rightarrow h_C X} = dx_a dx_b dz_c \cdot f_a(x_a, \mu_F) \cdot f_b(x_b, \mu_F) \times d\sigma_{a+b \rightarrow c+x}(\alpha_s(\mu_R)) \times D_c(z_c, \mu_F), \quad (3)$$

506 where $f_{a(b)}(x_{a(b)}, \mu_F)$ is called parton distribution function (PDF) which is probability to find a
 507 parton $a(b)$ at its momentum fraction at $x_{a(b)}$ in a proton $A(B)$.

508 There, $x_{a(b)}$ = momentum of parton $a(b)$ /momentum of proton $A(B)$. $d\sigma_{a+b \rightarrow c+x}(\alpha_s(\mu_R))$ is a
 509 production cross section of parton c from scattering between parton a and b . $D_c(z_c, \mu_F)$ is
 510 fragmentation function (FF) which describes probability to hadronize into a hadron h_C from a
 511 parton c at momentum fraction z_c , where z_c = momentum of h_C /momentum of parton c . μ_F :
 512 factorization scale and μ_R : re-normalization scale are dummy parameters introduced to avoid
 513 divergence in theoretical calculations. Usually, they are fixed to transverse momentum of the
 514 particle ($\mu_F = \mu_R = p_T$) in calculations.

515 1.4.2 Nuclear modification factor R_{AA}

516 One of ideas to observe medium-induced effects is to compare particle yields between A–A
 517 collision and pp collisions. Due to the large number of partons in A–A collisions, particle yields
 518 in A–A collisions is normalized by the number of binary nucleon-nucleon collisions N_{coll} . If there
 519 are medium-induced effects in A–A collisions, particle yields in A–A collisions may be different
 520 from N_{coll} scaling. The medium-induced effects to high p_T particles is quantified by a ratio of
 521 particle yields in A–A collisions to that in pp collisions at the same center-of-mass energy $\sqrt{s_{\text{NN}}}$,
 522 called R_{AA} :

$$R_{AA} = \frac{d^2 N / dp_T dy|_{AA}}{T_{AA} \times d^2 \sigma / dp_T dy|_{pp}} = \frac{d^2 N / dp_T dy|_{AA}}{N_{\text{coll}} \times d^2 N / dp_T dy|_{pp}}, \quad (4)$$

523 where $d^2 N / dp_T dy|_{AA}$ is differential particle yields in A–A collisions, $d^2 \sigma / dp_T dy|_{pp}$ is differential
 524 production cross section in pp collisions and T_{AA} is called nuclear overlap function which is

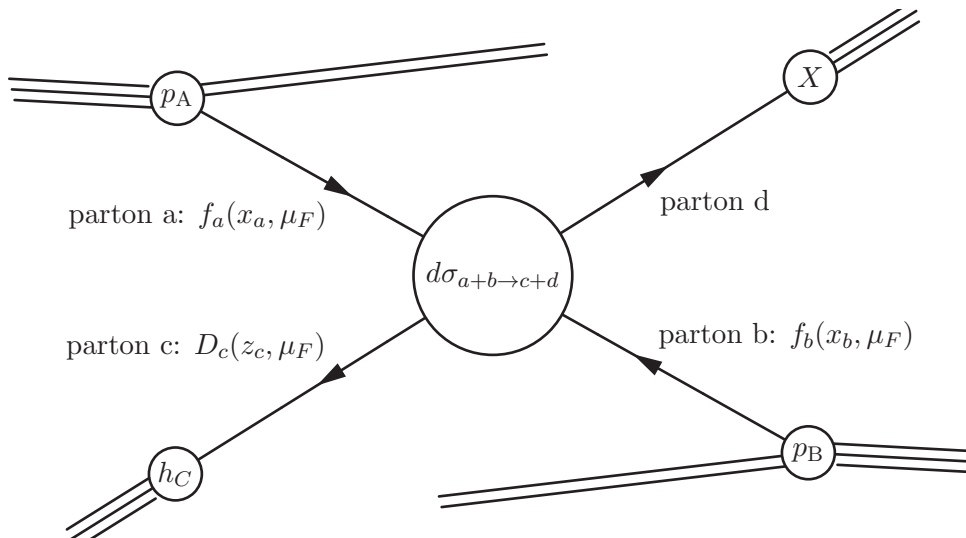


Figure 6: A schematic diagram $a + b \rightarrow c + d$, where hadron X represents anything else.

525 connected to the average number of inelastic collisions by $T_{AA} = N_{\text{coll}}/\sigma_{\text{pp}}^{\text{INEL}}$. In case of no
 526 medium-induced effects, $R_{AA} = 1$ at high p_T . Hence, R_{AA} is an excellent probe to see medium-
 527 induced effects. As of 2018, it has been known that $R_{AA} < 1$ for hadrons, $R_{AA} = 1$ for
 528 electro-weak bosons ($\gamma, W^\pm/Z$) respectively.

529 1.4.3 Cold nuclear matter effects

530 In order to understand hadron suppression in A–A compared to pp ($R_{AA} < 1$), it is important
 531 to test particle productions in p–A collisions where the hot and dense QCD medium is not likely
 532 created. Possible effects to modify particle yields are multiple soft scatterings or different parton
 533 distribution function in a nucleus, which are generally called “cold nuclear matter effects”.

534 **Cronin effect** It was observed that the produc-
 535 tion cross section in p–A collisions is not scaled by
 536 mass number A of the target nucleus [15] at ISR in
 537 1970, compared to that in pp collisions. They got
 538 these results by incident proton beam at 200, 300
 539 and 400 GeV to fixed Be, Ti and W targets. They
 540 found production cross section in p–A collisions as
 541 a function of p_T and A can be expressed by :

$$E \frac{d^3\sigma}{dp^3}(p_T, A) = E \frac{d^3\sigma}{dp^3}(p_T, 1) \times A^{\alpha(p_T)}, \quad (5)$$

542 where power $\alpha > 1$ for $p_T > 2$ GeV as shown by
 543 Figure. 7. Thus, an enhancement of particle yields
 544 in p–A collisions compared to the expectation from
 545 pp collisions was observed. This effect is referred
 546 as “Cronin effect” and interpreted as multiple soft
 547 scatterings of incoming nucleons, which cause an
 548 additional p_T broadening of particles.

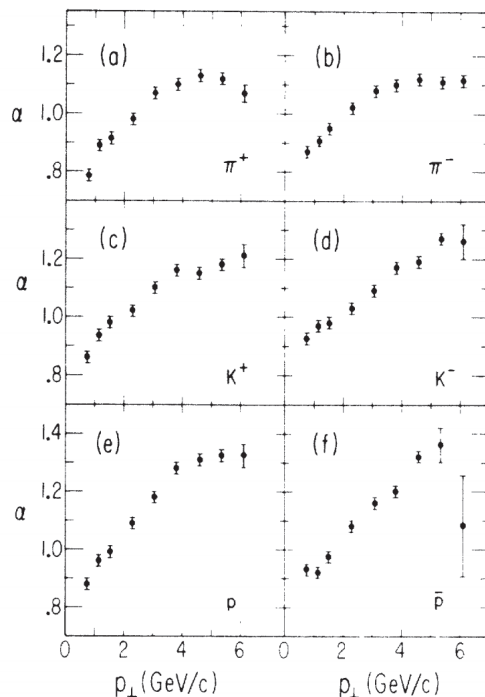


Figure 7: Power parameter α vs. p_T [15].

549 **Nuclear shadowing** Another initial effect is different parton distribution function in a nucleus.
 550 European Muon Collaboration (EMC) firstly reported that nuclear structure function in a nucleus
 551 is different from that in a free proton by deep inelastic scattering (DIS) with μ -Fe(d) collisions [17].
 552 This results in different parton distribution function in a nucleus from one in a free proton. Figure 8
 553 shows the ratio of nuclear structure function in a heavier ion to that in a Carbon ion measured by New Muon
 554 Collaboration (NMC) [16].
 555 $F_2^A/F_2^C < 1$ at $x < 0.07$ refereed as “shadowing”,
 556 $F_2^A/F_2^C > 1$ at $0.07 < x < 0.3$ refereed as “antishadowing” and there is a dip at $0.3 < x$ called
 557 “EMC effect”. The relevant x of a parton can be estimated from transverse momentum p_T of a leading
 558 hadron which carries the largest momentum fraction of the original scattered parton by means
 559 of :

$$x \approx \frac{2p_T}{\sqrt{s_{NN}}} \quad (6)$$

560 At LHC energies $\sqrt{s_{NN}} = 2.76 \sim 5.5$ TeV and leading $p_T^h \sim O(100)$ GeV, hence $x < 0.05$ where the shadowing effect is the most relevant.

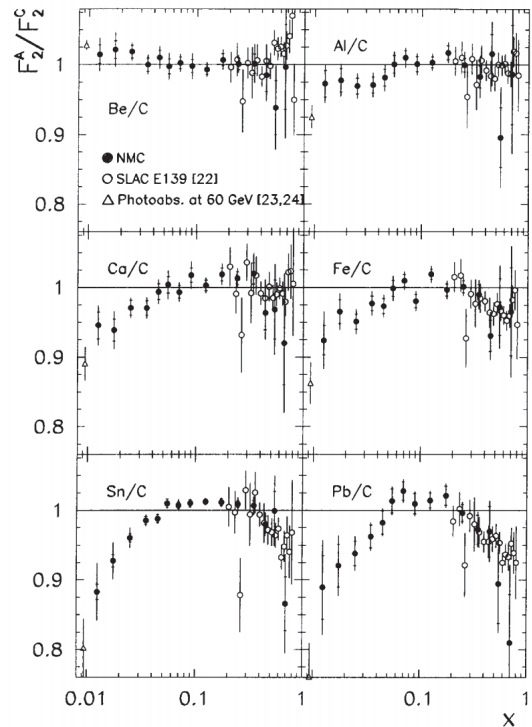


Figure 8: The ratio of nuclear structure function, in heavy nuclei to one in Carbon [16].

570 1.4.4 Parton energy-loss

571 One possible explanation for $R_{AA} < 1$ is parton energy-loss in interaction with the hot and
 572 dense QCD medium. By traversing the QCD medium, the parton loses its energy by elastic
 573 scattering or gluon radiation. Initially, only radiative energy-loss in static QCD medium (non-
 574 moving constituents) was assumed in theoretical models such as GLV [18, 19], DGLV [20],
 575 BDMPS[21, 22] till ~ 2008 . The radiative energy is similar to Bremsstrahlung of an electron
 576 in an electro-magnetic field. However, these calculation gave disagreement with experimental
 577 results. Then, one of theoretical models have included radiative energy-loss in dynamical QCD
 578 medium (moving constituents) [23, 24]. Currently, it is considered that radiative and elastic
 579 energy-losses are comparable in dynamical QCD medium [25, 26]. Theoretical models shown in
 580 this thesis are described below.

581 **DREENA-C [25] and DREENA-B [26]** Descriptions are taken from [25, 26]. DREENA
 582 stands for Dynamical Radiative and Elastic ENergy loss Approach and C denotes the constant-
 583 temperature QCD medium and B stands for Bjorken expansion of the QCD medium. They aim
 584 to calculate the nuclear modification factor R_{AA} and the azimuthal anisotropy v_2 simultaneously
 585 in their framework. First, let T be an averaged temperature of the medium, L be an averaged
 586 path-length traversed by particles and $\Delta E/E$ be fractional energy-loss. In a simple case for the
 587 purpose of these estimations, it is assumed that

$$\Delta E/E \approx \eta TL, \quad (7)$$

588 where η is a proportionality factor. The nuclear modification R_{AA} is commonly estimated [27]
589 as :

$$R_{AA} \approx \left(1 - \frac{1}{2} \frac{\Delta E}{E}\right)^{n-2}, \quad (8)$$

590 where n is the steepness of the initial momentum distribution function. Here, different path-
591 length between in-plane ($L_{in} = L - \Delta L$) and out-of-plane ($L_{out} = L + \Delta L$) is introduced. For the
592 constant-temperature QCD medium, the nuclear modification factor R_{AA} can be expressed as :

$$R_{AA} \approx \frac{1}{2}(R_{AA}^{in} + R_{AA}^{out}) \approx 1 - \xi TL, \quad (9)$$

593 The azimuthal anisotropy v_2 can be :

$$v_2 \approx \frac{1}{2} \frac{R_{AA}^{in} - R_{AA}^{out}}{R_{AA}^{in} + R_{AA}^{out}} \approx \frac{\xi T \Delta L}{2} \quad (10)$$

594 For the evolving system, the average temperature along in-plane is higher than that along out-
595 of-plane ($T_{in} = T + \Delta T$ and $T_{out} = T - \Delta T$). In this case,

$$R_{AA} \approx 1 - \xi TL, \quad (11)$$

596 and

$$v_2 \approx \frac{\xi T \Delta L - \xi \Delta T L}{2} \quad (12)$$

597 Therefore, DREENA-B and -C predict the similar R_{AA} , while the smaller v_2 is predicted by
598 DREENA-B. Only R_{AA} is compared to experimental data in this thesis.

599 1.5 Direct photons production

600 The direct photon is an unique tool to study space-time evolution of the hot and dense matter.
601 Direct photons are defined as photons not originating from hadron decays, for example $\pi^0 \rightarrow \gamma\gamma$,
602 $\eta \rightarrow \gamma\gamma$ and so on. Because they are not involved in the strong interaction, they carry undistorted
603 information at the time of their productions. Moreover, direct photons are divided into to two
604 sources. One is “thermal photon” originating from the thermal radiation from the hot and dense
605 medium. An averaged temperature T_{eff} of locally equilibrated medium over the all space-time
606 evolution can be measured by the p_T spectrum of thermal photons, assuming the Boltzmann
607 distribution $A \times \exp(-p_T/T_{eff})$. The previous measurement by PHENIX at RHIC reported $T_{eff} =$
608 $221 \pm 19(\text{stat.}) \pm 19(\text{syst.})$ MeV [28, 29] via virtual photons and $T_{eff} = 239 \pm 25(\text{stat.}) \pm 7(\text{syst.})$
609 MeV [30] via real photons in 0-20 % central Au–Au collisions at $\sqrt{s_{NN}} = 0.2$ TeV. In ALICE,
610 $T_{eff} = 294 \pm 12(\text{stat.}) \pm 47(\text{syst.})$ MeV [31] in 0-20 % central Pb–Pb collisions at $\sqrt{s_{NN}} = 2.76$ TeV.
611 The other one is “prompt photon” produced by initial hard scatterings between partons. The
612 prompt photon is a powerful probe to test pQCD calculations. Thermal photons are dominant
613 at low p_T ($1 < p_T < 3$) regime, while prompt photons exhibit at high p_T . Figure 9 illustrates
614 Feynman diagrams for direct photon productions. Thermal photons are also emitted from a hot
615 hadron gas (HHG), which is the last stage of collisions. Main constituents of the hot hadron gas
616 are pions and ρ mesons. They produce photon as $\pi^\pm \rho \rightarrow \pi^\pm \gamma$, $\pi^+ \pi^- \rightarrow \rho \gamma$ and $\rho \rightarrow \pi^+ \pi^- \gamma$.

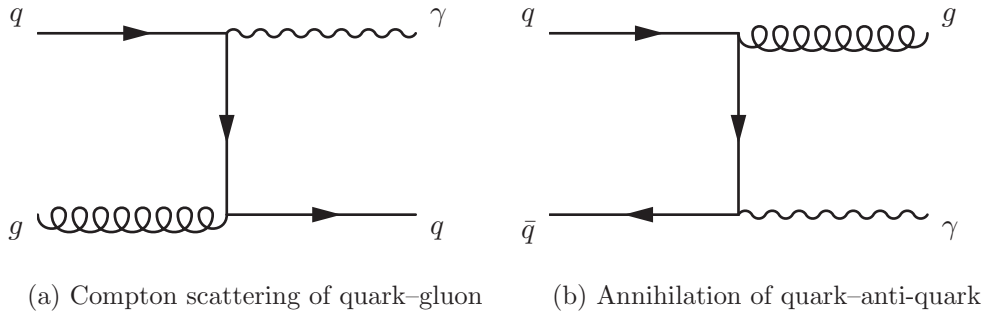


Figure 9: Feynman diagrams for direct photon productions

617 1.5.1 Pioneers of the direct photon measurement

618 WA80

619 The first attempt to measure thermal photons was performed by the WA80 (West Area) col-
 620 laboration [32, 33]. WA80 is a fixed-target experiment at the SPS in CERN colliding ^{16}O and
 621 ^{32}S beam at 200A GeV with Au. They reported upper limits on the direct photon yield at the
 622 90% confidence level in central ^{32}S -Au collisions by employing a statistical subtraction method,
 623 as shown by Figure 10b. It is a technique to subtract decay photon yields simulated by known
 624 sources (e.g. $\pi^0 \rightarrow \gamma\gamma$, $\eta \rightarrow \gamma\gamma$ e.t.c.) from inclusive photon yields. The dotted curve is the
 625 calculated thermal photon production from a QGP by reference [34]. The solid curve is the ex-
 626 pected thermal photon production from a hot hadron gas by reference [34]. The dashed curve is
 627 also thermal emissions from a hot hadron gas taken from reference [35]. This was the important
 628 step, as hadron gas scenarios were excluded by their upper limits.

629 WA98

630 WA98 [36, 37] is also a fixed-target experiment upgraded from WA80. The improvement was
 631 a lead glass calorimeter which has excellent energy resolution. The WA98 collaboration has
 632 measured direct photon yields in central 158A GeV Pb-Pb collisions for the first time. They
 633 used the same statistical subtraction method explained above. Figure 11a shows excess of direct
 634 photons beyond decay photons from known sources. The upper (lower) panel is for peripheral
 635 (central) collisions. If the ratio is greater than unity beyond statistical (bar at each point)
 636 and systematic (shaded band around unity) uncertainties, there are direct photons. Figure 11b
 637 shows invariant yields of direct photons in central 158A GeV Pb-Pb collisions. Clear direct
 638 photon signals were observed at $p_T > 1.5 \text{ GeV}c$. Downward arrows indicate upper limits at 90%
 639 confidence level.

640 1.5.2 Direct photon puzzle

641 The PHENIX collaboration at RHIC reported not only the invariant yield [30], but also the
 642 azimuthal anisotropy $v_2 = \langle \cos(2\Delta\varphi) \rangle$ of direct photons [38] at low p_T as shown by Figure 12.
 643 It was surprisingly a big discovery of the large v_2 of direct photons. The observed large v_2
 644 together with the large direct photon yield contradicts our interpretations. The large direct
 645 photon yield are produced at the very early stage, when the temperature of the medium is the
 646 highest where the collective flow of the medium is small. Contrary to this, the large v_2 suggests
 647 that photons are produced at the very late stage of the collision, when the collective flow of the
 648 system is fully developed where the temperature and the corresponding thermal emission rate is

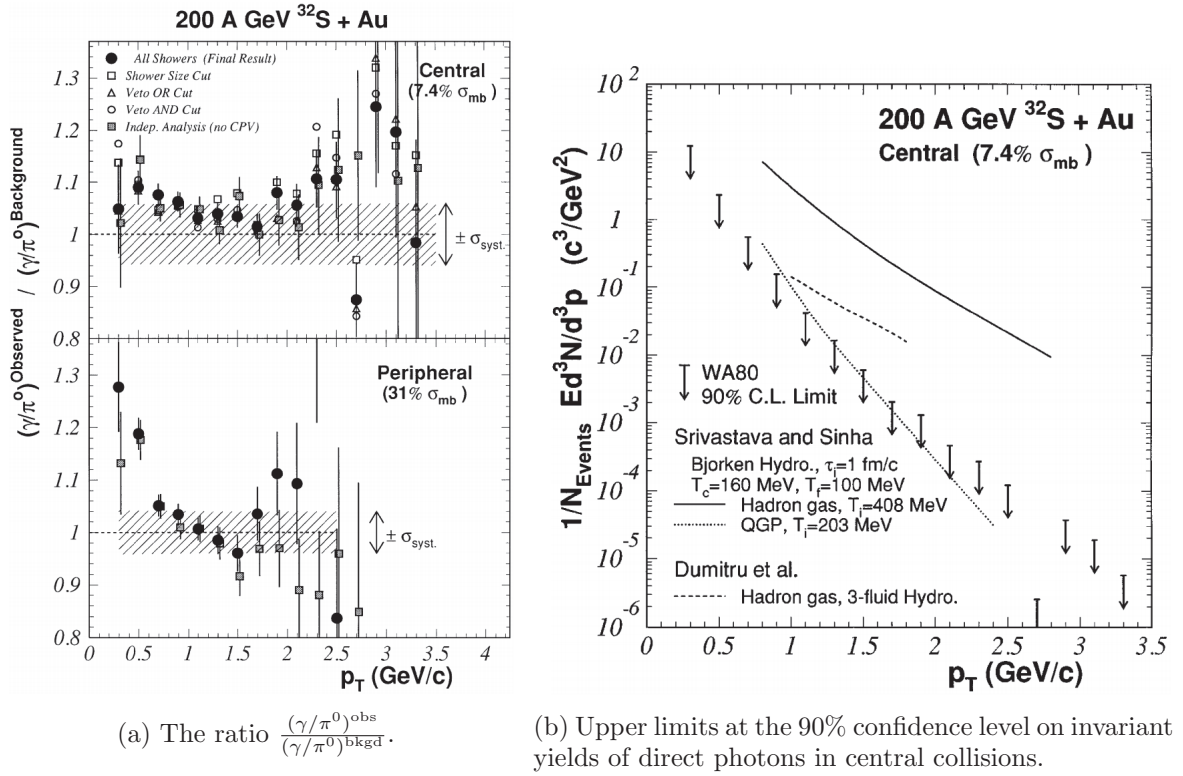


Figure 10: Results from WA80 [33].

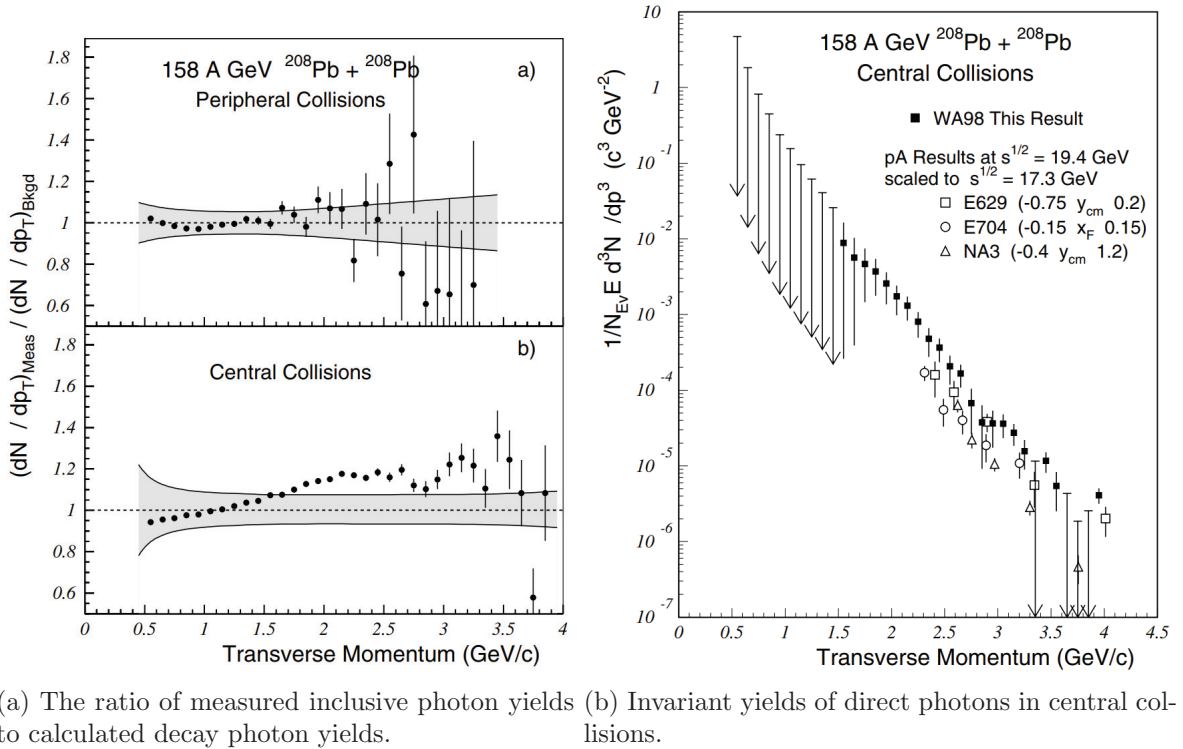


Figure 11: Results from WA98 [37].

649 small. Hence, there is difficulty in theoretical models to describe the large yield and the large
 650 v_2 for direct photons at the same time. This is called “direct photon puzzle”, which is not solved
 651 yet as of now. On the other hand, due to the large uncertainty, there is not direct photon puzzle
 at the LHC energy (Figure 13).

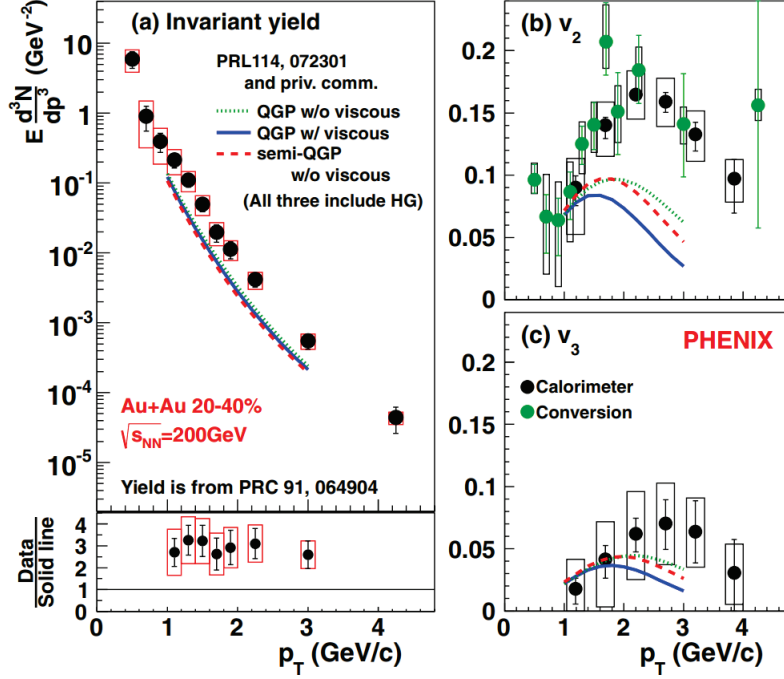


Figure 12: Direct photon yields and flow in 20-40 % Au–Au collisions at $\sqrt{s_{NN}} = 0.2$ TeV with PHENIX [30, 38].

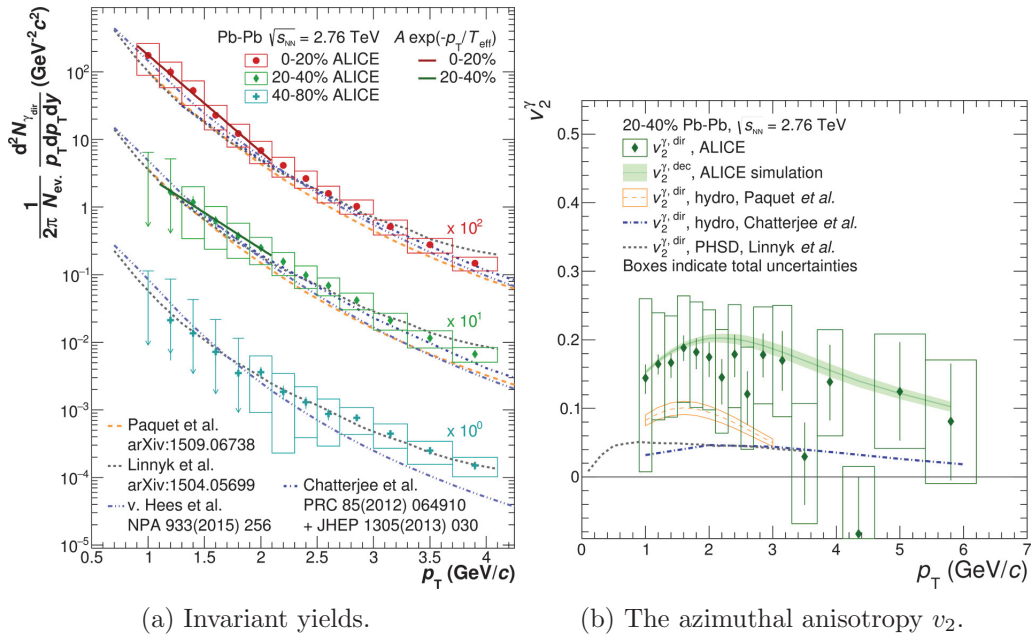


Figure 13: Direct photon yields and v_2 in 20-40% Pb–Pb collisions at $\sqrt{s_{NN}} = 5.02$ TeV with ALICE [31, 39].

653 1.6 Organization of this thesis

654 Neutral mesons (π^0 , η) and direct photon γ^{dir} production in pp and Pb–Pb collisions at $\sqrt{s_{\text{NN}}} = 5.02$ TeV in ALICE with the PHOS detector are described. This thesis is organized by
655 following. The LHC and ALICE detectors are introduced in Chapter 2. Data sets and its
656 quality assurance for this thesis are written in Chapter 3. Chapter 4 introduces analysis method
657 for neutral mesons measurements. Systematic uncertainties of neutral mesons measurements are
658 summarized in Chapter 5. Results of neutral mesons measurements are discussed in Chapter 6.
659 After that, analysis method for direct photons are given in Chapter 7. Systematic uncertainties
660 of inclusive and direct photons measurements are summarized in Chapter 8. Results of photons
661 measurements are discussed in Chapter 9. Finally, the conclusion of this thesis is in Chapter 10.
662

2 The LHC and the ALICE apparatus

This section is aimed at basic informations about the LHC accelerator at CERN and the ALICE detectors which are relevant to this thesis.

2.1 The Large Hadron Collider (LHC)

Descriptions about the LHC are taken from these references [40, 41, 42]. The Large Hadron Collider (LHC) is located at CERN across the border between France and Switzerland. The LHC underground tunnel was previously hosted by the Large Electron Positron (LEP) collider. It is the most powerful particle accelerator in the world, whose circumference length is 27 km. The LHC can collide protons at a center-of-mass energy up to 14 TeV and Pb ions up to 5.5 TeV per nucleon.

First, protons are produced from Hydrgen gas by stripping electrons in an electric field. They are accelerated through LINear ACcelerator 2 (LINAC2) up to 50 MeV and injected to a booster for Proton Synchrotron (PS). At the booster for PS, they are accelerated up to 1.4 GeV. PS accelerates proton beams up to 25 GeV, then sends them to Super Proton Synchrotron (SPS) where they are futher accelerated up to 450 GeV. Finally, proton beams are delivered to the LHC ring and accelerated up to 6500. The designed maximum energy is 7000 GeV per beam, but it is operated at 6500 GeV during Run2 which means center-of-mass energy is at 13 TeV. Lead (Pb) ions are produced by heating slid ^{208}Pb to make a vapour [43]. Ion beams are accelerated up to 4.2 MeV per nucleon by LINear ACcelerator 3 (LINAC3). Low Energy Ion Ring (LIER) takes them from LINAC3 and accelerates to 72 MeV/n. The rest of path is the same as proton beams, but beam energy is 5.9 GeV/n at the PS, 177 GeV/n at the SPS, 2510 GeV/n at the LHC.

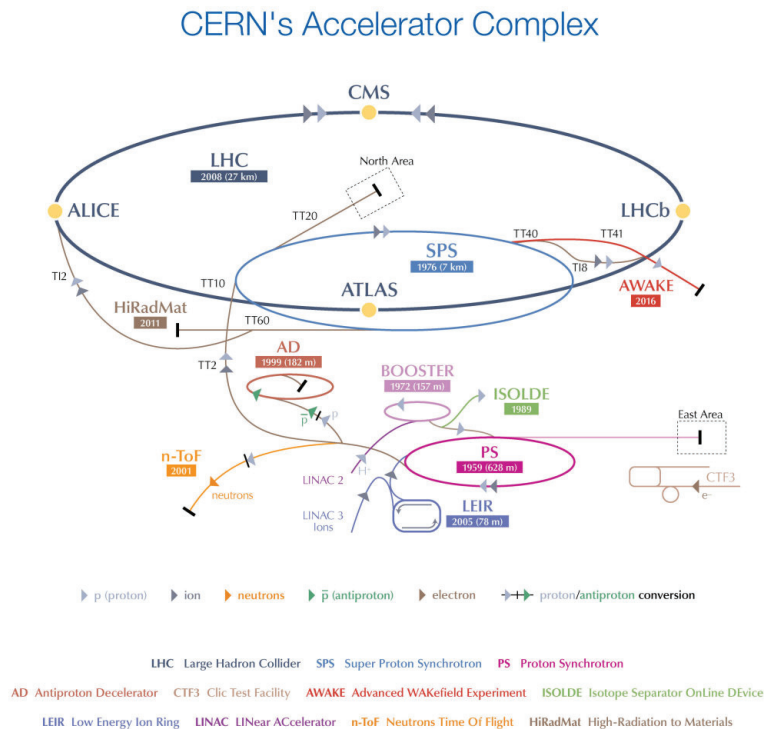


Figure 14: CERN accelerator complex [44].

2.2 ALICE apparatus

Detectors descriptions are taken from these references [45, 46].

2.2.1 Overview of ALICE apparatus

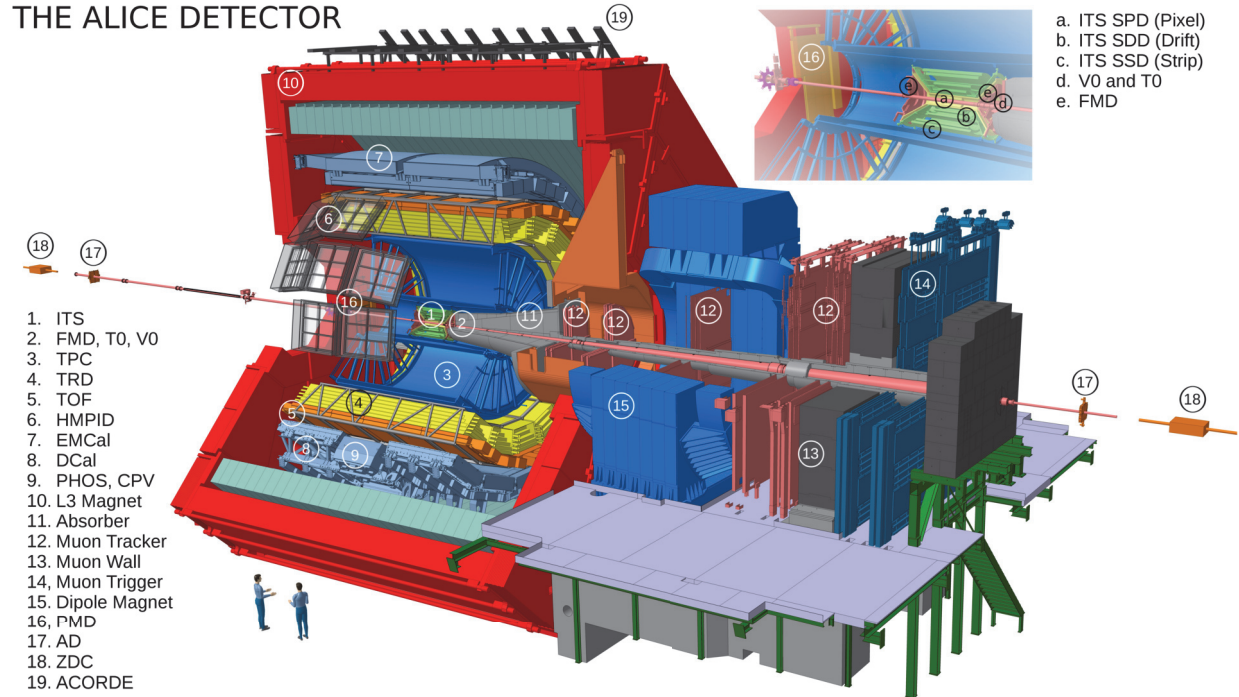


Figure 15: Overview of ALICE detectors in Run2

From the inner side of the central barrel, Inner Tracking System (ITS) which is six layers of silicon tracker and Time Projection Chamber (TPC) which also provides particle identification (PID) by ionization energy loss dE/dx are installed. They are central tracking systems to measure momenta of charged particles under a solenoid magnet $B = 0.5$ T in ALICE. Two type of electro-magnetic calorimeters (Photon Spectrometer (PHOS) and EMCal/DCal) are located from 4.6/4.4 m from a interaction point to measure photon and electron energy and its hit position. In addition to them, there are several PID detectors such as Time of Flight (TOF), High Momentum Particle Identification Detector (HMPID), Transition Radiation Detector (TRD) at mid-rapidity. Trigger detectors (VZERO, T0) are installed to study event property (e.g. event plane and multiplicity) at forward and backward rapidity. Zero Degree Calorimeter (ZDC) at forward and backward rapidity is used to reject events induced by beam-gas interactions. Muon tracker and trigger are installed at only forward rapidity under a dipole magnet $B = 0.7$ T. Hereafter, V0A(C) denotes VZERO detector at A(C)-side, same for T0. In ALICE, A-side is for $\eta > 0$ and C-side is for $\eta < 0$.

2.2.2 Basic kinematic variables in ALICE coordinate

The coordinate system in ALICE for emitted particles from the interaction point (IP) is right-handed Cartesian coordinate system (x, y, z) . The point $(0, 0, 0)$ is the center of ALICE detectors. The beam axis is in parallel to the z -axis and the x - y plane is transverse to the beam(z -) axis. The positive direction of x -axis is defined as the direction from the IP to the center of the LHC ring. The positive direction of y -axis is upward. More often, a spherical coordinate system

708 (r, θ, φ) is used. The azimuthal angle around the beam(z -) axis $\varphi = \arctan(y/x)$, the polar angle
 709 from beam(z -) axis $\theta = \arctan(\sqrt{x^2 + y^2}/z)$, and the distance from the IP $r = \sqrt{x^2 + y^2 + z^2}$.
 710 The azimuthal angle φ in the transverse plane starts from $\varphi = 0$ pointing to $x = 0$, the center
 711 of the LHC ring. Rapidity y of a particle is defined as :

$$y = \frac{1}{2} \ln \left(\frac{E + p_z}{E - p_z} \right),$$

712 where E is energy of the particle, p_z is momentum along the z -axis. Pseudo-rapidity η , the
 713 relativistic limit of rapidity y , is also used to point the particle position.

$$\eta = -\ln \left(\tan \left(\frac{\theta}{2} \right) \right)$$

714 Furthermore, to be Lorentz-invariant in high-energy particle physics, transverse momentum p_T
 715 which is momentum along the transverse plane is defined as :

$$p_T = p \sin \theta = \sqrt{p_x^2 + p_y^2}$$

716 Especially, p_T is important variable, as it is given by collisions.

717 The distance in $\eta - \varphi$ plane ΔR is used for jet reconstruction and particle isolation as :

$$\Delta R = \sqrt{\Delta \eta^2 + \Delta \varphi^2}$$

$$\Delta \eta = \eta_i - \eta_j$$

$$\Delta \varphi = \varphi_i - \varphi_j,$$

718 where $\eta_{i(j)}$, $\varphi_{i(j)}$ represent the position of particle $i(j)$.

719 **2.2.3 Trigger detectors**

720 **VZERO** The VZERO detector [47] consisting of 32×2 plastic scintillators covers $-3.7 <$
 721 $\eta < -1.7$ V0C and $2.8 < \eta < 5.1$ V0A. This detector provides minimum-bias (MB) triggers
 722 V0OR/V0AND. V0OR (INT5) requires at least one hit on either V0A or V0C. V0AND (INT7)
 723 requires at least one hit on each V0A and V0C. The VZERO detector also measures event
 multiplicity and event plane in Pb-Pb collisions.

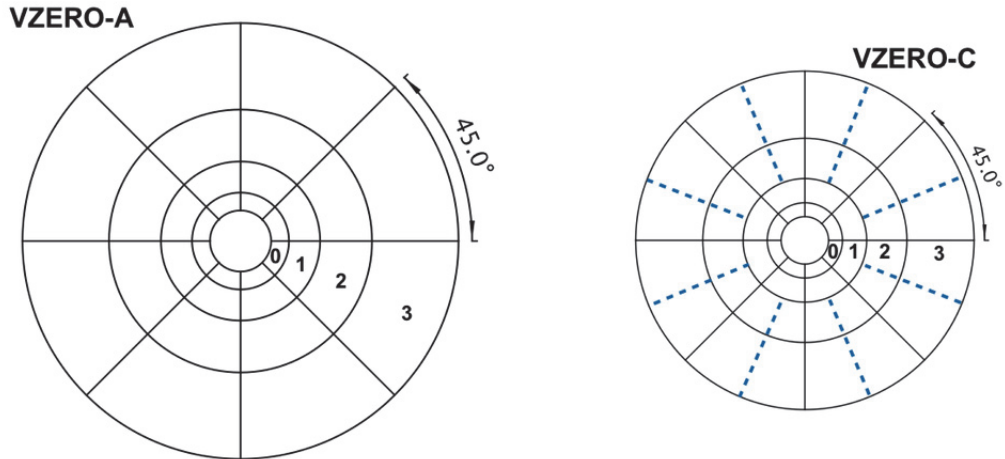


Figure 16: Sketches of V0A and V0C arrays [48].

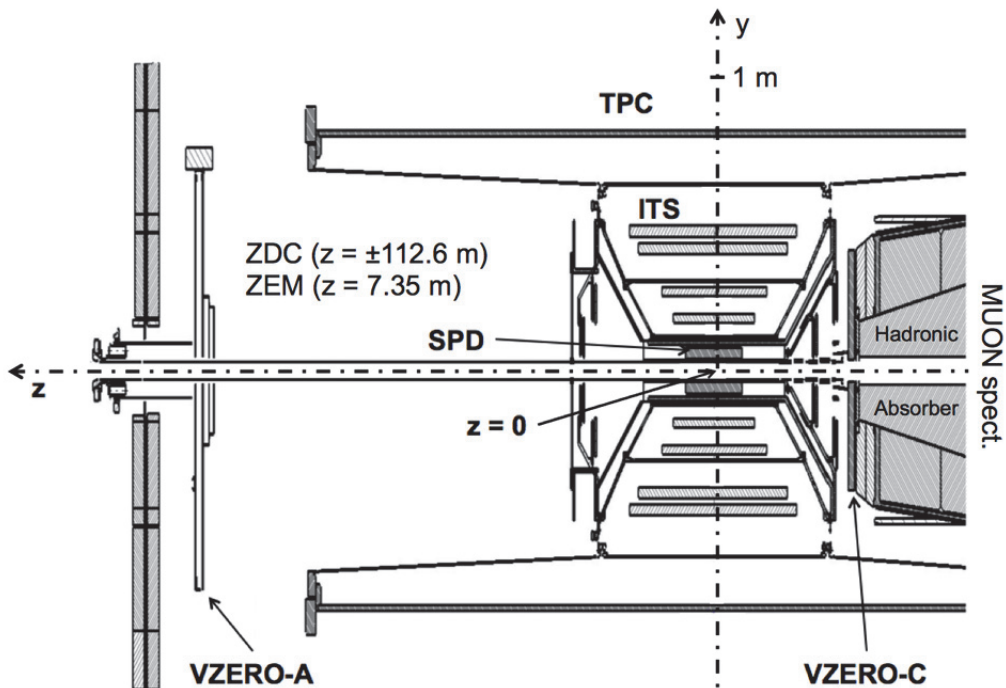


Figure 17: Position of VZERO (A-C) arrays and ITS around the beam pipe [48].

724

725 It also rejects beam-gas interactions by collision timing. As shown by Figure.19, three event
 726 classes are observed: collisions at (8.3 ns,14.3 ns), beam-gas interactions at (-14.3 ns,-8.3 ns)
 727 and (14.3 ns,8.3 ns).

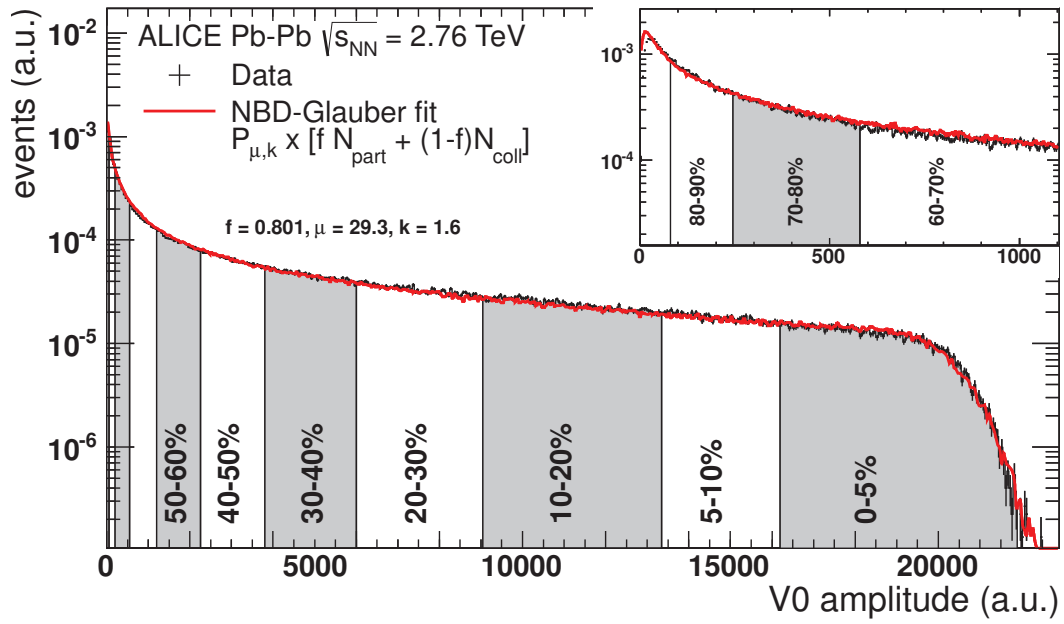


Figure 18: V0 (V0A + V0C) amplitude distribution [46].

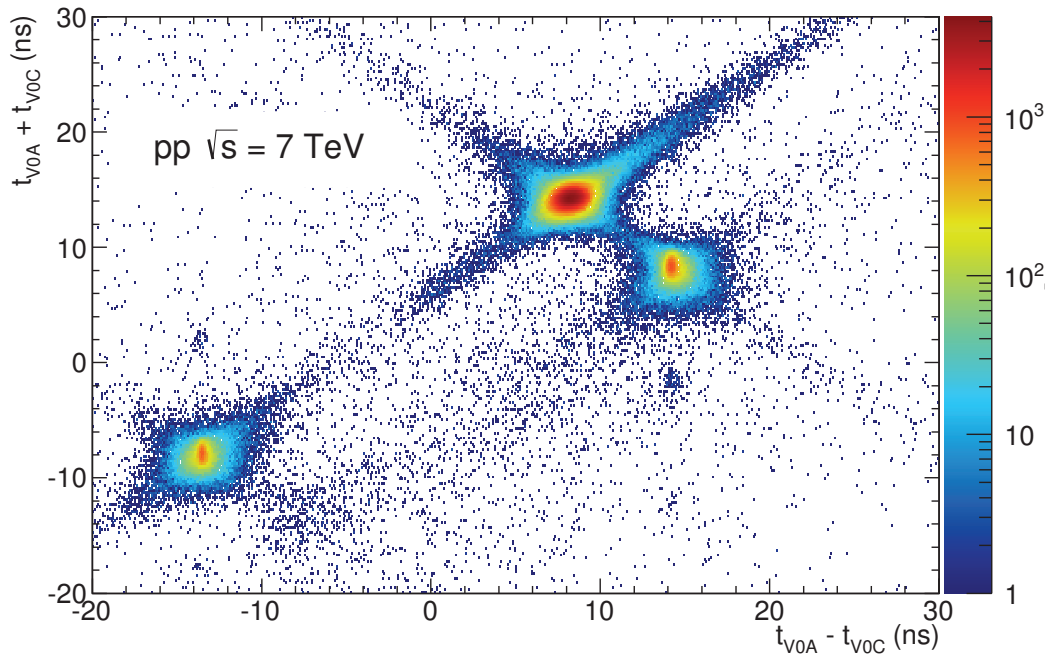


Figure 19: Correlation between the sum and the difference of hit timing of V0A and V0C [46].

728 **T0** The T0 detector [47], quartz Cherenkov detector, measures collision timing and the position
 729 of the interaction along the beam line precisely. It also delivers luminosity at IP2 to LHC
 730 operators. The acceptance of the T0 detector is $-3.3 < \eta < -3.0$ for T0C and $4.6 < \eta < 4.9$ for
 T0A.

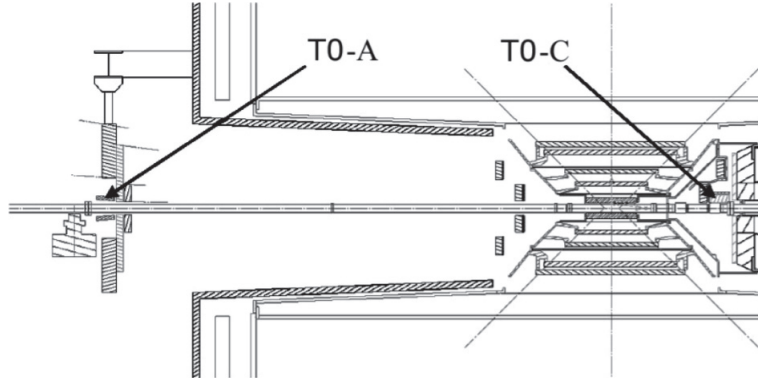


Figure 20: Positions of T0A and T0C [49].

731

732 2.2.4 Central Tracking System

733 **Inner Tracking System (ITS)** The ITS
 734 detector [51] is inner-most silicon tracker to
 735 reconstruct a primary vertex of a collision and
 736 momenta of charged particles. The coverage
 737 of the ITS is $|\eta| < 0.9$ and 2π in azimuth. It
 738 consists of three different types that are Sil-
 739 icon Pixel Detector (SPD), Silicon Strip De-
 740 tector (SSD) and Silicon Drift Detector (SDD)
 741 from inner to outer layer. Each of them has
 742 two layers. SSD and SDD also provide ioniza-
 743 tion energy loss dE/dx for PID at low trans-
 744 verse momentum.

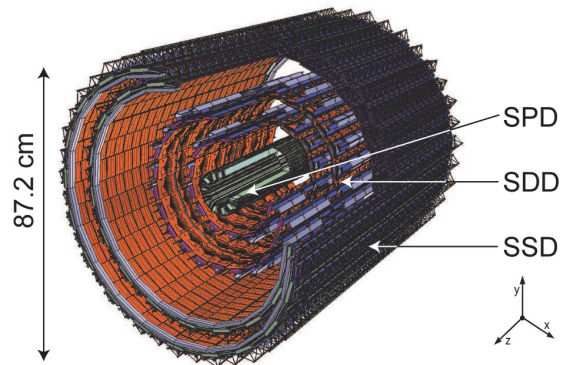


Figure 21: The layout of ITS [50].

745 **Time Projection Chamber (TPC)** TPC [54]
 746 is the main tracking detector which mea-
 747 sures momenta of charged particles and ion-
 748 ization energy loss dE/dx for PID in AL-
 749 ICE. Advantages of TPC are great spatial res-
 750 olution under high multiplicity environment
 751 $N_{ch} \sim O(10^3)$ produced by Pb–Pb collisions
 752 and strong PID performance. The coverage
 753 is $|\eta| < 0.9$, 2π in azimuth and its radius is
 754 between 85 and 250 cm around the beam axis.

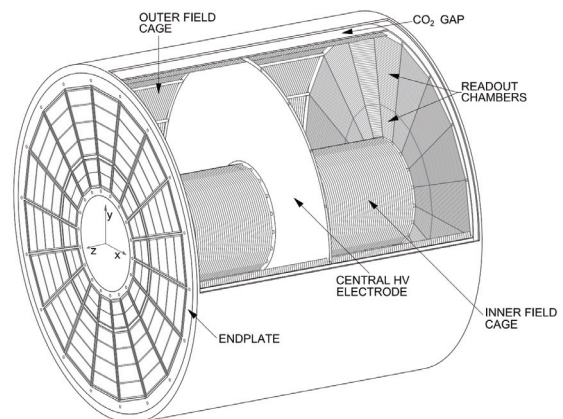


Figure 23: The layout of TPC [52, 53].

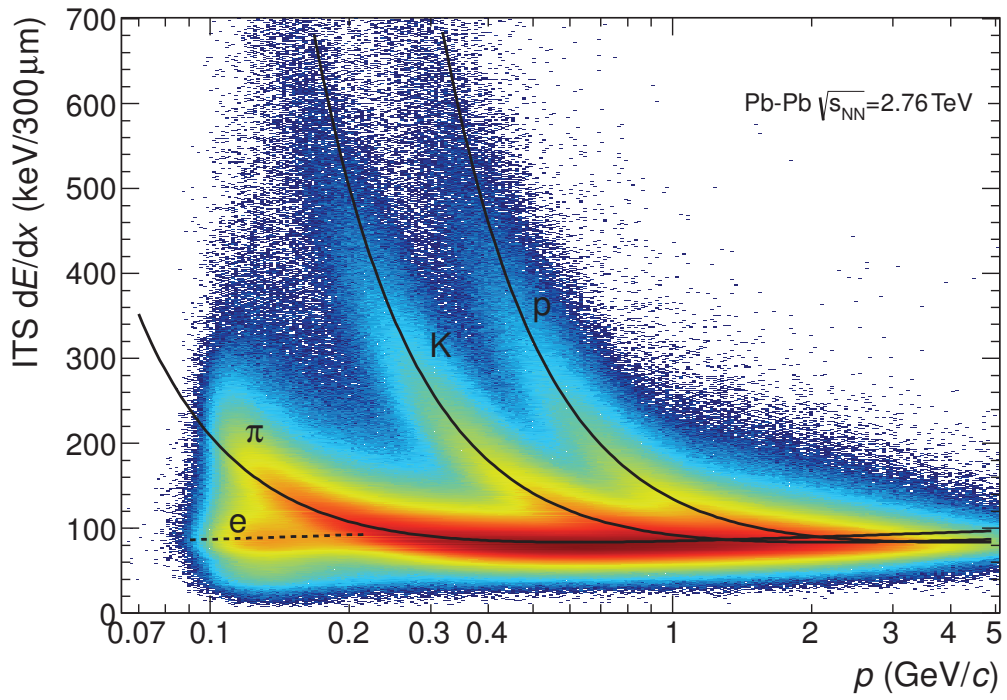


Figure 22: dE/dx measured in ITS standalone as a function momentum of charged particle [46].

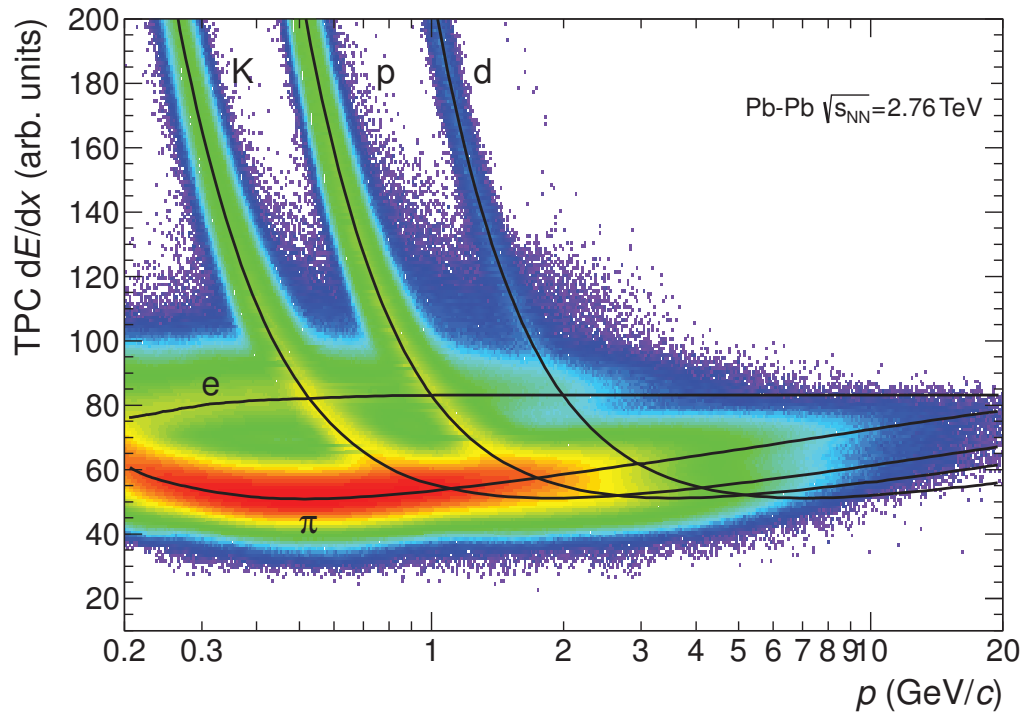


Figure 24: dE/dx measured in TPC as a function momentum of charged particle [46].

755 **2.2.5 Electro-magnetic calorimeters**

756 **Photon Spectrometer (PHOS)** PHOS [55, 45] is the main detector in this thesis. PHOS is
 757 a homogeneous electro-magnetic calorimeter located from 4.6 m from the interaction point. It
 758 consists of fine-segmented 12,544 PbWO₄ crystals readout by Avalanche Photo Diode (APD)s,
 759 operated at -25 degrees Celcius. A Moliere radius of the PbWO₄ crystal is 2.2 cm which allows us
 760 to distinguish two photons decayed from π^0 at high p_T with a small opening angle. A radiation
 761 length X_0 is 0.89 cm and a density is 8.29 g/cm³ for the PbWO₄ crystal. Volume of one crystal
 762 is $2.2 \times 2.2 \times 18$ cm³, which corresponds to 20 X_0 . The acceptance of the PHOS detector is
 763 $|\eta| < 0.12$, $250^\circ < \varphi < 320^\circ$, $\Delta\varphi = 20^\circ$ for one module. The energy resolution as a function of
 764 energy E in GeV is [56] :

$$\frac{\sigma_E}{E} (\%) = \sqrt{\left(\frac{0.013}{E}\right)^2 + \left(\frac{0.036}{\sqrt{E}}\right)^2 + (0.0112)^2}$$

765 The position resolution as a function of energy E in GeV is [55] :

$$\sigma_{x,z} (\text{mm}) = \sqrt{\left(\frac{3.26}{\sqrt{E}}\right)^2 + 0.44^2}$$

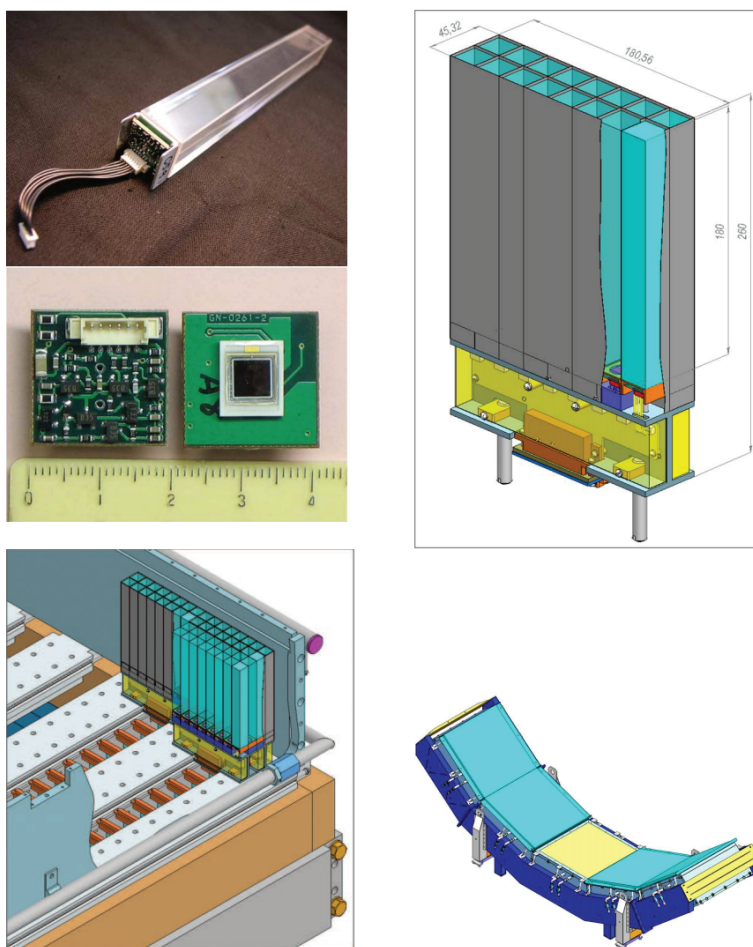


Figure 25: Elements of the PHOS detector.

767 PHOS is constructed as shown by Figure 25. The PbWO_4 crystal readout by the APD for
768 one element on top left, one strip unit has 8×2 elements on to right. One module consists of
769 $64 \times 56 = 3584$ elements on bottom left. Finally, there are three and a half modules are installed
770 in ALICE. (A half module have been installed since 2015.) The PHOS detector provides Level-
771 0 and Level-1 triggers to select events containing high energy deposition in the area of 4×4
772 cells on PHOS. Energy thresholds of triggers are configurable and were set to 4 GeV (L0) in
773 pp collisions at $\sqrt{s} = 5.02$ TeV (2017) and 8 GeV (L1 High), 4 GeV (L1 Midium) in Pb–Pb
774 collisions at $\sqrt{s_{\text{NN}}} = 5.02$ TeV (2015). The latency of the L0 and the L1 trigger is 1.2 and 7 μs
775 respectively [57].

776 2.2.6 Other detectors

777 ALICE detectors that are not relevant to this thesis (ACORDE, AD, CPV, EMCal, FMD,
778 HMPID, MCH, MTR, PMD, TOF, TRD, ZDC) are explained in [45, 46].

3 Data sets

The detailed event selection, cluster selection on PHOS and quality of data are described in this section.

3.1 Data sets in pp collisions at $\sqrt{s} = 5.02$ TeV

Minimum-bias events and PHOS triggered events have been analyzed in this these. The integrated luminosity used in this analysis is 19 nb^{-1} for Minimum-bias and 550 nb^{-1} for PHOS L0 triggered events respectively.

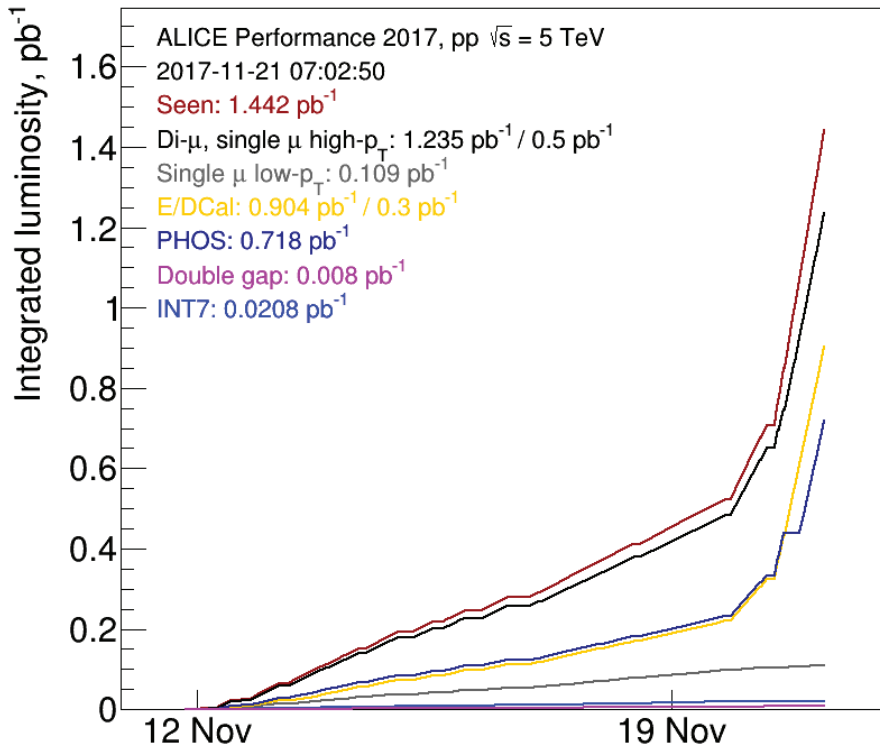


Figure 26: The integrated luminosity in pp collisions at $\sqrt{s} = 5.02$ TeV taken in 2017.

Run lists

LHC17p

282343, 282342, 282341, 282340, 282314, 282313, 282312, 282309, 282307, 282306, 282305, 282304, 282303, 282302, 282247, 282230, 282229, 282227, 282224, 282206, 282189, 282147, 282146, 282127, 282126, 282125, 282123, 282122, 282120, 282119, 282118, 282099, 282098, 282078, 282051, 282050, 282031, 282030, 282025, 282021, 282016, 282008.

LHC17q

282441, 282440, 282439, 282437, 282399, 282398, 282393, 282392, 282391, 282367, 282366, 282365.

In LHC17q, MB events were recorded in only 282367, 282366, 282365.

Monte-Carlo simulation samples

LHC17l3b PYTHIA8 for LHC17p-q (~ 200 M events)

LHC17j3[a,b,c][1,2] single particle simulation (π^0 , η , γ) for LHC17pq (main efficiency for correction in LHC17pq)

Event selection

physics selection (reject beam-gas interactions)
the number of charged track associated with the primary vertex > 0
pileup rejection by SPD
 $|Z_{\text{vtx}}| < 10$ cm

Minimal cluster selection

$E_{\text{cluster}} > 0.2$ GeV (to extract photon signal as much as possible at low energy)
 $M02 > 0.1$ cm for only $E > 1$ GeV (to extract photon signal as much as possible at low energy)
 $M20 > 0.1$ cm for only $E > 2$ GeV (to extract photon signal as much as possible at low energy)
 $M20 < 2.0$ cm (to remove clusters whose size is too large)
 $|\text{TOF}| < 12.5$ ns in real data (to remove photons from other bunch crossings)

The total number of events after these event selection is about 975 M MB events and 1.0 M PHOS triggered events. A cluster means “a group of cells”. Photons interact with PbWO_4 crystals and generate electro-magnetic showers, depositing energy in a group of cells around the impact point of each photon. This group of cells is defined as a cluster. The sum of amplitudes measured in each cell in the cluster is proportional to the initial photon energy. The center of gravity in cell coordinates weighted by the cell energy logarithmically defines the hit position. Second moments ($M20$, $M02$) of the cluster is used to discriminate electro-magnetic or hadronic showers [58, 59].

3.1.1 Quality assessment of MB data

The minimum-bias (MB) trigger configuration was V0AND (INT7 in Figure.26) in this data taking period. As a first check of PHOS data, an average cluster energy and an average number of hits are plotted. The average values are stable in all runs. π^0 peak parameters are plotted run-by-run to verify that PHOS was stable in this period. As a result, M1,2,3 are all stable. Especially, π^0 peak could not be seen well on M4, because M4 has limited detector acceptance. A peak position in M1,2,3 are consistent within statistical error bar. There are poor statistics in some runs where π^0 peak is not so clear. M4 was excluded from the beginning because a systematic uncertainty of material budget is large in front of M4 due to TOF + TRD, which is not suitable for the precise photon measurement.

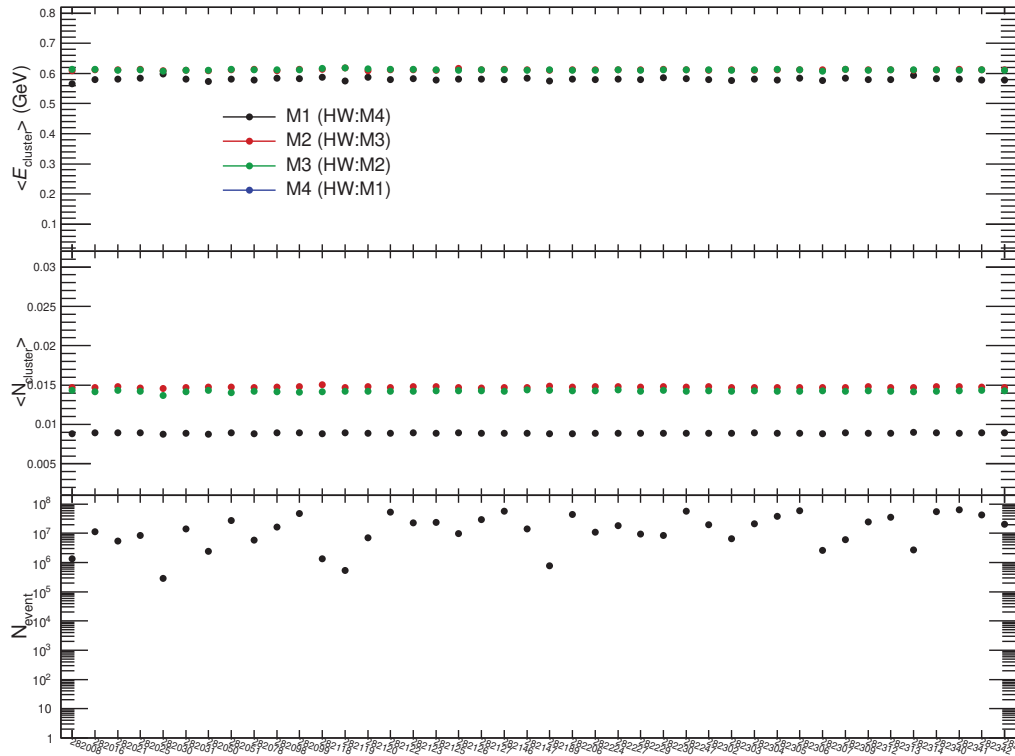


Figure 27: The average cluster energy and number of hits in each run on PHOS in LHC17p pass1.

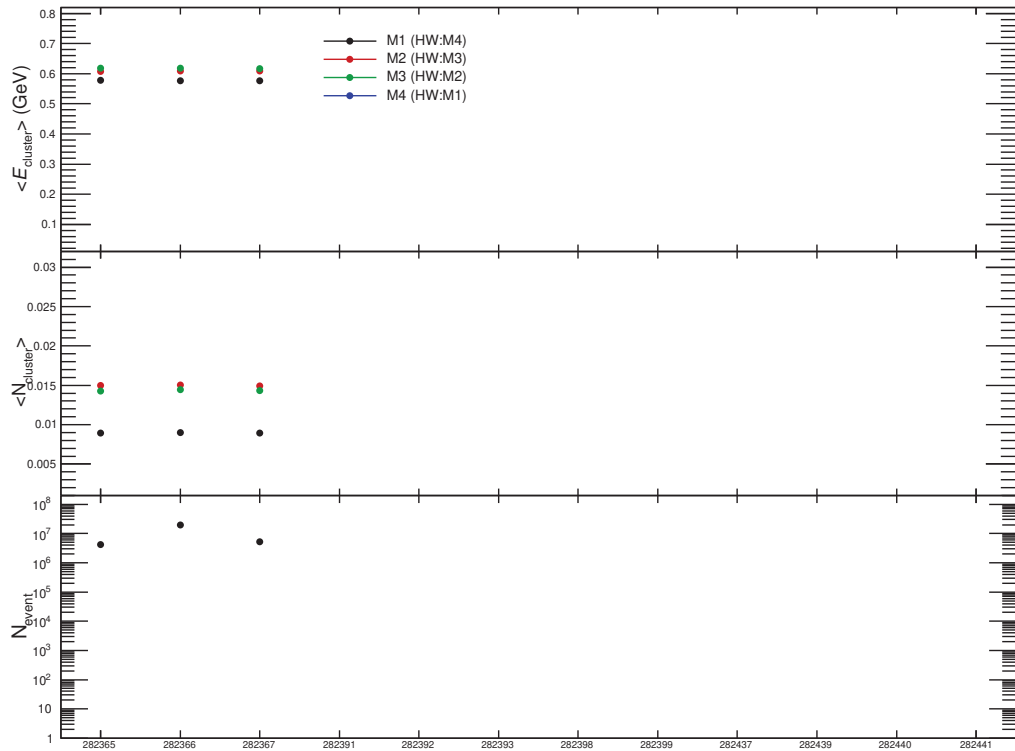
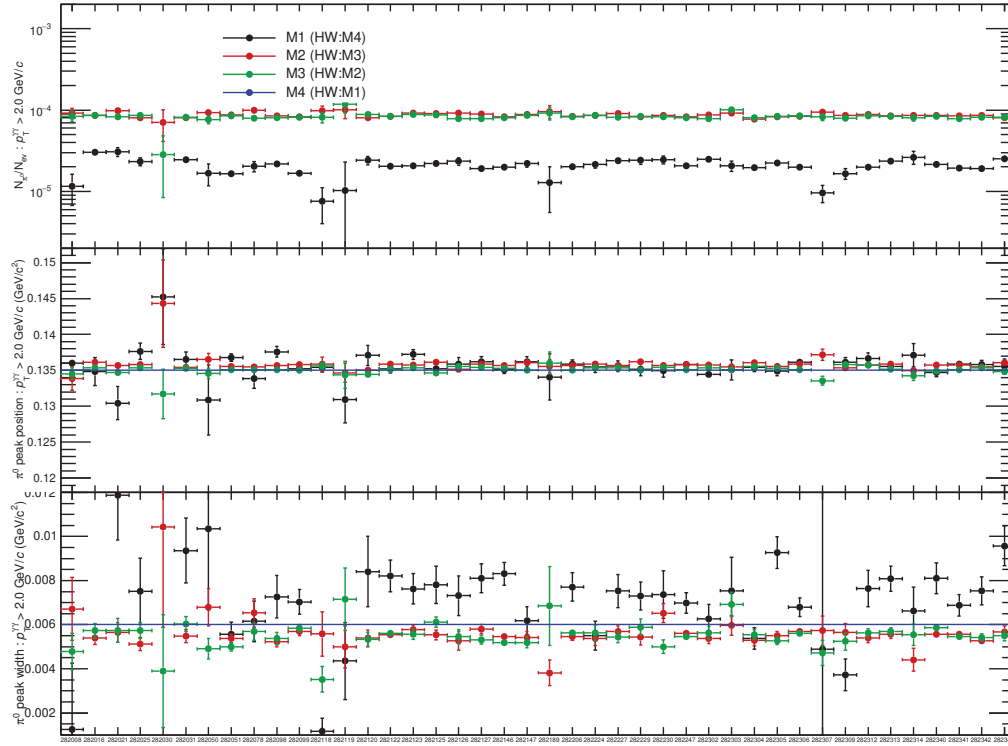
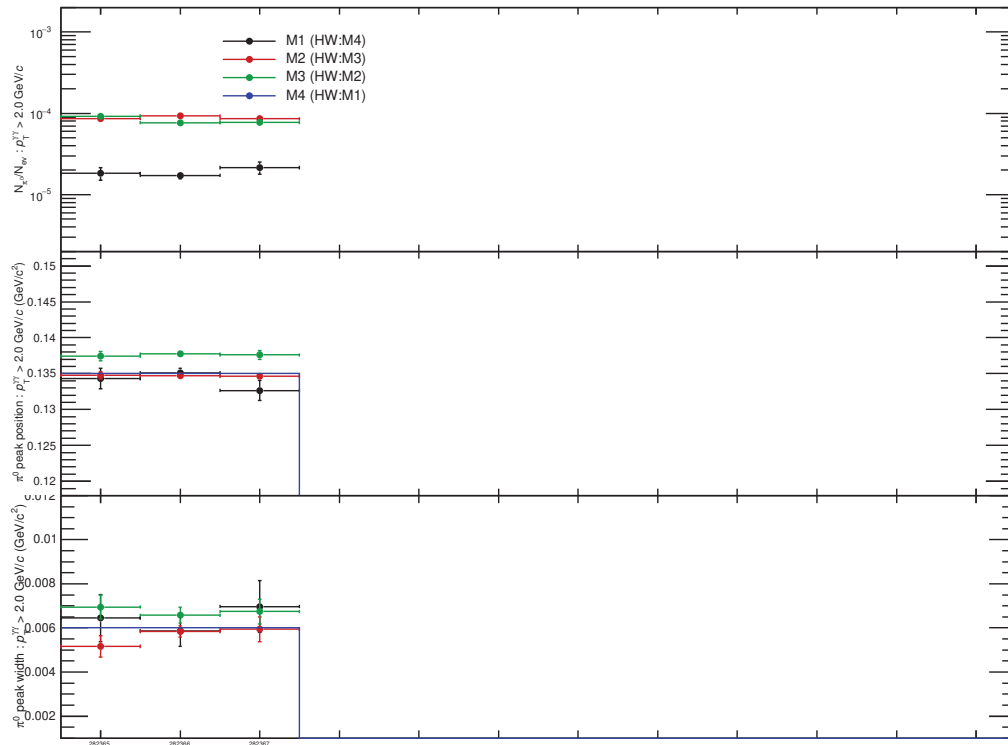
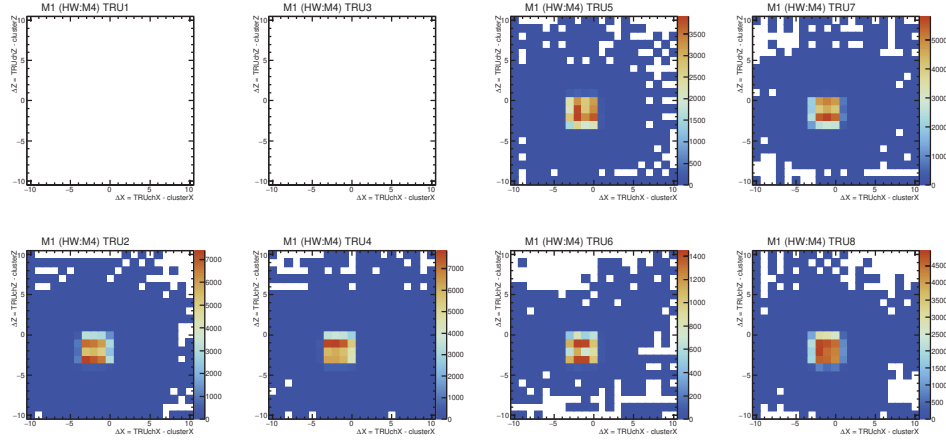


Figure 28: The average cluster energy and number of hits in each run on PHOS in LHC17q pass1.

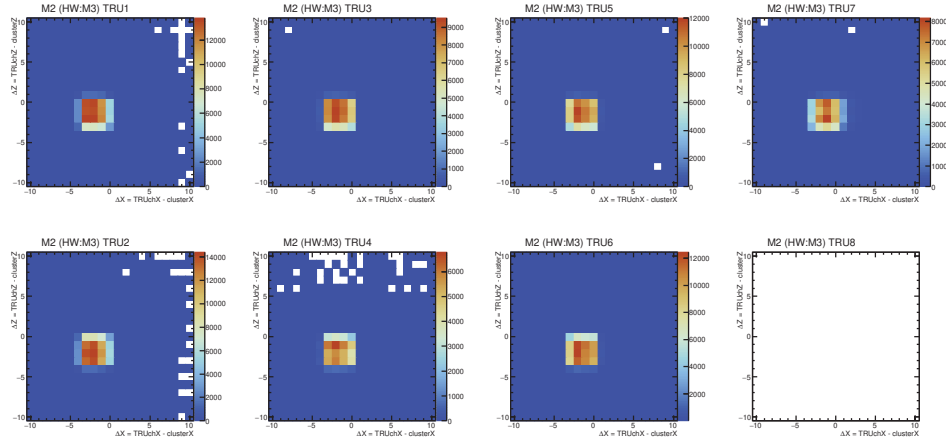
Figure 29: π^0 yield, peak position and sigma in each run in LHC17p pass1.Figure 30: π^0 yield, peak position and sigma in each run in LHC17q pass1.

834 3.1.2 Quality assessment of PHOS triggered data

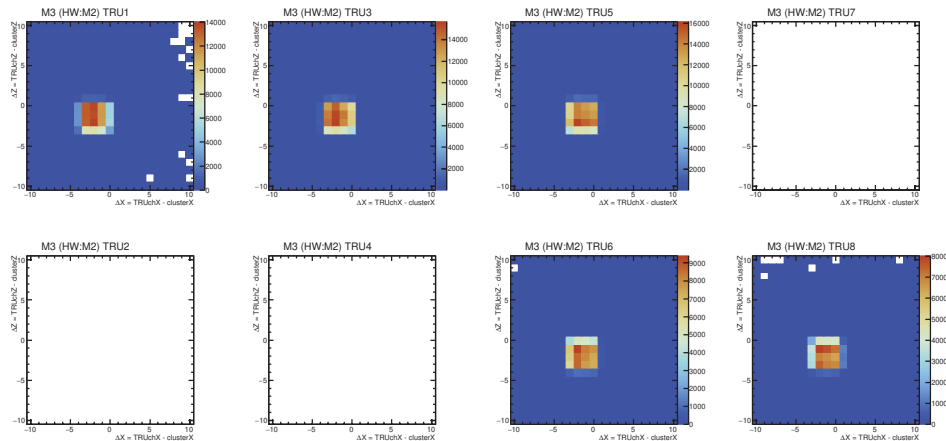
835 In addition to minimal event selection described above, at least one high energy hit on PHOS
836 is required for the PHOS trigger. Additional quality assessments were performed in case of
837 PHOS triggered data. PHOS L0 trigger decision is taken by each TRU by the sliding window
838 algorithm. If analogue sum of 2×2 FastORs ($= 4 \times 4$ cells) is greater than the threshold,
839 PHOS L0 trigger fires. On the other hand, PHOS L1 trigger decision is taken by STU. STU
840 stands for Summary Trigger Unit and it is new trigger device since Run2. STU summarizes all
841 TRU information and scan them by the same sliding window algorithm beyond TRU borders.
842 Thanks to STU, PHOS L1 trigger can detect high energy hits between borders of TRUs, while
843 L0 can not. At first, one has to check distance between a fired TRU channel and cluster hit
844 positions in X and Z coordinate respectively. Since TRU stores cell indices at the bottom-left of
845 fired channels, a typical distance is expected to be $[-3,0]$ in X and $[-3,0]$ in Z. Figure 31 proves
846 that the typical distance is $[-3,0]$ in X and $[-3,0]$ in Z. Based on this fact, a matching criterion
847 between a fired TRU channel and a cluster is set to $[-3,0]$ in X and $[-3,0]$ in Z respectively. The
848 dead TRUs are in white (Figure 31,32). PHOS triggered events must contain at least one cluster
849 which matches the fired TRU channel decided by the criterion based on the distance between
850 fired TRU channels and clusters. Fig.32 shows energy distribution in PHOS L0 triggered events.
851 The matching efficiency is close to 100% above the trigger threshold at 4 GeV in pp collisions
852 at $\sqrt{s} = 5.02$ TeV (LHC17pq). The rejection factor of the PHOS L0 trigger in pp collisions at
853 $\sqrt{s} = 5.02$ TeV is stable at 30.6 k as shown by Figure 33.



(a) The distance between fired TRU channels and cluster position on M1 in LHC17pq.

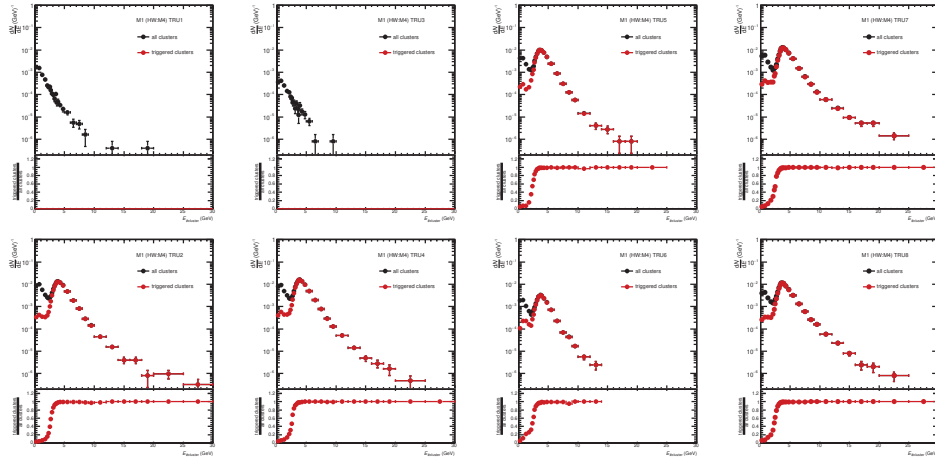


(b) The distance between fired TRU channels and cluster position on M2 in LHC17pq.

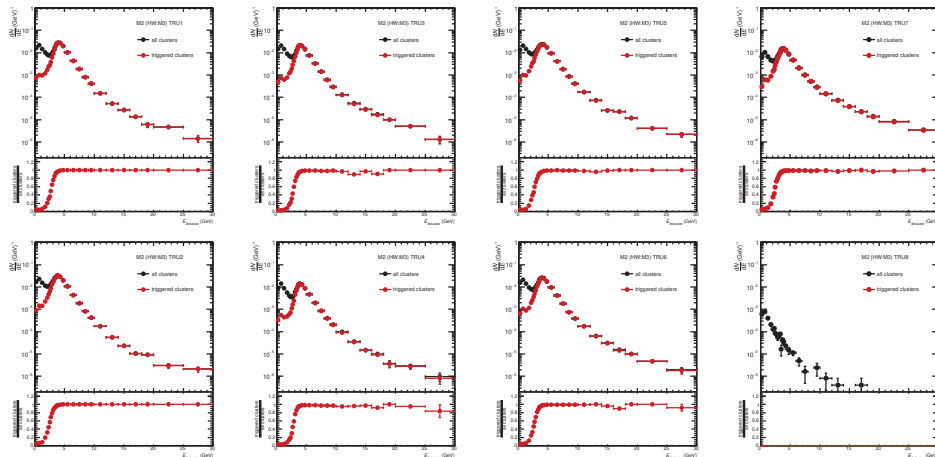


(c) The distance between fired TRU channels and cluster position on M3 in LHC17pq.

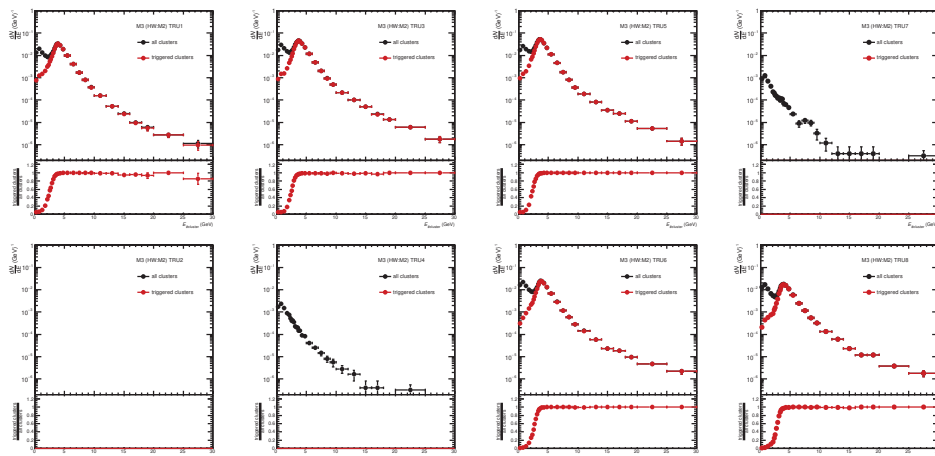
Figure 31: The distance between fired TRU channels and cluster position in different module for $E_{\text{cluster}} > 4$ GeV in LHC17pq.



(a) Energy distribution on M1 in LHC17pq.



(b) Energy distribution on M2 in LHC17pq.



(c) Energy distribution on M3 in LHC17pq.

Figure 32: Energy distribution of all clusters and triggered clusters and ratios in LHC17pq.

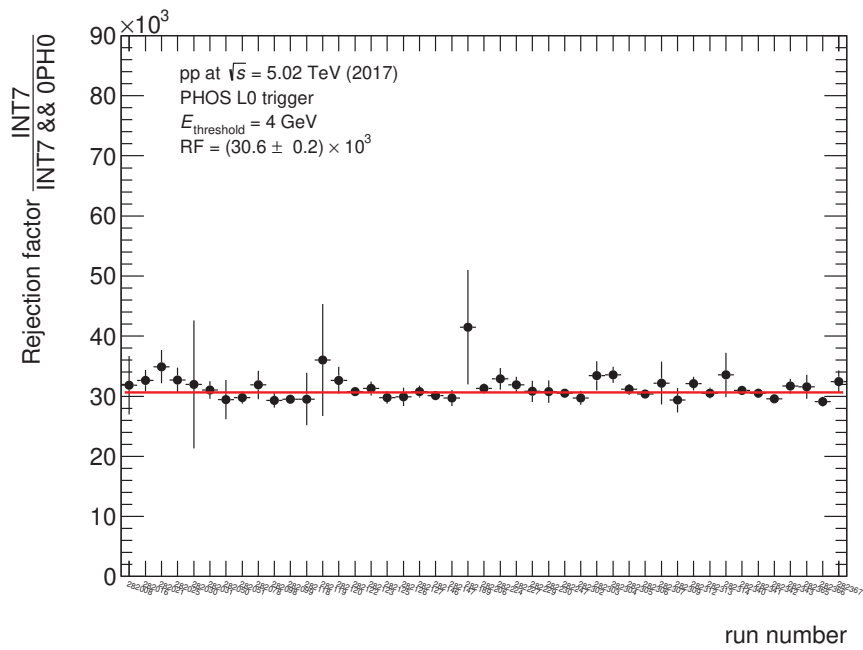
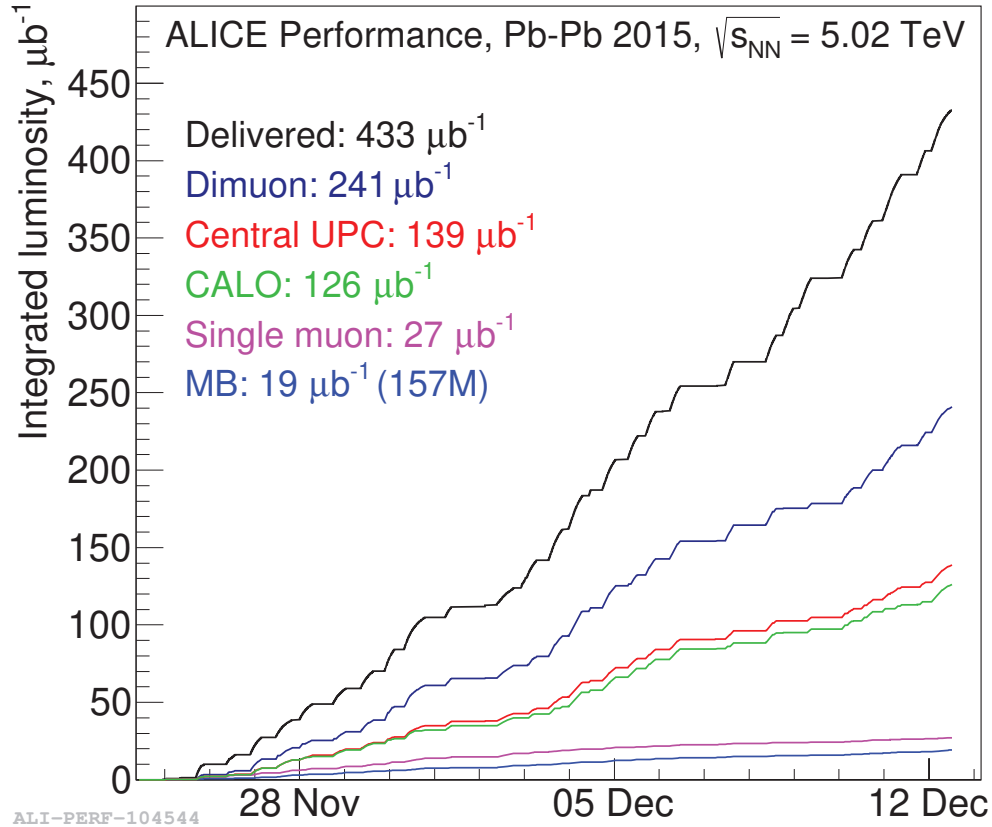


Figure 33: The rejection factor of PHOS L0 trigger (run-by-run) in pp collisions at $\sqrt{s} = 5.02$ TeV

854 **3.2 Data sets in Pb–Pb collisions at $\sqrt{s_{\text{NN}}} = 5.02$ TeV**855 The integrated luminosity used in this analysis is $12 \mu\text{b}^{-1}$ for Minimum-bias and $70 \mu\text{b}^{-1}$ for PHOS L1 triggered events respectively.Figure 34: The integrated luminosity in Pb–Pb collisions at $\sqrt{s_{\text{NN}}} = 5.02$ TeV taken in 2015.

856

857 **Run lists**858 **LHC15o**

859 pass1

860 246982, 246980, 246937, 246930, 246928, 246867, 246865, 246855, 246851, 246847, 246846,
 861 246845, 246844, 246810, 246809, 246808, 246807, 246805, 246804, 246766, 246765, 246763,
 862 246760, 246759, 246758, 246757, 246751, 246750, 246676, 246675, 246495, 246493, 246488,
 863 246487, 246434, 246431, 246428, 246424, 246275, 246271, 246225, 246222, 246217, 246185,
 864 246182, 246181, 246180, 246178, 246153, 246152, 246151, 246148, 246115, 246113, 246089,
 865 246087, 246049, 246048, 246042, 246037, 246036, 246012, 246003, 246001, 245963, 245954,
 866 245952, 245949, 245923, 245831, 245829, 245705, 245702, 245700, 245692, 245683.

867 pass1_pidfix

868 245545, 245544, 245543, 245542, 245540, 245535, 245507, 245505, 245504, 245501, 245497,
 869 245496, 245454, 245453, 245452, 245450, 245446, 245441, 245439, 245410, 245409, 245407,
 870 245401, 245397, 245396, 245353, 245349, 245347, 245346, 245345, 245343, 245259, 245233,
 871 245232, 245231, 245152, 245151, 245146, 245145

872 low_IR pass5

873 246392, 246391, 246390, 245068, 245066, 245064, 244983, 244982, 244980, 244975, 244918

874

Monte-Carlo simulation samples

LHC16g1[a,b,c] HIJING for LHC15o (~ 10 M events)
 LHC17i7[a,b,c][1,2] single particle simulation (π^0 , η , γ) for LHC15o (main efficiency for correction in LHC15o)

Event selection

physics selection (reject beam-gas interactions)
 the number of charged track associated with the primary vertex > 0
 pileup rejection by SPD
 $|Z_{\text{vtx}}| < 10$ cm
 centrality estimator : V0 multiplicity (V0M)

Minimal cluster selection

$E_{\text{cluster}} > 0.2$ GeV (to extract photon signal as much as possible at low energy)
 $M02 > 0.1$ cm for only $E > 1$ GeV (to extract photon signal as much as possible at low energy)
 $M20 > 0.1$ cm for only $E > 2$ GeV (to extract photon signal as much as possible at low energy)
 $M20 < 2.0$ cm (to remove too large size cluster)
 $|\text{TOF}| < 50.0$ ns in real data (to remove photons from other bunch crossings)

3.2.1 Quality assessment of MB data

The minimum-bias (MB) trigger configuration was V0AND (MB in Figure.34) in this data taking period. As a first check of PHOS data, an average cluster energy and an average number of hits are plotted here. Average values stay stable in all runs. π^0 peak parameters are plotted (Figure.38, Figure.39 and Figure.40) run-by-run to verify that PHOS was stable in this period. As a result, M1,2,3 are all stable. Especially, π^0 peak could not be seen well on M4, because M4 has limited detector acceptance. A peak position in M1,2,3 are consistent within statistical error bar. There are poor statistics in some runs where π^0 peak is not so clear. Note that M4 was excluded from analyses in Pb–Pb, too.

3.2.2 Quality assessment of PHOS triggered data

In this data taking period (LHC15o), 2 different L1 triggers that are high (L1H) and medium (L1M) threshold triggers were active. As it has been known that PHOS L1 triggers on M3 did not work because of poor matching efficiency between trigger units and readout units from the beginning of analyses in this data taking period, Since STU stores cell indices at the top-left of fired channels, a typical distance is expected to be $[-3,0]$ in X and $[-1,2]$ in Z. Based on Figure 41 and 42, a matching criterion between a fired TRU channel and a cluster is set to $[-3,0]$ in X and $[-3,0]$ in Z for module 1 and $[-3,0]$ in X and $[-1,2]$ in Z for module 2. M3 is excluded from trigger analyses in Pb–Pb collisions at $\sqrt{s_{\text{NN}}} = 5.02$ TeV. The matching efficiency is close to 100% above the trigger thresholds at 4 GeV for medium (L1M) and 8 GeV for high (L1H) in Pb–Pb collisions at $\sqrt{s_{\text{NN}}} = 5.02$ TeV (LHC15o). The rejection factor of PHOS L1 triggers in Pb–Pb collisions at $\sqrt{s_{\text{NN}}} = 5.02$ TeV is stable at 9.66 k for L1H and 0.835 k for L1M as shown by Figure 45. According to Figure 45a, runs 245233, 245439 and 246391 have small rejection, which means the L1H trigger have fired too often. Thus, these 3 runs were excluded from PHOS L1 trigger analyses.

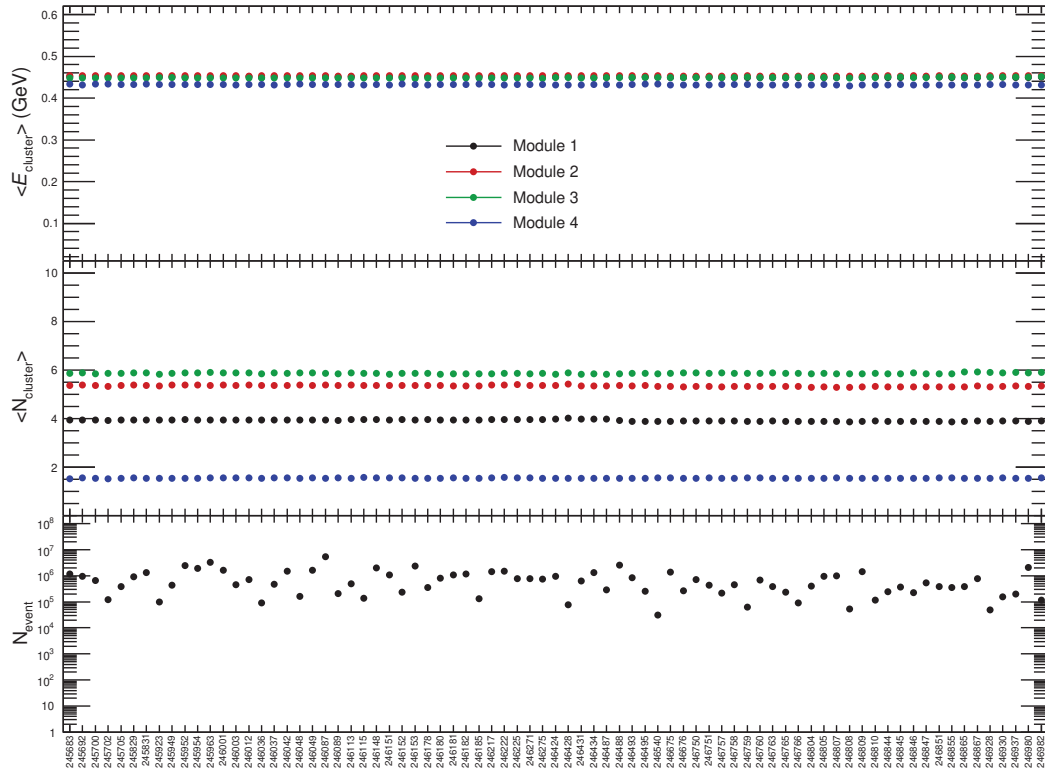


Figure 35: The average cluster energy and number of hits in each run on PHOS in LHC15o pass1.

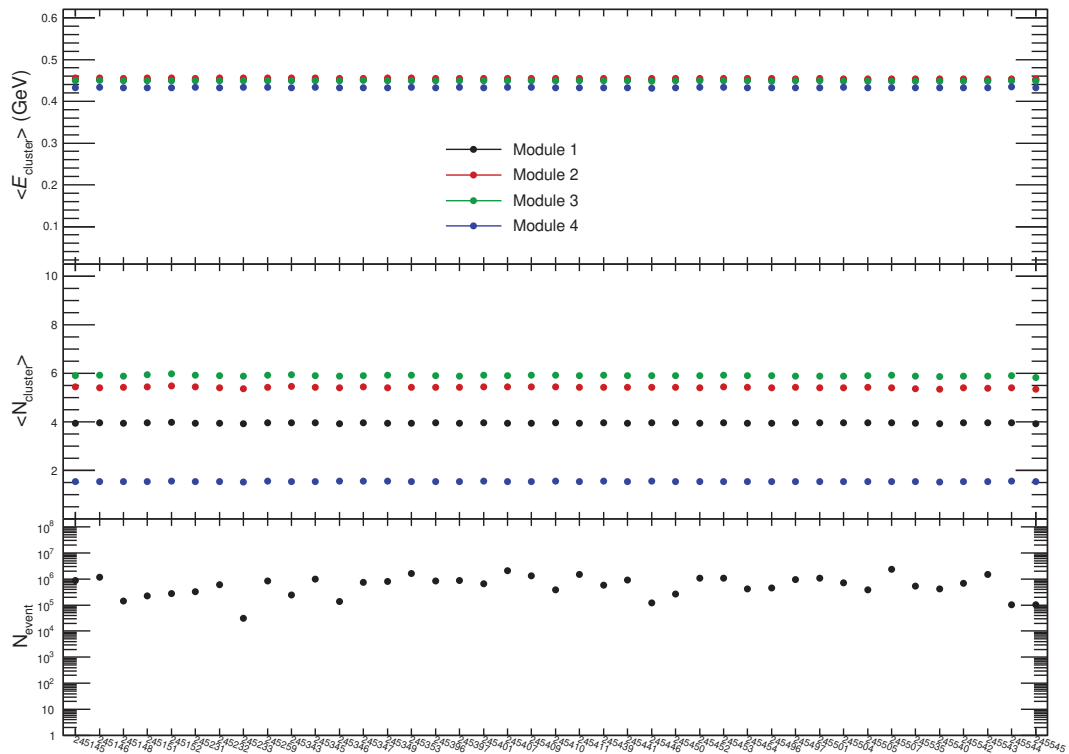


Figure 36: The average cluster energy and number of hits in each run on PHOS in LHC15o pass1_pidfix.

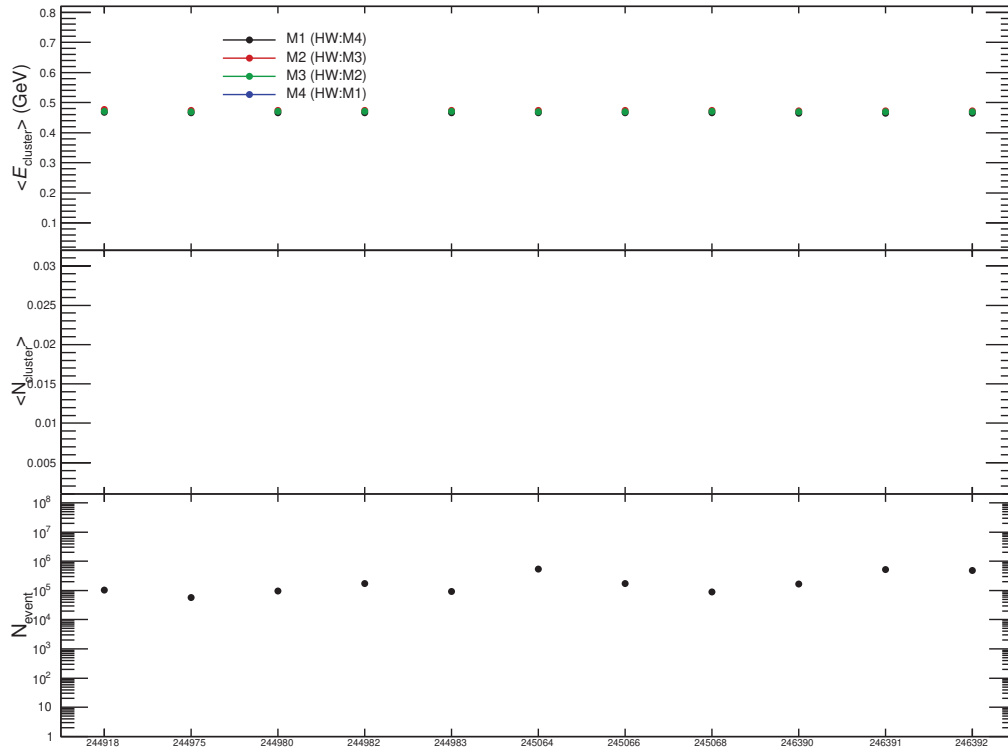


Figure 37: The average cluster energy and number of hits in each run on PHOS in LHC15o lowIR pass5.

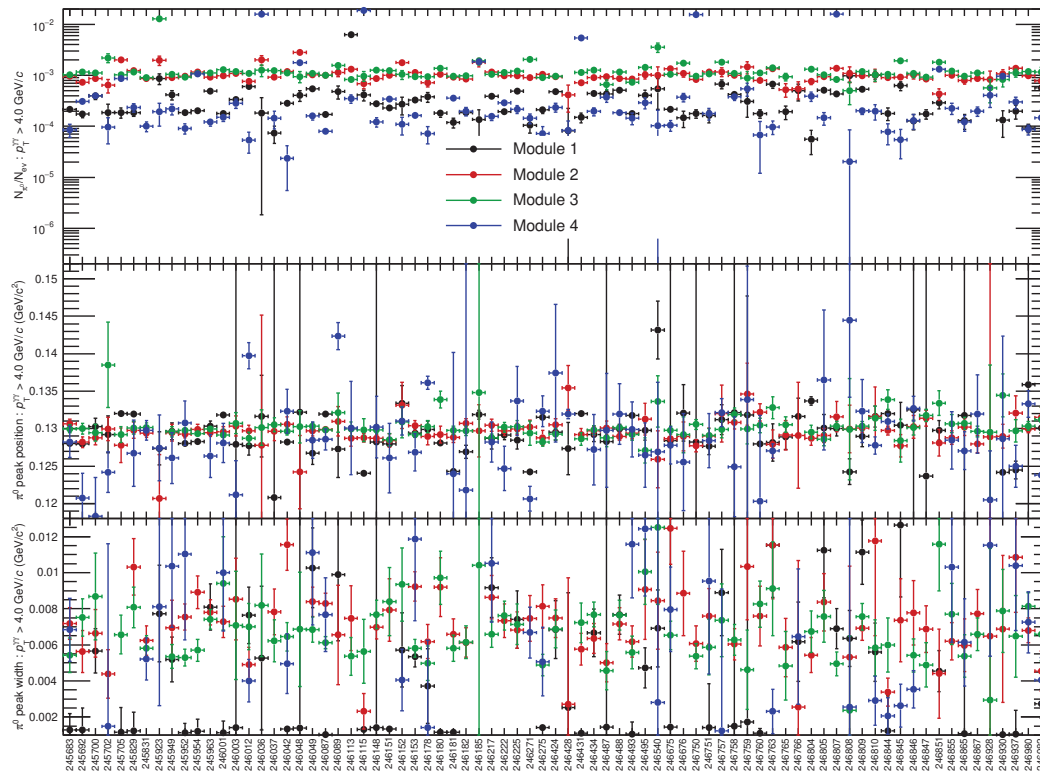


Figure 38: π^0 yield, peak position and sigma in each run in LHC15o pass1.

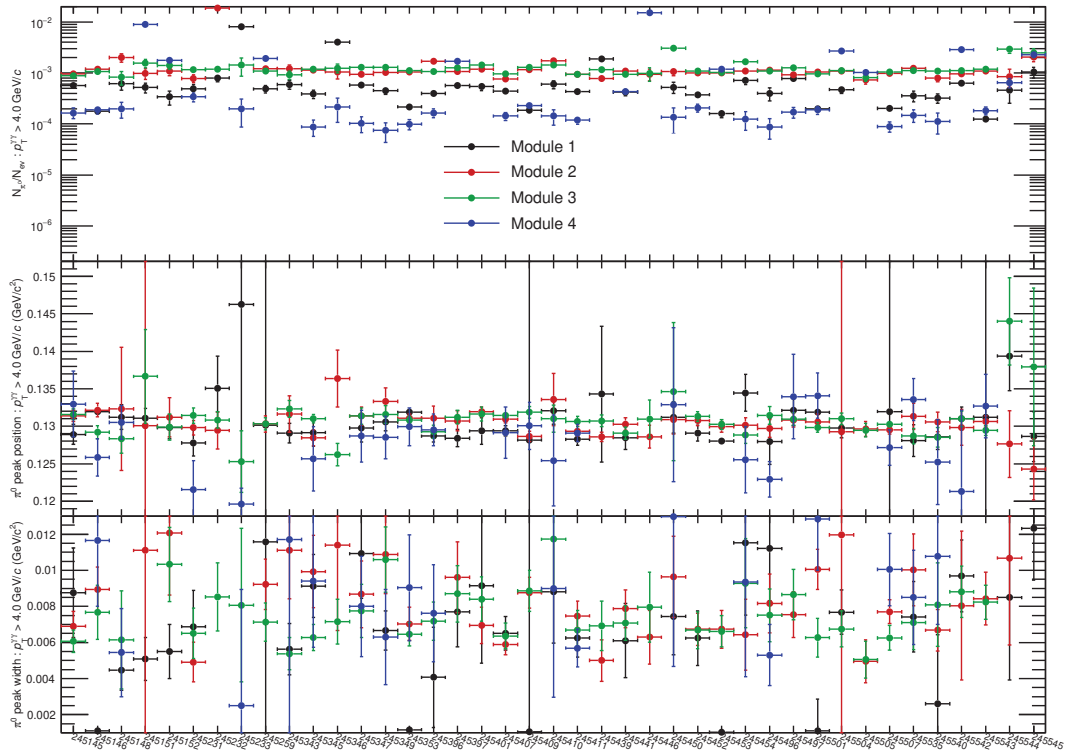


Figure 39: π^0 yield, peak position and sigma in each run in LHC15o pass1_pidfix.

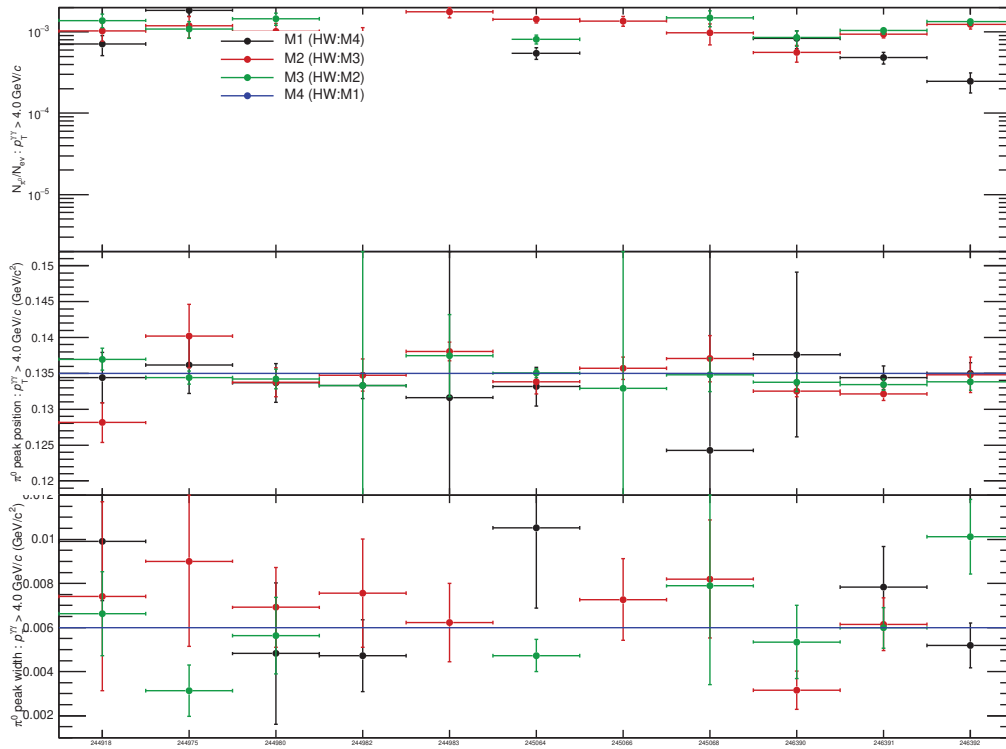
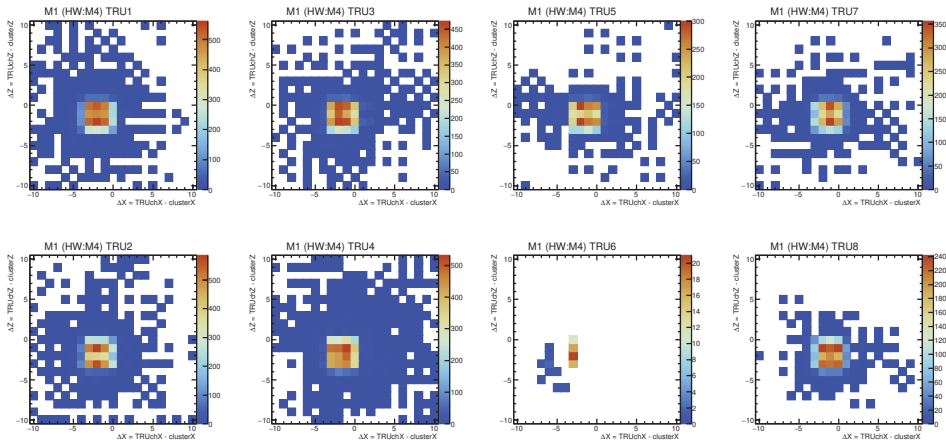
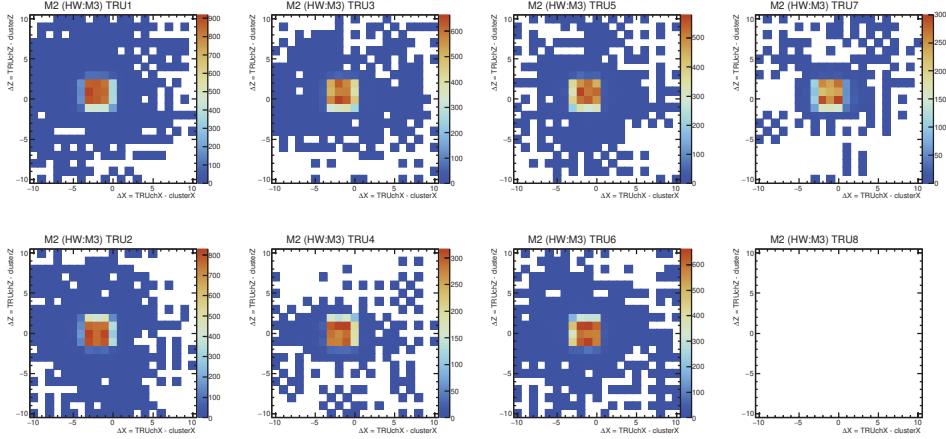


Figure 40: π^0 yield, peak position and sigma in each run in LHC15o lowIR pass5.

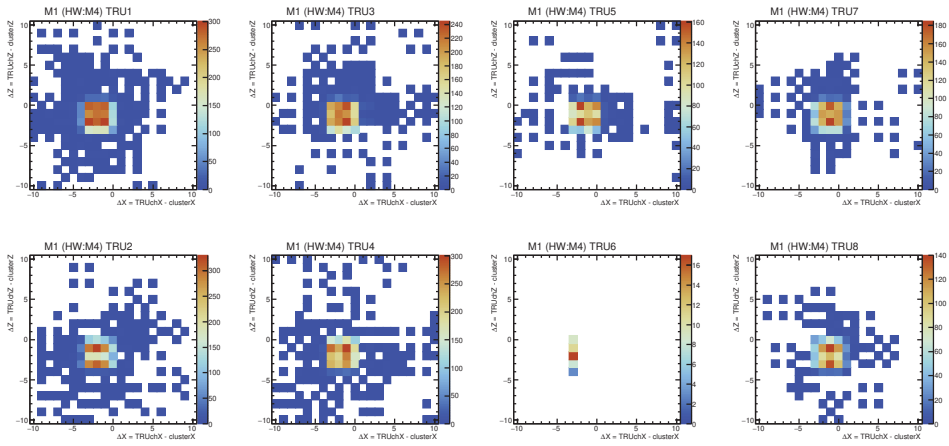


(a) Module 1.

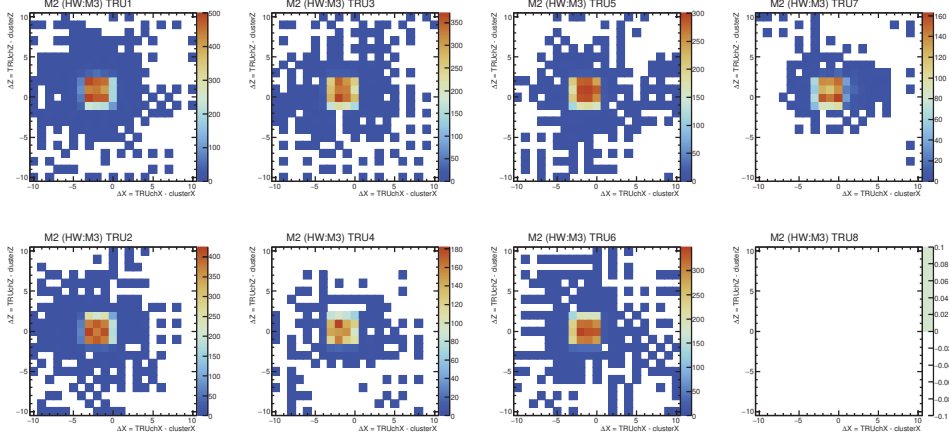


(b) Module 2.

Figure 41: The distance between fired TRU channels and cluster position on different modules for L1H at $E_{\text{cluster}} > 8$ GeV in Pb–Pb collisions at $\sqrt{s_{\text{NN}}} = 5.02$ TeV

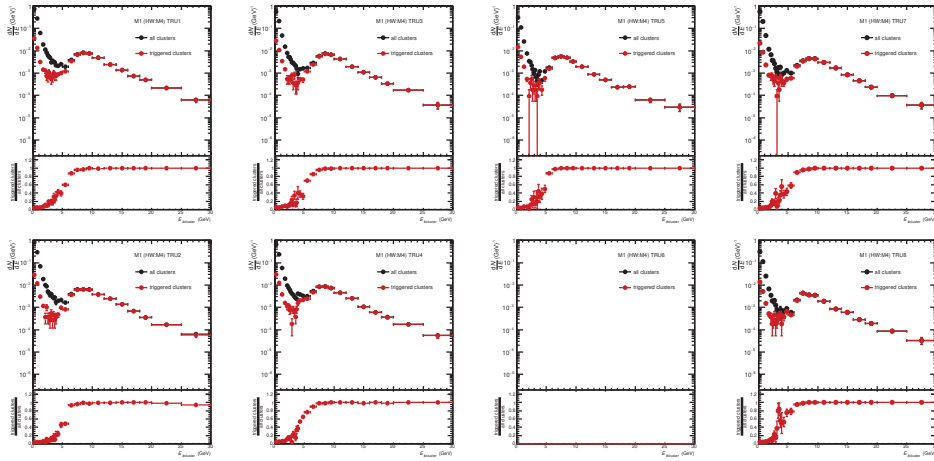


(a) Module 1.

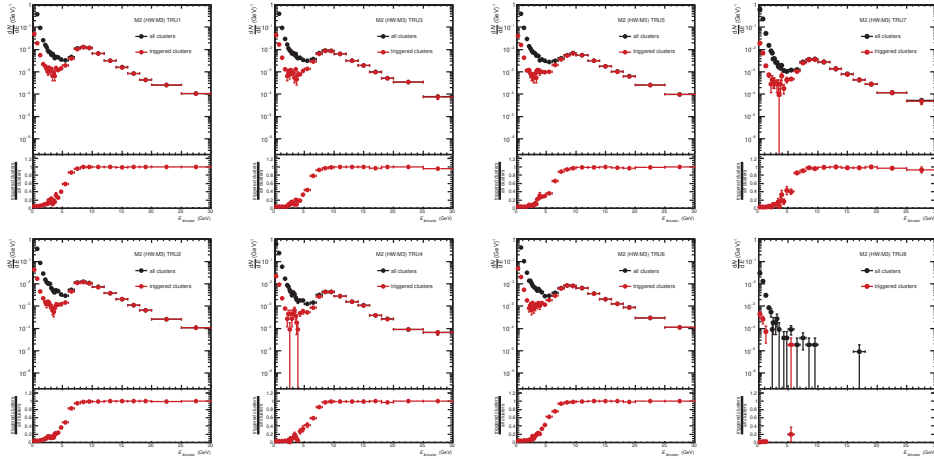


(b) Module 2.

Figure 42: The distance between fired TRU channels and cluster position on different modules for L1M at $E_{\text{cluster}} > 4$ GeV in Pb–Pb collisions at $\sqrt{s_{\text{NN}}} = 5.02$ TeV

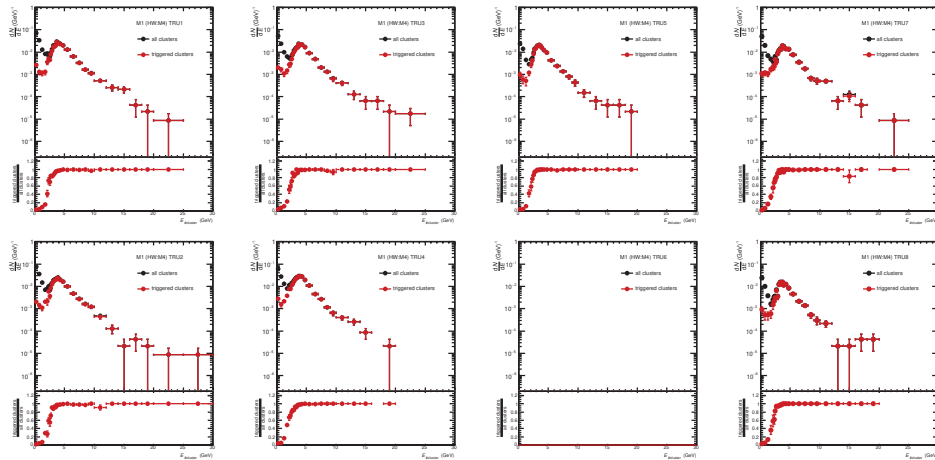


(a) Module 1.

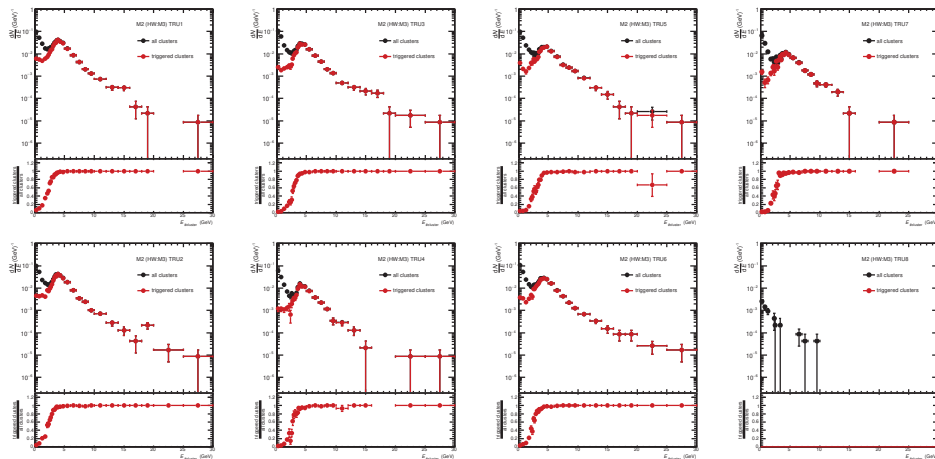


(b) Module 2.

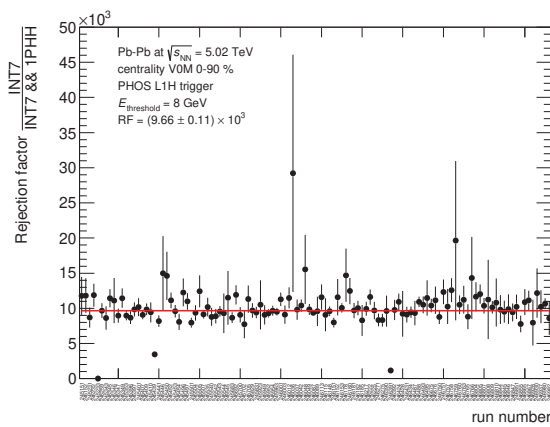
Figure 43: Energy distribution of all clusters and triggered clusters and ratios on different modules for L1H in Pb–Pb collisions at $\sqrt{s_{\text{NN}}} = 5.02$ TeV



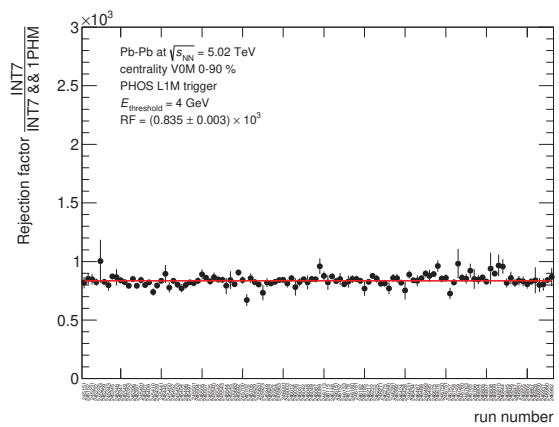
(a) Module 1.



(b) Module 2.

Figure 44: Energy distribution of all clusters and triggered clusters and ratios on different modules for L1M in Pb–Pb collisions at $\sqrt{s_{NN}} = 5.02$ TeV

(a) PHOS L1H trigger



(b) PHOS L1M trigger

Figure 45: The rejection factor of PHOS L1 trigger (run-by-run) in Pb–Pb collisions at $\sqrt{s_{NN}} = 5.02$ TeV

4 Analyses of neutral mesons

Procedure to measure production cross section of neutral mesons are described in this section. At first, an analysis strategy to give an overview of analyses is summarized in 4.1. Since photon identification is a key of this thesis, criteria for photon selection is in 4.2. The detailed explanation about analyses in pp and Pb–Pb are in section 4.3 and 4.4, respectively.

4.1 Analysis strategy

The PHOS detector is used to measure energies and positions of produced photons. The minimum-bias trigger is V0AND which requires at least 1 hit on each V0A and V0C. Neutral mesons (π^0 and η) are reconstructed by invariant mass method defined by Eq. 13, which is based on 4-momentum conservation between a particle and its decay products.

$$M_{\gamma\gamma} = \sqrt{2E_1E_2(1 - \cos\theta_{12})}, \quad (13)$$

where $E_{1/2}$ is energy of photon1/2, θ_{12} is opening angle between photon1 and photon2. The invariant mass reconstruction is performed over all possible combinations in each event. Raw yields of neutral mesons are obtained by counting histogram entries around 135 MeV/ c^2 for π^0 and 547 MeV/ c^2 for η respectively. The background is subtracted by mixed-event technique (a first photon is taken from a current event and a second photon is from another event). 4-momentum of particles never conserves in this technique and this gives us only background. Same procedure is performed in M.C. simulation. Since generated particle is known in simulation, an acceptance \times reconstruction efficiency ε can be measured by :

$$\text{acc.} \times \text{rec. efficiency } \varepsilon = \frac{\text{Number of reconstructed particles on PHOS}}{\text{Number of generated particles in } |y| < 0.5 \text{ and } 2\pi \text{ in azimuth}} \quad (14)$$

Finally, a production cross section of particle is given by :

$$E \frac{d^3\sigma}{dp^3} = \frac{1}{2\pi} \times \frac{1}{p_T} \frac{dN}{dp_T} \times \frac{1}{\Delta y} \times \frac{1}{\varepsilon} \times \frac{1}{L_{\text{int}}}, \quad (15)$$

where $\frac{dN}{dp_T}$ is transverse momentum-(p_T -)differential raw yield of particle and $L_{\text{int}} = \frac{N_{\text{ev}}}{\sigma_{\text{pp}}^{\text{V0AND}}}$ is an integrated luminosity. The cross section of V0AND trigger $\sigma_{\text{pp}}^{\text{V0AND}} = 51.2 \pm 1.2$ mb and the total inelastic cross section $\sigma_{\text{pp}}^{\text{INEL}} = 67.6 \pm 0.6$ mb [60] in pp collisions at $\sqrt{s} = 5.02$ TeV. In case of rare-triggered data (e.g. high-energy photon trigger in PHOS), the particle yields have to be further normalized by a trigger rejection factor (RF).

$$\text{RF} = \frac{\text{MB}}{\text{MB \& rare-trigger input}} \quad (16)$$

$$L_{\text{int}} = \frac{N_{\text{ev}}}{\sigma_{\text{pp}}^{\text{V0AND}}} \times \text{RF} \quad (17)$$

Once neutral mesons yields are measured in both pp and Pb–Pb collisions, the nuclear modification factor R_{AA} for each particle is measured based on 4.

4.2 Photon identification

There are two types of photon identification cut to clusters measured by PHOS. They are Charged Particle Veto (CPV) and shower shape cut called dispersion cut.

4.2.1 CPV cut

This cut is to reject charged particles. As photon is neutral and can not be tracked, photon hits on PHOS should not match extrapolated tracks from ITS/TPC. Hence, if a distance in the $x - z$ plane between a cluster and an extrapolated track is closer than a certain threshold, the cluster is rejected.

4.2.2 Dispersion cut

This cut is to select electro-magnetic clusters by an elliptic shape of the electro-magnetic shower evolution in PbWO_4 crystals. It is characterized by eigenvalues in a cluster [58, 59] :

$$M02 \text{ (cm)} = \frac{1}{2} \left(\sigma_{xx}^2 + \sigma_{zz}^2 + \sqrt{(\sigma_{xx}^2 - \sigma_{zz}^2)^2 + 4\sigma_{xz}^4} \right) \text{ for long axis}$$

$$M20 \text{ (cm)} = \frac{1}{2} \left(\sigma_{xx}^2 + \sigma_{zz}^2 - \sqrt{(\sigma_{xx}^2 - \sigma_{zz}^2)^2 + 4\sigma_{xz}^4} \right) \text{ for short axis,}$$

where $\sigma_{xz}^2 = \langle xz \rangle - \langle x \rangle \langle z \rangle$, $\langle x \rangle = \frac{1}{w_{\text{total}}} \sum_i w_i x_i$ is the weighted average over all cells in a cluster. The weight w_i is given by $w_i = \max(0, 4.5 + \ln(E_i/E))$, where E_i is cell energy at i and $w_{\text{total}} = \sum_i w_i$. Clusters are required to pass a criterion based on correlation between $M02$ and $M20$ as a function of the energy. Especially for clusters at low energy, simple minimum and maximum thresholds to N_{cell} and $M02$ as a function of their energy are imposed, instead of the dispersion cut. N_{cell} is the number of cells in a cluster (i.e. how many cells a cluster consists of). In order to save photon clusters at low energy, these criteria are loose for low energy clusters where the evolution of the electro-magnetic shower is poor.

965 4.3 Analyses in pp collisions at $\sqrt{s} = 5.02$ TeV

966 Details of analyses in pp collisions are described here. First, neutral meson reconstruction via
 967 two photons were performed. Second, M.C. tuning to reproduce realistic peak parameters and
 968 determine efficiency. Then, various cut efficiencies (cluster timing, triggering, feed down from
 969 strange hadrons) have been evaluated.

970 4.3.1 Raw yield extraction

971 π^0 and η mesons are reconstructed via their two photons decay with invariant mass method.
 972 The neutral meson peaks are fitted by Gaussian function and integrated over the mean value
 973 $\pm 3\sigma$. Backgrounds are estimated by mixed event technique. Varying fitting ranges, functions
 974 and integral ranges are included in systematic uncertainties.

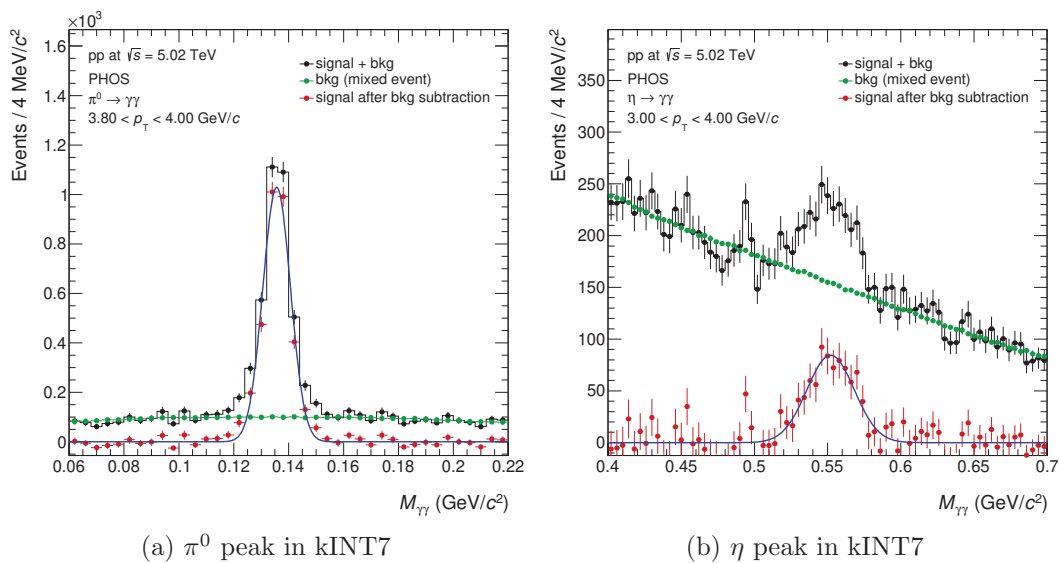


Figure 46: Invariant mass distributions in pp collisions at $\sqrt{s} = 5.02$ TeV (INT7)

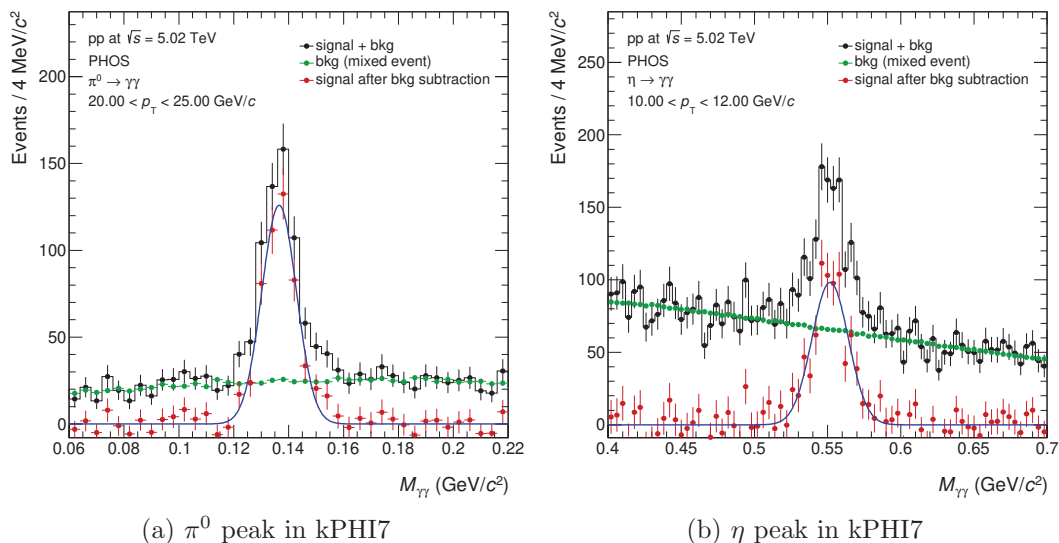


Figure 47: Invariant mass distributions in pp collisions at $\sqrt{s} = 5.02$ TeV (PHI7)

975 Figure 46, 47 are invariant mass distributions for MB and L0 PHOS triggered events respectively.
 976 Neutral meson signal are clearly seen. The number of neutral meson signals is obtained by bin-
 977 counting on the invariant mass distribution at each p_T bin.

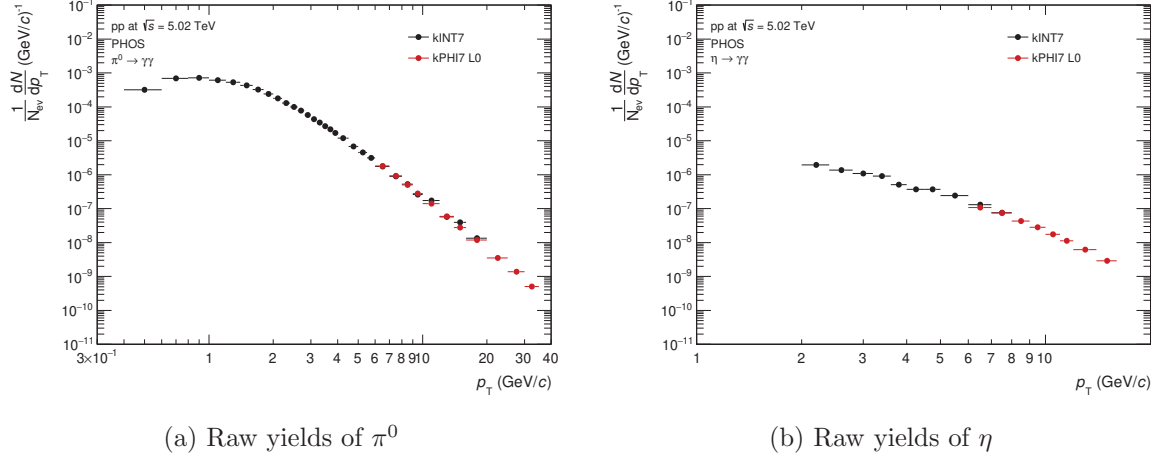


Figure 48: Raw yields of neutral mesons in pp collisions at $\sqrt{s} = 5.02$ TeV

978 Raw yields are plotted on Figure 48. No PID cut was applied in π^0 signal extraction in pp,
 979 while an energy asymmetry cut ($\alpha = \frac{|E_1 - E_2|}{E_1 + E_2} < 0.7$) and CoreDisp 2.5σ only in INT7 events
 980 were applied for the η meson measurement. As η has heavier mass ($547 \text{ MeV}/c^2$) than π^0 mass
 981 ($135 \text{ MeV}/c^2$), the tighter cut is helpful to extract its signal.

982 4.3.2 Acceptance \times reconstruction efficiency

983 The efficiency is obtained by M.C. simulation. First, M.C. simulation has to reproduce realistic
 984 peak position and width of neutral mesons by tuning energy measurement in M.C.. Figure 49,
 985 50 show good agreement of peak parameters by Gaussian fitting to π^0 and η meson between
 986 data and M.C..

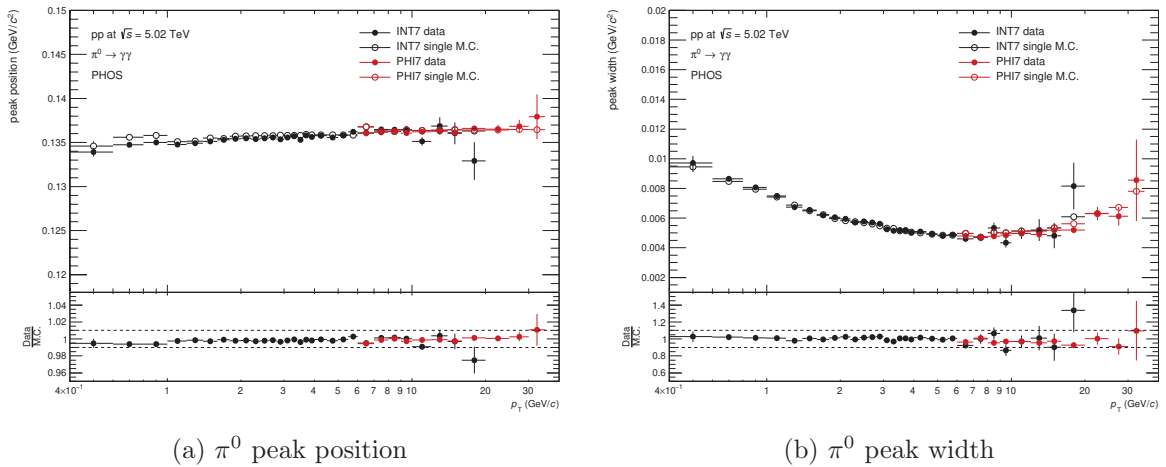
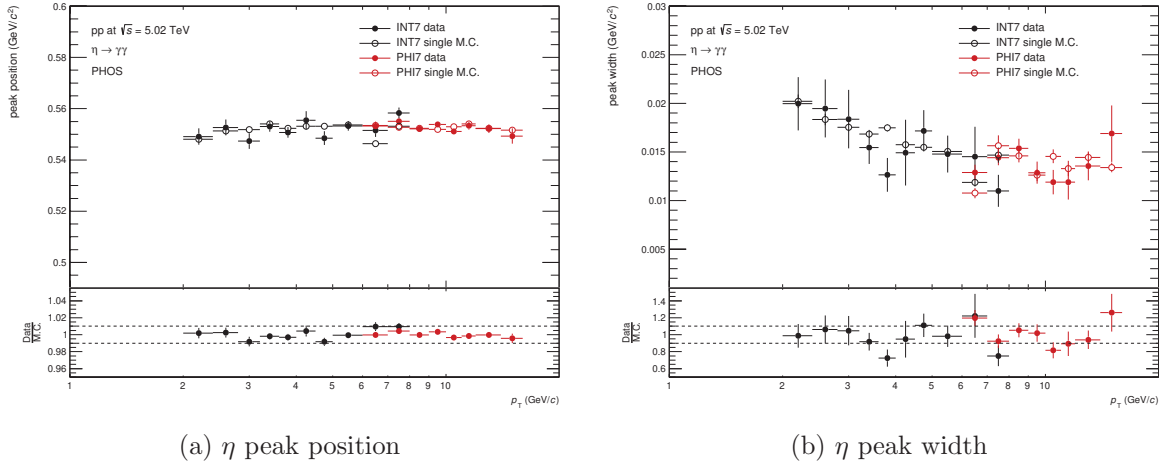
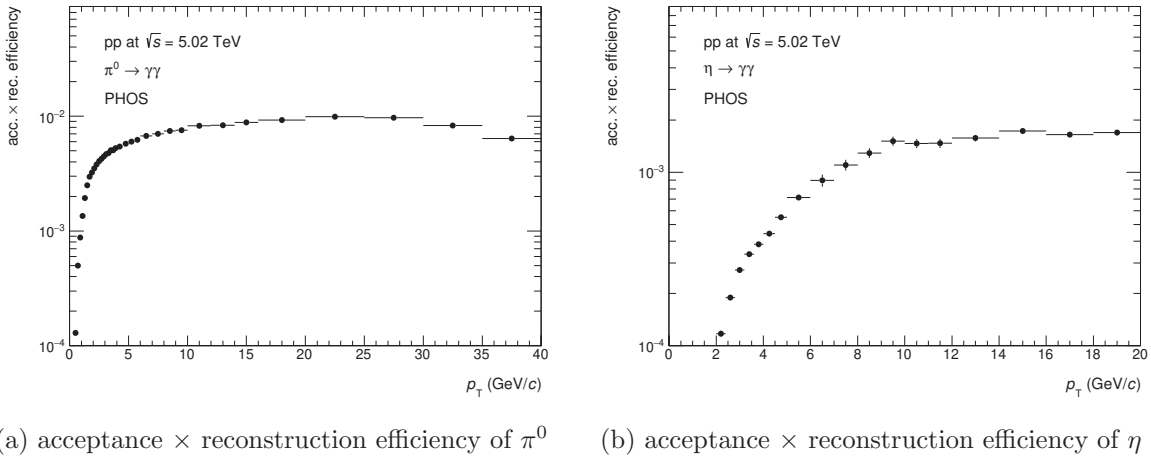


Figure 49: π^0 peak parameters in pp collisions at $\sqrt{s} = 5.02$ TeV

Figure 50: η peak parameters in pp collisions at $\sqrt{s} = 5.02$ TeV

987 Once properties of neutral meson peak are reproduced by M.C., acceptance \times reconstruction
 988 efficiency has been measured based on Eq. 14.

Figure 51: acceptance \times reconstruction efficiency of neutral mesons in pp collisions at $\sqrt{s} = 5.02$ TeV with PHOS

989 4.3.3 Timing cut

990 The bunch space of each proton beam bunch was 25 ns during LHC-Run2 operation. Timing
 991 cut ($|\text{TOF}_{\text{cluster}}| < 12.5$ ns) was applied at cluster level to reject clusters from other BCs. The
 992 timing of a cluster is defined as the timing of a leading cell which has the highest amplitude in
 993 APDs. TOF cut efficiency (ε_{TOF}) is defined by :

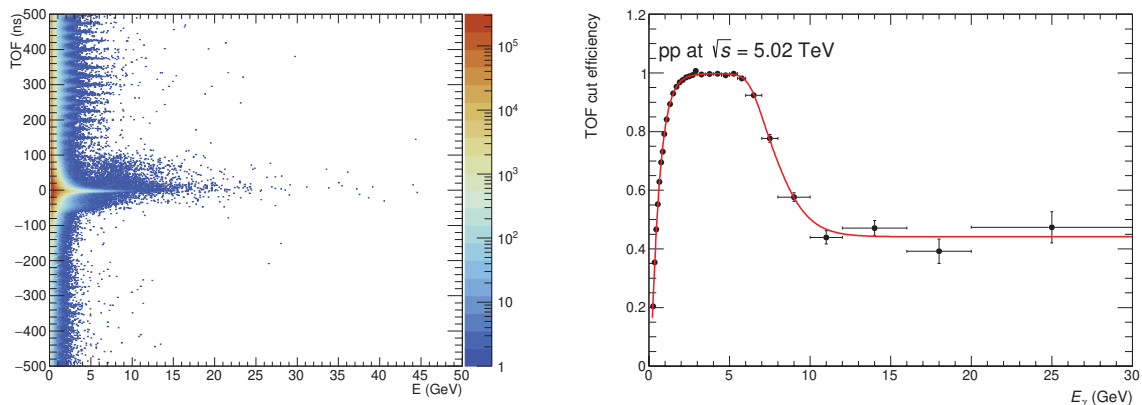
$$\varepsilon_{\text{TOF}} = \frac{N_{\text{TOF } \gamma}^{\text{triggered BC}}}{N_{\text{all } \gamma}^{\text{triggered BC}}}, \quad (18)$$

994 where $N_{\text{TOF } \gamma}^{\text{triggered BC}}$ is the number of photons after TOF cut in the triggered BC and $N_{\text{all } \gamma}^{\text{triggered BC}}$
 995 is the number of all photons in the triggered BC respectively. The efficiency is measured by
 996 data driven, called tag-and-probe method. This technique is widely applicable for any kinds
 997 of efficiency, e.g. trigger efficiency, PID cut efficiency and so on. The first photon is required

998 to pass the timing cut (tagged photon) and reconstructing invariant mass with two photons in
 999 same events. If the reconstructed invariant mass is in the π^0 (η) meson signal window, typically
 1000 $0.12 < M_{\gamma\gamma} < 0.15$ GeV/ c^2 ($0.5 < M_{\gamma\gamma} < 0.6$ GeV/ c^2), the second photon is called probe
 1001 photon. Then, the efficiency can be measured with probe photons by :

$$\varepsilon = \frac{\text{The number of probe photons which pass criteria}}{\text{The number of all probe photons}} \quad (19)$$

1002 The drop of TOF efficiency in Figure 52b at $E_{\text{cluster}} > 6$ GeV is due to switching high gain
 1003 (HG) to low gain (LG) channels in the PHOS readout electronics. Timing resolution is worse
 1004 in LG, as LG channels have lower gain. Then, the number of photons is corrected by ε_{TOF} as a
 1005 function of photon energy. Since ε_{TOF} is measured as a function of photon energy, $\frac{1}{\varepsilon_{\text{TOF}} \times \varepsilon_{\text{TOF}}^2}$ is
 necessary at neutral mesons level which is reconstructed from two photons.

(a) TOF vs. E_{cluster} .

(b) TOF cut efficiency as a function of photon energy.

Figure 52: The cluster timing distribution and TOF cut efficiency

1006

1007 4.3.4 Trigger efficiency

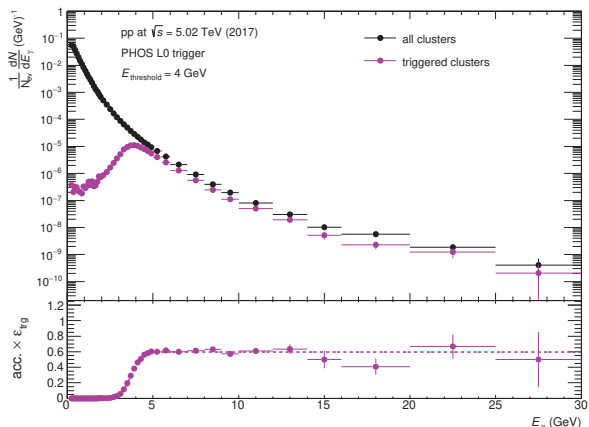
1008 The PHOS trigger allows us to measure high
 1009 energy photons/electrons efficiently in AL-
 1010 ICE. The energy threshold of the PHOS L0
 1011 trigger in pp collisions at $\sqrt{s} = 5.02$ TeV
 1012 (LHC17pq) period was set to 4 GeV in sum of
 1013 4×4 analogue signal (FastOR). The rejection
 1014 factor is defined by :

$$\text{RF} = \frac{\text{MB}}{\text{MB \& 0PH0 and matched with cluster}}, \quad (20)$$

1015 as shown by The PHOS trigger efficiency is
 1016 measured in MB events by means of :

$$\varepsilon_{\text{trg}} = \frac{\text{Number of triggered clusters in kINT7}}{\text{Number of all clusters in kINT7}} \quad (21)$$

1017 Charged particle veto and dispersion cut were applied for both nominator and denominator to
 1018 get high photon purity. The trigger efficiency in pp collisions at $\sqrt{s} = 5.02$ TeV (LHC17pq)

Figure 53: PHOS L0 trigger efficiency in pp collisions at $\sqrt{s} = 5.02$ TeV

1019 reaches 0.6 above the energy threshold. For the neutral meson reconstruction, at least one
 1020 triggered cluster (logical-OR) is required in this analysis. The trigger efficiency for π^0 and η is
 1021 $\varepsilon_{\text{trg}}^{\text{OR}} = \varepsilon_{\text{trg}}^1 + \varepsilon_{\text{trg}}^2 - \varepsilon_{\text{trg}}^1 \times \varepsilon_{\text{trg}}^2$.

1022 4.3.5 Feed down correction from strange hadrons

1023 π^0 from strange hadrons decays such as $K_S^0 \rightarrow$
 1024 $\pi^0\pi^0$ (BR = 30.69%, $c\tau = 2.7$ cm) and $\Lambda \rightarrow$
 1025 $n\pi^0$ (BR = 35.8 %, $c\tau = 7.9$ cm (negligible))
 1026 contribute the total number of π^0 , while π^0
 1027 from primary interaction is focused on. Hence,
 1028 they have to be subtracted from the total
 1029 number of π^0 . For this study, M.C. simula-
 1030 tion with PYTHIA8 event generator was used
 1031 to estimate this contribution. However, it
 1032 is known that PYTHIA event generator does
 1033 not reproduce realistic K^\pm/π^\pm ratio. There-
 1034 fore, re-weighting to K_S^0 spectrum is neces-
 1035 sary. Since K^\pm/π^\pm ratio in pp collisions at
 1036 $\sqrt{s} = 5.02$ TeV has not been published as of
 1037 January 31 2019, K^\pm/π^\pm ratio in pp collisions
 1038 at $\sqrt{s} = 2.76$ TeV [61, 62] are taken as a reference. K^\pm/π^\pm ratio does not depend on collision
 1039 energy at \sim TeV energy region [61, 63]. The feed down factor is defined as :

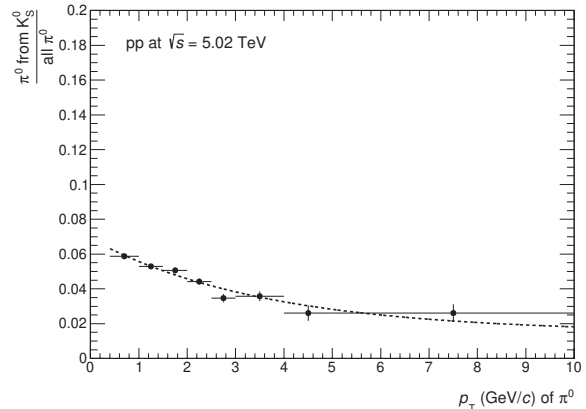
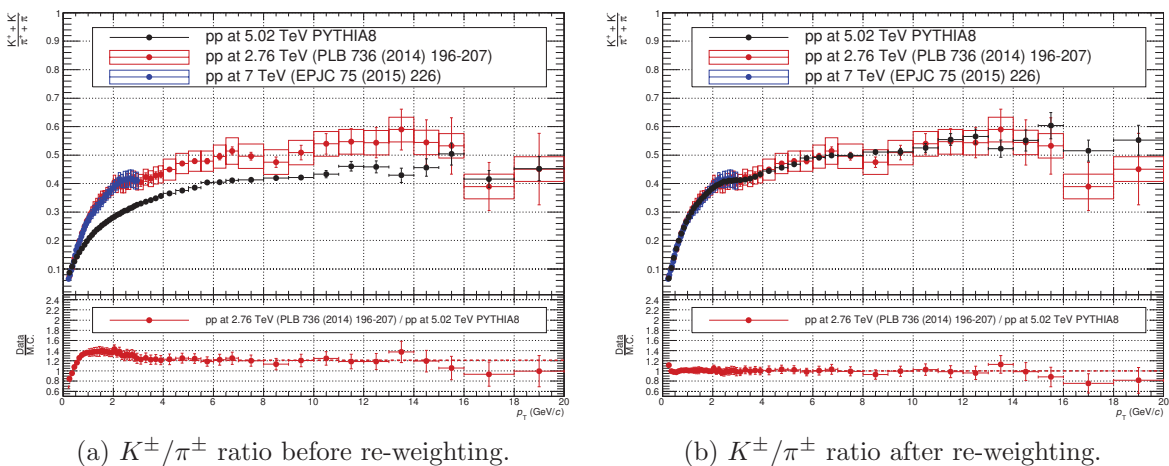


Figure 54: Feed down factor for π^0 from K_S^0 in pp collisions at $\sqrt{s} = 5.02$ TeV

$$\text{FD} = \frac{\text{Number of reconstructed } \pi^0 \text{ from } K_S^0}{\text{Number of all reconstructed } \pi^0} \quad (22)$$

1040 Figure 55 shows K^\pm/π^\pm ratio before and after the re-weighting procedure. The FD factor is plotted on Figure 54, which is about 6% at the maximum and decreases with p_T .



(a) K^\pm/π^\pm ratio before re-weighting.

(b) K^\pm/π^\pm ratio after re-weighting.

Figure 55: K^\pm/π^\pm ratio in PYTHIA8

1041

1042 4.4 Analyses in Pb–Pb collisions at $\sqrt{s_{\text{NN}}} = 5.02$ TeV

1043 Details of analyses in Pb–Pb collisions are described in this section. They are generally the
 1044 same as in pp collisions. In addition to analyses in pp, events are classified by multiplicity
 1045 on the VZERO detector called “centrality class”. The centrality at 0 % indicates the highest
 1046 multiplicity class and the higher value of centrality, the lower multiplicity class. There were
 1047 two active L1 PHOS triggers in Pb–Pb collisions recorded in 2015. One is CINT7PHH, high
 1048 energy threshold at 8 GeV for all centrality classes. The other is CPER7PHM, medium energy
 1049 threshold at 4 GeV for peripheral collisions (centrality > 60%). As shown by Figure 56, the
 1050 centrality distribution in Minimum-Bias events (CINT7) is well calibrated and flat. However,
 1051 they are biased in PHOS triggered data. It is understood that the probability to detect a
 1052 high energy photon under the high multiplicity environment is higher than that in peripheral
 1053 collisions, because the number of produced photons is also large in central collisions. Trigger
 rejection factors for L1H and L1M are biased, too.

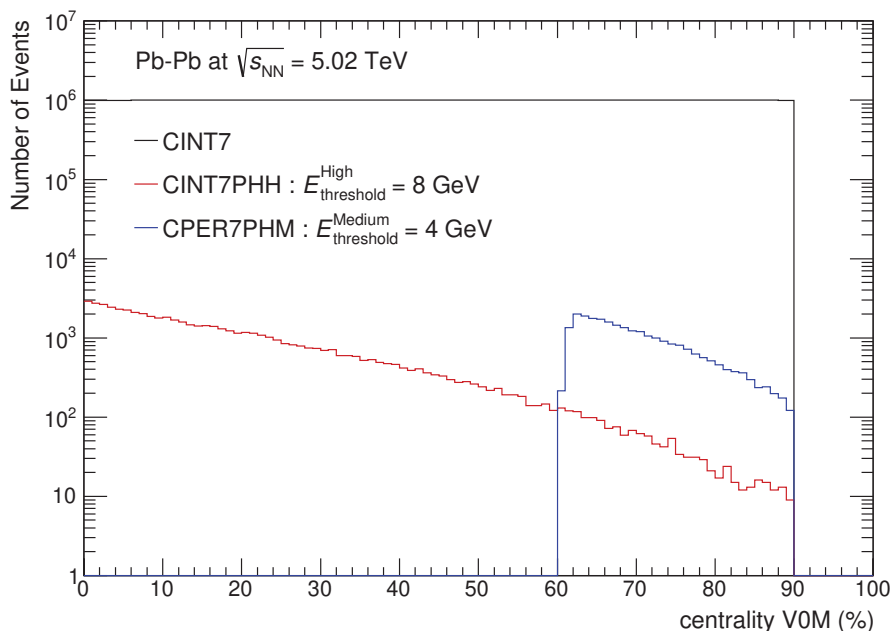
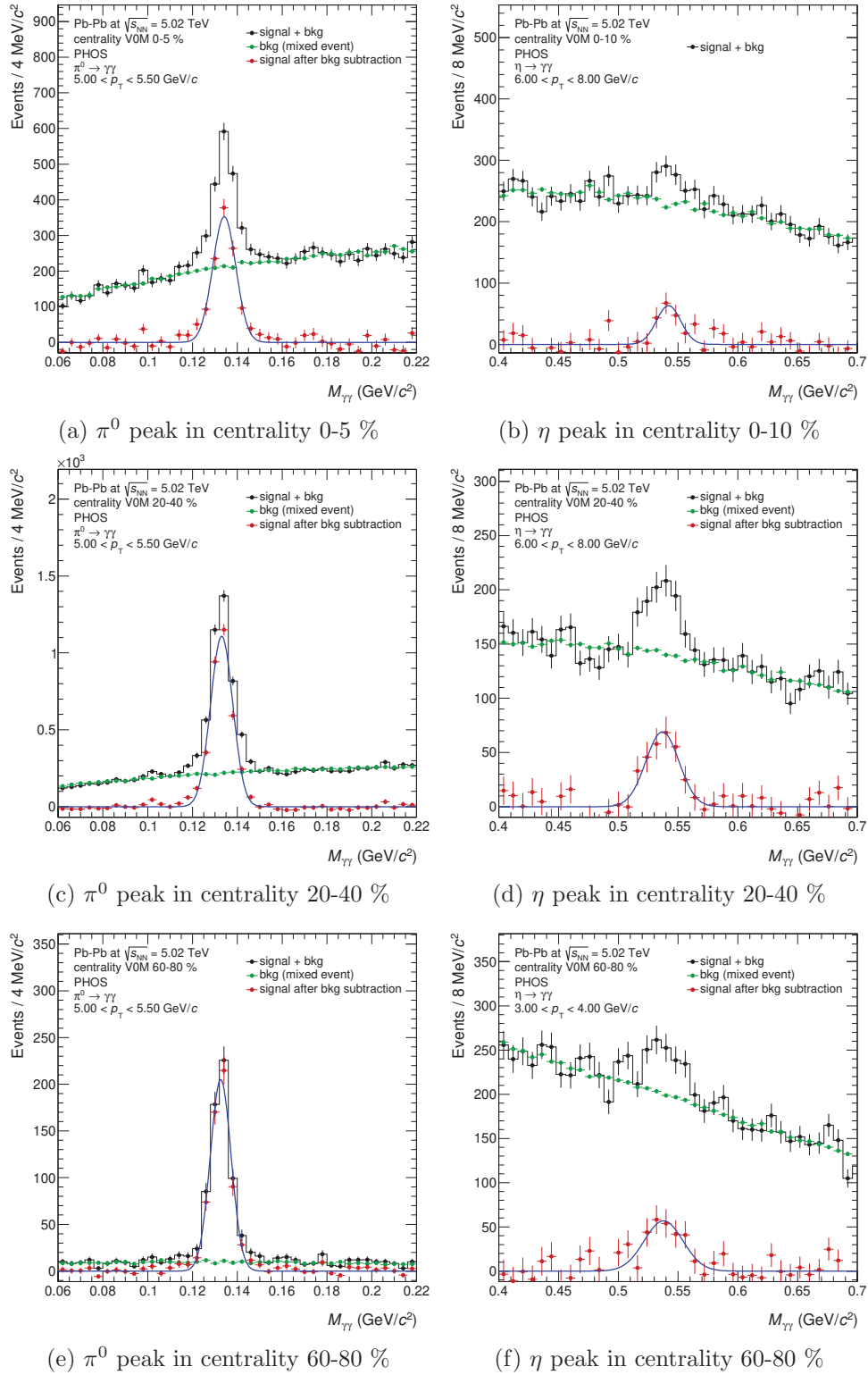


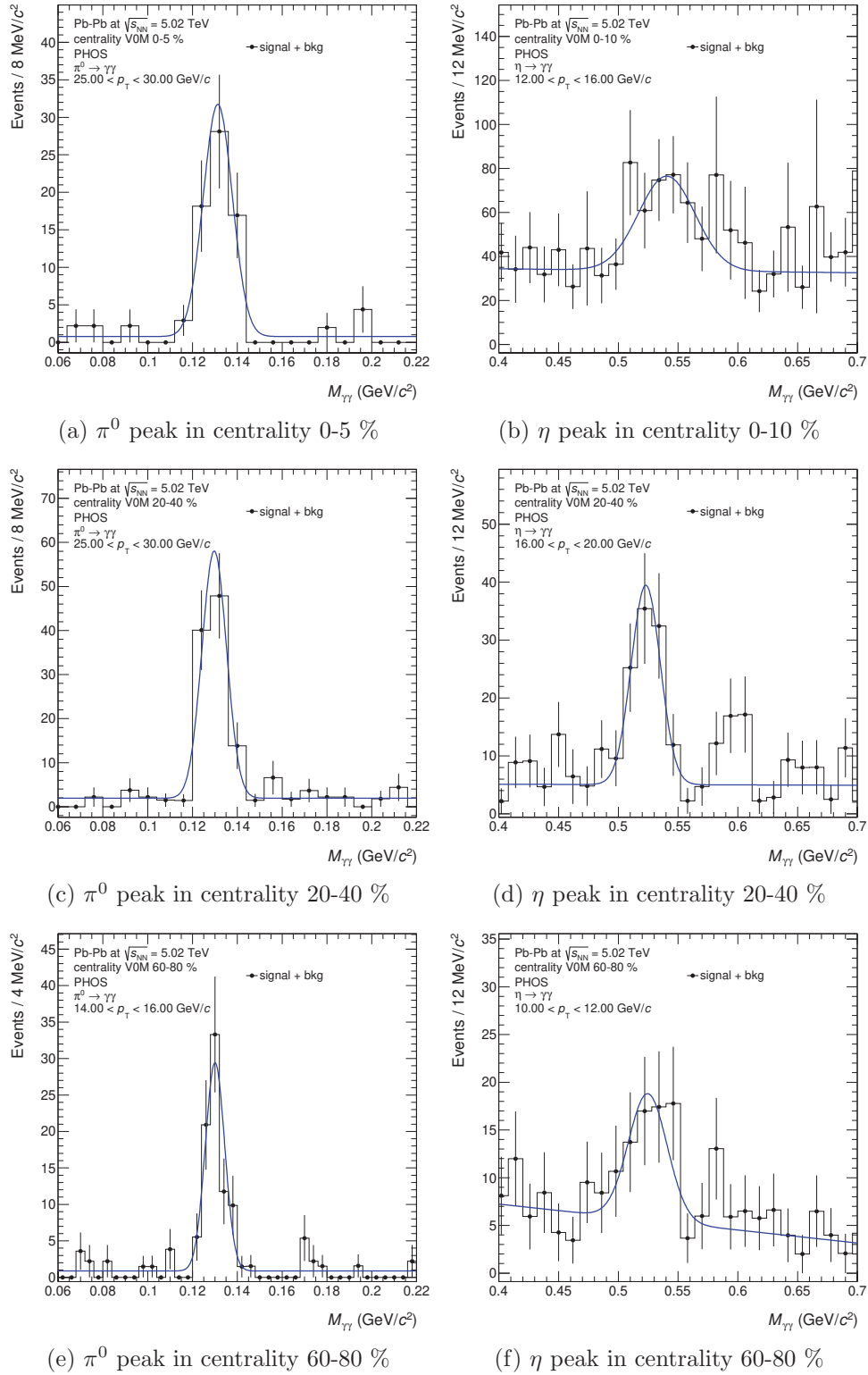
Figure 56: Centrality V0M distributions in Pb–Pb collisions at $\sqrt{s_{\text{NN}}} = 5.02$ TeV (2015)

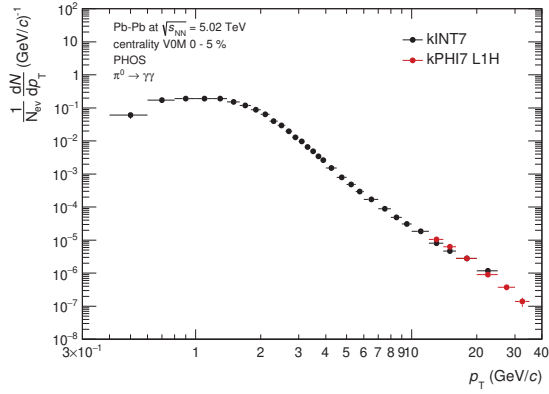
1054

1055 4.4.1 Raw yield extraction

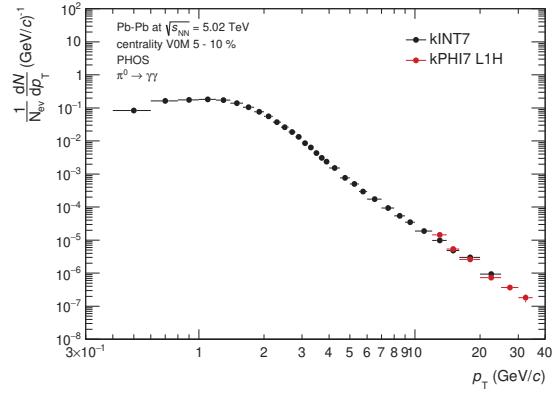
1056 Figure 57, 58 are invariant mass distributions for MB and L1 PHOS triggered events respectively.
 1057 Neutral meson signal are clearly seen in all centrality classes. The number of neutral meson
 1058 signals is obtained by bin-counting on the invariant mass distribution at each p_{T} bin. Raw yields
 1059 are plotted on Figure 59, 60 in different centrality classes. Both CPV and core-dispersion cuts
 1060 were applied to clusters in Pb–Pb collisions. Furthermore, energy asymmetry $\alpha = \frac{|E_1 - E_2|}{E_1 + E_2} < 0.8$
 1061 for π^0 and $\alpha < 0.7$ for η mesons were also applied.

Figure 57: Invariant mass distributions in Pb-Pb collisions at $\sqrt{s_{NN}} = 5.02$ TeV (INT7)

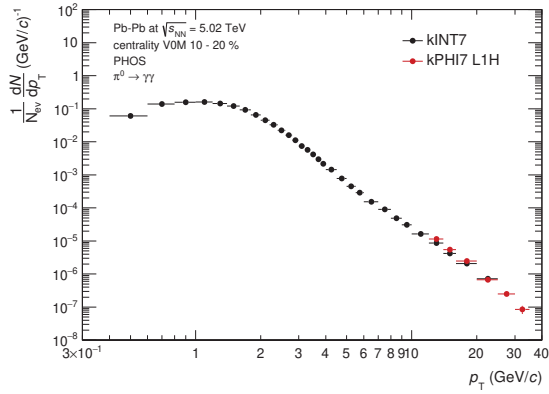
Figure 58: Invariant mass distributions in Pb-Pb collisions at $\sqrt{s_{NN}} = 5.02$ TeV (PHI7)



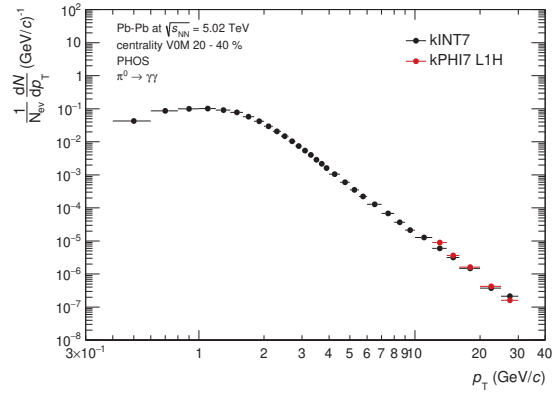
(a) centrality 0-5 %



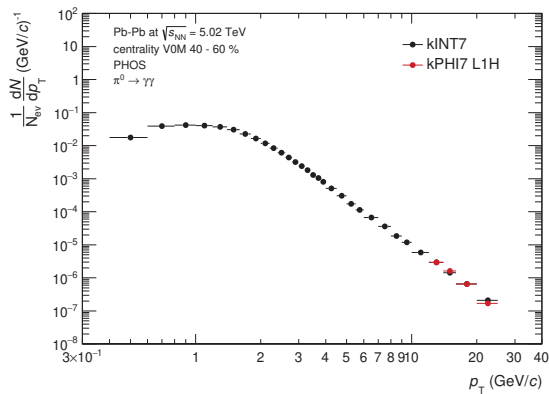
(b) centrality 5-10 %



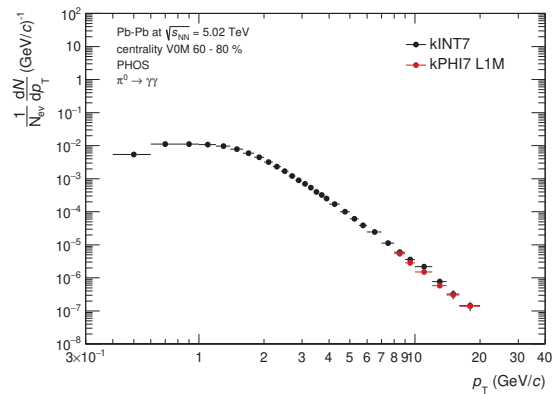
(c) centrality 10-20 %



(d) centrality 20-40 %

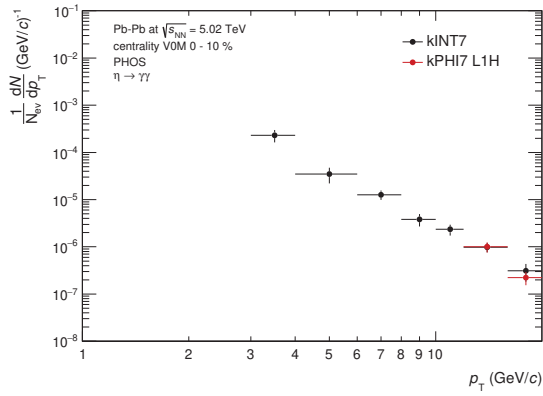


(e) centrality 40-60 %

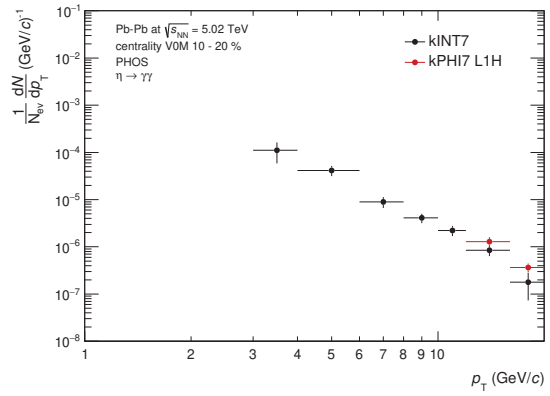


(f) centrality 60-80 %

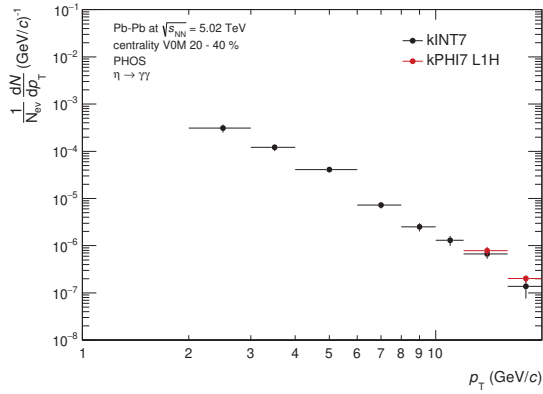
Figure 59: Raw yields of π^0 in Pb-Pb collisions at $\sqrt{s_{NN}} = 5.02$ TeV



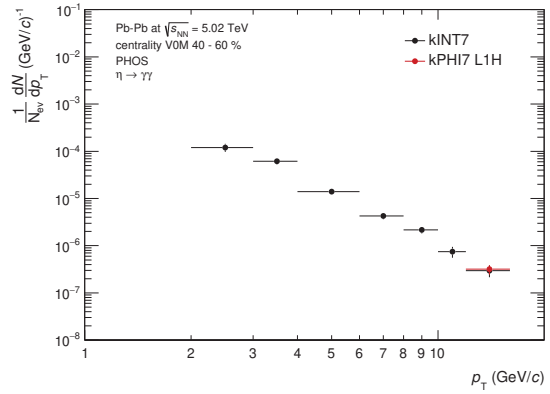
(a) centrality 0-10 %



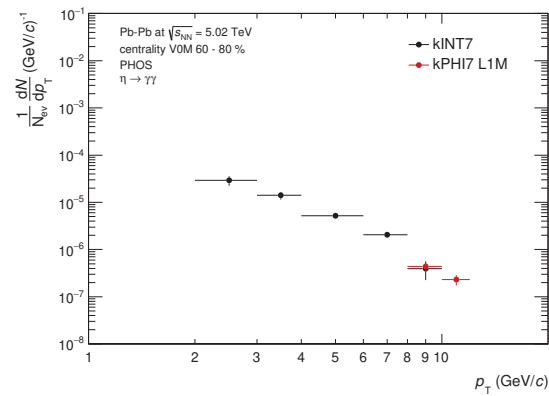
(b) centrality 10-20 %



(c) centrality 20-40 %



(d) centrality 40-60 %



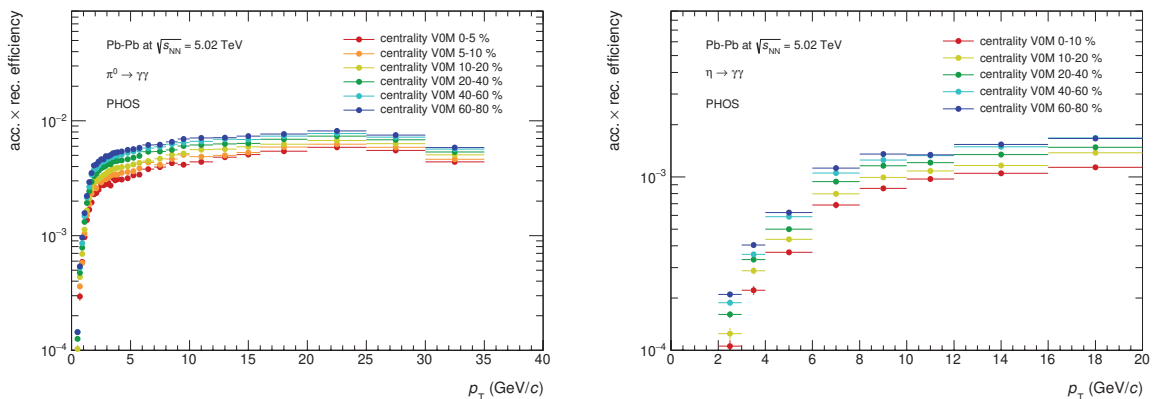
(e) centrality 60-80 %

Figure 60: Raw yields of η in Pb-Pb collisions at $\sqrt{s_{NN}} = 5.02$ TeV

1062 **4.4.2 Acceptance \times reconstruction efficiency**

1063 Due to the extremely high charged particle multiplicity $dN_{\text{ch}}/d\eta \approx O(10^3)$ [64, 65] in central
 1064 Pb–Pb collisions, the reconstruction efficiency for photons and neutral mesons is influenced and
 1065 centrality-dependent. In order to take high multiplicity environment into account, the efficiency
 1066 in Pb–Pb collisions is obtained by using embedding technique. The main idea of embedding
 1067 technique is to merge real data as underlying events (UE) with events from single particle
 1068 simulation (π^0 , η and γ) and to reconstruct data again. This allows us to study how clusters are
 1069 modified under the realistic high multiplicity environment. The general procedure is following :

- 1070 1. embed 1 simulated particle per 1 underlying event.
- 1071 2. cell information in both UE and simulation are inversely calibrated to ADC values from cell
 1072 energy. At this step, global energy scale and non-linear response of energy measurement
 1073 in simulation is also inversely applied.
- 1074 3. merge all cells at ADC level.
- 1075 4. clusterize merged cells by the same clustering algorithm.



(a) acceptance \times reconstruction efficiency of π^0 (b) acceptance \times reconstruction efficiency of η

Figure 61: acceptance \times reconstruction efficiency of neutral mesons in Pb–Pb collisions at $\sqrt{s_{\text{NN}}} = 5.02$ TeV with PHOS

1076 As well as analyses in pp, M.C. simulation has to reproduce realistic peak position and width
 1077 of neutral mesons. To avoid overlapping effect under high multiplicity environment, π^0 peak
 1078 parameters were tuned in peripheral collisions. Figure 62, 63, 64, 65 are the comparison of
 1079 peak parameters for π^0 and η between data and embedding M.C.. Peak parameters are in good
 1080 agreement in peripheral collisions, while 1% of discrepancy in peak position is found in central
 1081 collisions. The global energy scale and the non-linearity response of energy measurement in M.C.
 1082 are fully detector response and should not depend on event multiplicity. Therefore, $\Delta E/E \approx 0.01$
 1083 in central collisions is attributed to an additional systematic uncertainty of the global energy
 1084 scale.

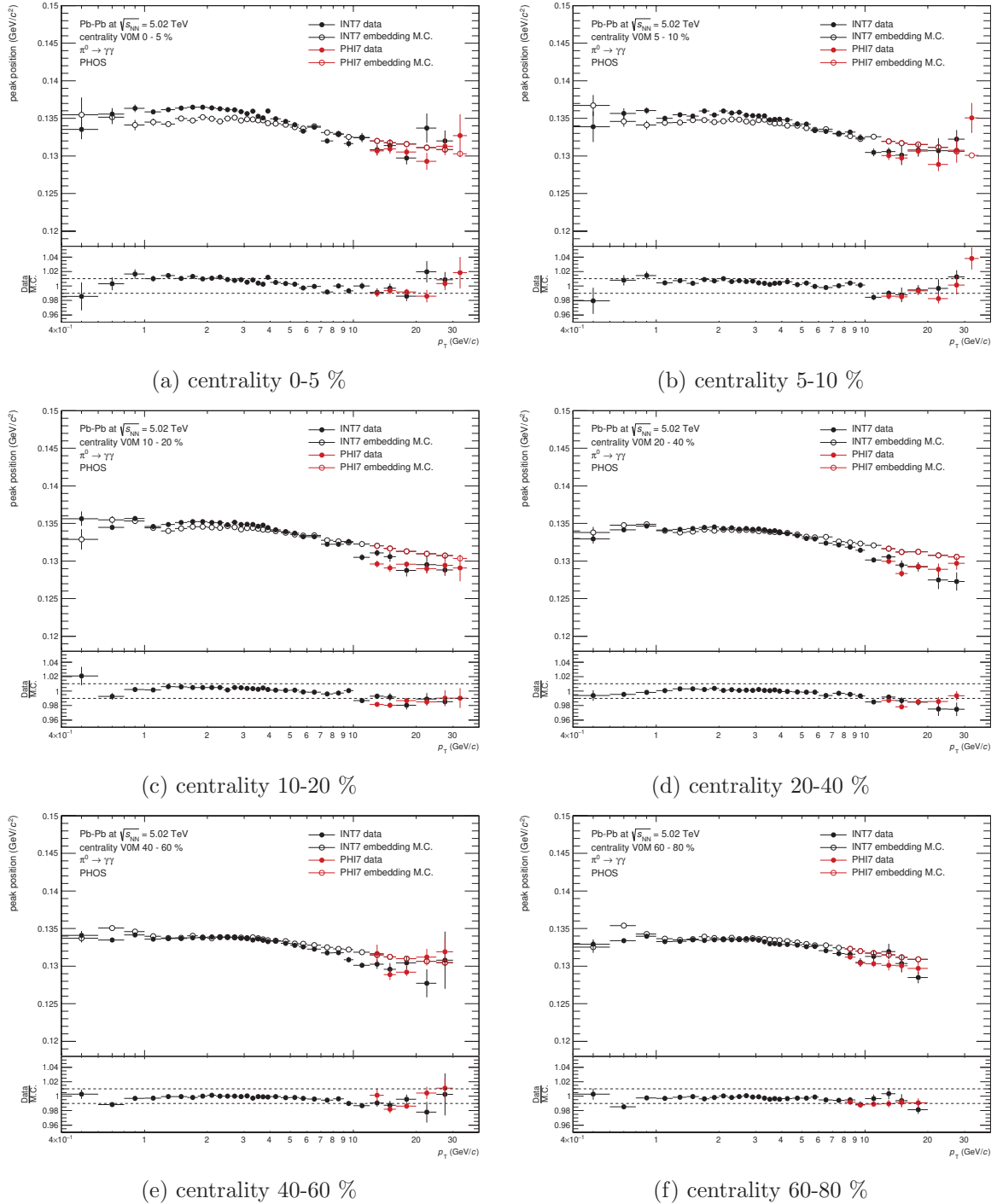
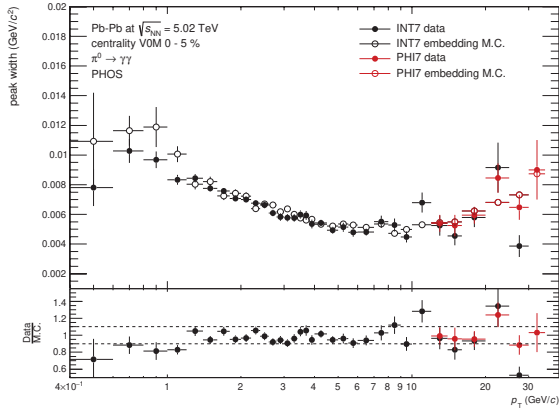
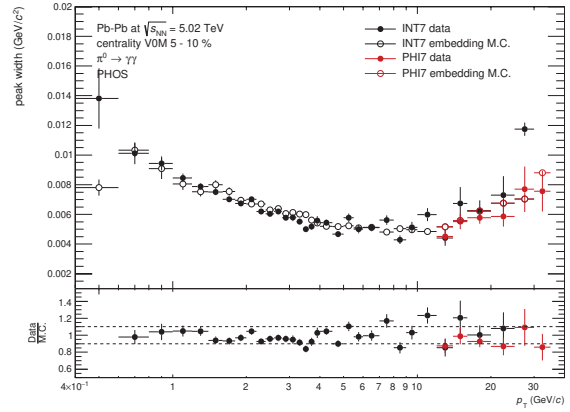


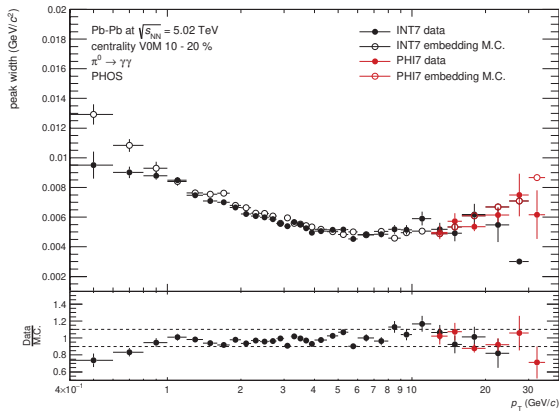
Figure 62: π^0 peak position in Pb-Pb collisions at $\sqrt{s_{NN}} = 5.02$ TeV for different centrality classes



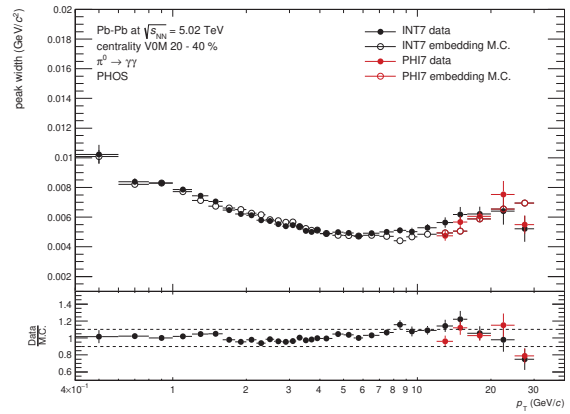
(a) centrality 0-5 %



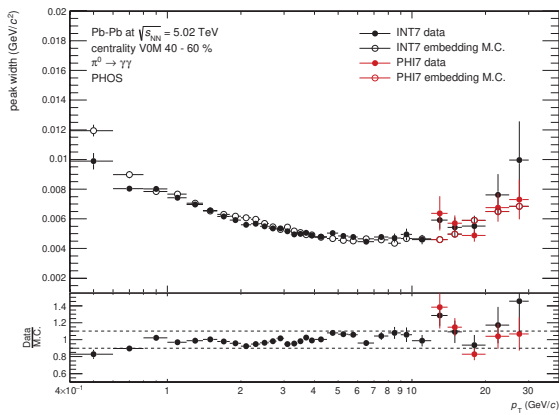
(b) centrality 5-10 %



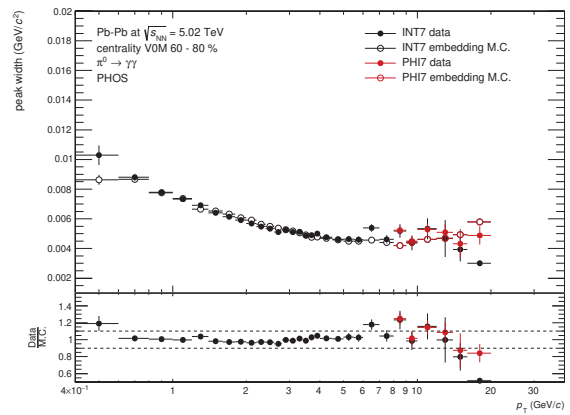
(c) centrality 10-20 %



(d) centrality 20-40 %



(e) centrality 40-60 %



(f) centrality 60-80 %

Figure 63: π^0 peak width in Pb-Pb collisions at $\sqrt{s_{NN}} = 5.02$ TeV for different centrality classes

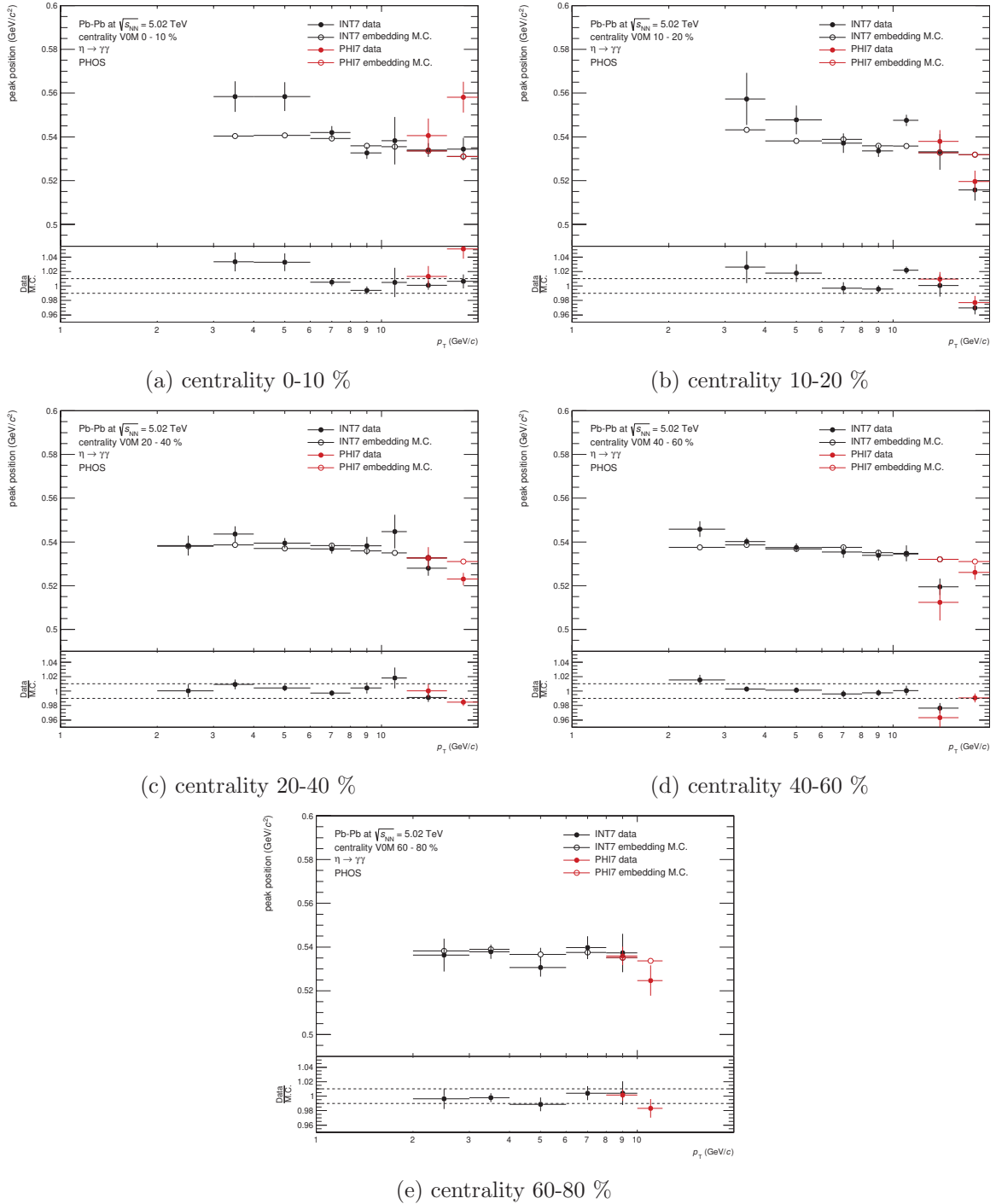
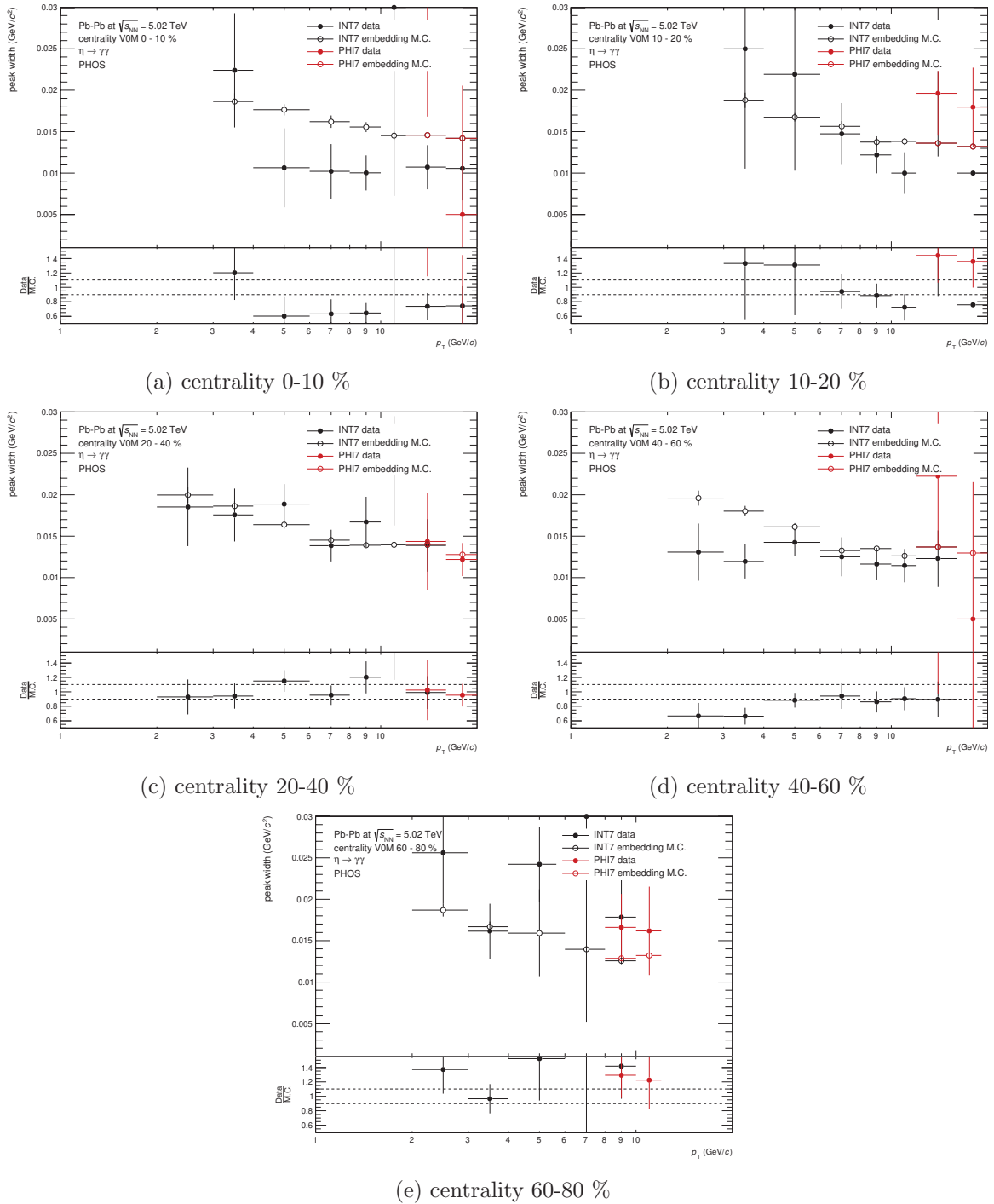


Figure 64: η peak position in Pb-Pb collisions at $\sqrt{s_{NN}} = 5.02$ TeV for different centrality classes

Figure 65: η peak width in Pb–Pb collisions at $\sqrt{s_{\text{NN}}} = 5.02$ TeV for different centrality classes

1085 **4.4.3 Timing cut**

1086 The general procedure is the same as in pp, but the bunch space was 100/150/175/225 ns in
 1087 Pb–Pb collisions (2015). So, the timing cut for clusters is $|\text{TOF}| < 50$ ns. This wide time window
 1088 leads higher TOF cut efficiency than one in pp. The drop of TOF efficiency in Figure 66b at
 1089 $E_{\text{cluster}} > 6$ GeV is due to switching high gain (HG) to low gain (LG) channels in the PHOS
 readout electronics.

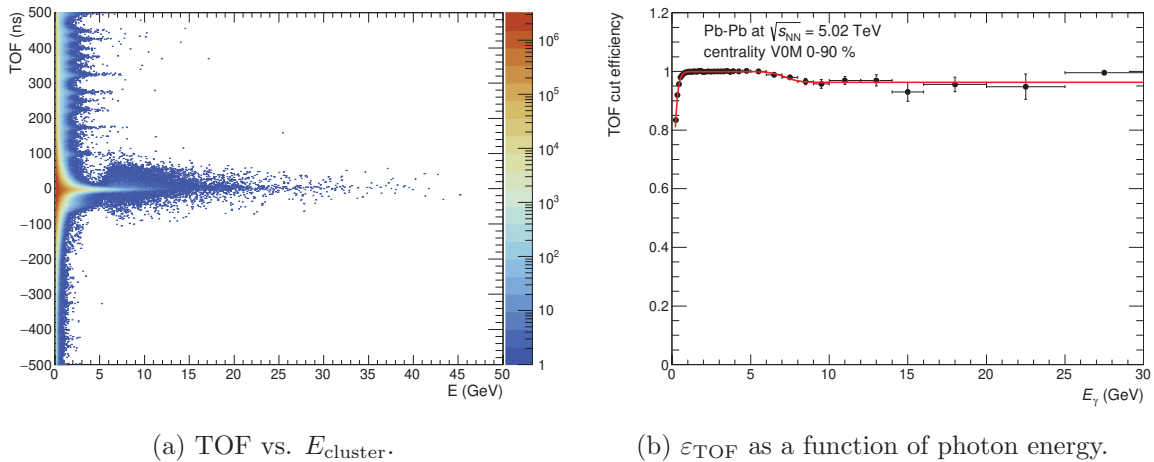
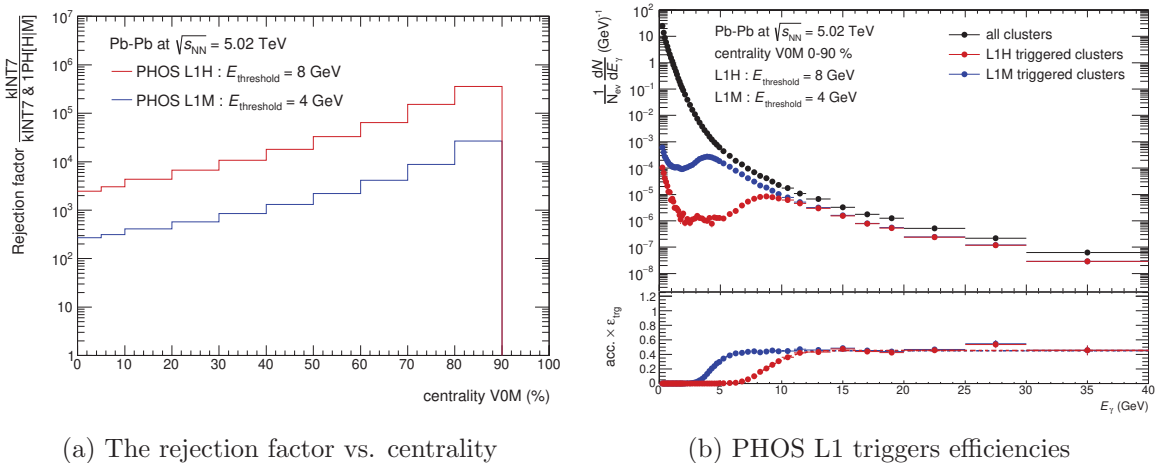


Figure 66: Timing distribution of clusters and TOF cut efficiency

1090

1091 **4.4.4 Trigger efficiency**

1092 There were two active L1 PHOS triggers in Pb–Pb collisions recorded in 2015. One is CINT7PHH,
 1093 high energy threshold at 8 GeV for all centrality classes. The other is CPER7PHM, medium
 1094 energy threshold at 4 GeV for peripheral collisions (centrality $> 60\%$). As the rejection factor
 1095 strongly depends on centrality (Figure 67a), this bias was also taken into account for the event
 1096 normalization. The trigger efficiency has a plateau region at 0.45 above the threshold shown
 1097 by Figure 67b. The rejection factor and trigger efficiency are plotted for centrality 0-90 %,
 1098 because they have been measured in MB events. This method is available, since all fired triggers
 information is stored even in MB events.



(a) The rejection factor vs. centrality

(b) PHOS L1 triggers efficiencies

Figure 67: PHOS L1 triggers performance in Pb–Pb collisions at $\sqrt{s_{\text{NN}}} = 5.02$ TeV

1099

1100 4.4.5 Feed down correction from strange hadrons

1101 HIJING event generator was used to estimate feed down in Pb–Pb collisions. The re-
 1102 weighting to K_S^0 spectrum is necessary, because it is also known that HIJING does not
 1103 reproduce realistic K^\pm/π^\pm ratio. K^\pm/π^\pm ratio in Pb–Pb collisions at $\sqrt{s} = 2.76$ TeV [61]
 1104 are taken as a reference. Figure 69, 70 show K^\pm/π^\pm ratio before and after the re-weighting
 1105 procedure. The FD factor in different centrality classes is plotted on Figure 68. It is
 1106 about 11% at the maximum in central (0–5%) collisions and becomes smaller in peripheral
 1107 (60–80%) collisions.

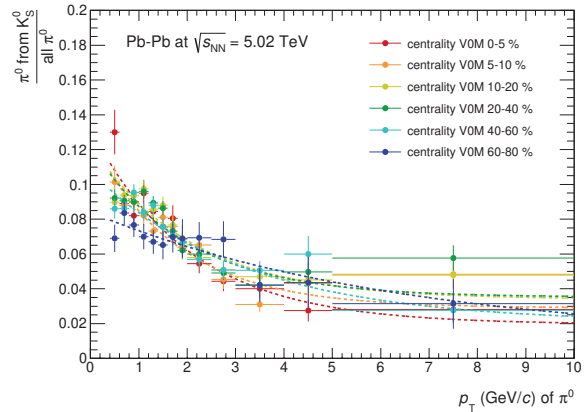


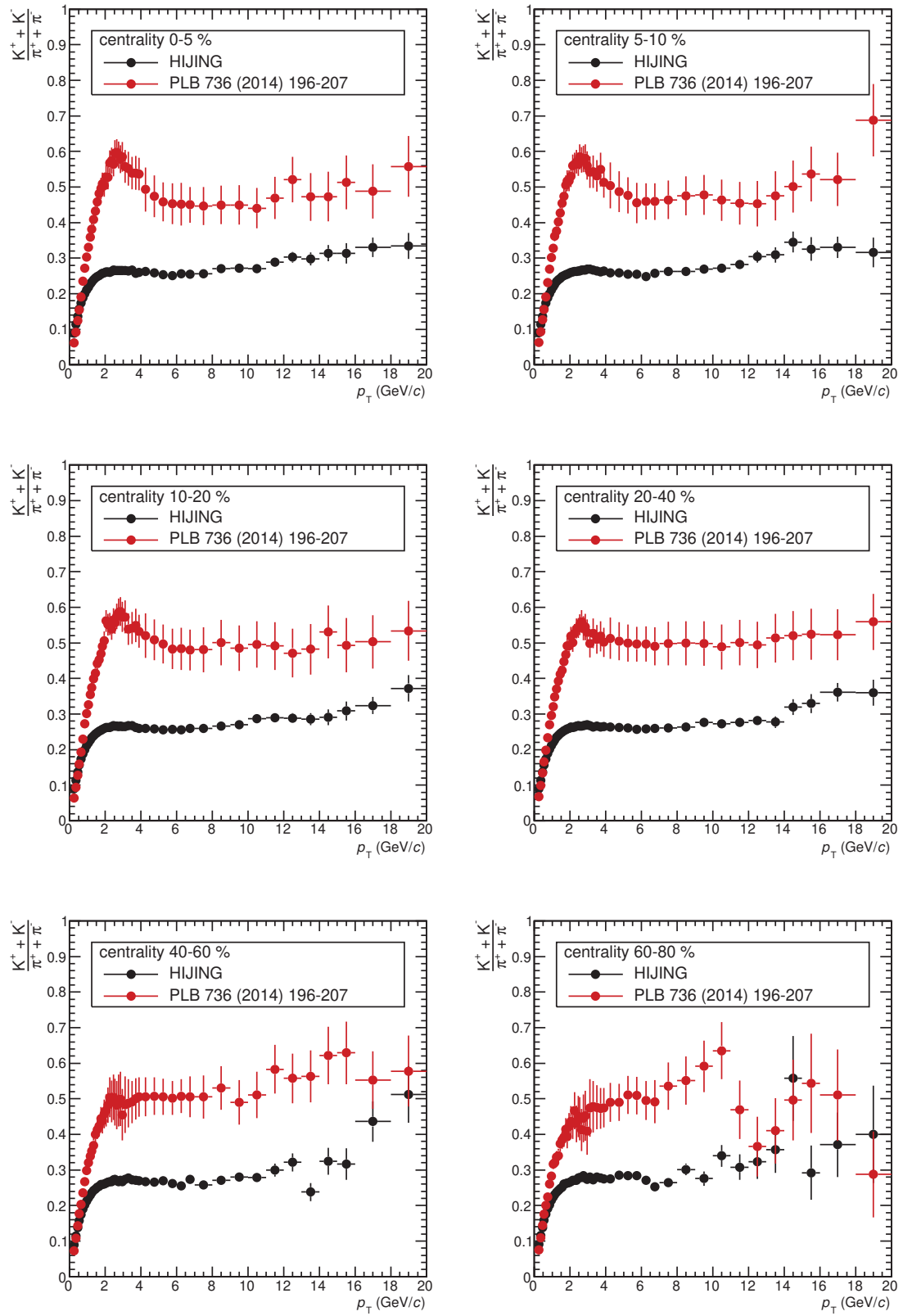
Figure 68: Feed down factor for π^0 from K_S^0 in Pb–Pb collisions at $\sqrt{s_{\text{NN}}} = 5.02$ TeV

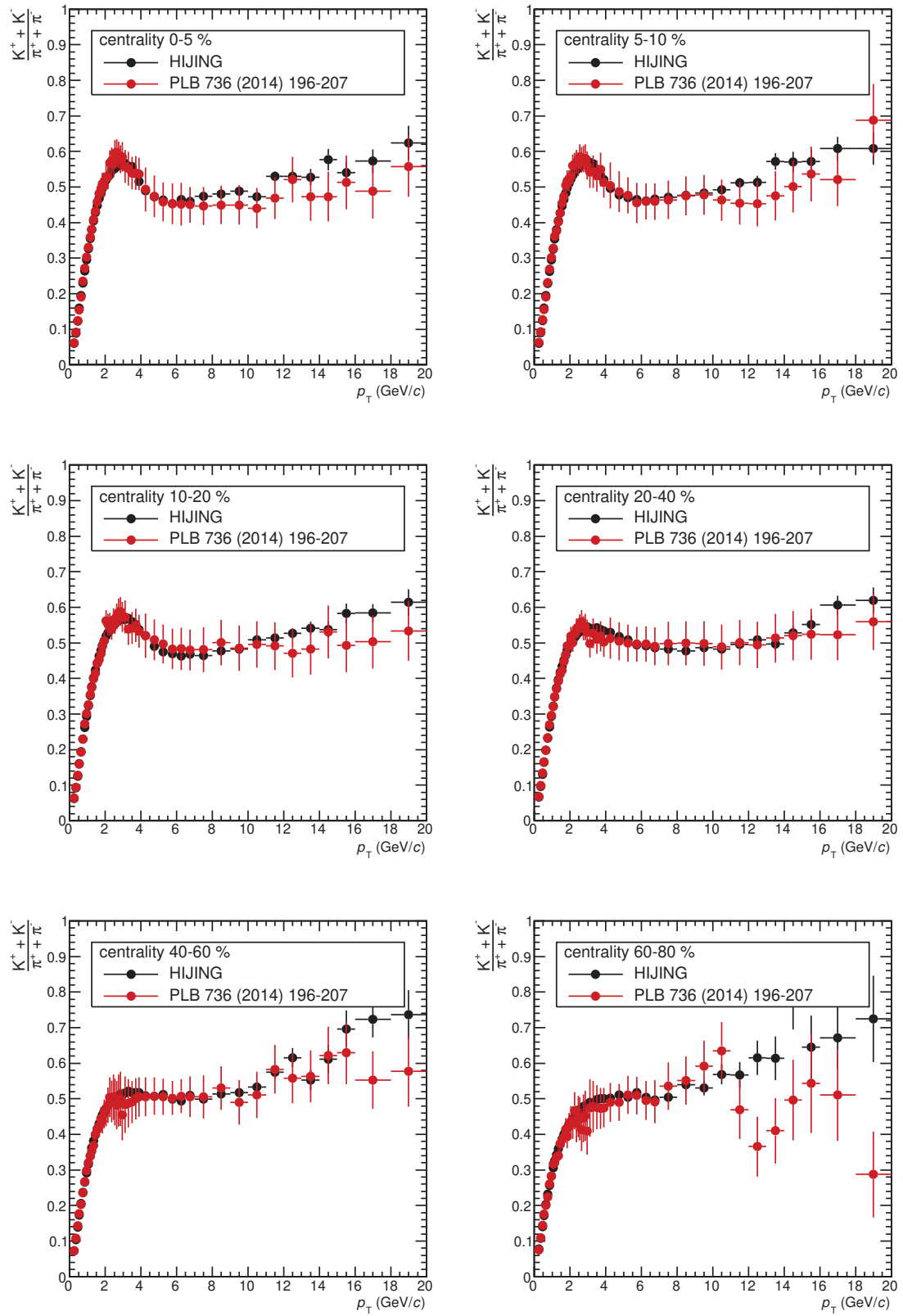
1114 4.5 Combining MB and PHOS triggered data

1115 Neutral meson spectra have been measured independently in minimum bias data and PHOS
 1116 triggered data. Finally, they have been combined by the weighted average described in [66].
 1117 Since systematic uncertainties of global energy scale, PID, material budget, feed down in case
 1118 of π^0 and acceptance of detector are common between minimum bias and PHOS triggered data,
 1119 quadratic sum of uncertainties of yield extraction, TOF in INT7, trigger efficiency in PHI7 and
 1120 statistical uncertainty are used as weights. The weighted average is defined as :

$$\hat{\mu} = \frac{1}{w} \sum_i^n w_i y_i, \quad (23)$$

1121 where $w_i = \frac{1}{\sigma_i^2}$ and $w = \sum_i^n w_i$. The standard deviation of $\hat{\mu}$ is $\frac{1}{\sqrt{w}}$.

Figure 69: K^\pm/π^\pm ratio in M.C. before re-weighting.

Figure 70: K^\pm/π^\pm ratio in M.C. after re-weighting.

5 Systematic uncertainties for neutral mesons

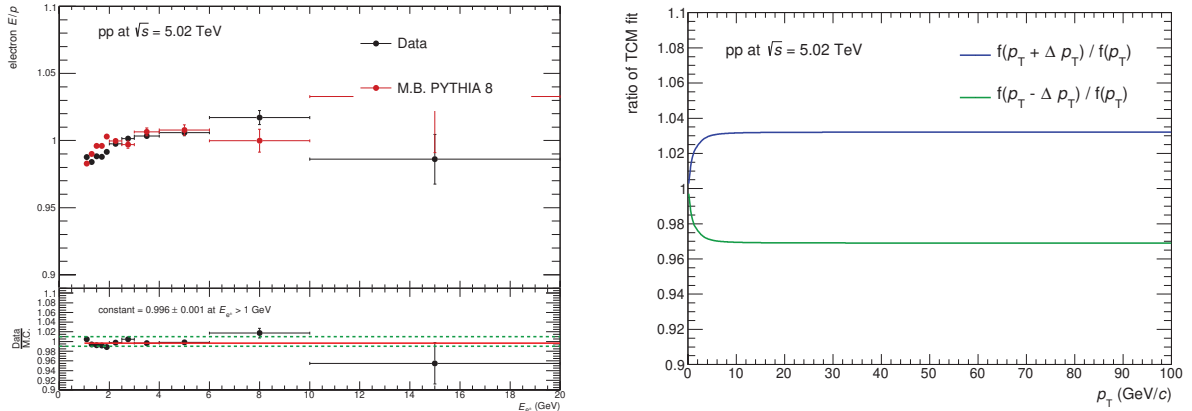
5.1 Yield extraction

A systematic uncertainty of yield extraction was estimated by varying fitting functions, fitting ranges and integral regions. In total, 24 combinations were performed for each neutral mesons. The relative systematic uncertainty of the yield extraction is defined as standard deviation/mean value of 24 samples.

- Fitting function for signal : Gaussian/CrystalBall [67]
- Fitting function for background : polynomial 1/2
- Fitting ranges for π^0 : [0.06,0.22], [0.04,0.20], [0.08,0.24] GeV/c^2
- Fitting ranges for η : [0.4,0.7], [0.35,0.65], [0.45,0.75] GeV/c^2
- Integral region : $[-3\sigma,+3\sigma]$, $[-2\sigma,+2\sigma]$ around the peak

5.2 Global energy scale

The global energy scale was evaluated by energy to momentum ratio E/p of electrons (positrons) in data and M.C.. Criteria for e^\pm identification are $-2 < n\sigma_e < 3$ in dE/dx measured by TPC and matched with a PHOS cluster which pass dispersion cut (2.5σ). Here, the $n\sigma_e$ represents accepted deviation in unit of standard deviation from the dE/dx value expected for the electron signal. Figure.71 shows electron E/p reaches 1 at high energy and is well reproduced by M.C.. According to this study, the discrepancy between data and M.C. in $E/p \pm 0.5\%$ is assigned to an uncertainty of energy scale. The p_T of neutral meson is shifted by $\Delta p_T/p_T = \pm 0.005$ in TCM function (or Hagedorn function for η meson in pp) fitting, and the ratio to the function with $\Delta p_T/p_T = 0$ was taken. The larger side is assigned to the final systematic uncertainty of particle yields due to the global energy scale. In case of Pb–Pb collisions, the energy scale uncertainty



(a) E/p of e^\pm as a function of energy measured by PHOS.

(b) The ratio of TCM fit to π^0 .

Figure 71: E/p of e^\pm and the uncertainty of particle yield by the energy scale in pp collisions at $\sqrt{s} = 5.02$ TeV.

due to the discrepancy of peak position between data and M.C. ($\Delta p_T/p_T \sim 0.01$ for centrality 0-10 %, $\Delta p_T/p_T \sim 0.005$ for centrality 10-40 %) was added quadratically.

5.3 Non-linearity of energy measurement in simulation

The non-linear response of the energy measurement was studied in pp collisions at $\sqrt{s} = 5.02$ TeV taken in 2015 data, described in section B.8.6.

5.4 Trigger efficiency

The systematic uncertainty related to the trigger efficiency was estimated by varying fitting range at plateau region on Figure 53 and 67b. They have plateau region at 0.597 ± 0.015 for PHOS L0 trigger in pp collisions (2017) and at 0.45 ± 0.02 for PHOS L1H/M trigger in Pb–Pb collisions at $\sqrt{s_{NN}} = 5.02$ TeV, respectively. Since neutral meson yields are corrected by logical-OR (i.e. $\varepsilon_{NM}^{\text{trg}} = \varepsilon_{\gamma 1}^{\text{trg}} + \varepsilon_{\gamma 2}^{\text{trg}} - \varepsilon_{\gamma 1}^{\text{trg}} \times \varepsilon_{\gamma 2}^{\text{trg}}$), the uncertainty of trigger efficiency for 1 photon is analytically propagated to the uncertainty of their yields at high p_T .

5.5 Timing cut efficiency

There were data taking period when a bunch space of each pp collision was 1000 ns which was much wider than timing resolution of PHOS. These runs allow us to estimate systematic uncertainty of TOF cut efficiency. The idea is defined by Eq.24. The deviation from unity in the ratio is considered as a systematic uncertainty of TOF cut.

$$\text{ratio} = \frac{\pi^0 \text{ yield at BS} = 25 \text{ ns corrected by } \varepsilon_{\text{TOF}}^1 \times \varepsilon_{\text{TOF}}^2}{\pi^0 \text{ yield at BS} = 1000 \text{ ns } (\varepsilon_{\text{TOF}} = 1)} \quad (24)$$

As shown by Figure.72a, it is found to be 2% in pp collisions at $\sqrt{s} = 5.02$ TeV, not depending

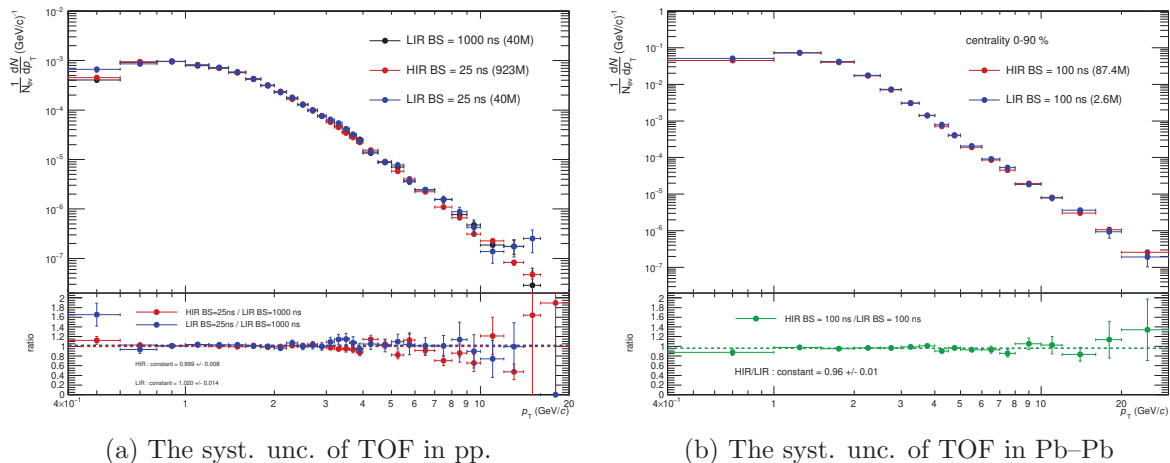


Figure 72: The ratio of π^0 raw yields in high intensity runs to those in low intensity runs.

on p_T . The same approach was applied for Pb–Pb analysis, but the nominal bunch space (BS) was 100 ns. It is found to be 4% in Pb–Pb collisions at $\sqrt{s_{NN}} = 5.02$ TeV.

5.6 PID cut efficiency

In order to check photon identification cut on PHOS, each PID cut efficiency as a function of photon energy was evaluated. i.e. Charged Particle Veto (2.5σ) and dispersion cut (2.5σ) were tested. Especially in pp collisions, the CPV cut efficiency is very close to unity, because average charged track multiplicity in pp collisions is expected to be $5 \sim 7$ tracks at mid-rapidity [68]. Hence, the probability of random matching between a photon hit and a charged particle is small.

1170 The deviation from unity in the ratio Data/M.C. is considered as systematic uncertainty of PID cut, which is $\sim 2\%$ without depending on photon energy in all centralities.

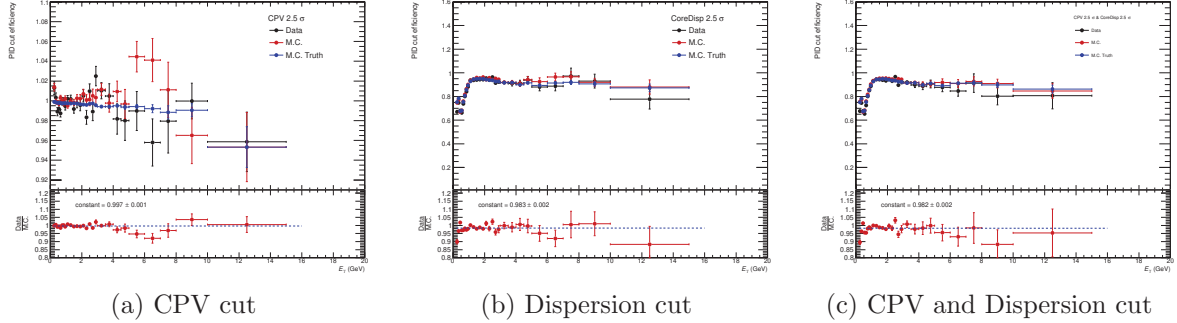


Figure 73: PID cut efficiency as a function of photon energy in pp collisions at $\sqrt{s} = 5.02$ TeV.

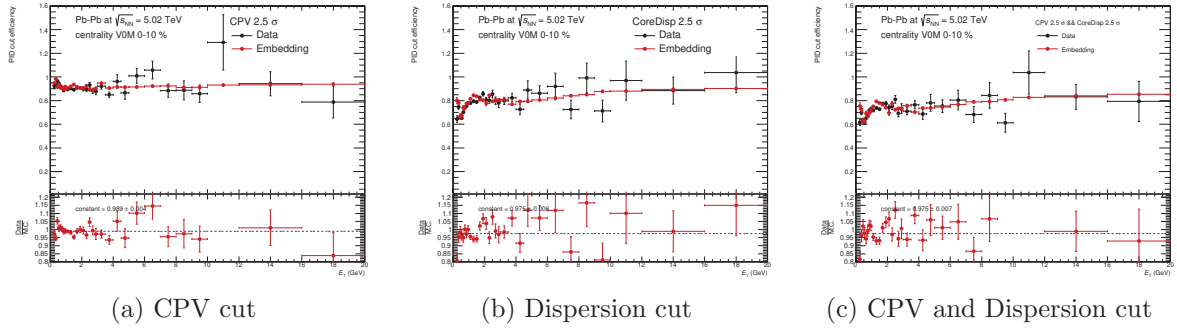


Figure 74: PID cut efficiency as a function of photon energy in Pb-Pb collisions at $\sqrt{s_{NN}} = 5.02$ TeV centrality 0-10%.

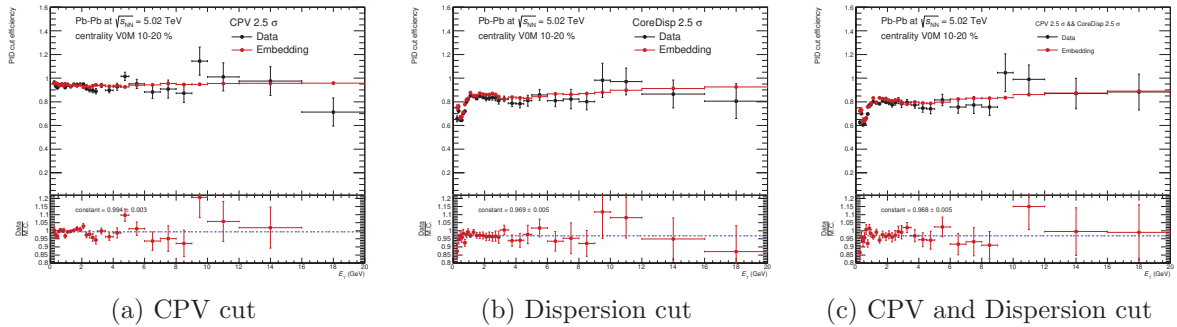


Figure 75: PID cut efficiency as a function of photon energy in Pb-Pb collisions at $\sqrt{s_{NN}} = 5.02$ TeV centrality 10-20%.

1171

1172 5.7 Feed down from strange hadrons

1173 The systematic uncertainty of feed down correction to π^0 is inherited from the systematic un-
 1174 certainty of the measured K^\pm/π^\pm ratio [61]. Typically, the systematic uncertainty of K/π ratio
 1175 is about 10 % at the maximum. Thus, it is feed down correction $\times 0.1$ in both pp and Pb-Pb
 1176 collisions.

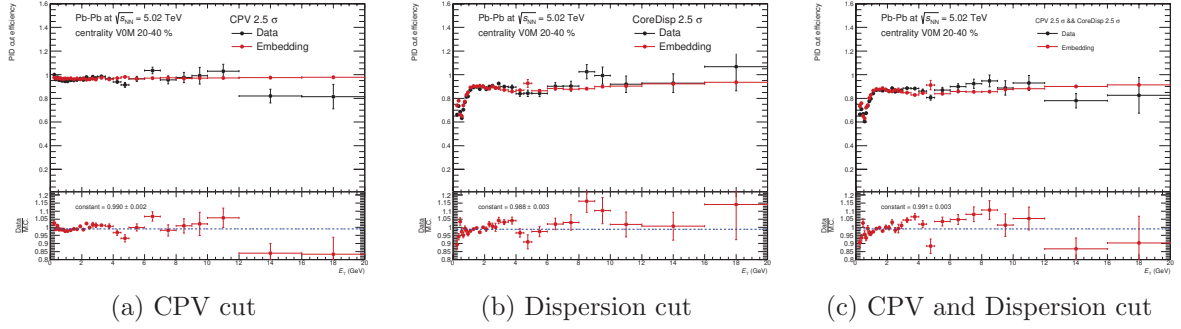


Figure 76: PID cut efficiency as a function of photon energy in Pb–Pb collisions at $\sqrt{s_{\text{NN}}} = 5.02$ TeV centrality 20-40%.

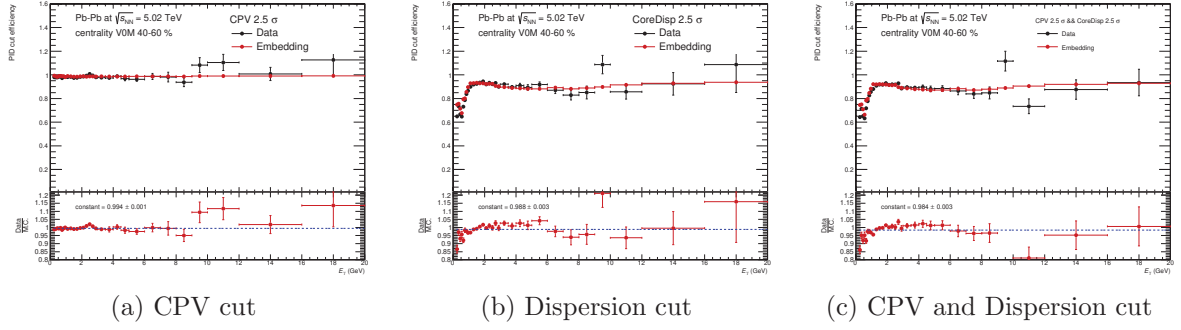


Figure 77: PID cut efficiency as a function of photon energy in Pb–Pb collisions at $\sqrt{s_{\text{NN}}} = 5.02$ TeV centrality 40-60%.

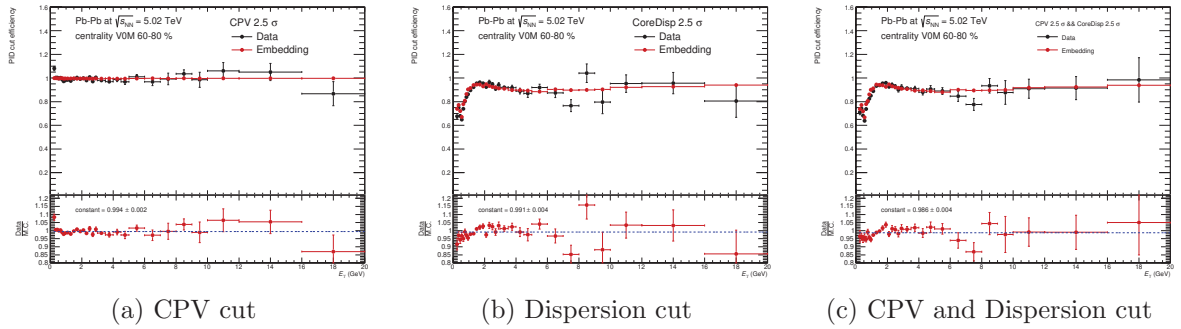


Figure 78: PID cut efficiency as a function of photon energy in Pb–Pb collisions at $\sqrt{s_{\text{NN}}} = 5.02$ TeV centrality 60-80%.

1177 **5.8 Acceptance of PHOS detector**

1178 This estimation was done in 2015 data of pp collisions at $\sqrt{s} = 5.02$ TeV by varying the distance
 1179 to the closest bad channel (0 or 1 cell), which is described in section B.8.7. Typically, it is 1.5
 1180 % for neutral mesons.

1181 **5.9 Material budget**

1182 This uncertainty is common in pp and Pb–Pb data, as ALICE detector did not change during
 1183 Run2 operation. The systematic uncertainty of the material budget has been estimated by
 1184 comparing π^0 yields between magnetic field ON and OFF taken in 2017 data (LHC17d). As
 1185 converted e^+e^- pairs do not bend without magnetic field, the e^+e^- pair is reconstructed as
 1186 same as a photon candidate. This results in increase of the reconstructed π^0 yields and allows
 1187 us to estimate description of the material budget in simulation. Note that there are TOF and
 1188 TRD in front of PHOS M4 (a half module). As shown by Fig.79, π^0 yields at $B = 0.0$ T is
 1189 higher those in 0.5 T and well described by M.C in M123 (1.01 ± 0.02). However, there are large
 1190 statistical error bars in M4 (1.11 ± 0.21). Thus, I decided to exclude M4 from my analyses and
 the systematic uncertainty of the material budget is 2% from this study.

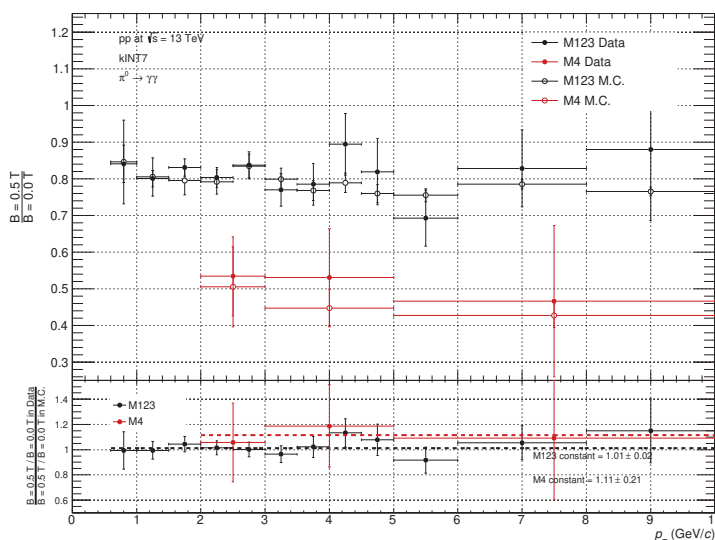
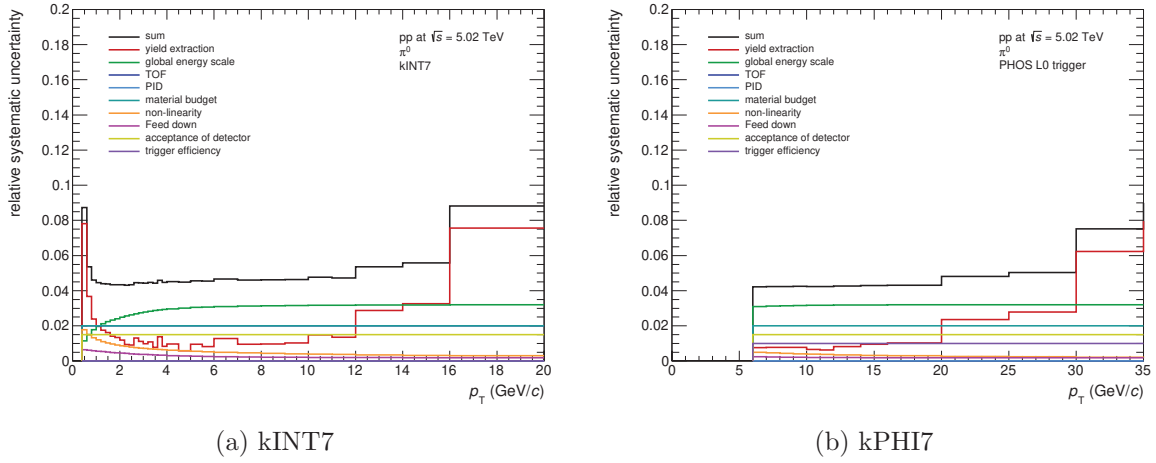
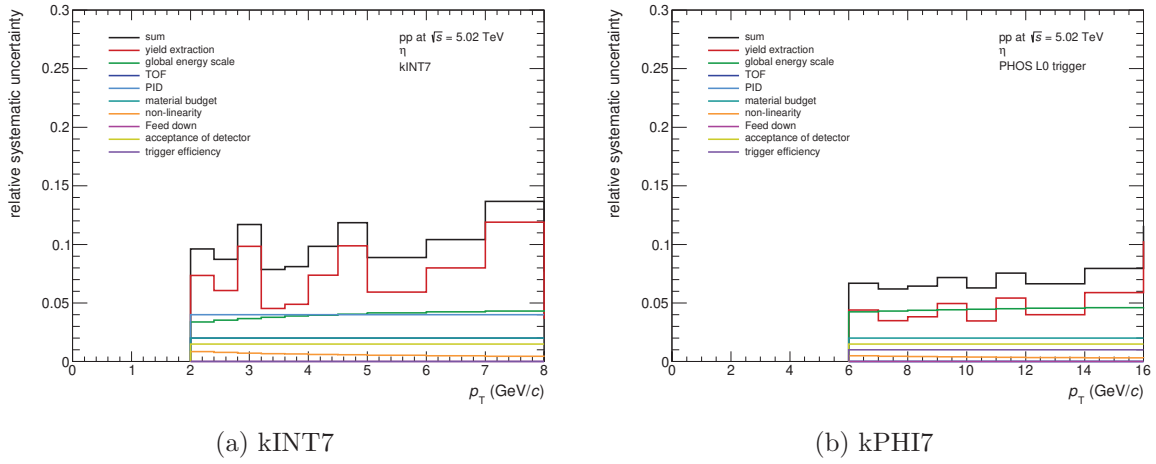


Figure 79: top : ratio of π^0 yields at $B = 0.5$ T to those at $B = 0.0$ T in data and M.C.. bottom : Double ratio of π^0 yields

1191

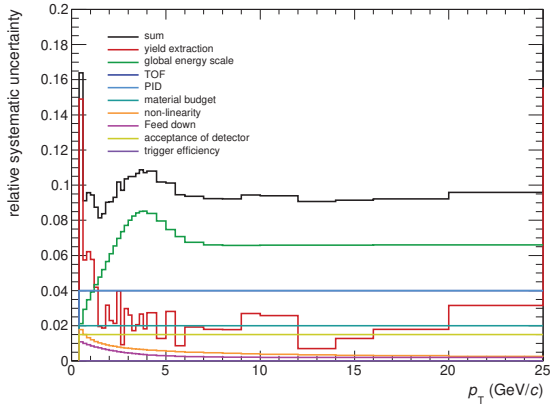
1192 **5.10 Summary of systematic uncertainties**

 1193 Total systematic uncertainties for π^0 and η mesons are summarized in this section.

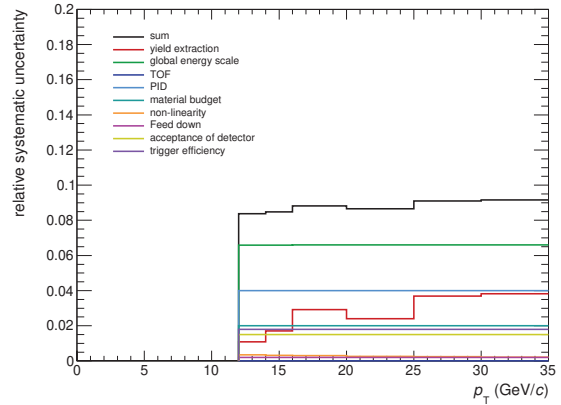
 1194 **5.10.1 Summary of systematic uncertainties in pp collisions at $\sqrt{s} = 5.02$ TeV**

 Figure 80: The summary of systematic uncertainties of the π^0 measurement in pp collisions at $\sqrt{s} = 5.02$ TeV

 Figure 81: The summary of systematic uncertainties of the η measurement in pp collisions at $\sqrt{s} = 5.02$ TeV

 1195 **5.10.2 Summary of systematic uncertainties in Pb–Pb collisions at $\sqrt{s_{NN}} = 5.02$ TeV**

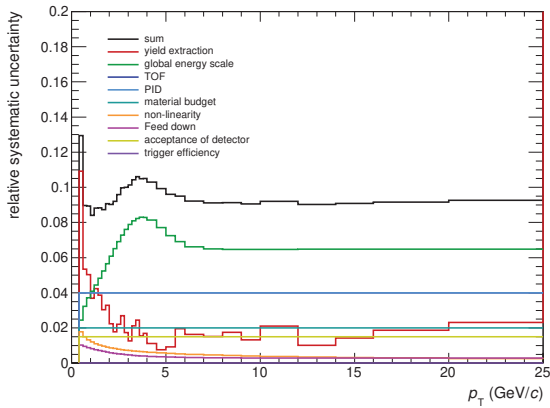
1196



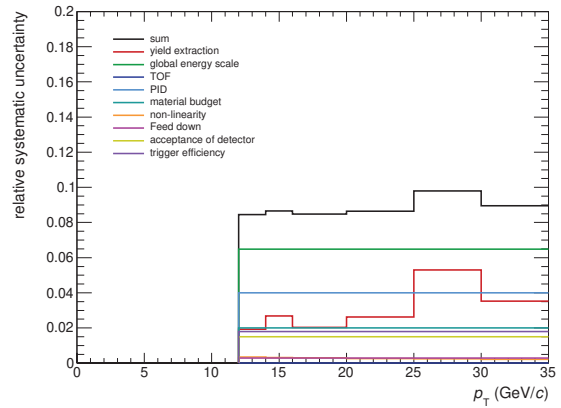
(a) kINT7



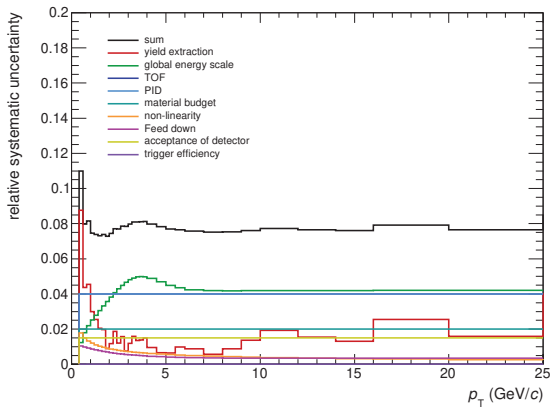
(b) kPHI7

 Figure 82: The summary of systematic uncertainties of the π^0 measurement in Pb–Pb collisions at $\sqrt{s_{NN}} = 5.02$ TeV (0-5 %)


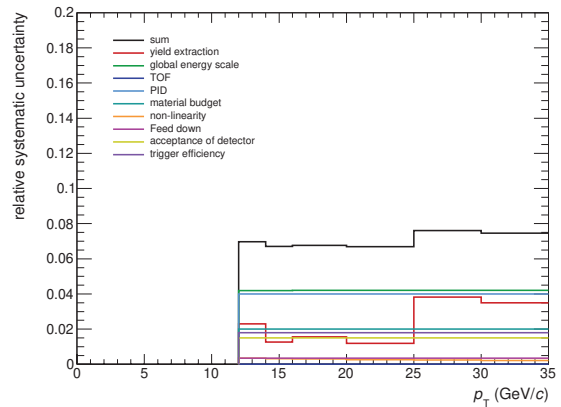
(a) kINT7



(b) kPHI7

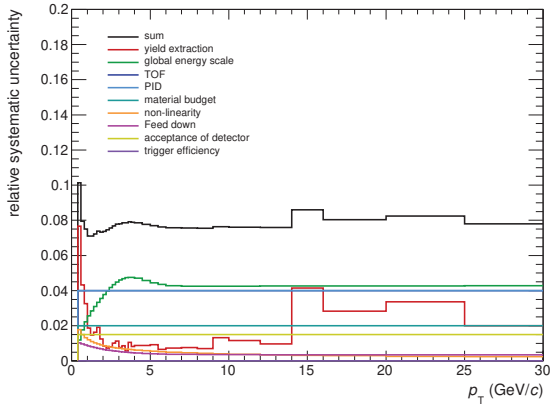
 Figure 83: The summary of systematic uncertainties of the π^0 measurement in Pb–Pb collisions at $\sqrt{s_{NN}} = 5.02$ TeV (5-10 %)


(a) kINT7

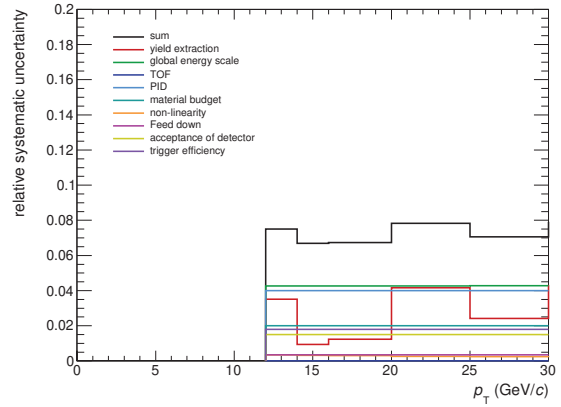


(b) kPHI7

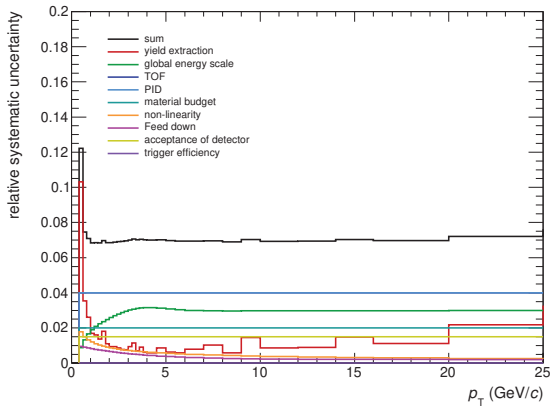
 Figure 84: The summary of systematic uncertainties of the π^0 measurement in Pb–Pb collisions at $\sqrt{s_{NN}} = 5.02$ TeV (10-20 %)



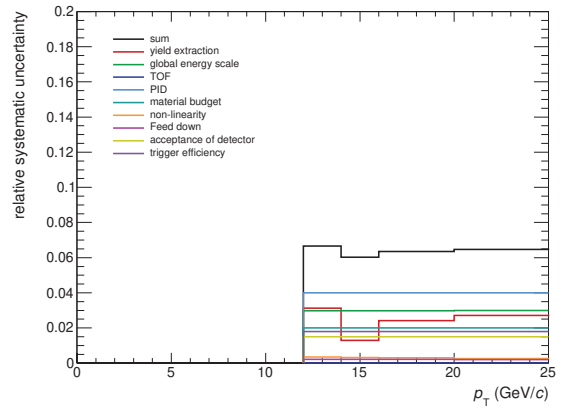
(a) kINT7



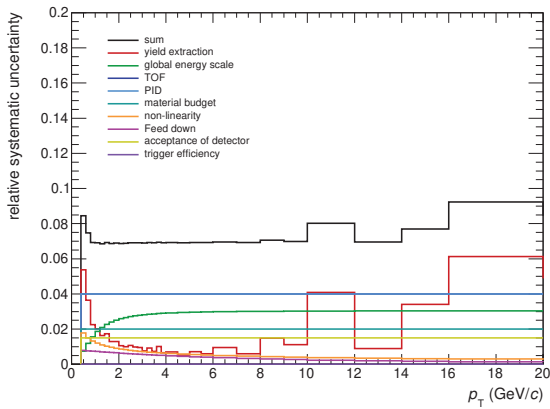
(b) kPHI7

 Figure 85: The summary of systematic uncertainties of the π^0 measurement in Pb–Pb collisions at $\sqrt{s_{NN}} = 5.02$ TeV (20–40 %)


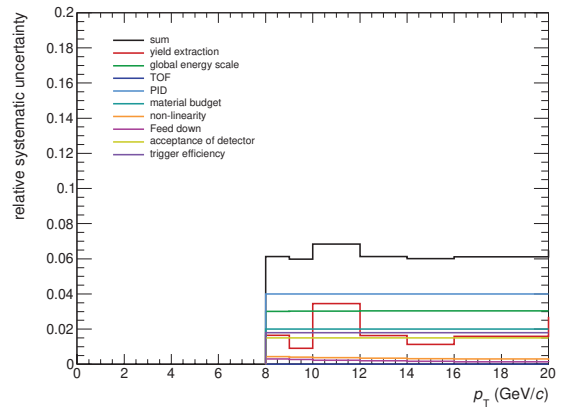
(a) kINT7



(b) kPHI7

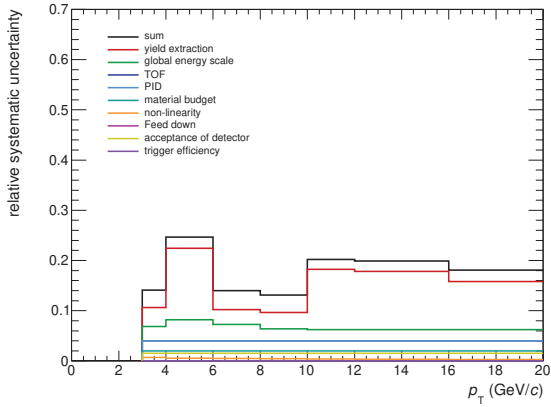
 Figure 86: The summary of systematic uncertainties of the π^0 measurement in Pb–Pb collisions at $\sqrt{s_{NN}} = 5.02$ TeV (40–60 %)


(a) kINT7

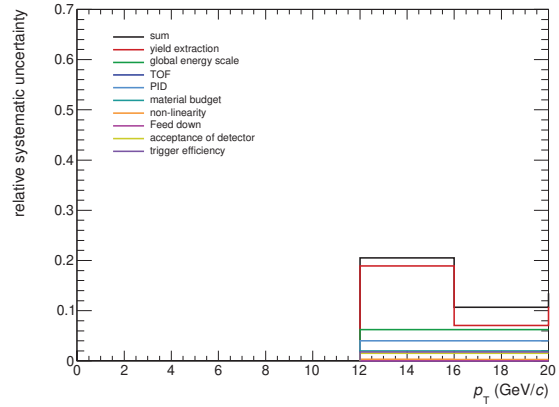


(b) kPHI7

 Figure 87: The summary of systematic uncertainties of the π^0 measurement in Pb–Pb collisions at $\sqrt{s_{NN}} = 5.02$ TeV (60–80 %)

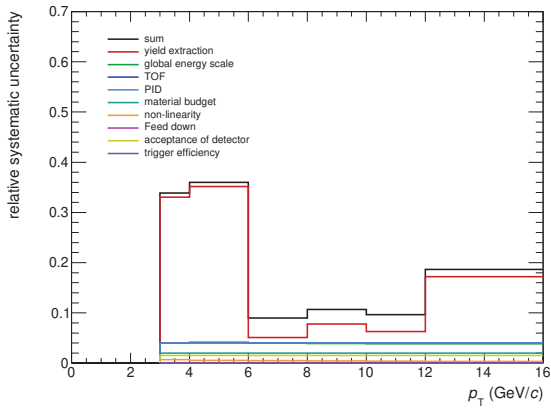


(a) kINT7

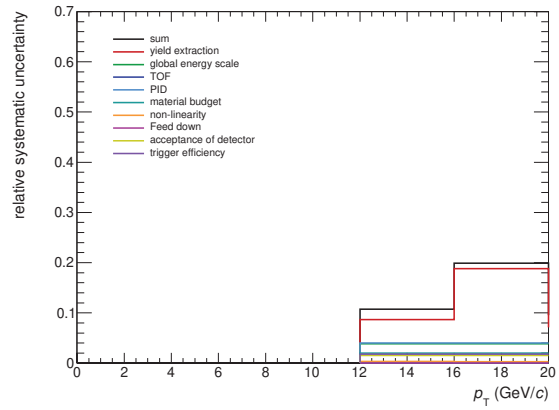


(b) kPHI7

Figure 88: The summary of systematic uncertainties of the η measurement in Pb–Pb collisions at $\sqrt{s_{NN}} = 5.02$ TeV (0-10 %)

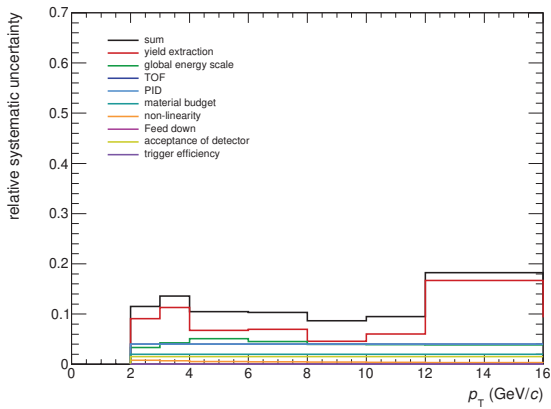


(a) kINT7

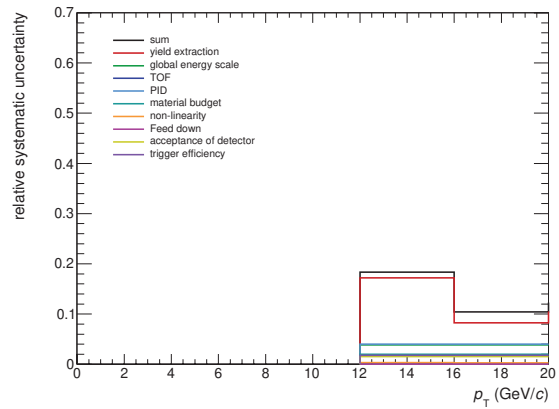


(b) kPHI7

Figure 89: The summary of systematic uncertainties of the η measurement in Pb–Pb collisions at $\sqrt{s_{NN}} = 5.02$ TeV (10-20 %)

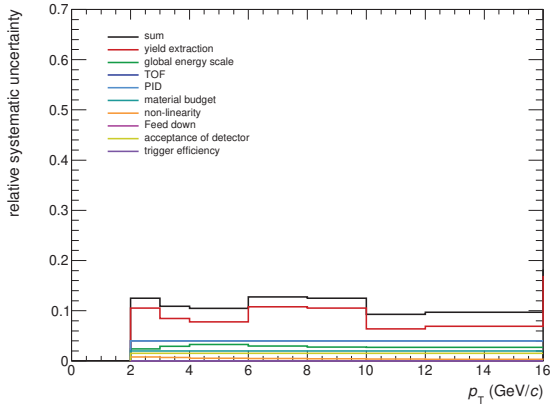


(a) kINT7

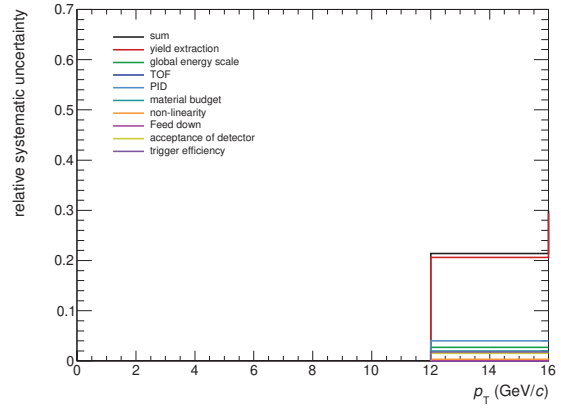


(b) kPHI7

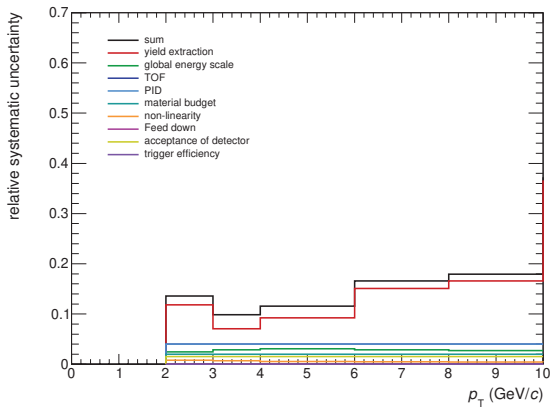
Figure 90: The summary of systematic uncertainties of the η measurement in Pb–Pb collisions at $\sqrt{s_{NN}} = 5.02$ TeV (20-40 %)



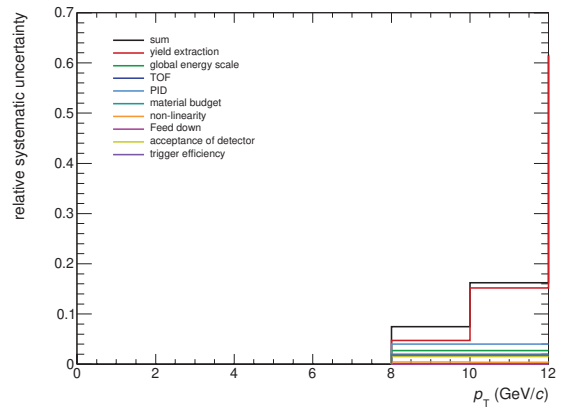
(a) kINT7



(b) kPHI7

 Figure 91: The summary of systematic uncertainties of the η measurement in Pb–Pb collisions at $\sqrt{s_{NN}} = 5.02$ TeV (40-60 %)


(a) kINT7



(b) kPHI7

 Figure 92: The summary of systematic uncertainties of the η measurement in Pb–Pb collisions at $\sqrt{s_{NN}} = 5.02$ TeV (60-80 %)

6 Results and discussions for neutral mesons

Results of neutral mesons analyses are summarized in this section. Production cross sections, invariant yield, particle ratio η/π^0 , and nuclear modification factor R_{AA} are described. In all figures, vertical bars represent statistical error and boxes indicate the systematic uncertainty.

6.1 Invariant cross section of particles

The production cross section of π^0 and η mesons have been measured in pp collisions at $\sqrt{s} = 5.02$ TeV. Neutral mesons spectra are fitted by either two-component model (TCM) function [69, 70, 71] or Hagedorn function [72]. Two-component model function is :

$$E \frac{d^3\sigma}{dp^3} = A_e \exp\left(-\frac{E_{T\text{kin}}}{T_e}\right) + A \left(1 + \frac{p_T^2}{T^2 \cdot n}\right)^{-n}, \quad (25)$$

where A_e , T_e , A , T and n are free parameters for fitting and $E_{T\text{kin}} = \sqrt{p_T^2 + m^2} - m$ is transverse kinetic energy (m is mass of particle). The exponential term is for soft, and the power-law is for hard particle production. Hagedorn function is :

$$E \frac{d^3\sigma}{dp^3} = A \left(1 + \frac{p_T}{p_0}\right)^{-n}, \quad (26)$$

$$\left(1 + \frac{p_T}{p_0}\right)^{-n} \rightarrow \begin{cases} \exp\left(-\frac{n}{p_0} p_T\right) & \text{for } p_T \ll p_0 \\ p_T^{-n} & \text{for } p_T \rightarrow \infty \end{cases}$$

where A , p_0 and n is free parameters for fitting. Hagedorn function behaves exponential at low p_T and power-law at high p_T . Fitting parameters are listed in Table. 1, 2, 3, 4.

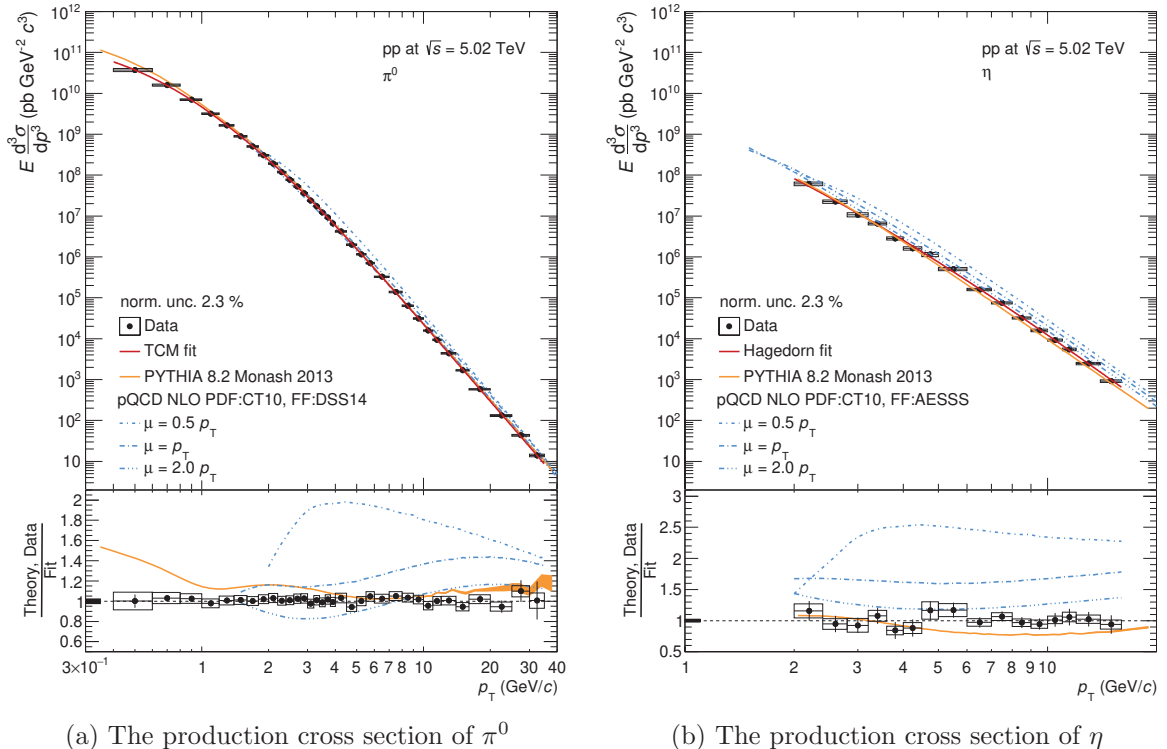


Figure 93: Production cross sections of neutral mesons in pp collisions at $\sqrt{s} = 5.02$ TeV

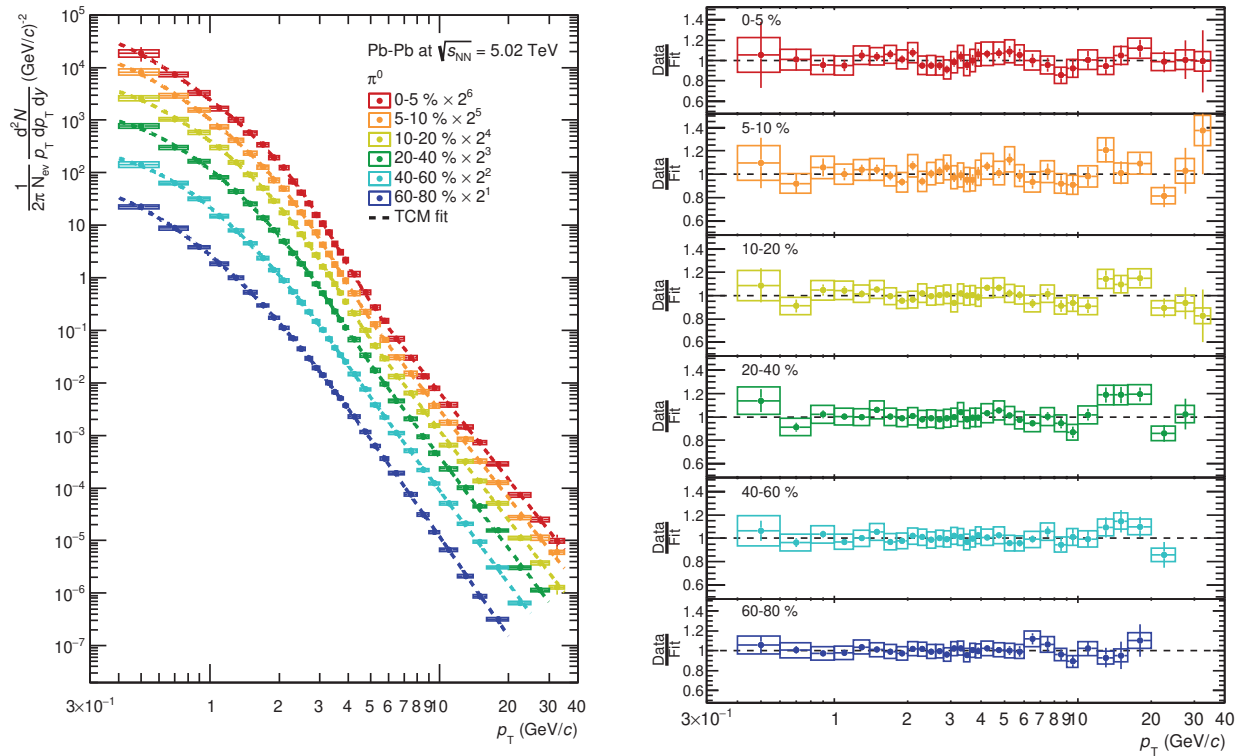
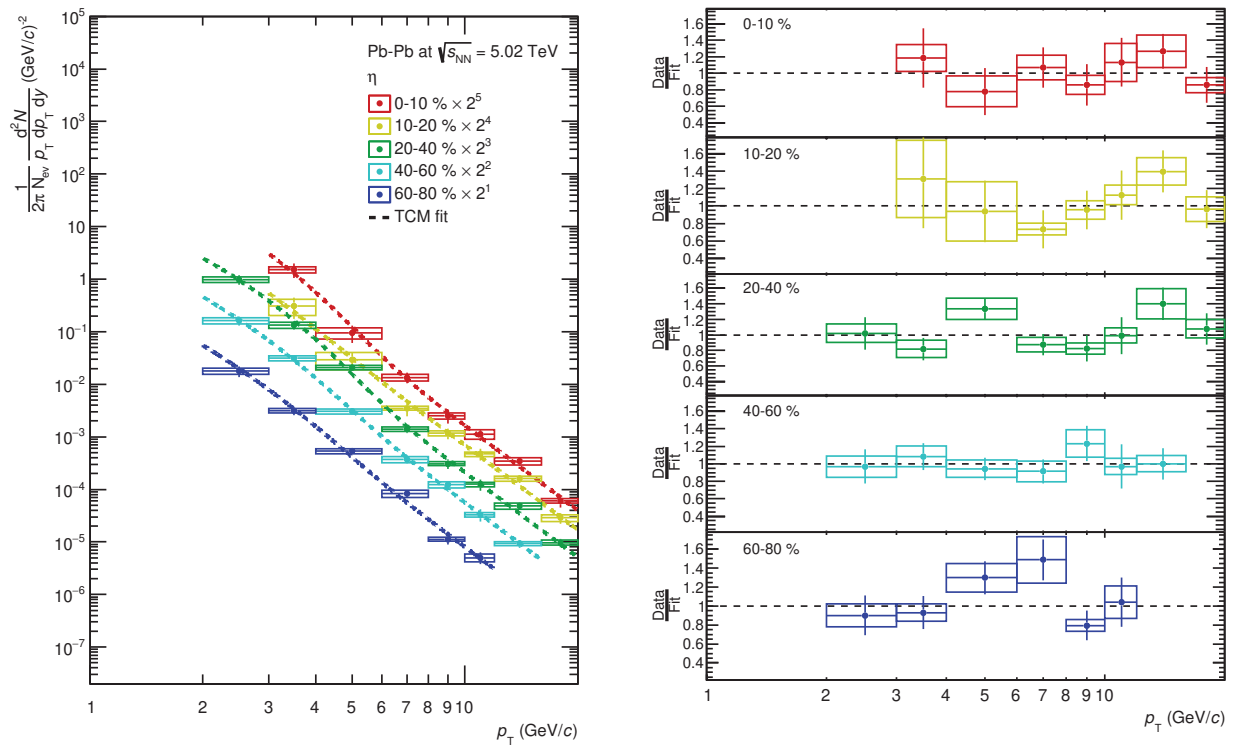

 (a) The invariant yield of π^0

 (b) The invariant yield of η

 Figure 94: Invariant yields of neutral mesons in Pb-Pb collisions at $\sqrt{s_{NN}} = 5.02$ TeV

Table 1: Fitting parameters of TCM function in pp collisions at $\sqrt{s} = 5.02$ TeV

particle	A_e (pb GeV ⁻² c ³)	T_e (GeV/c)	A (pb GeV ⁻² c ³)	T (GeV/c)	n
π^0	$(2.57 \pm 0.58) \times 10^{11}$	0.18 ± 0.02	$(0.16 \pm 0.04) \times 10^{11}$	0.67 ± 0.03	3.16 ± 0.02

Table 2: Fitting parameters of Hagedorn function in pp collisions at $\sqrt{s} = 5.02$ TeV

particle	A (pb GeV ⁻² c ³)	p_0 (GeV/c)	n
η	$(1.58 \pm 0.58) \times 10^{11}$	0.96 ± 0.08	6.7 ± 0.1

Table 3: Fitting parameters of TCM function for π^0 in Pb–Pb collisions at $\sqrt{s_{NN}} = 5.02$ TeV

centrality (%)	A_e (GeV ⁻² c ³)	T_e (GeV/c)	A (GeV ⁻² c ³)	T (GeV/c)	n
0-5	187 ± 26	0.39 ± 0.01	1526 ± 1055	0.29 ± 0.05	2.75 ± 0.04
5-10	144 ± 22	0.39 ± 0.01	1026 ± 500	0.33 ± 0.04	2.78 ± 0.04
10-20	105 ± 15	0.39 ± 0.01	421 ± 129	0.39 ± 0.03	2.85 ± 0.03
20-40	40.7 ± 7.4	0.40 ± 0.01	233 ± 52	0.41 ± 0.02	2.89 ± 0.03
40-60	5.9 ± 1.9	0.43 ± 0.02	92 ± 16	0.44 ± 0.02	2.93 ± 0.03
60-80	78 ± 36	0.16 ± 0.03	5.9 ± 2.8	0.64 ± 0.06	3.17 ± 0.04
0-10	185 ± 24	0.39 ± 0.01	1062 ± 466	0.32 ± 0.03	2.76 ± 0.03
0-90	43.7 ± 7.1	0.39 ± 0.01	163 ± 43	0.41 ± 0.02	2.88 ± 0.02

Table 4: Fitting parameters of TCM function for η in Pb–Pb collisions at $\sqrt{s_{NN}} = 5.02$ TeV

centrality (%)	A_e (GeV ⁻² c ³)	T_e (GeV/c)	A (GeV ⁻² c ³)	T (GeV/c)	n
0-10	6.1 ± 2.9	0.55	202 ± 27	0.36	2.68
10-20	0.78 ± 2.0	0.55	171 ± 21	0.36	2.68
20-40	3.1 ± 0.6	0.55	103 ± 10	0.36	2.68
40-60	0.81 ± 0.25	0.55	55.5 ± 6.2	0.36	2.68
60-80	0.15 ± 0.07	0.55	15.8 ± 2.1	0.36	3.68
0-90	2.6 ± 1.5	0.55 ± 0.05	112 ± 89	0.36 ± 0.05	2.68 ± 0.10

1210 Especially, η meson spectra in Pb–Pb collisions have only $6 \sim 7$ data points, that leads poor
 1211 quality of the fitting or divergence. Therefore, centrality classes are merged into 0-90 % to
 1212 get the full statistics of data and fitted by TCM function. When η meson spectra in different
 1213 centrality classes are fitted by TCM, T_e , T and n are fixed to those in centrality 0-90 % to
 1214 avoid divergence of the fitting. Hence, yield parameters A_e and A are free parameters in each
 1215 centrality class.

1216 Figure 95 shows the ratio of p_T spectra of π^0 at $\sqrt{s_{NN}} = 5.02$ TeV to those at $\sqrt{s_{NN}} = 2.76$
 1217 TeV [73, 74] in Pb–Pb (color filled marker) and pp (black open marker) collisions for same
 1218 centrality classes. Ratios of spectra increase with p_T in both pp and Pb–Pb collisions which
 means harder p_T spectra at higher collision energy.

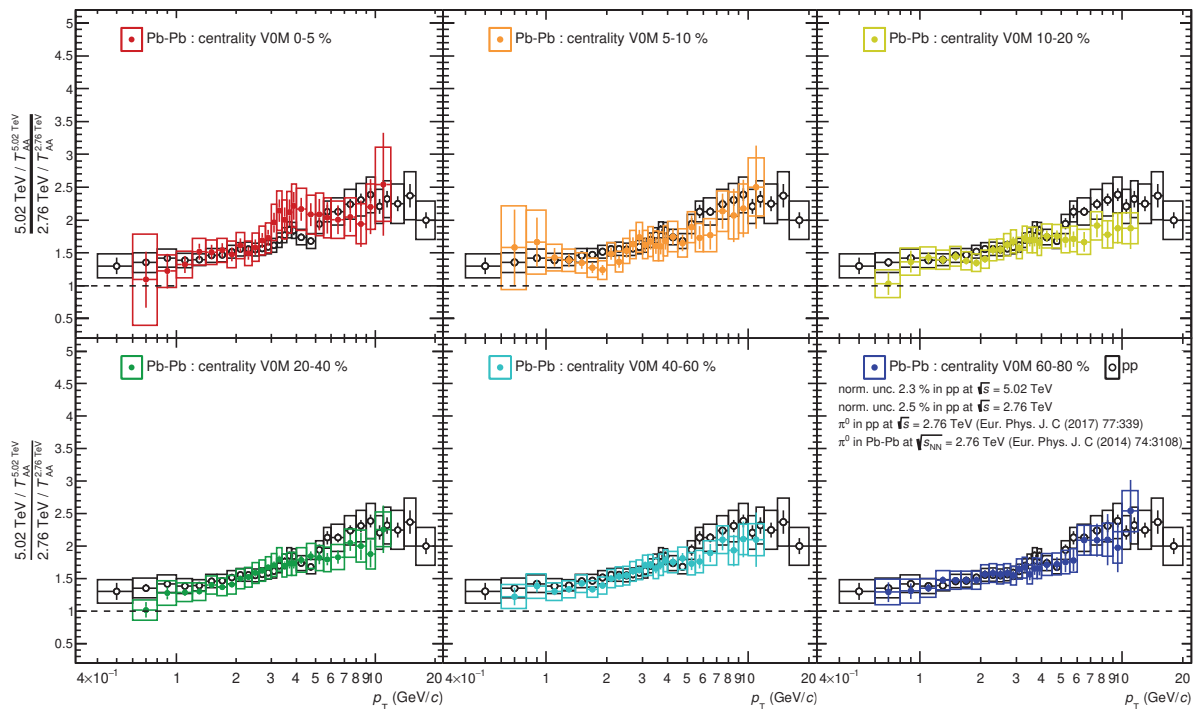
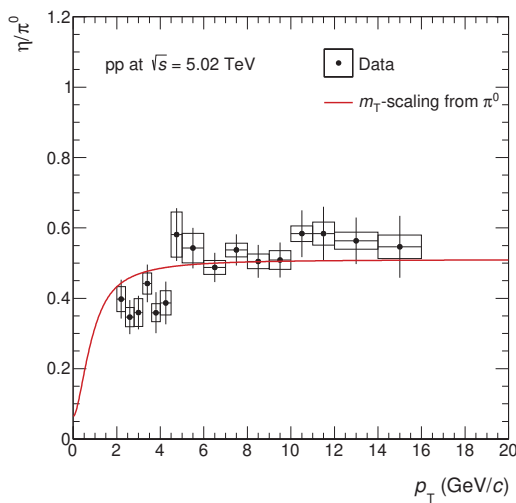
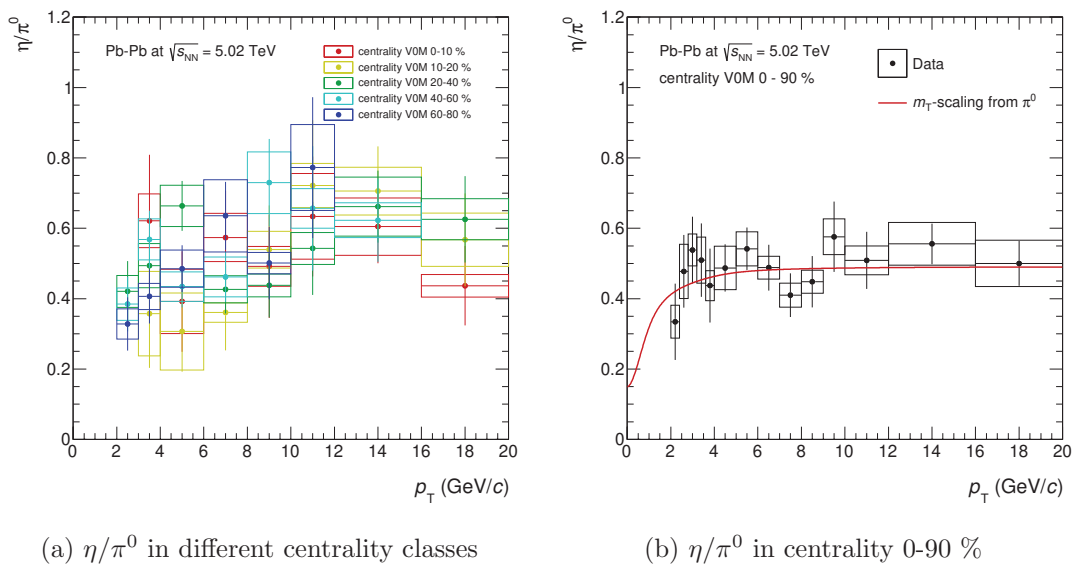


Figure 95: Comparison of p_T spectra for π^0 between $\sqrt{s_{NN}} = 5.02$ and 2.76 TeV in Pb–Pb collisions

1219

1220 **6.2 Particle ratio**

1221 η/π^0 ratios have been measured in pp and Pb–Pb collisions at $\sqrt{s_{NN}} = 5.02$ TeV for different
 1222 centrality classes, as shown by Figure 96 and Figure97. As, the statistical uncertainty is large,
 1223 no centrality dependence of η/π^0 ratios in Pb–Pb collisions is observed. In order to reduce
 1224 statistical and systematic uncertainties, all centrality (Figure.97b) have been combined in Pb–
 1225 Pb collisions. The η/π^0 ratio is found to be $0.507 \pm 0.017(\text{stat.}) \pm 0.008(\text{syst.})$ in pp collisions
 1226 and $0.491 \pm 0.022(\text{stat.}) \pm 0.017(\text{syst.})$ at $p_T > 3.6$ GeV/c in centrality 0-90% Pb–Pb collisions
 1227 at $\sqrt{s_{NN}} = 5.02$ TeV. The measured η/π^0 ratios may be claimed to be consistent with published
 1228 ALICE results [74, 75, 76, 77] within experimental uncertainties, although the ratio in pp collisions at $\sqrt{s} = 5.02$ TeV is a bit higher than that in pp collisions at $\sqrt{s} = 8$ TeV [78].

Figure 96: The η/π^0 ratio in pp collisions at $\sqrt{s} = 5.02$ TeV(a) η/π^0 in different centrality classes(b) η/π^0 in centrality 0-90 %Figure 97: η/π^0 ratios in Pb–Pb collisions at $\sqrt{s_{NN}} = 5.02$ TeV

1229

6.3 Nuclear modification factors R_{AA} of neutral mesons

Since neutral mesons spectra have been measured in both pp and Pb–Pb collisions at $\sqrt{s_{NN}} = 5.02$ TeV, nuclear modification factors R_{AA} in different centrality class have been determined. The typical values of the nuclear overlap function T_{AA} used in this thesis are summarized in Table.5. These are taken from the reference [79]. Boxes around unity is the total normalization uncertainty, namely, square root of the quadratic sum of systematic uncertainty of T_{AA} and systematic uncertainty of normalization for spectra in pp collisions. R_{AA} reaches 0.13 at $p_T = 5 - 6$ GeV/c in central Pb–Pb collisions for both π^0 and η mesons and increase with p_T .

Table 5: Geometrical parameters in Pb–Pb collisions at $\sqrt{s_{NN}} = 5.02$ TeV [79]

centrality	T_{AA} (mb $^{-1}$)	syst. T_{AA} (mb $^{-1}$)	N_{coll}	syst. N_{coll}	N_{part}	syst. N_{part}
0-5 (%)	25.92	0.37	1752	28	382.3	2.4
5-10 (%)	20.22	0.52	1367	37	329.1	5
10-20 (%)	14.27	0.36	964.8	25	260.2	5.2
20-40 (%)	6.872	0.21	464.5	15	158.5	3.1
40-60 (%)	2.046	0.05	138.3	3.1	70.61	1.1
60-80 (%)	0.4173	0.014	28.21	0.81	23.34	0.43

6.3.1 Collision energy $\sqrt{s_{NN}}$ dependence

R_{AA} of π^0 mesons in Pb–Pb collisions at $\sqrt{s_{NN}} = 5.02$ and 2.76 TeV are compared on Figure 98. In spite of the fact that p_T spectra become harder at higher collision energy both in pp and Pb–Pb collisions, R_{AA} is found to be the same at two collision energies. This indicates the larger parton energy-loss at the higher collision energy.

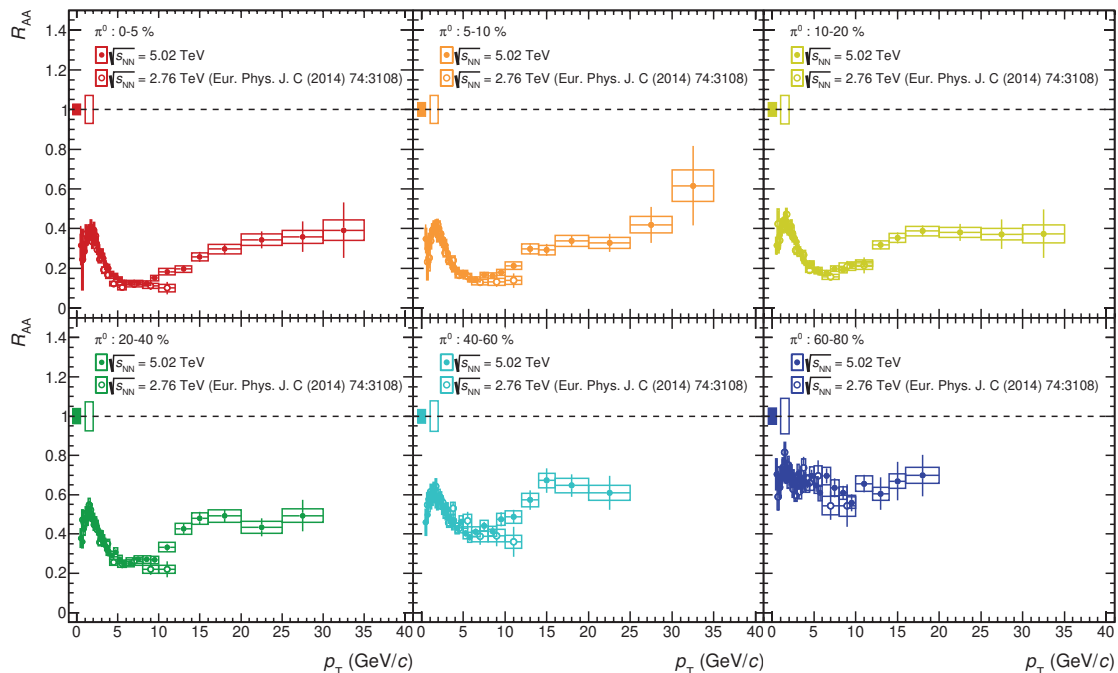


Figure 98: R_{AA} of π^0 in Pb–Pb collisions at $\sqrt{s_{NN}} = 5.02$ and 2.76 TeV

There is one more possibility to compare the p_T spectrum and R_{AA} of π^0 in central collisions

1244 (0-10%) with higher statistics [76]. Those were recorded in 2011, so called LHC11h period,
 1245 in Pb–Pb collisions at $\sqrt{s_{NN}} = 2.76$ TeV. As published results are available up to $p_T = 20$
 1246 GeV/ c , the comparison has been performed at only $p_T < 20$ GeV/ c here. Considering the large
 1247 experimental uncertainties for both results, comparisons on Figure 99 again indicate the harder
 1248 p_T spectrum at higher collision energy, but the same suppression level at two collision energies
 up to $p_T = 20$ GeV/ c .

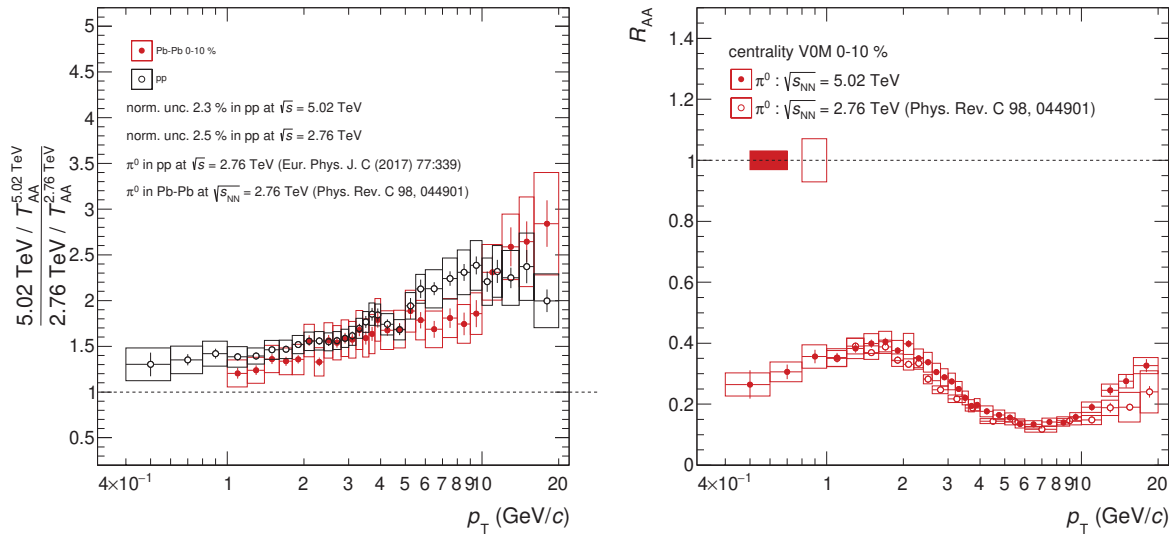
(a) The ratio of p_T spectrum for π^0 .(b) R_{AA} for π^0 .

Figure 99: Comparison of the ratio of p_T spectrum and R_{AA} in Pb–Pb collisions at $\sqrt{s_{NN}} = 5.02$ and 2.76 TeV (2011 sample)

1249

6.3.2 Comparison to theoretical models

R_{AA} of π^0 and η mesons are compared to theoretical models (Figure 100). The prediction including both radiative and elastic energy-loss in the hydrodynamically expanding QCD medium by M.Djordjevic [26] shows quantitatively good agreement with data in all centrality classes for both π^0 and η mesons. The model based on the same approach in the constant-temperature QCD medium without the evolution by M.Djordjevic [25] also gives good agreement again. This can be interpreted as that the evolution of the medium affects the azimuthal anisotropy v_2 of hadrons, rather than to R_{AA} , as she explains [26, 25]. Models by M.Djordjevic aim to reproduce R_{AA} and v_2 for hadrons simultaneously in her framework. So, it might be interesting to see them for comprehensive studies in the future.

6.3.3 Hadron species dependence

R_{AA} of π^0 and η mesons are consistent with each other within experimental uncertainties at $p_T > 4$ GeV/ c . However, it seems R_{AA} for η meson is systematically higher than that of π^0 at low p_T , which is similar to those previously measured in Pb–Pb collisions at $\sqrt{s_{NN}} = 2.76$ TeV [76, 80]. R_{AA} for different hadron species in central Pb–Pb collisions at $\sqrt{s_{NN}} = 5.02$ TeV are summarized on Figure 102. The suppression of neutral and charged [81] pions is consistent with each other, as expected (centrality classes 0-5 and 5-10% were merged into 0-10% for π^\pm and K^\pm). The comparison indicates the similar suppression pattern between η and K^\pm [81] mesons for whole p_T range, but seems to differ from pions at $p_T < 4$ GeV/ c . This is explained by that both η and K^\pm mesons consist of a strange quark and an up, down quark, while pions contain up, down quarks. However, with the present accuracy of the η meson measurement, it is not enough to determine whether the suppression is different/same for π^0 and η at low p_T . On the other hand, comparing R_{AA} between π^0 and D mesons [82], the suppression of D mesons is clearly weaker than that of π^0 mesons at $p_T < 10$ GeV/ c . This is because of smaller energy-loss for charm quarks than for up and down quarks due to its heavier mass. At high p_T , the parton energy-loss does not depend on the quark mass [84, 85] and thus, R_{AA} is the same for light and heavy flavor hadrons. B^\pm mesons which contain a bottom quark and a light quark have been measure in centrality class 0-100% by CMS [83] by triggering muons from from $B^\pm \rightarrow J/\psi K^\pm \rightarrow \mu^+ \mu^- K^\pm$ at high p_T . So, it would be interesting to see R_{AA} of charm-hadrons and bottom-hadrons at low p_T in Run3 at $\sqrt{s_{NN}} = 5.5$ TeV.

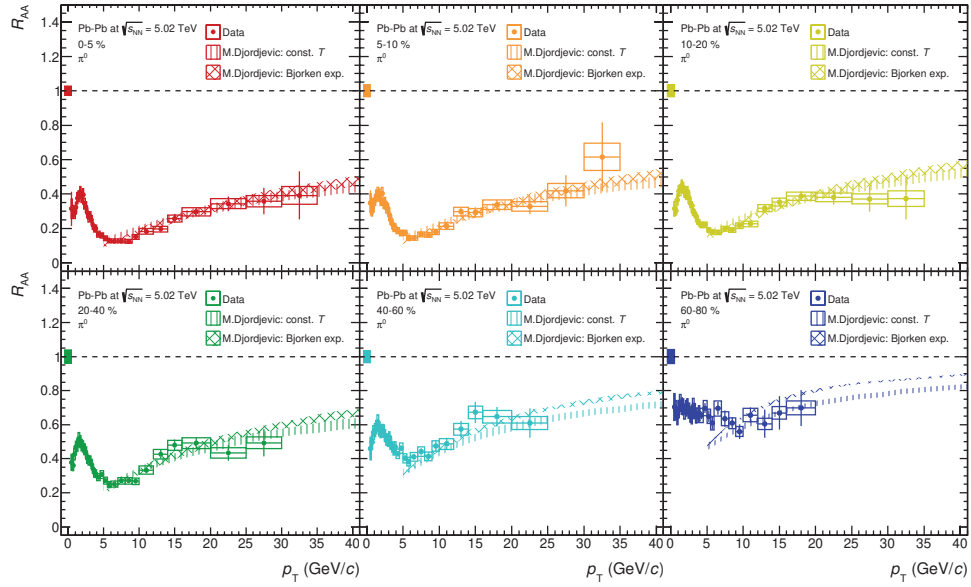
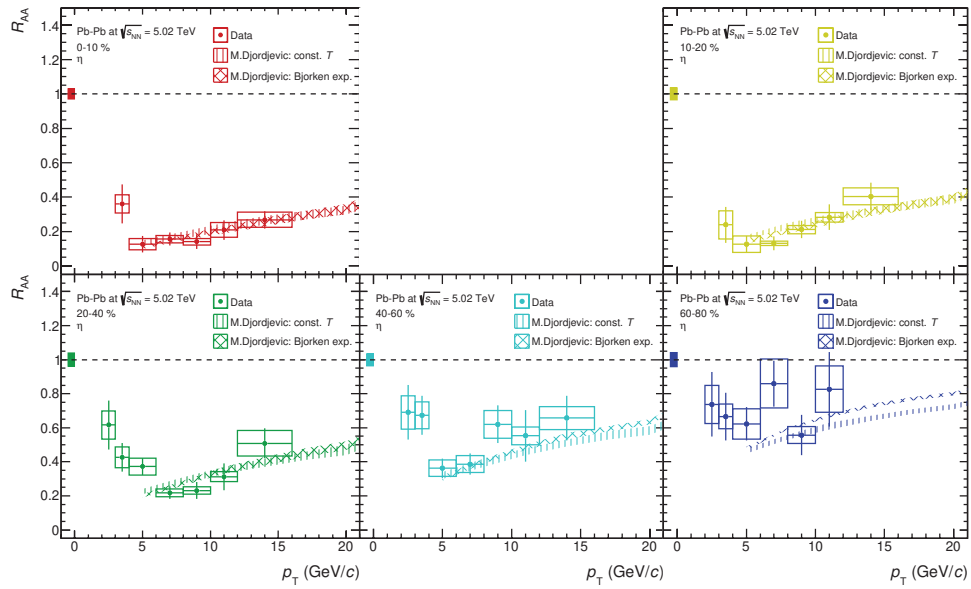

 (a) For π^0 mesons.

 (b) For η mesons.

 Figure 100: Comparison of R_{AA} with theoretical models in Pb-Pb collisions at $\sqrt{s_{NN}} = 5.02$ TeV

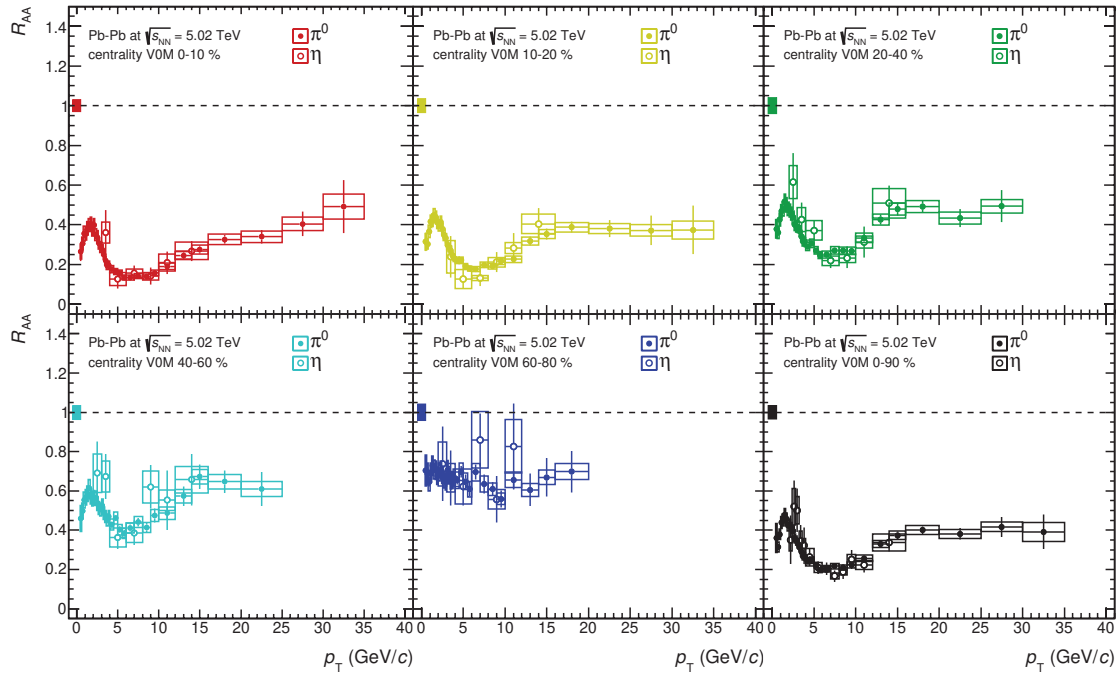


Figure 101: Comparison of R_{AA} between π^0 and η in Pb–Pb collisions at $\sqrt{s_{NN}} = 5.02$ TeV for different centrality classes.

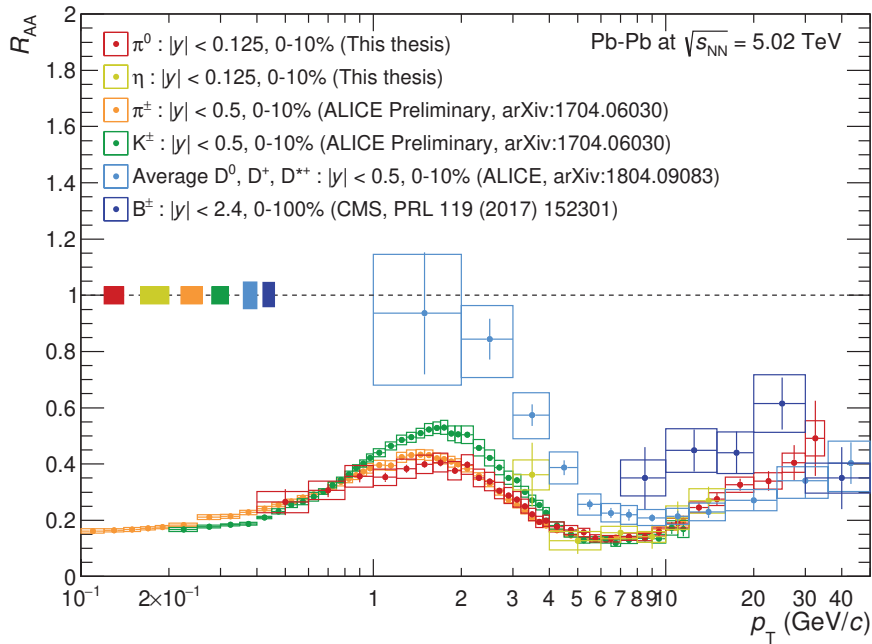
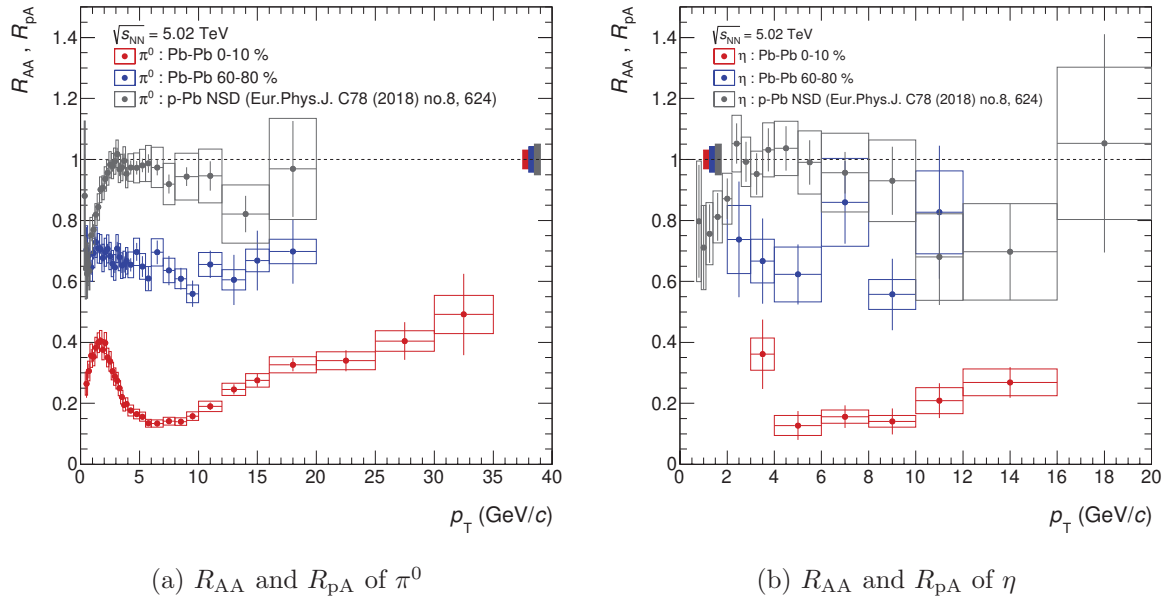


Figure 102: R_{AA} of π^0 , η , π^\pm , K^\pm , D and B^\pm mesons in central (0-10%) Pb–Pb collisions at $\sqrt{s_{NN}} = 5.02$ TeV [81, 82, 83]

1281 **6.3.4 Comparison of R_{AA} and R_{pA} at $\sqrt{s_{NN}} = 5.02$ TeV**

1282 Comparing the suppression of high p_T hadrons between A–A and p–A collisions can distinguish
 1283 whether the suppression is initial state or final state effects. Figure 103 shows there is no
 1284 suppression in p–Pb collisions [77], while the strong suppression is observed in Pb–Pb collisions.
 1285 This demonstrates that the strong suppression observed in Pb–Pb collisions is not related to
 initial state effect, but to the formation of hot and dense QCD medium.

Figure 103: R_{AA} , R_{pA} of π^0 and η mesons

1286

7 Analyses for direct photon

Detailed descriptions for the direct photon γ^{dir} measurement by using measured π^0 and η mesons are described in this section.

7.1 Analysis strategy

First of all, the inclusive photon γ^{inc} spectrum has to be measured as :

$$E \frac{d^3 N_{\gamma^{\text{inc}}}}{dp^3} = \frac{1}{2\pi} \times \frac{1}{p_T} \frac{dN}{dp_T} \times P \times \frac{1}{\Delta y} \times \frac{1}{\varepsilon} \times \frac{1}{N_{\text{ev}}}, \quad (27)$$

where P is photon purity in the total number of clusters. The photon purity is estimated by a data driven approach described in section 7.7.

Direct photons γ^{dir} are defined as produced photons not originating from hadron decays as follows :

$$\gamma^{\text{dir}} = \gamma^{\text{inc}} - \gamma^{\text{decay}} = \gamma^{\text{inc}} \cdot \left(1 - \frac{1}{R_\gamma} \right), \quad (28)$$

where γ^{inc} indicates inclusive photons and γ^{decay} denotes decay photons from hadrons. In order to observe direct photon signals, it is convenient to introduce a variable R_γ which is the ratio of inclusive photons yields to decay photons yields.

$$R_\gamma = \frac{\gamma^{\text{inc}}}{\gamma^{\text{decay}}} = \frac{(\gamma^{\text{inc}}/\pi^0)_{\text{data}}}{(\gamma^{\text{decay}}/\pi^0)_{\text{cocktail}}} \quad (29)$$

The π^0 spectrum is inserted in R_γ because experimentally systematic uncertainties related to the energy measurement cancel out in the ratio. The cocktail simulation (mixture of hadrons which decay into photons such as π^0 , η , ω , η' , ρ and ϕ e.t.c.) is used to determine decay photon yields. Thus, neutral mesons measurements described in the previous section are important inputs to this cocktail simulation. Finally, if $R_\gamma > 1$, inclusive photon yields in data are larger than decay photon yields, which means the excess of direct photon signals beyond decay photon yields. If R_γ is consistent with unity within experimental uncertainties, upper limits at the 90% confidence level (C.L.) are set. The invariant yield of direct photon is obtained by :

$$\frac{1}{2\pi} \frac{d^2 N_{\gamma^{\text{dir}}}}{N_{\text{ev}} p_T dp_T dy} = \frac{1}{2\pi} \frac{d^2 N_{\gamma^{\text{inc}}}}{N_{\text{ev}} p_T dp_T dy} \times \left(1 - \frac{1}{R_\gamma} \right) \quad (30)$$

In case of upper limits on direct photon yields at the 90% confidence level, mean data point + 1.28σ is considered at each p_T bin.

1309 **7.2 Raw yields of clusters**

1310 At first, raw yields of cluster have been constructed as shown by Figure 104. Only the core-
 1311 dispersion cut was applied to clusters in pp and both CPV_T and core-dispersion cuts was used in
 Pb-Pb collisions.

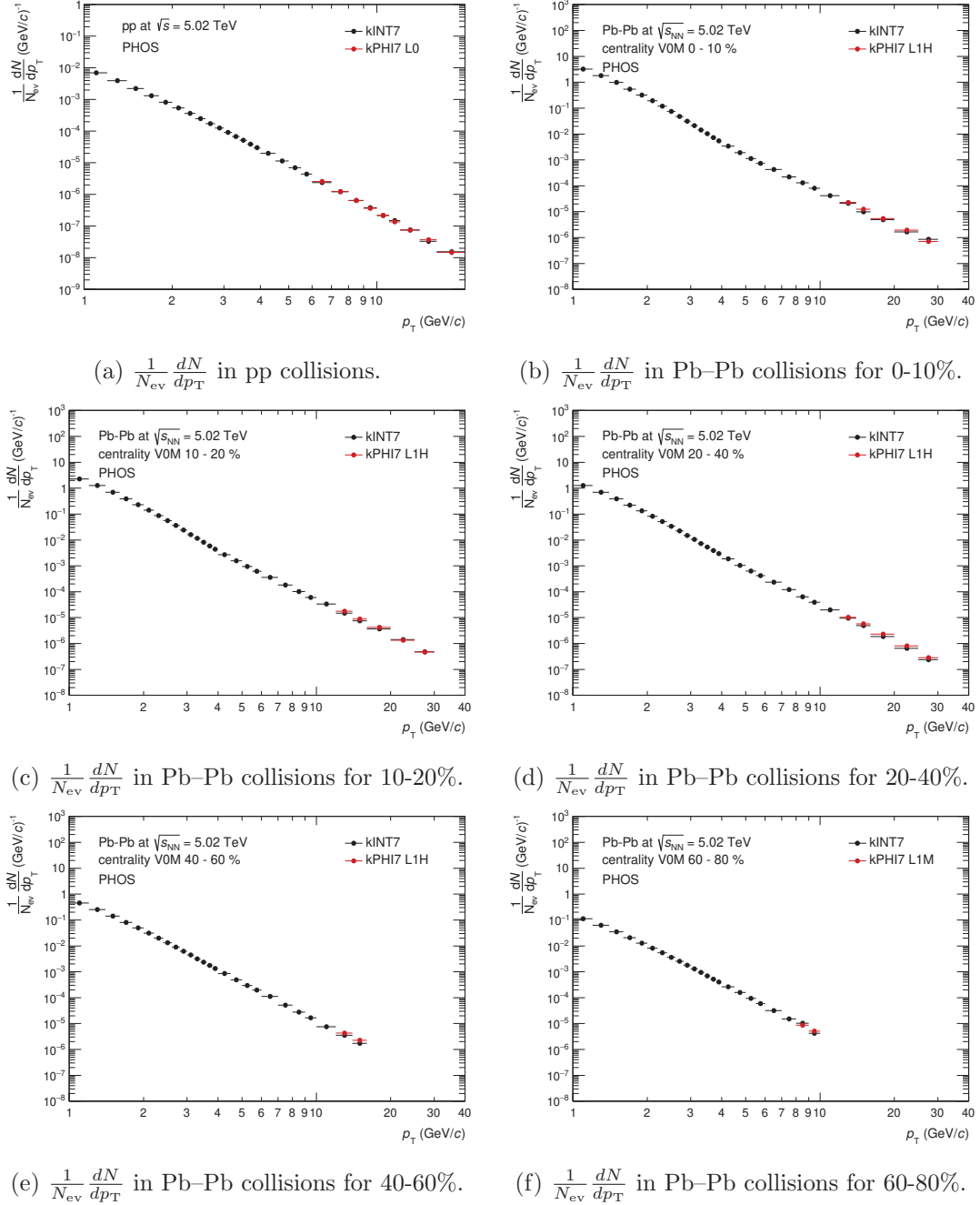
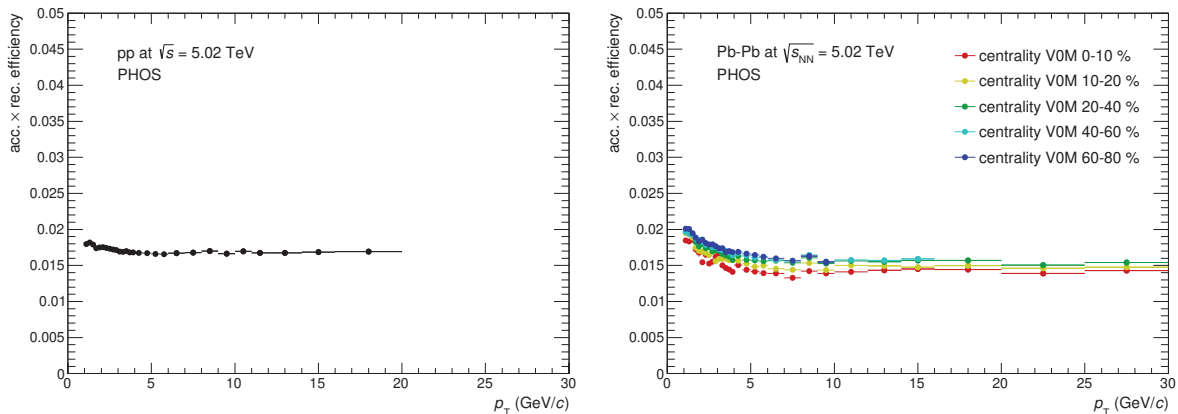


Figure 104: Raw yields of clusters in pp and Pb-Pb collisions at $\sqrt{s_{NN}} = 5.02$ TeV

1312

1313 7.3 Acceptance \times reconstruction efficiency

1314 The acceptance \times reconstruction efficiency has been measured by the same procedure as neutral
 1315 mesons analyses, namely the single γ simulation in pp and the embedded simulation (single γ
 1316 events + real underlying events) in Pb–Pb collisions. One should keep different active area of
 1317 the PHOS detector in different data taking periods in mind. As single γ simulation on only the
 1318 PHOS detector was employed, there is no tracking information in single γ simulation for pp case.
 1319 Thus, only the dispersion cut was applied to clusters in pp collisions for both data and M.C..
 1320 However, the CPV cut efficiency in pp collisions is close to 100% due to the low multiplicity
 1321 environment $\frac{dN_{ch}}{dy} = 5 \sim 7$ at mid-rapidity [68]. On the other hand, after embedding photons
 1322 into real underlying events, track matching between a cluster and a track was available in Pb–
 1323 Pb case. Late conversion electrons ($\gamma \rightarrow e^+e^-$ outside of TPC) are also considered as photon
 1324 signals, because they can not be rejected by the CPV cut. Efficiencies are plotted on Figure 105.
 1325 The higher efficiency is observed in peripheral collisions due to the small overlapping probability
 between clusters, as expected.



(a) The efficiency in pp collisions.

(b) The efficiency in Pb–Pb collisions.

Figure 105: Acceptance \times reconstruction efficiencies in pp and Pb–Pb collisions at $\sqrt{s_{NN}} = 5.02$ TeV

1326

1327 7.4 TOF cut efficiency

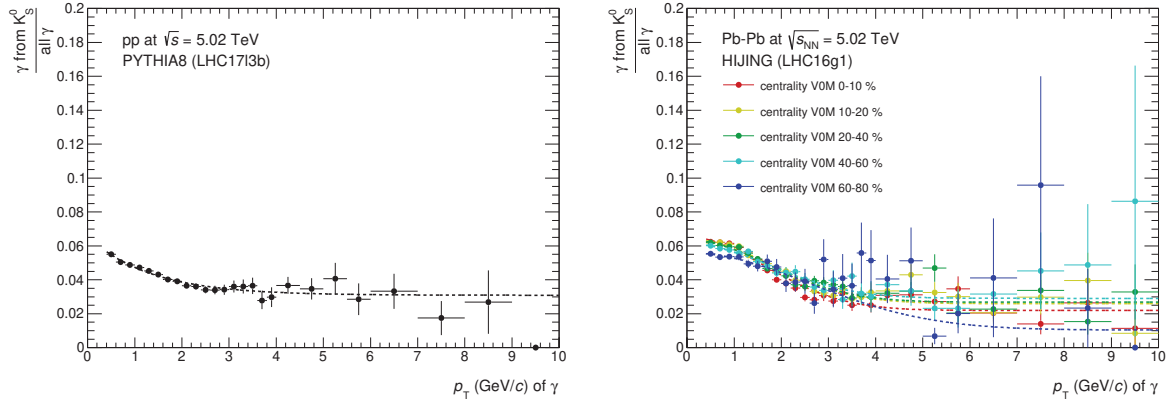
1328 This is the same as the neutral mesons analysis, but corrected by $1/\varepsilon_{\text{TOF}}$.

1329 7.5 Trigger efficiency

1330 This is the same as the neutral mesons analysis, but corrected by $1/\varepsilon_{\text{trg}}$.

1331 7.6 Feed down correction for $K_S^0 \rightarrow \pi^0\pi^0 \rightarrow 4\gamma$

1332 Photons from strange hadron decays were subtracted based on PYTHIA and HIJING event
 1333 generator for pp and Pb–Pb respectively. K^\pm/π^\pm has been already tuned for the π^0 measurement
 1334 explained in the previous section. They are about 5-6% at low p_T and 2-3% at high p_T .



(a) The feed down correction in pp collisions. (b) The feed down correction in Pb–Pb collisions.

Figure 106: Feed down corrections from K_S^0 in pp and Pb–Pb collisions at $\sqrt{s_{NN}} = 5.02$ TeV

7.7 Photon purity

In order to measure inclusive and direct photons spectra, the photon purity has been estimated by a data driven approach. The definition of photon purity is a fraction of the number of photon clusters in the total number of clusters.

7.7.1 Data driven approach for photon purity estimation

The total number of cluster N_{cluster} can be expressed as $N_{\text{cluster}} = N_{\gamma} + N_{e^{\pm}} + N_{\pi^{\pm}} + N_{K^{\pm}} + N_p + N_{\bar{p}} + N_n + N_{\bar{n}} + N_{K_L^0} + N_{\mu^{\pm}} + N_{\nu} + N_{\bar{\nu}}$. It is known that $\bar{p}/p \sim 1$ in high-energy hadron collisions [86] and $N_p \sim N_n$ based on isospin symmetry. In this analysis, there are 4 independent PID cuts (no PID, CPV, Disp, and CPV+Disp). Then, a system 31 can be constructed to estimate particle composition in PHOS clusters.

$$\begin{pmatrix} N_{\text{all}} \\ N_{\text{CPV}} \\ N_{\text{Disp}} \\ N_{\text{both}} \end{pmatrix} = \begin{pmatrix} 1 & C_{\text{ch}} + C_{\text{nh}} & 2 & 1 \\ \varepsilon_{\gamma}^{\text{CPV}} & \varepsilon_{\pi^{\pm}}^{\text{CPV}} C_{\text{ch}} + \varepsilon_{\gamma}^{\text{CPV}} C_{\text{nh}} & \varepsilon_{\bar{p}}^{\text{CPV}} + \varepsilon_{\gamma}^{\text{CPV}} & \varepsilon_{e^{\pm}}^{\text{CPV}} \\ \varepsilon_{\gamma}^{\text{Disp}} & \varepsilon_{\pi^{\pm}}^{\text{Disp}} (C_{\text{ch}} + C_{\text{nh}}) & 2\varepsilon_{\bar{p}}^{\text{Disp}} & \varepsilon_{e^{\pm}}^{\text{Disp}} \\ \varepsilon_{\gamma}^{\text{CPV}} \times \varepsilon_{\gamma}^{\text{Disp}} & (\varepsilon_{\pi^{\pm}}^{\text{CPV}} C_{\text{ch}} + \varepsilon_{\gamma}^{\text{CPV}} C_{\text{nh}}) \times \varepsilon_{\pi^{\pm}}^{\text{Disp}} & (\varepsilon_{\bar{p}}^{\text{CPV}} + \varepsilon_{\gamma}^{\text{CPV}}) \times \varepsilon_{\bar{p}}^{\text{Disp}} & \varepsilon_{e^{\pm}}^{\text{CPV}} \times \varepsilon_{e^{\pm}}^{\text{Disp}} \end{pmatrix} \begin{pmatrix} N_{\gamma} \\ N_{\pi^{\pm}} \\ N_{\bar{p}} \\ N_{e^{\pm}} \end{pmatrix} \quad (31)$$

where $C_{\text{ch}} = 1 + K^{\pm}/\pi^{\pm} + p/\pi^{\pm}$ (sum of relative π^{\pm} , K^{\pm} and p contributions) and $C_{\text{nh}} = 0.5 \times K_L^0/\pi^{\pm} + p/\pi^{\pm}$ (sum of relative K_L^0 and n contributions) as a function of p_T^{cluster} on PHOS. ε_X^i is efficiency of PID cut i for particle X . Charged particles are identified by dE/dx in TPC. It has been reported that electrons/positrons from semi-leptonic decays of heavy flavor hadrons becomes larger at the higher collision energy at LHC [87], compared to RHIC. So, electrons/positrons contributions has to be taken into account. Here, anti-protons contribution is different from protons because of detector response. Protons behave as minimum ionizing particles (MIP) in an electro-magnetic calorimeter. On the other hand, anti-protons can deposit higher energy because of annihilation. Finally, N_{γ} , $N_{\pi^{\pm}}$, $N_{\bar{p}}$, $N_{e^{\pm}}$ are obtained by solving system 31. Adding/removing C_{nh} is considered as a systematic uncertainty of photon purity. To evaluate

1355 the CPV cut efficiency for charged particles, the mixed event technique was used to subtract
 1356 random matchings. The distance between a PHOS cluster in a current event and a charged
 1357 particle in another event is measured to make a random matching distribution (Figure 107).
 1358 Then, the CPV cut efficiency for charged particles (i.e. how many charged particles can survive
 1359 after applying the CPV cut) is defined as :

$$\varepsilon_{\text{ch}}^{\text{CPV}} = \frac{\text{Number of entries beyond a criterion in the real matching distribution}}{\text{Number of all entries in the real matching distribution}}, \quad (32)$$

1360 and the dispersion cut efficiency for charged particles is defined as :

$$\varepsilon_{\text{ch}}^{\text{Disp}} = \frac{\text{Number of particles with Disp cut}}{\text{Number of charged particles without Disp cut}} \quad (33)$$

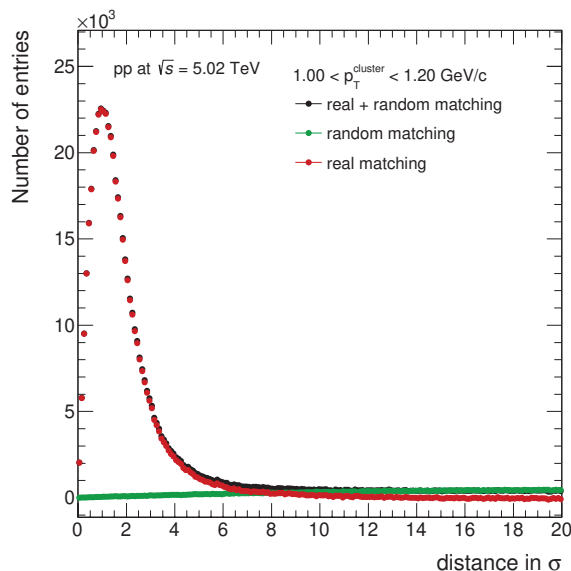


Figure 107: The distance between a cluster on PHOS and a charged particle in pp collisions at $\sqrt{s} = 5.02$ TeV.

1361

1362 7.7.2 Photon purity in pp collisions at $\sqrt{s} = 5.02$ TeV

1363 Figure 108 shows particle ratios on PHOS that are inputs for C_{ch} and C_{nh} . Figure 109 shows
 1364 PID cut efficiencies for different particles. The matching criterion between a charged particle
 1365 with a cluster on PHOS is $r < 2\sigma$ for evaluation of the dispersion cut efficiency. Especially for
 1366 e^{\pm} , $0.8 < E/p < 1.2$ was applied to get higher electron purity. To avoid statistical fluctuation
 1367 at high p_{T} ($p_{\text{T}} > 4$ GeV/c), each efficiency is fitted by constant and used as matrix elements.
 1368 The particle abundance on PHOS is summarized on Figure 110. The photon purity is 90 %
 1369 with the dispersion cut and 97 % with the CPV and the dispersion cuts at high p_{T} . Electrons
 1370 and positrons converted from photons outside of TPC, so-called late conversion electrons, can
 1371 not be tracked, because there is no tracking detector there. Therefore, late conversion electrons
 1372 denoted by L.C. e^{\pm} are treated as photon signals in M.C. truth.

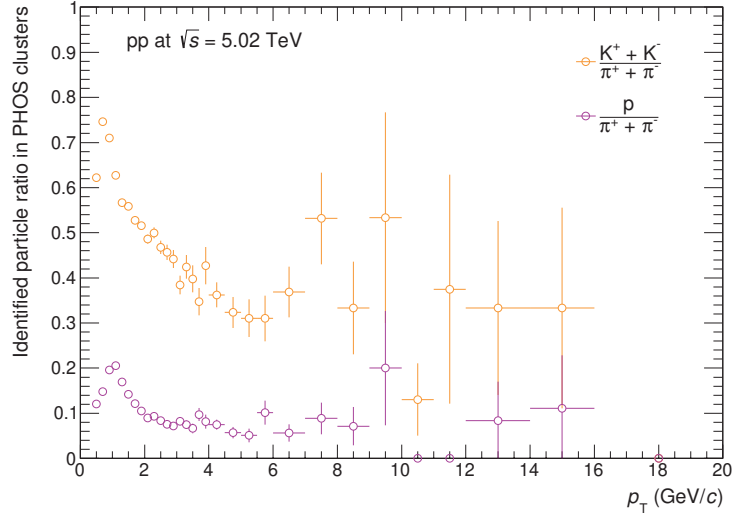
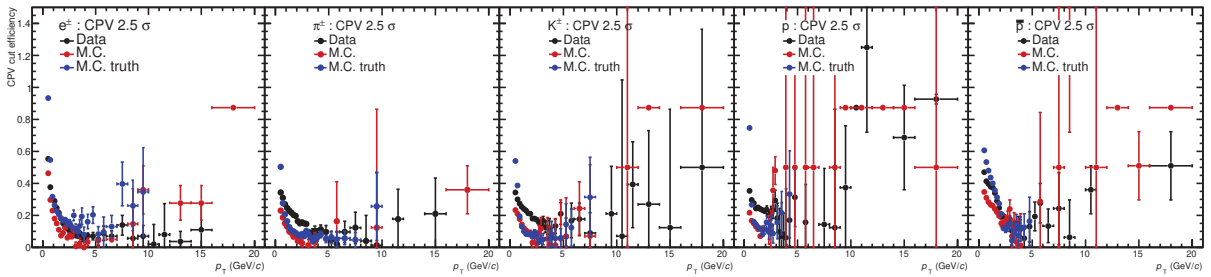
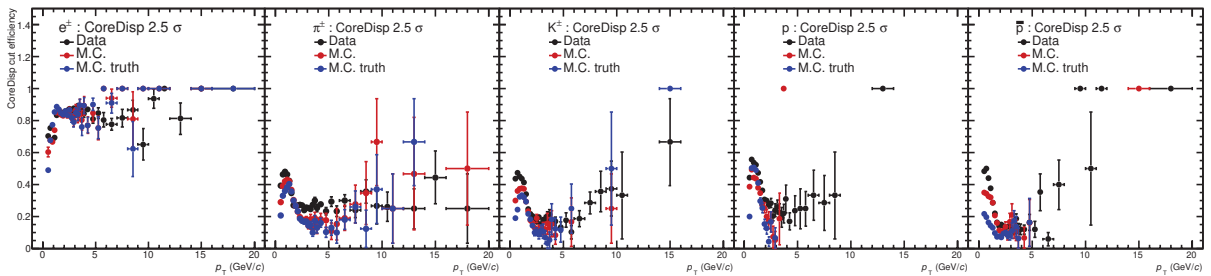


Figure 108: Measured particle ratios on PHOS in pp collisions at $\sqrt{s} = 5.02$ TeV.



(a) CPV cut efficiency for charged particles.



(b) CoreDisp cut efficiency for charged particles.

Figure 109: PID cut efficiencies for identified charged particles in pp collisions at $\sqrt{s} = 5.02$ TeV. From left to right, e^\pm , π^\pm , K^\pm , p and \bar{p} . Black for data, red for M.C. DDA, blue for M.C. truth.

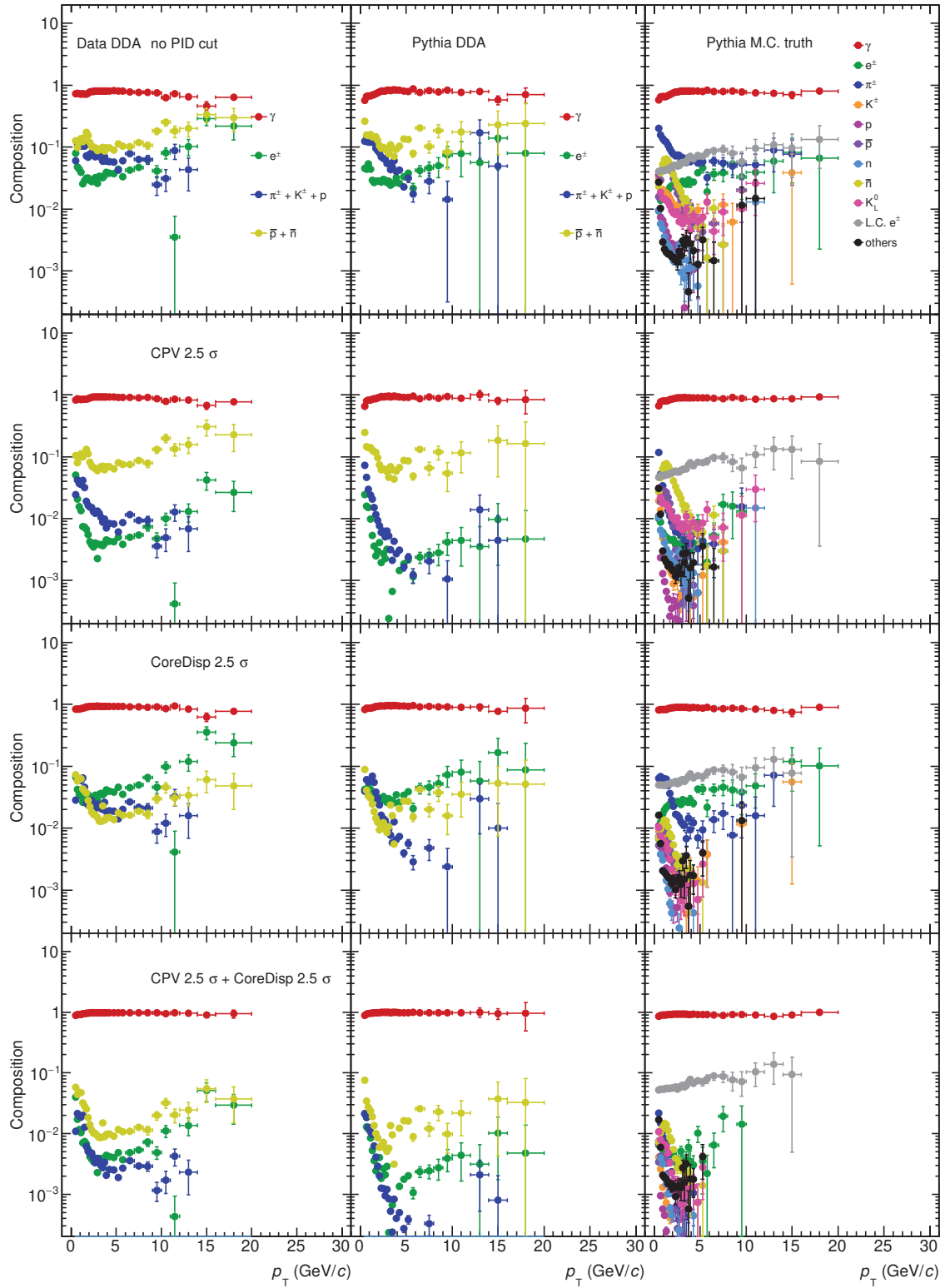


Figure 110: The summary of particle abundance on PHOS in pp collisions at $\sqrt{s} = 5.02$ TeV for $C_{nh} = 0$.

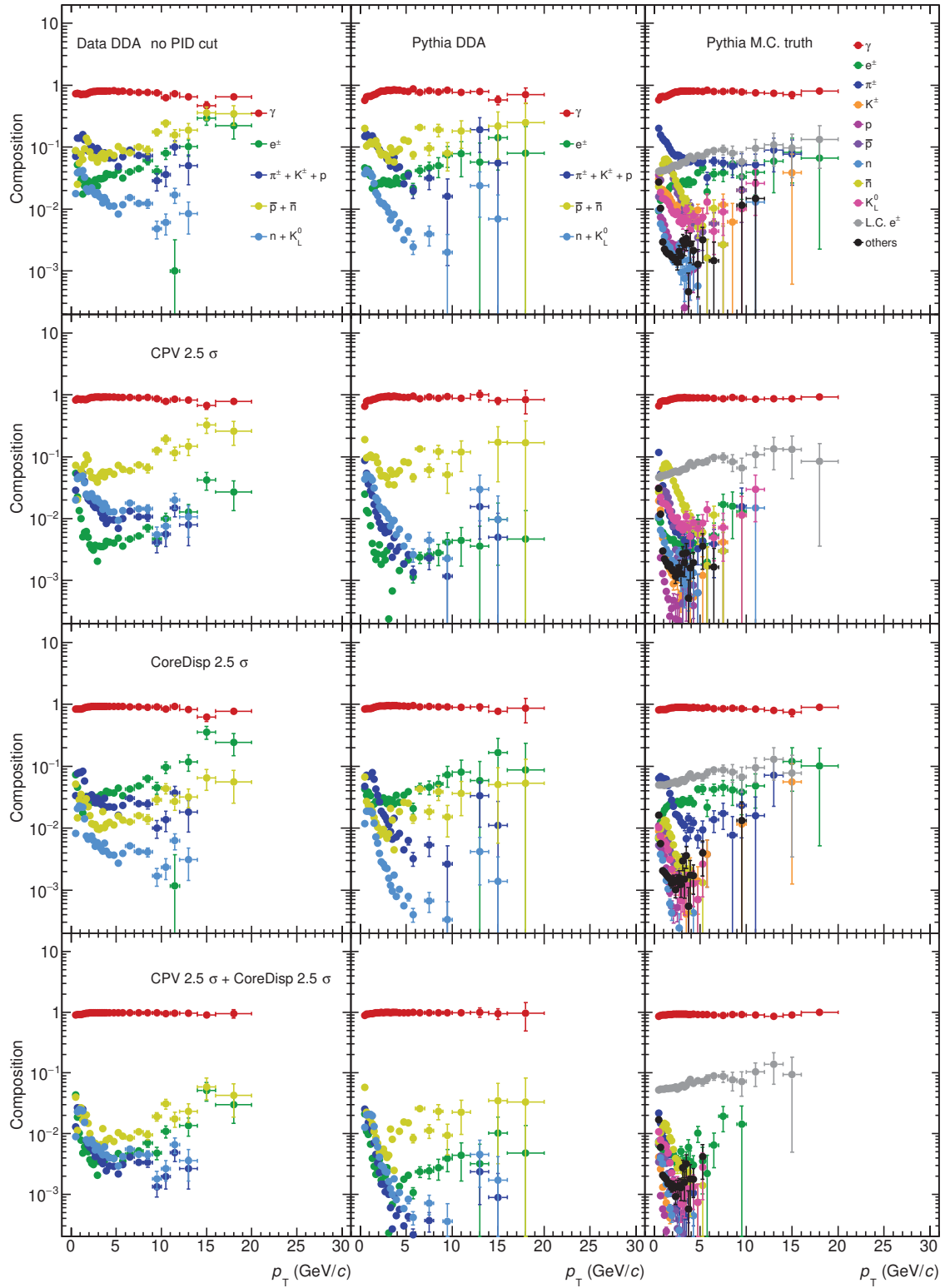


Figure 111: The summary of particle abundance on PHOS in pp collisions at $\sqrt{s} = 5.02$ TeV for $C_{nh} = 0.5 \times K^\pm/\pi^\pm + p/\pi^\pm$.

1373 **7.7.3 Photon purity in Pb–Pb collisions at $\sqrt{s_{NN}} = 5.02$ TeV**

The procedure is the same as the pp case.

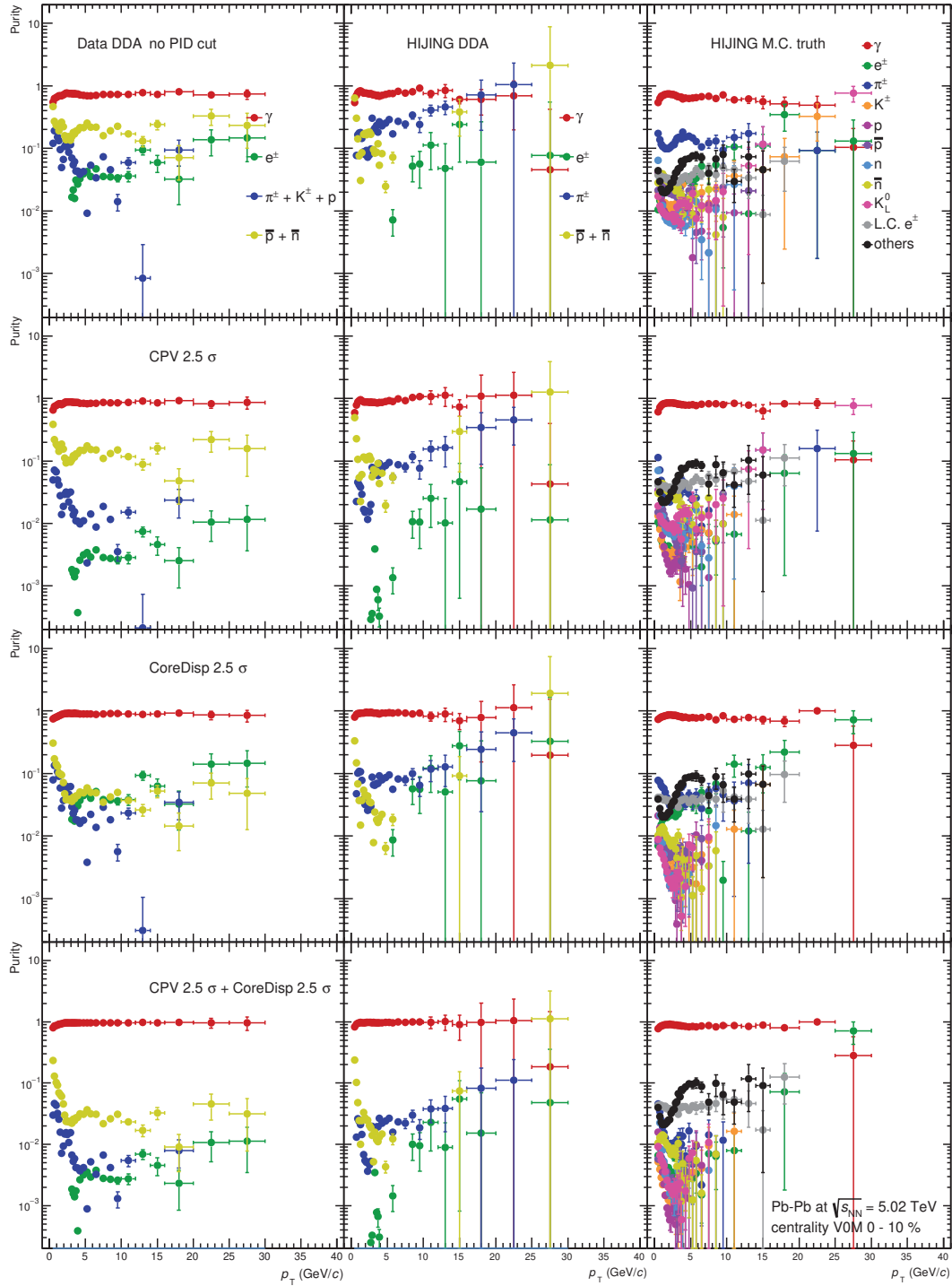


Figure 112: The summary of particle abundance on PHOS in 0–10% Pb–Pb collisions at $\sqrt{s_{NN}} = 5.02$ TeV for $C_{nh} = 0$.

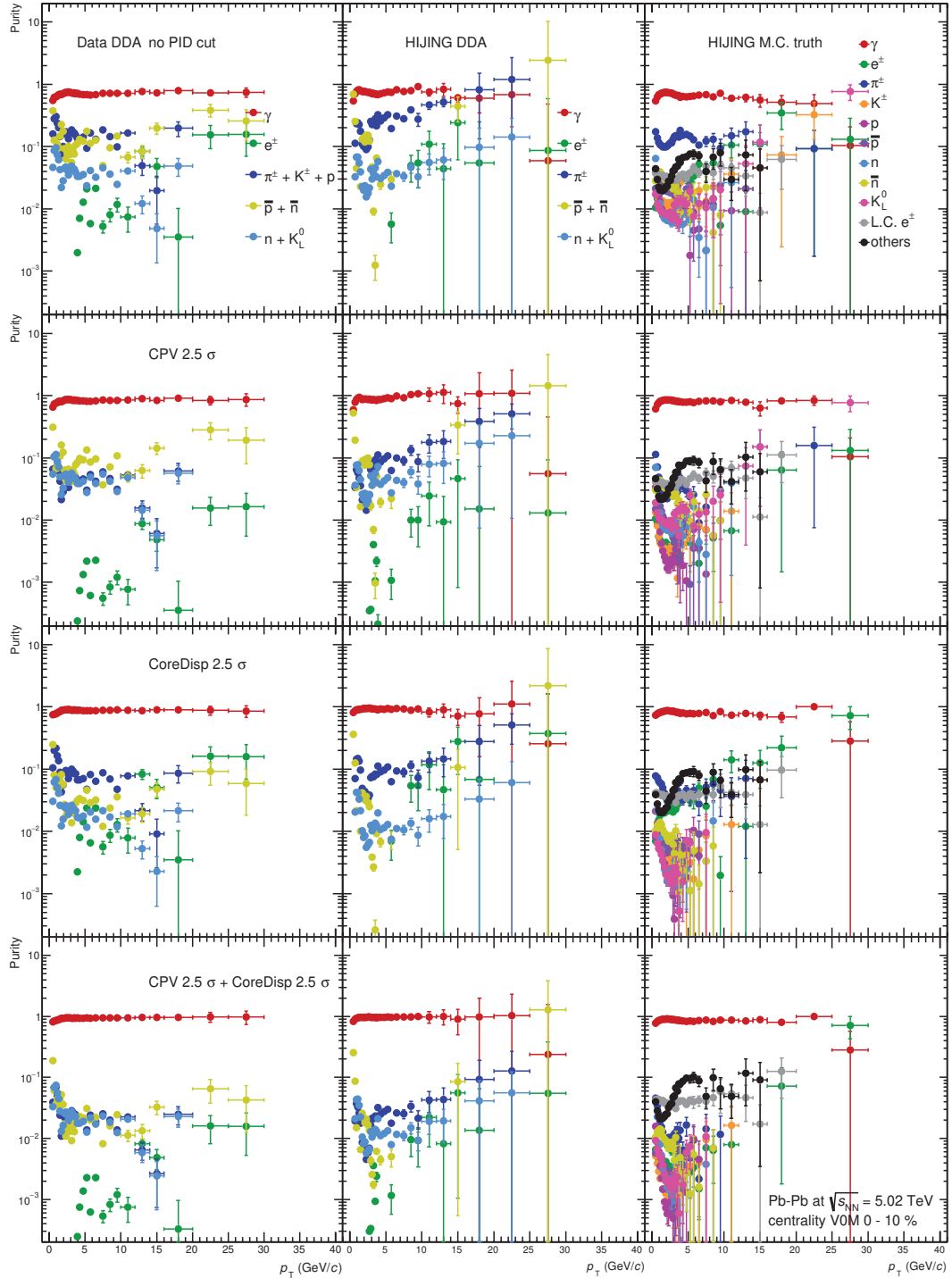


Figure 113: The summary of particle abundance on PHOS in 0-10% Pb-Pb collisions at $\sqrt{s_{NN}} = 5.02$ TeV for $C_{nh} = 0.5 \times K^\pm/\pi^\pm + p/\pi^\pm$.

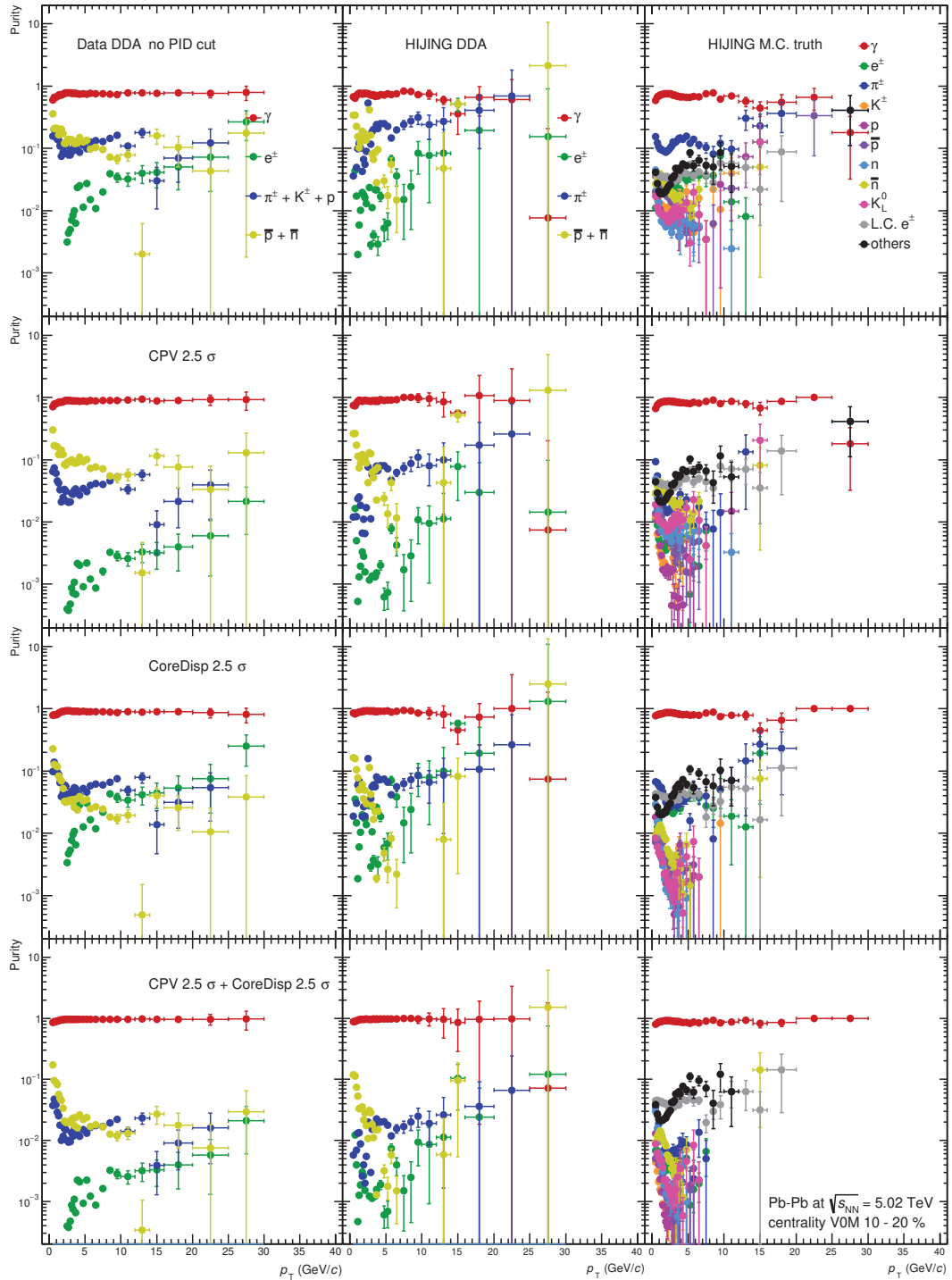


Figure 114: The summary of particle abundance on PHOS in 10-20% Pb-Pb collisions at $\sqrt{s_{NN}} = 5.02$ TeV for $C_{nh} = 0$.

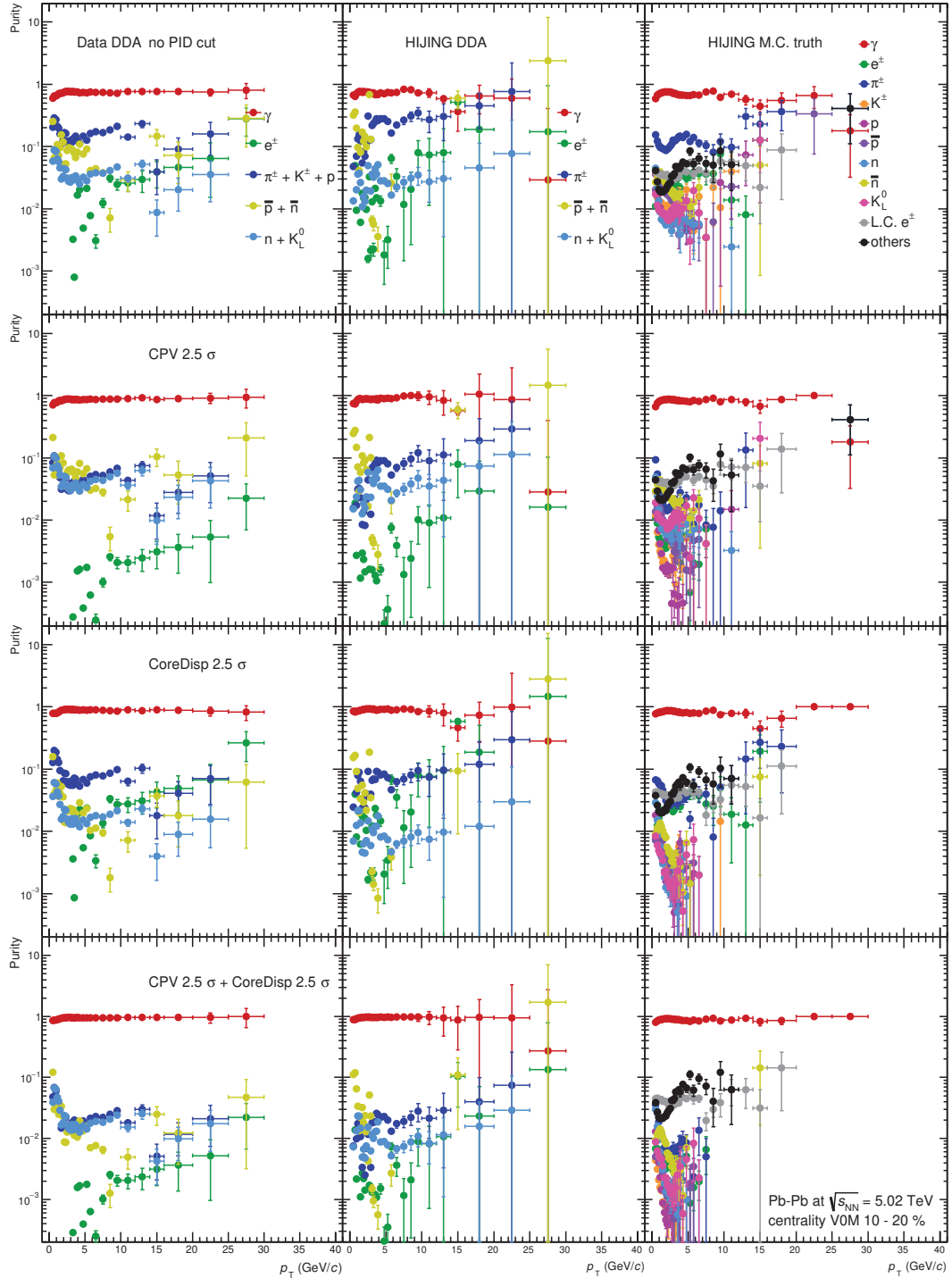


Figure 115: The summary of particle abundance on PHOS in 10-20% Pb-Pb collisions at $\sqrt{s_{NN}} = 5.02$ TeV for $C_{nh} = 0.5 \times K^\pm/\pi^\pm + p/\pi^\pm$.

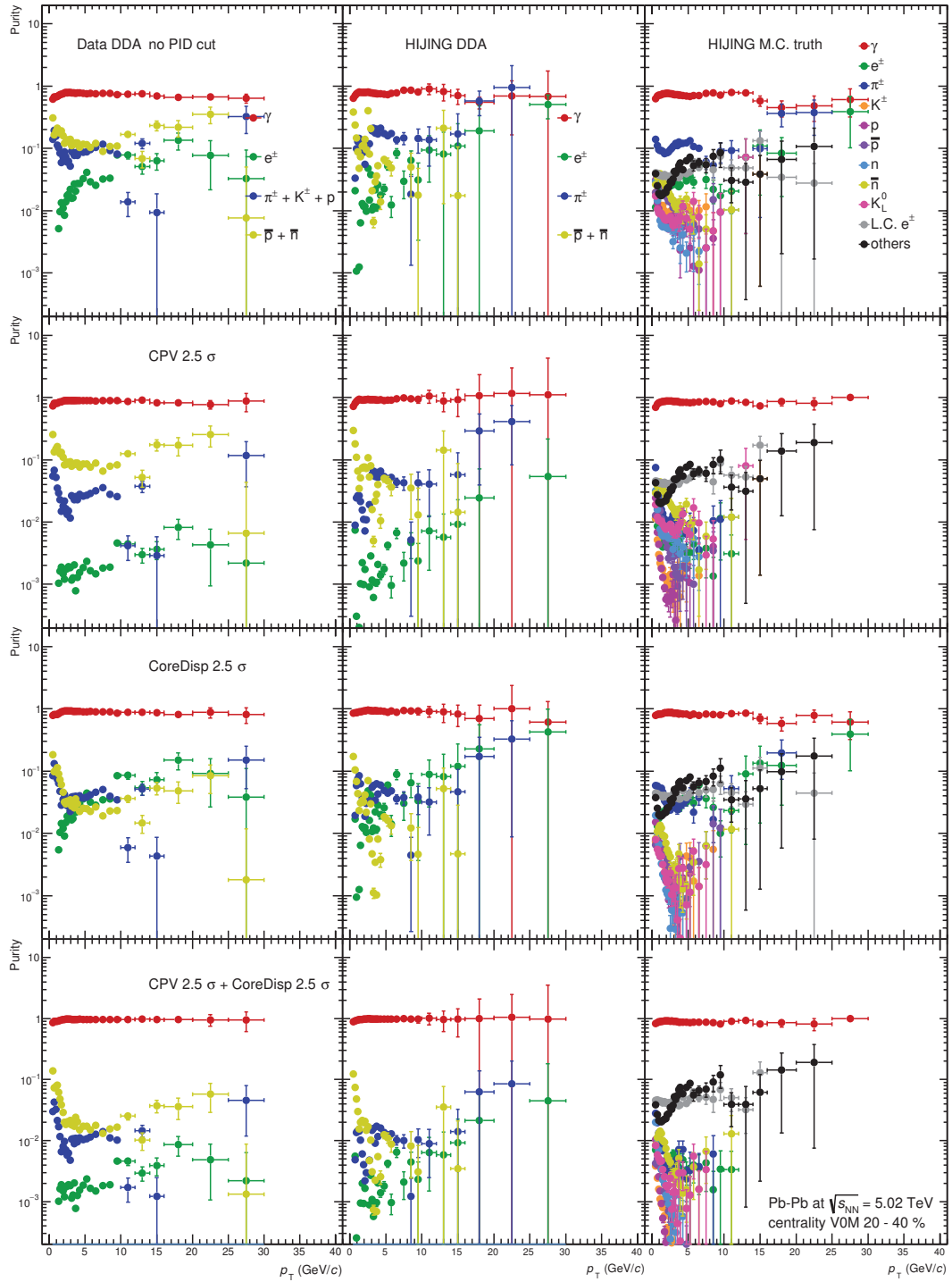


Figure 116: The summary of particle abundance on PHOS in 20-40% Pb-Pb collisions at $\sqrt{s_{NN}} = 5.02$ TeV for $C_{nh} = 0$.

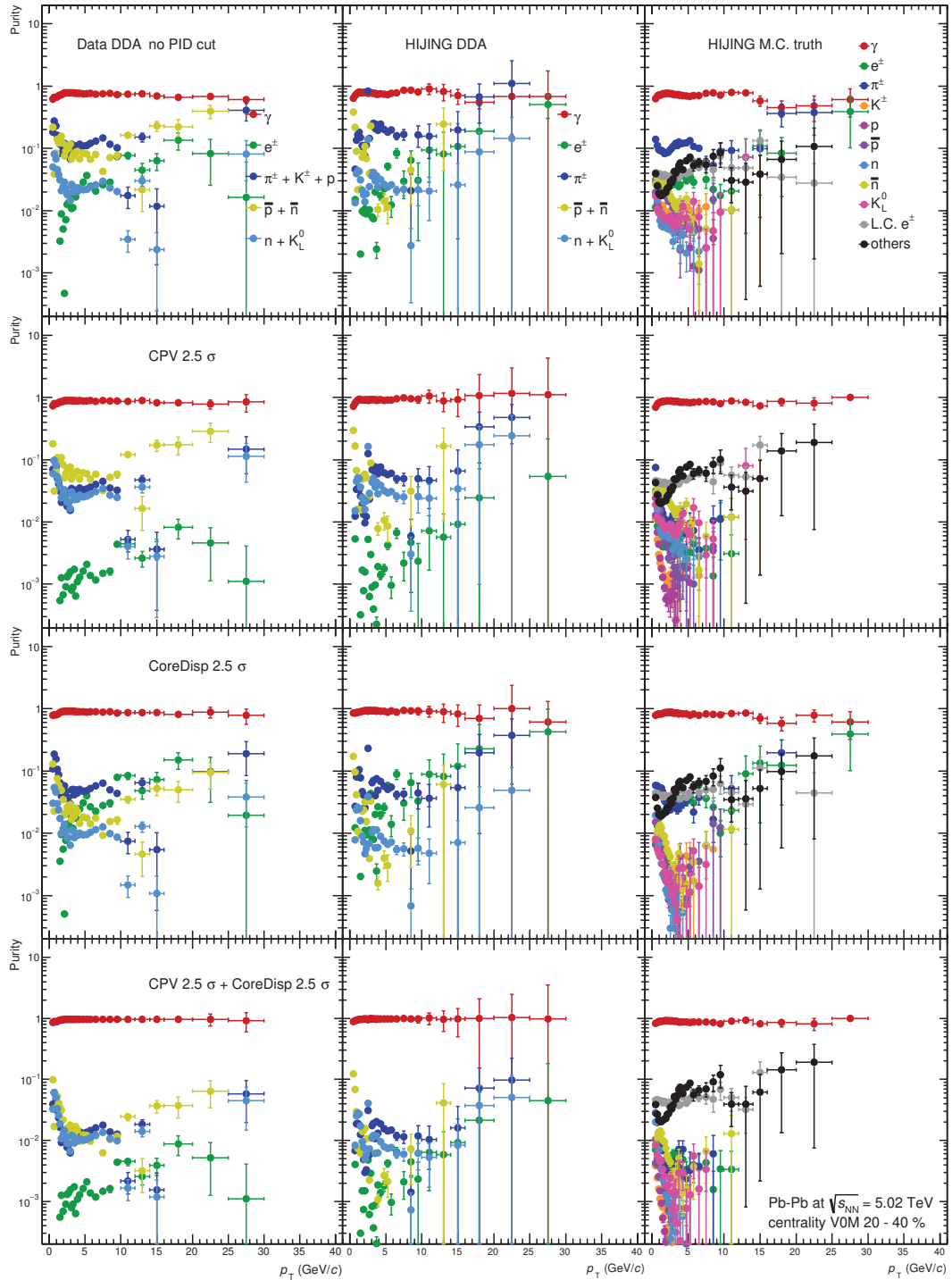


Figure 117: The summary of particle abundance on PHOS in 20-40% Pb-Pb collisions at $\sqrt{s_{NN}} = 5.02$ TeV for $C_{nh} = 0.5 \times K^\pm/\pi^\pm + p/\pi^\pm$.

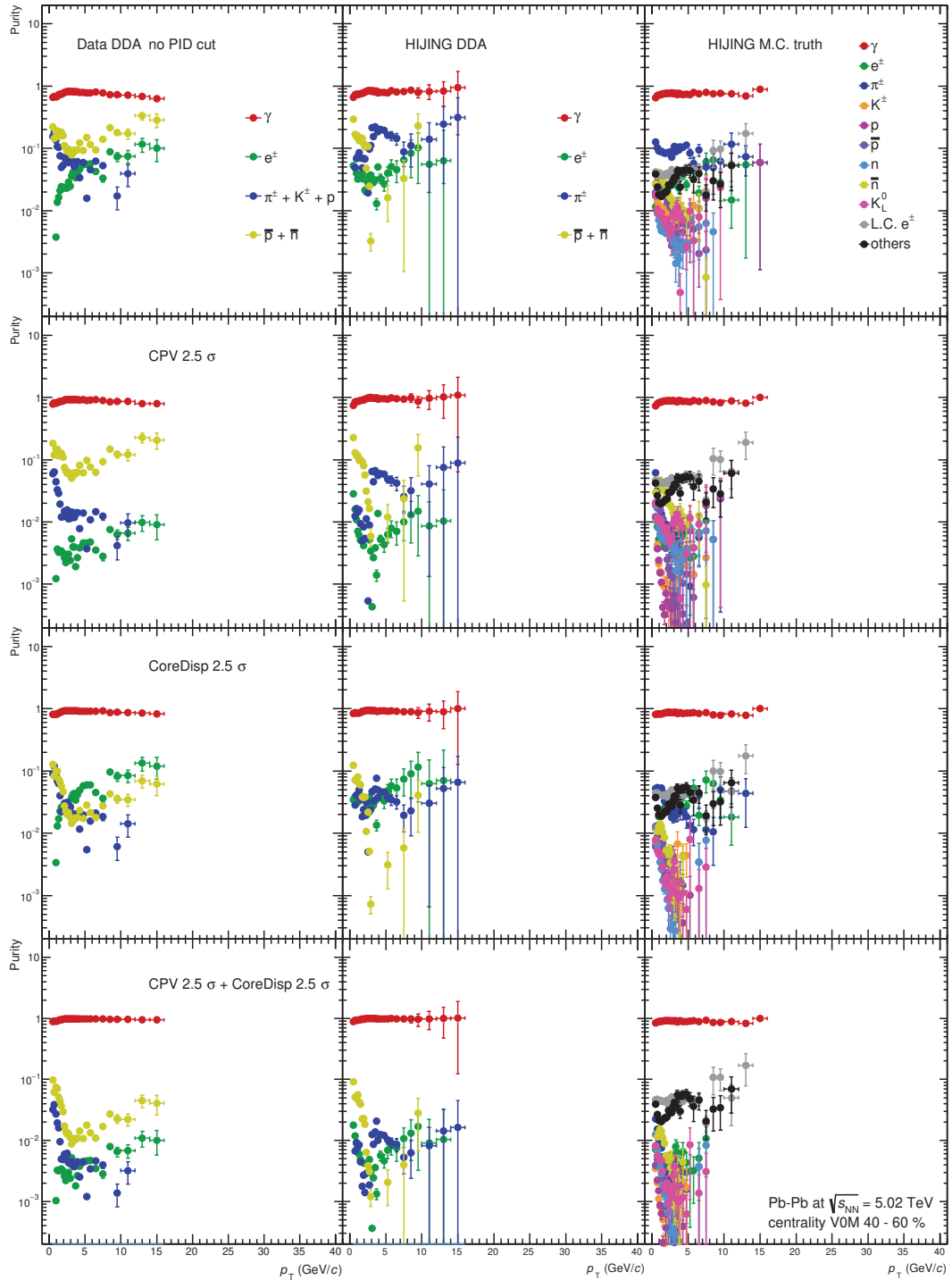


Figure 118: The summary of particle abundance on PHOS in 40-60% Pb-Pb collisions at $\sqrt{s_{NN}} = 5.02$ TeV for $C_{nh} = 0$.

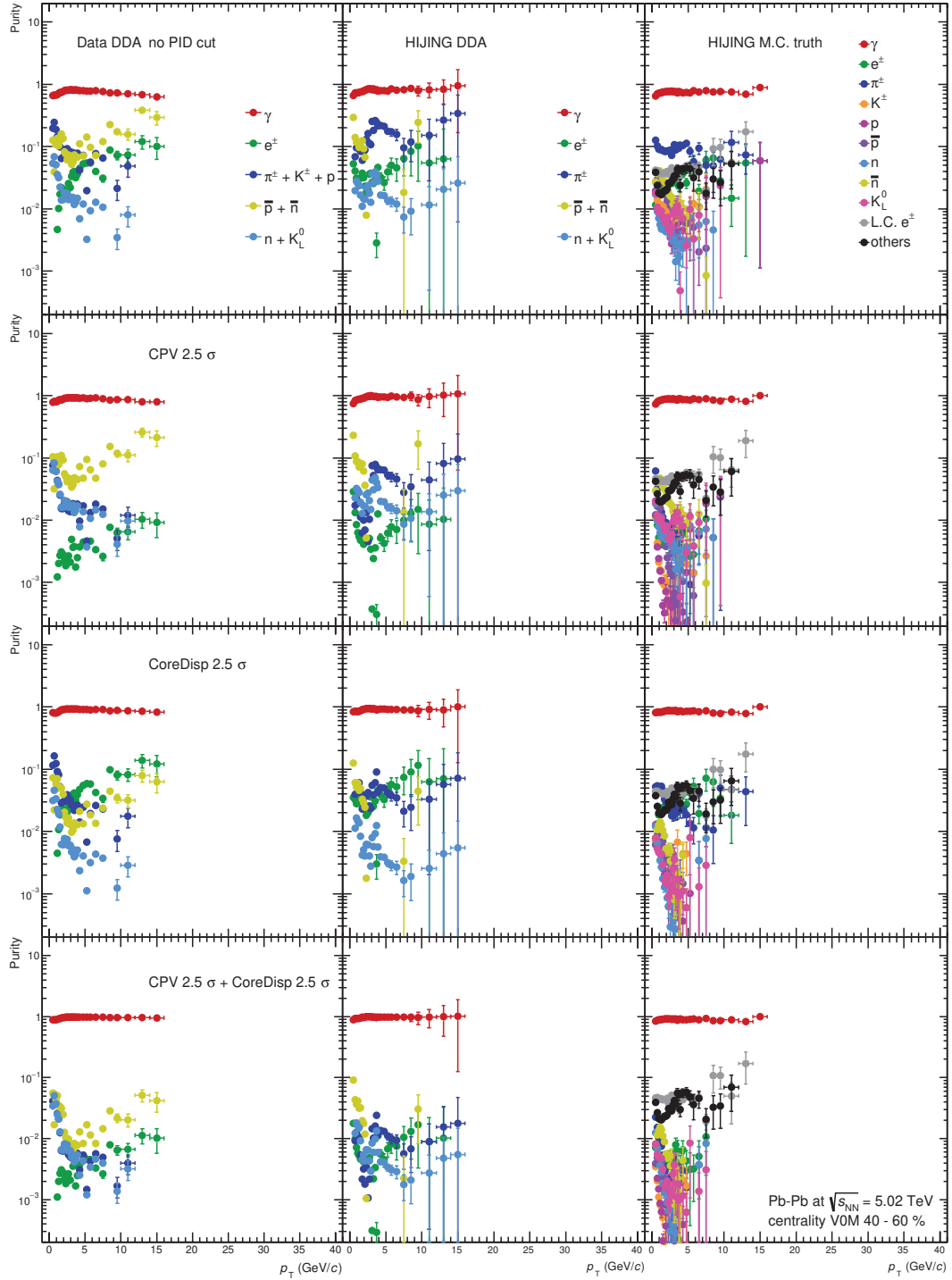


Figure 119: The summary of particle abundance on PHOS in 40-60% Pb-Pb collisions at $\sqrt{s_{NN}} = 5.02$ TeV for $C_{nh} = 0.5 \times K^\pm/\pi^\pm + p/\pi^\pm$.

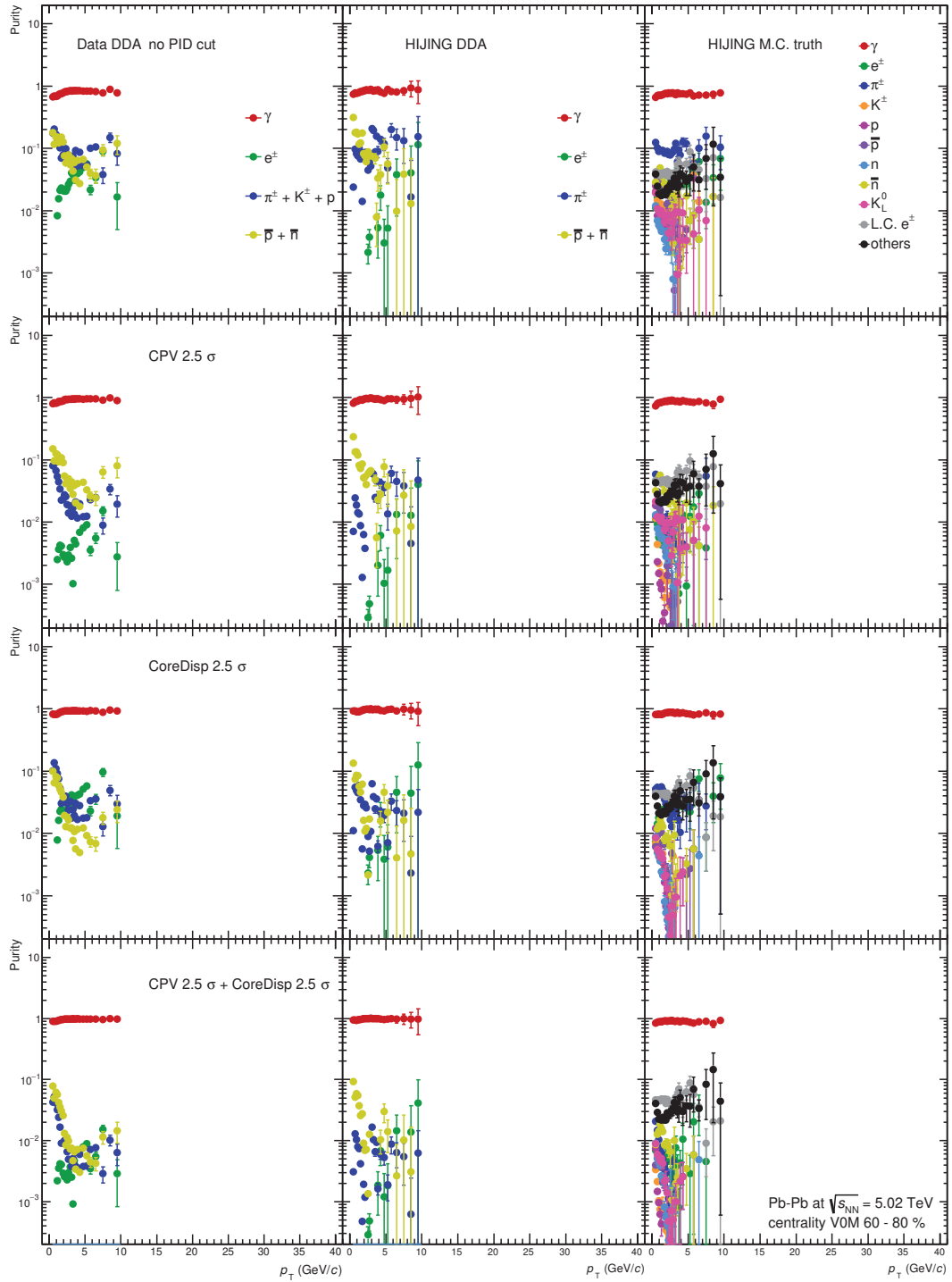


Figure 120: The summary of particle abundance on PHOS in 60-80% Pb-Pb collisions at $\sqrt{s_{NN}} = 5.02$ TeV for $C_{nh} = 0$.

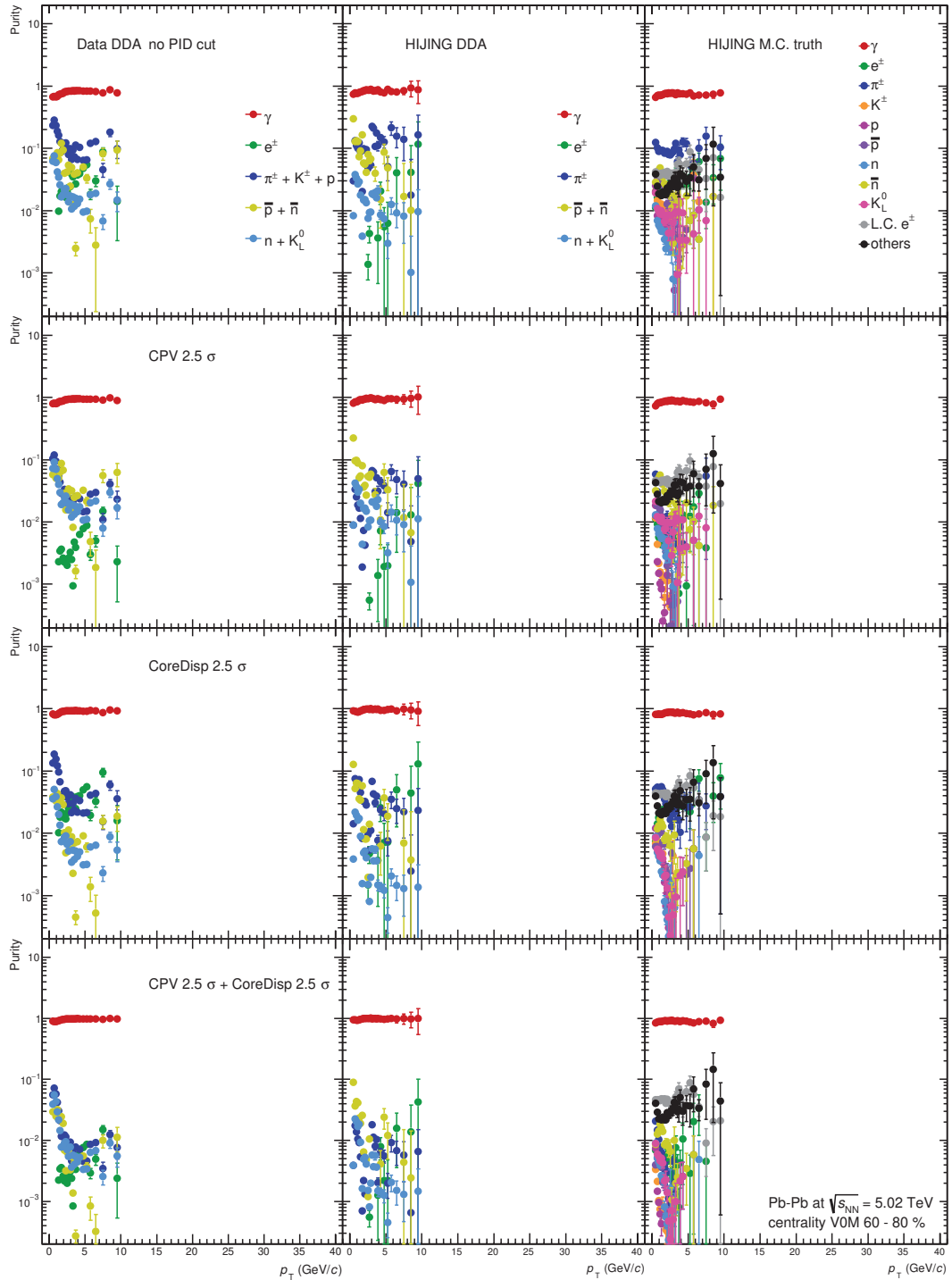


Figure 121: The summary of particle abundance on PHOS in 60-80% Pb-Pb collisions at $\sqrt{s_{NN}} = 5.02$ TeV for $C_{nh} = 0.5 \times K^\pm/\pi^\pm + p/\pi^\pm$.

7.8 Photon cocktail simulation

The cocktail simulation is used to determine decay photon yield from hadrons. Measured p_T spectra of hadrons described in section 6 are inputs to the cocktail simulation. Technically, TPythia6Decayer in ROOT6 framework based on PYTHIA 6.4 [88] with flat p_T , azimuthal angle and rapidity distribution is used for decay simulation. The source of cocktail simulation considered in this thesis is summarized in Table.6.

Non-measured particles (ω and η') are scaled from the π^0 spectrum using m_T scaling [89]. The

Table 6: Particles which decay into photons

Particle	mass (MeV/ c^2)	decay channel	branching ratio (%)
π^0	135	$\gamma\gamma$	98.8
		$\gamma e^+ e^-$	1.2
η	547	$\gamma\gamma$	39.2
		$\gamma\pi^+\pi^-$	4.8
		$\gamma e^+ e^-$	4.9×10^{-3}
ω	782	$\pi^0\gamma$	8.3
		$\eta\gamma$	4.6×10^{-4}
η'	958	$\gamma\gamma$	2.2
		$\rho^0\gamma$	29.1
		$\omega\gamma$	2.8

m_T is called transverse mass which is defined by $m_T = \sqrt{p_T^2 + m^2}$. The relation to the invariant yield is:

$$\frac{1}{p_T} \frac{d^2 N}{dp_T dy} = \frac{1}{m_T} \frac{d^2 N}{dm_T dy}$$

The meaning of m_T scaling is that particle yields at the same m_T can be scaled from light hadron yields (e.g. $\pi^{\pm,0}$ for mesons or p for baryons) by a constant coefficient C_h . Therefore, one can write kinematic relation between π and particle of interest (h) as following:

$$\begin{aligned} p_{T,\pi}^2 + m_\pi^2 &= p_{T,h}^2 + m_h^2 \\ p_{T,\pi}^2 &= p_{T,h}^2 + m_h^2 - m_\pi^2 \end{aligned}$$

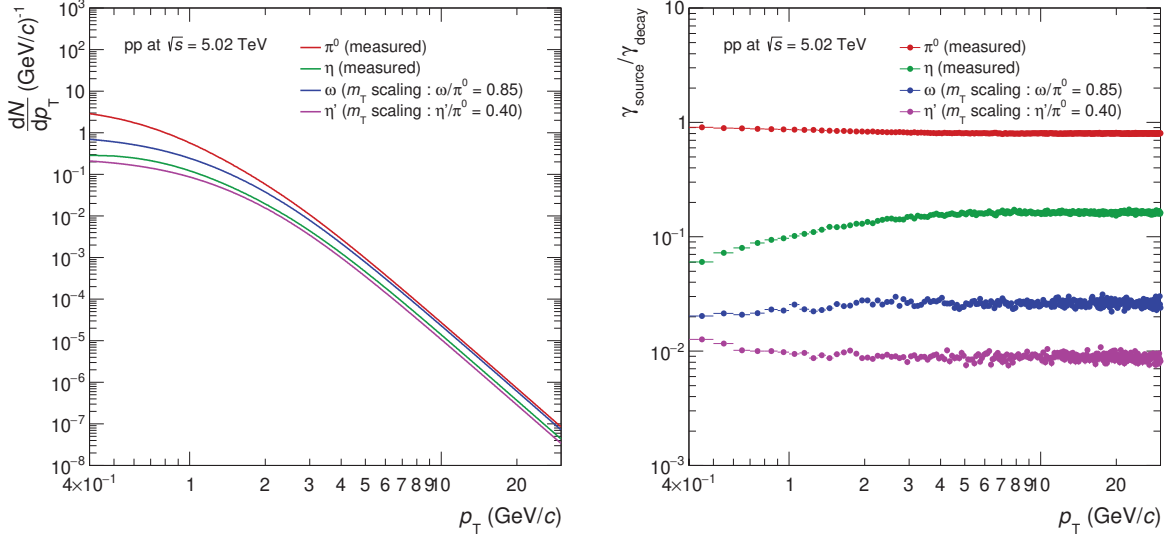
Finally, the invariant $p_{T,h}$ spectrum for particle h can be obtained by:

$$f_h(p_{T,h}) = C_h \times f_\pi(\sqrt{p_{T,h}^2 + m_h^2 - m_\pi^2})$$

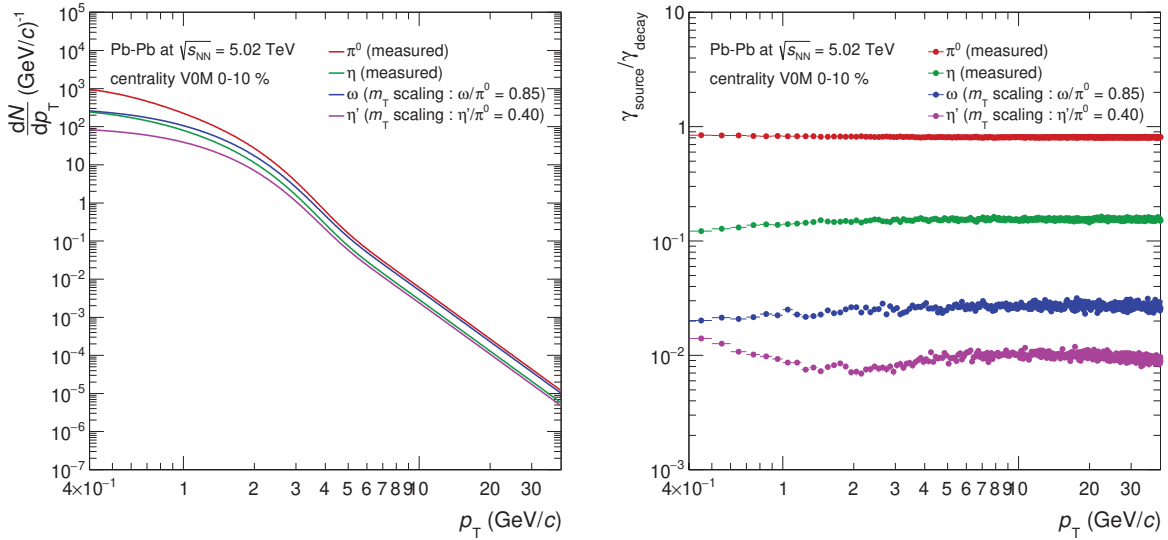
where, f_π represents parameterization of invariant p_T spectrum of reference particle π . Typically, $\omega/\pi^0 = 0.85$ [90] and $\eta'/\pi^0 = 0.40$ [88].

7.8.1 Cocktail simulation in pp at $\sqrt{s} = 5.02$ TeV

7.8.2 Cocktail simulation in Pb–Pb at $\sqrt{s_{NN}} = 5.02$ TeV

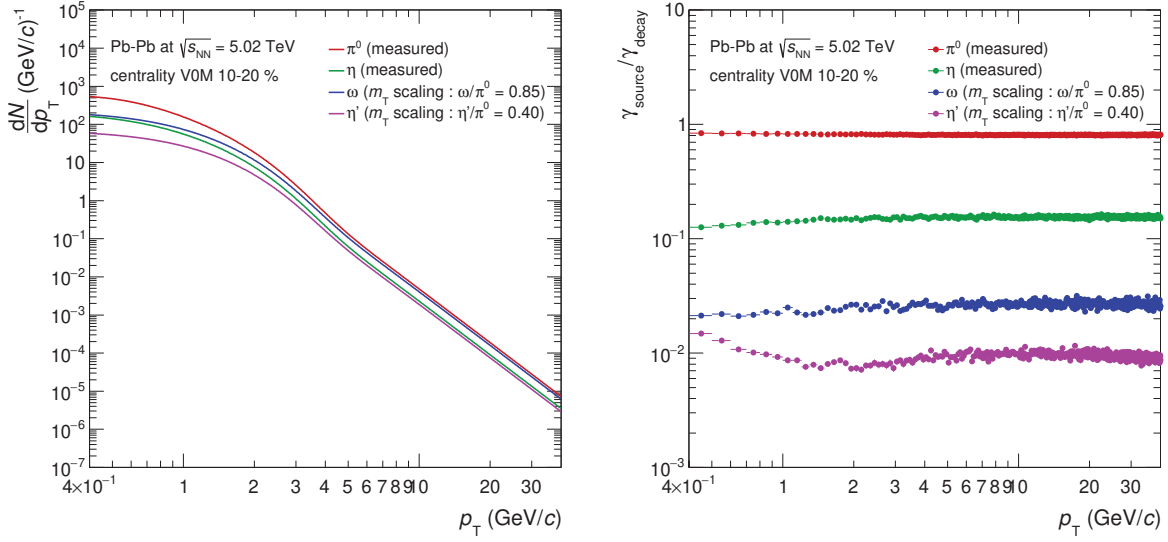
(a) The input p_T spectra from different mesons.

(b) The fraction of each decay photon source.

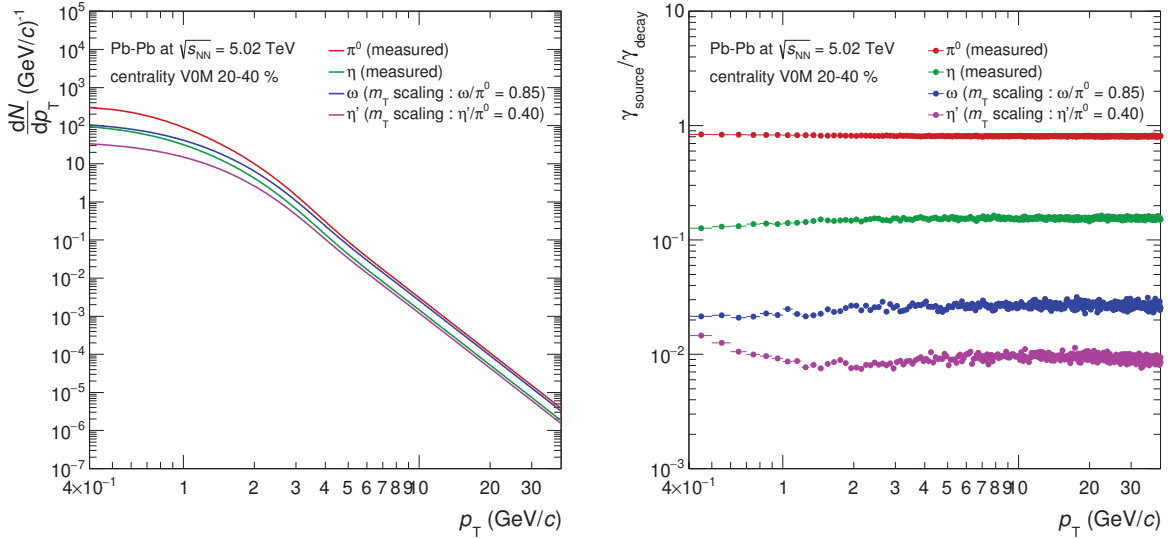
Figure 122: The decay photon cocktail in pp collisions at $\sqrt{s} = 5.02$ TeV(a) The input p_T spectra from different mesons.

(b) The fraction of each decay photon source.

Figure 123: The decay photon cocktail in Pb-Pb collisions at $\sqrt{s} = 5.02$ TeV centrality 0-10 %

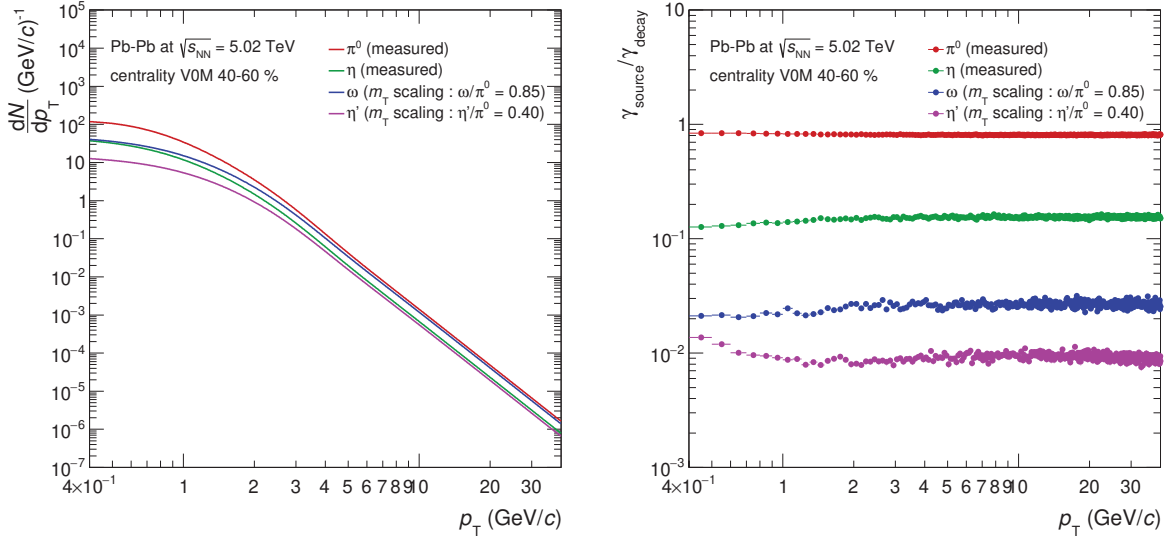
(a) The input p_T spectra from different mesons.

(b) The fraction of each decay photon source.

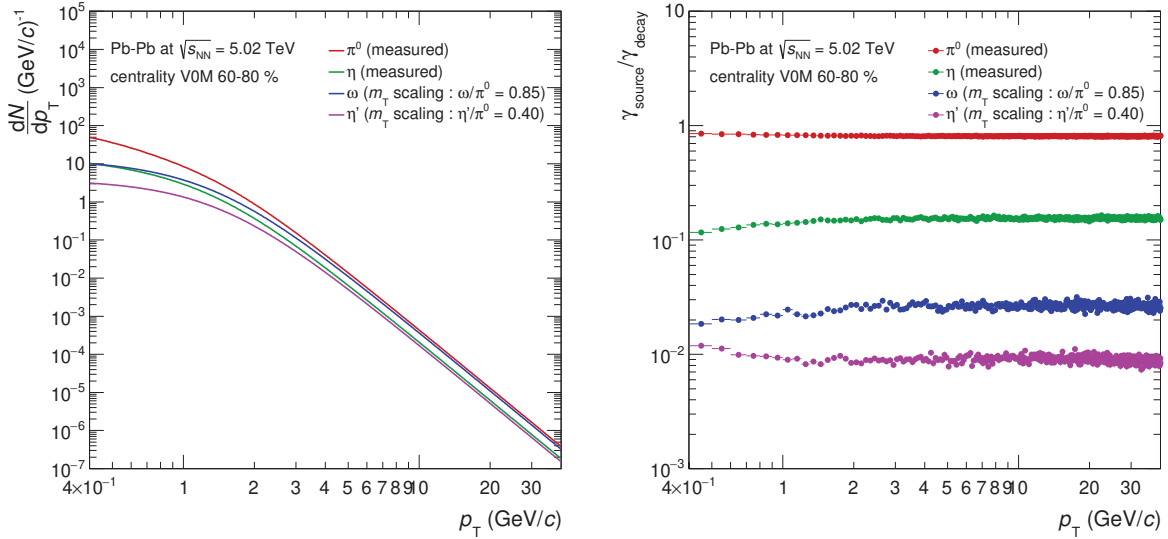
Figure 124: The decay photon cocktail in Pb-Pb collisions at $\sqrt{s} = 5.02$ TeV centrality 10-20 %(a) The input p_T spectra from different mesons.

(b) The fraction of each decay photon source.

Figure 125: The decay photon cocktail in Pb-Pb collisions at $\sqrt{s} = 5.02$ TeV centrality 20-40 %

(a) The input p_T spectra from different mesons.

(b) The fraction of each decay photon source.

Figure 126: The decay photon cocktail in Pb-Pb collisions at $\sqrt{s} = 5.02$ TeV centrality 40-60 %(a) The input p_T spectra from different mesons.

(b) The fraction of each decay photon source.

Figure 127: The decay photon cocktail in Pb-Pb collisions at $\sqrt{s} = 5.02$ TeV centrality 60-80 %

8 Systematic uncertainties for photon measurements

Systematic uncertainties for photon measurements are summarized in this section. Systematic uncertainties from the PID cut, the triggering, the global energy scale, the non-linearity, the acceptance of the PHOS detector and the material budget are common with neutral mesons measurements.

8.1 Photon purity

The systematic uncertainty of the photon purity is divided into two components. One is data driven approach (DDA) method itself. This has to be evaluated in M.C., because the true particle abundance is known. The other is due to the different assumption of the particle composition.

8.1.1 Data Driven approach method itself

The uncertainty due to the method itself was estimated by comparing photon purity between M.C. truth and DDA in M.C., since the true particle abundance is known in M.C.. This was performed in PYTHIA simulation (pp collisions) to avoid cluster overlappings under the high multiplicity environment. As shown by Figure 128, it is found to be $\sim 4\%$ at low p_T and almost vanishes (0.2%) at high p_T . The uncertainty of the DDA method itself is treated as common in pp and Pb–Pb collisions.

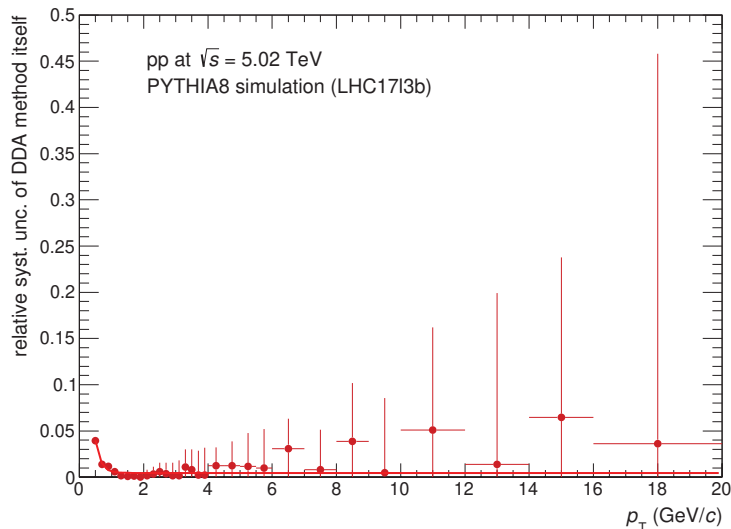


Figure 128: Systematic uncertainties of the DDA method itself.

8.1.2 Different assumption of particle composition

In the DDA, the system 31 was constructed to obtain the number of particles on PHOS under different assumptions of hadron contributions. This was evaluated by adding/removing neutral hadron components in system 31. The deviation from unity in the ratio $\frac{\gamma \text{ purity with } C_{nh}}{\gamma \text{ purity without } C_{nh}}$ is considered as the systematic uncertainty due to the different assumption.

8.2 Cocktail simulation

Mainly, there are two systematic uncertainties in the cocktail simulation. They are due to the different input parameterization of the measured π^0 spectrum and particle ratios.

1416 8.2.1 Shape of input π^0 spectrum

1417 The input π^0 spectrum is parameterized by TCM function described in the prevision section. In
 1418 order to take into account different parameterization, the measured π^0 spectra in pp collisions at
 1419 $\sqrt{s} = 5.02$ TeV is alternatively fitted by the modified Hagedorn function [29, 91, 92] developed
 1420 by the PHENIX collaboration at RHIC.

$$E \frac{d^3\sigma}{dp^3} = A \left(\exp(-(ap_T + bp_T^2)) + \frac{p_T}{p_0} \right)^{-n} \quad (34)$$

1421 When $a \rightarrow 0$ and $b \rightarrow 0$, the modified Hagedorn function becomes the original Hagedorn function.
 1422 On the other hand, the modified Hagedorn function does not fit to π^0 spectra measured for wide
 1423 p_T range in central Pb–Pb collision at $\sqrt{s_{NN}} = 5.02$ TeV due to a kink at $p_T = 4 \sim 5$ GeV/ c .
 1424 In other wards, the TCM function is necessary for describing hadron productions for such wide
 1425 p_T range in central Pb–Pb collisions. Hence, a simplified TCM-inspired function was tried for
 1426 alternative parameterizations of input π^0 spectra.

$$E \frac{d^3\sigma}{dp^3} = A_e \exp\left(-\frac{p_T}{T_e}\right) + A \left(1 + \frac{p_T^2}{T^2}\right)^{-n} \quad (35)$$

1427 The systematic uncertainty due to different π^0 paramterization was evaluated by the γ/π^0 ratio
 1428 in the cocktail simulation. The deviation from unity in the double ratio $\frac{(\gamma/\pi^0)_{alt}}{(\gamma/\pi^0)_{def}}$ in the cocktail
 1429 simulation is considered as the systematic uncertainty of the shape of the input π^0 spectrum.
 1430 However, since $(1 + \frac{p_T^2}{T^2})^{-n}$ is similar to the original TCM function, alternative parameterizations
 1431 for π^0 spectra fitted by Eq. 35 give too small difference from default ones in Pb–Pb collisions.
 1432 Thus, the systematic uncertainty due to the shape of the input π^0 spectrum in Pb–Pb collisions
 1433 is inherited from that in pp collisions. It is 4 % at low p_T and decreases with p_T down to 0.4 %.

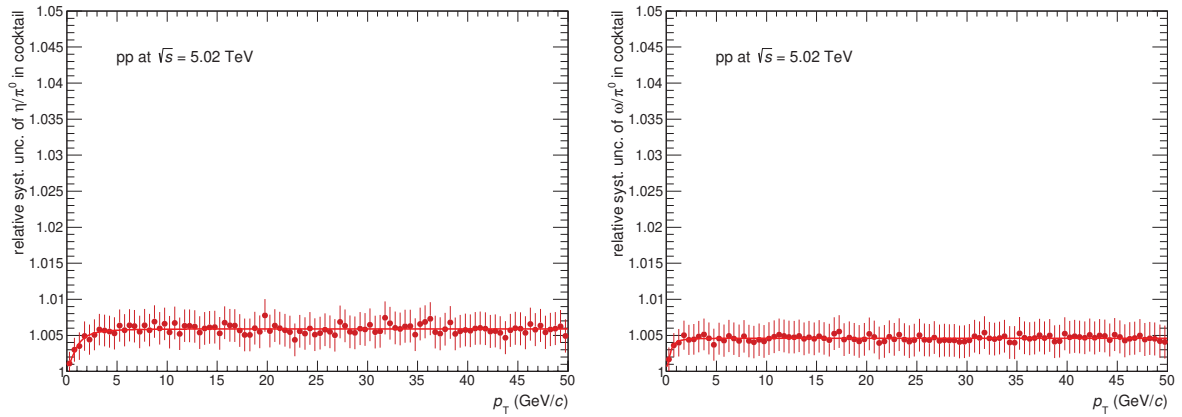
1434 8.2.2 Particle ratios

1435 The uncertainty due to particle ratios are originating from measured particle ratios. The η/π^0
 1436 and ω/π^0 are varied 0.50 ± 0.02 and 0.85 ± 0.15 respectively. As relative contributions to total
 1437 decay photon yields (15% for photons from η mesons and 2.5% for photons from ω mesons) are
 1438 known, the relative systematic uncertainty can be analytically estimated as :

$$\frac{\pm 0.02}{0.50} \times 0.15 \approx \pm 0.60\% \text{ for photons decayed from } \eta \text{ mesons} \quad (36)$$

$$\frac{\pm 0.15}{0.85} \times 0.025 \approx \pm 0.44\% \text{ for photons decayed from } \omega \text{ mesons} \quad (37)$$

1439 They were also estimated directly in the cocktail simulation, as shown on Figure 129, which
 1440 gives similar values to the analytical calculations, as expected. The uncertainty from η'/π^0 is
 1441 negligible, as the relative contribution of decay photons decayed from η' mesons to total the
 1442 decay photon is less than 1%.



(a) The systematic uncertainty due to the η/π^0 in the cocktail simulation. (b) The systematic uncertainty due to the ω/π^0 in the cocktail simulation.

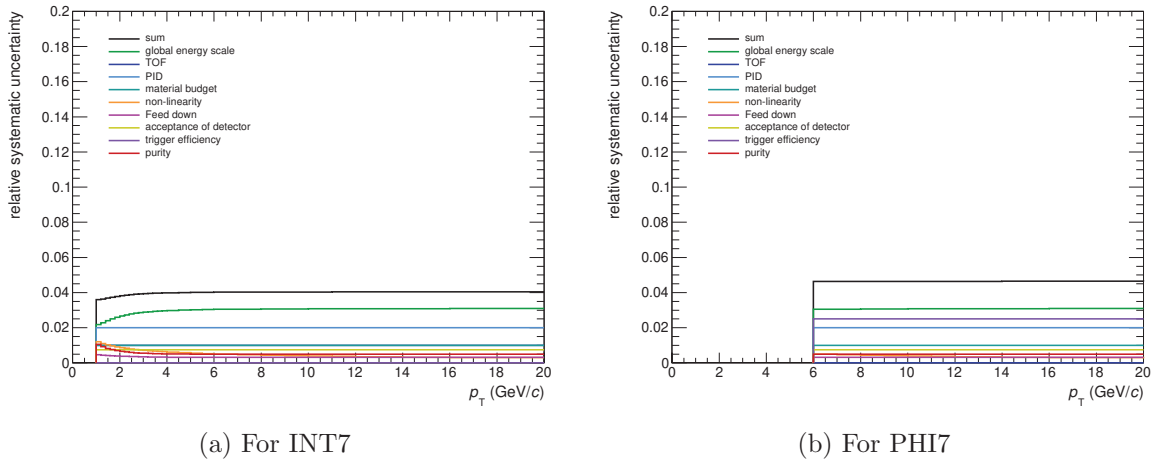
Figure 129: Systematic uncertainties due to particle ratios in the cocktail simulation

1443 8.3 Summary of systematic uncertainties for inclusive photons γ^{inc}

1444 The summary of systematic uncertainties for inclusive photons γ^{inc} is plotted in this section.

1445 8.3.1 Summary of systematic uncertainties for γ^{inc} in pp collisions at $\sqrt{s} = 5.02$ TeV

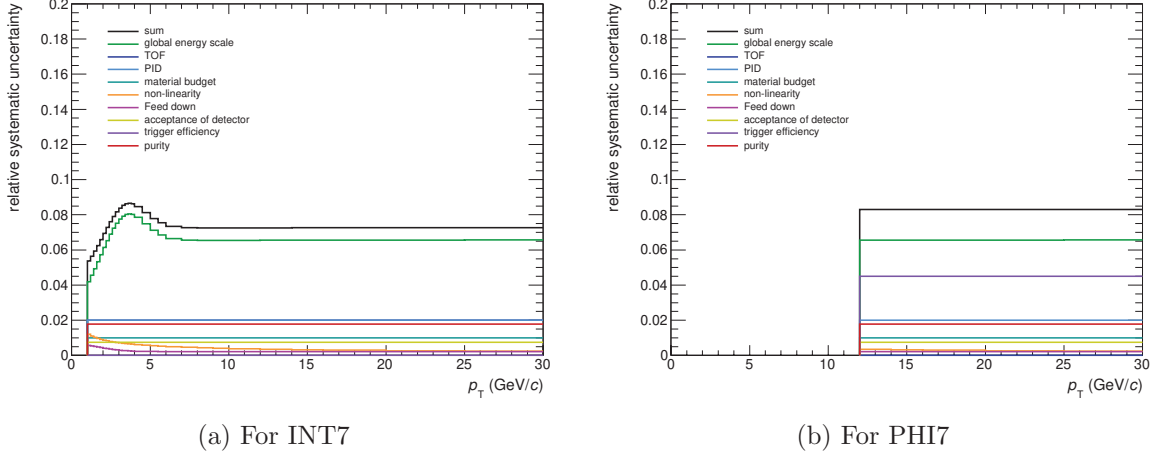
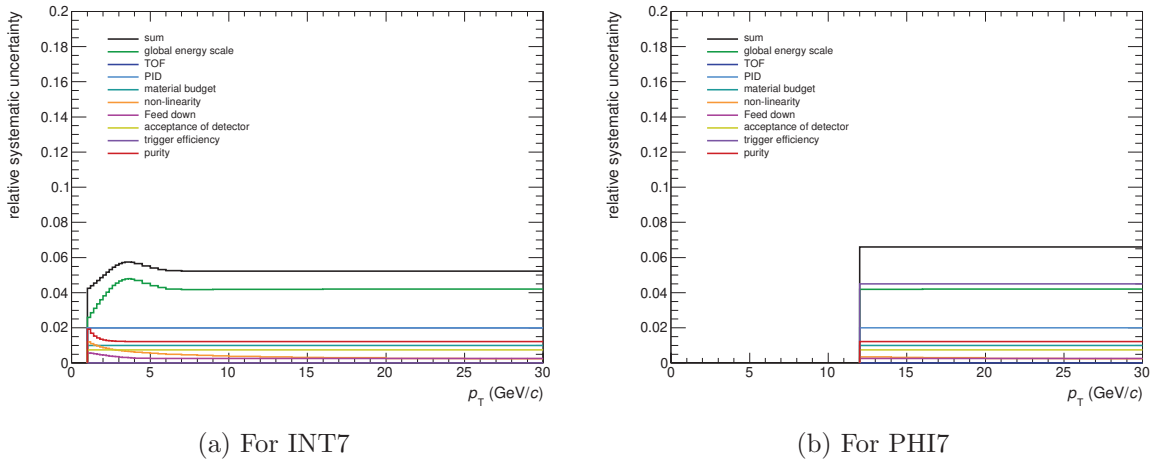
1446

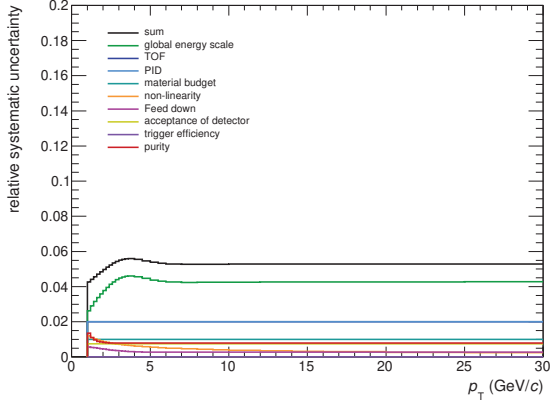


(a) For INT7

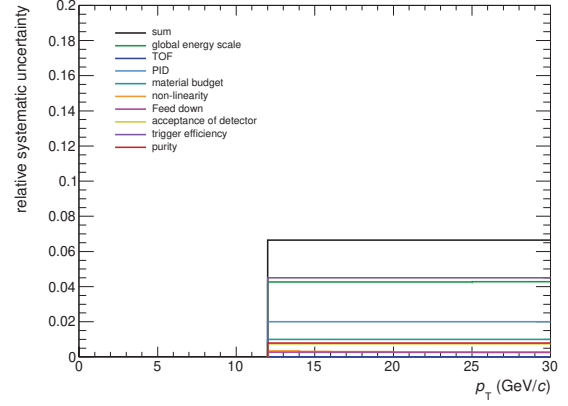
(b) For PHI7

Figure 130: Systematic uncertainties for γ^{inc} in pp collisions at $\sqrt{s} = 5.02$ TeV.

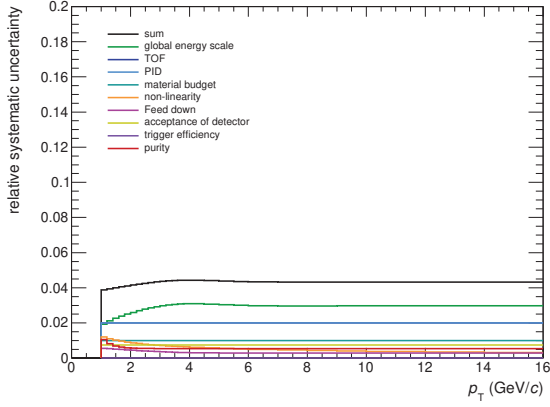
1447 **8.3.2 Summary of systematic uncertainties for γ^{inc} in Pb–Pb collisions at $\sqrt{s_{\text{NN}}} =$**
 1448 **5.02 TeV**

 Figure 131: Systematic uncertainties for γ^{inc} in Pb–Pb collisions at $\sqrt{s_{\text{NN}}} = 5.02$ TeV for centrality 0-10%.

 Figure 132: Systematic uncertainties for γ^{inc} in Pb–Pb collisions at $\sqrt{s_{\text{NN}}} = 5.02$ TeV for centrality 10-20%.



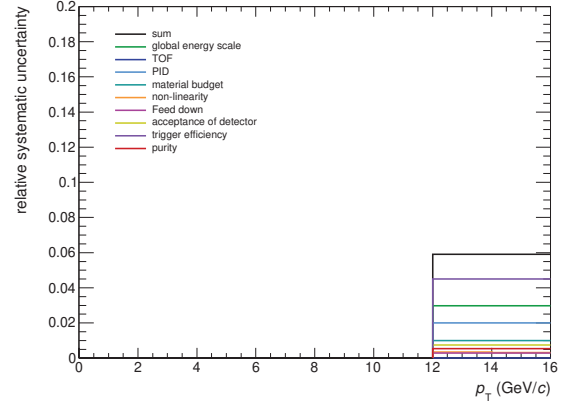
(a) For INT7



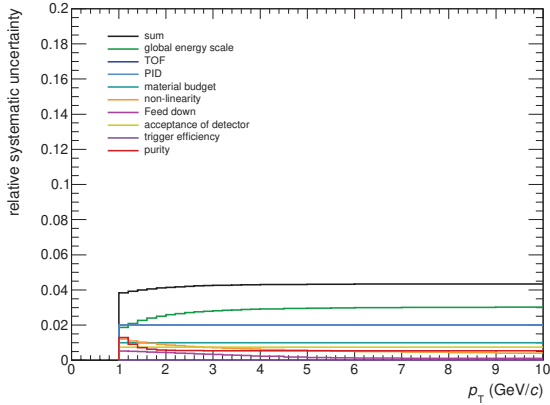
(b) For PHI7

 Figure 133: Systematic uncertainties for γ^{inc} in Pb–Pb collisions at $\sqrt{s_{\text{NN}}} = 5.02$ TeV for centrality 20–40%.


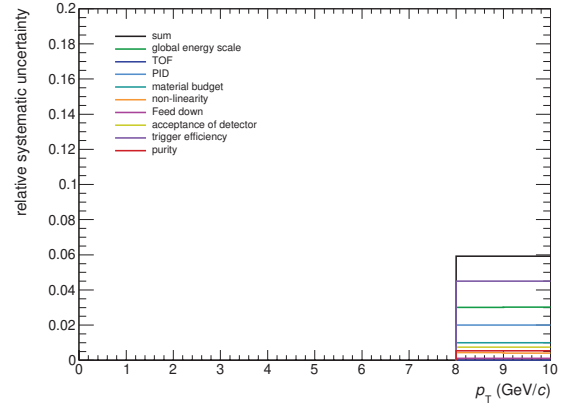
(a) For INT7



(b) For PHI7

 Figure 134: Systematic uncertainties for γ^{inc} in Pb–Pb collisions at $\sqrt{s_{\text{NN}}} = 5.02$ TeV for centrality 40–60%.


(a) For INT7



(b) For PHI7

 Figure 135: Systematic uncertainties for γ^{inc} in Pb–Pb collisions at $\sqrt{s_{\text{NN}}} = 5.02$ TeV for centrality 60–80%.

9 Results and discussions for photons

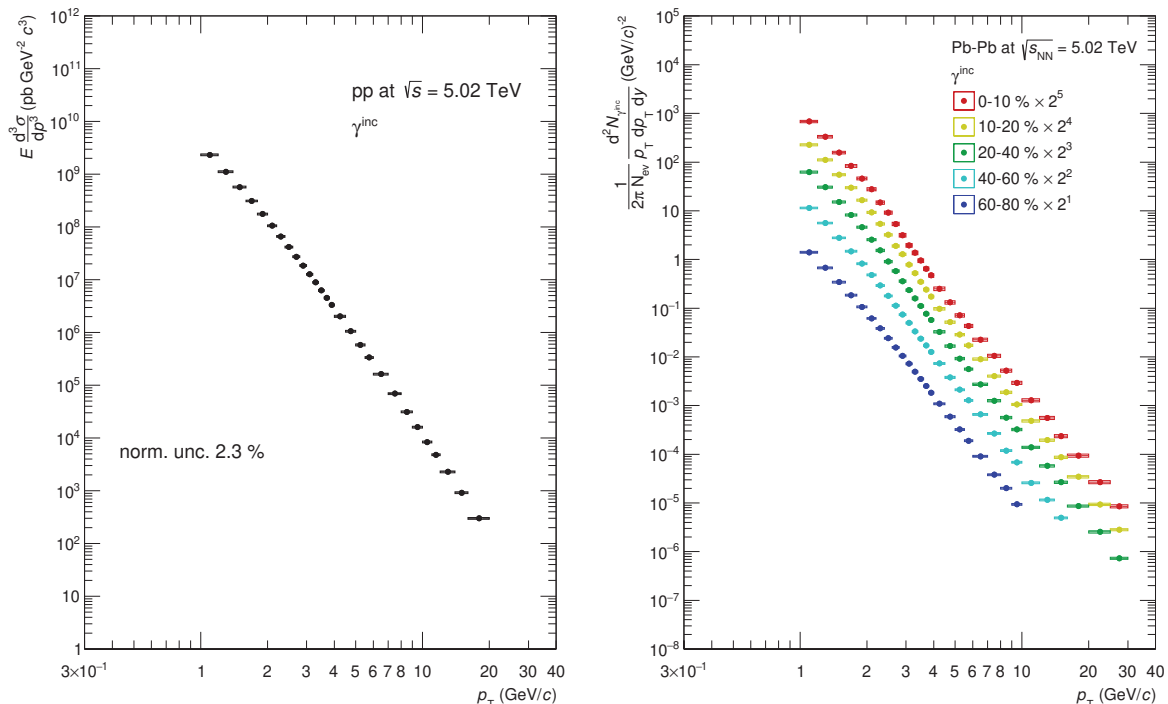
1449

1450 Results toward the direct photons measurement are described in this section. Inclusive photon
 1451 spectra γ^{inc} , $\gamma^{\text{inc}}/\pi^0$ ratios in data and cocktail simulation, R_γ which is the double ratio of
 1452 $\gamma^{\text{inc}}/\pi^0$ and finally, direct photon spectra.

9.1 Results on inclusive photons γ^{inc}

1453

1454 As a first step for the direct photons measurement, inclusive photon spectra have been measured
 in pp and Pb–Pb collisions at $\sqrt{s_{\text{NN}}} = 5.02$ TeV.



(a) The production cross section of inclusive photons in pp collisions at $\sqrt{s} = 5.02$ TeV.

(b) Invariant yields of inclusive photons in Pb–Pb collisions at $\sqrt{s_{\text{NN}}} = 5.02$ TeV.

Figure 136: Inclusive photons spectra in pp and Pb–Pb collisions at $\sqrt{s_{\text{NN}}} = 5.02$ TeV.

1455

9.2 Results on direct photons γ^{dir}

1456

9.2.1 $\gamma^{\text{inc}}/\pi^0$ ratio

1457

1458 Neutral mesons and inclusive photons have been measured as described in previous sections.
 1459 Secondly, the ratio of inclusive photon yields to π^0 yields are constructed in data and cocktail
 1460 simulation from known sources respectively for pp and Pb–Pb collisions (Figure 137). The main
 1461 advantage of $\gamma^{\text{inc}}/\pi^0$ ratio is to cancel out the systematic uncertainty of energy measurement,
 1462 namely global energy scale and non-linear response in M.C., that are dominant sources in the
 1463 PHOS detector.

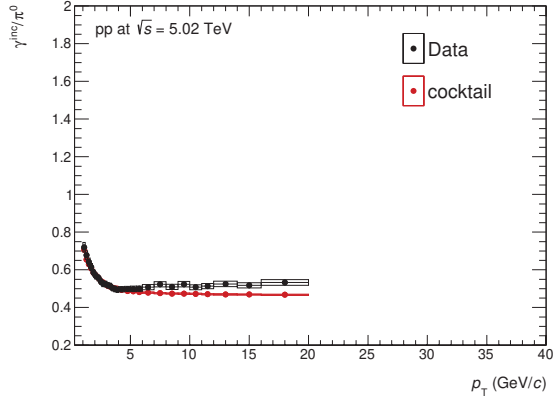
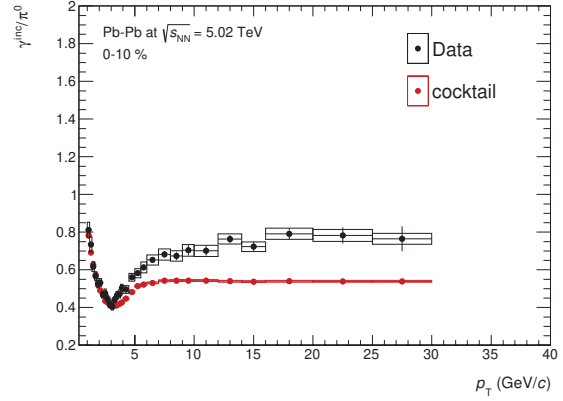
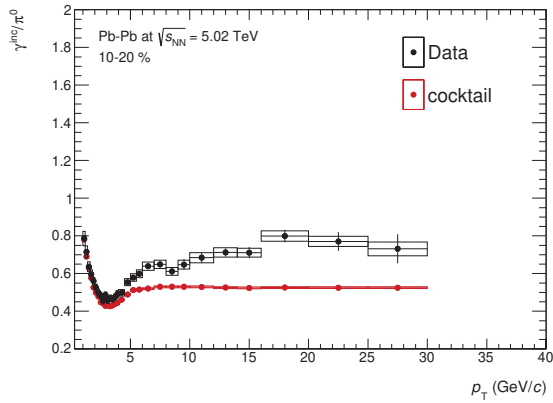
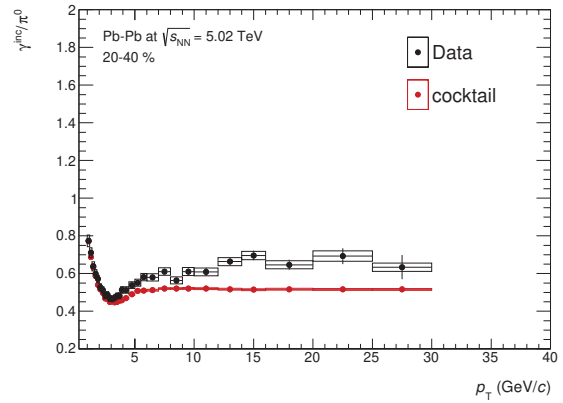
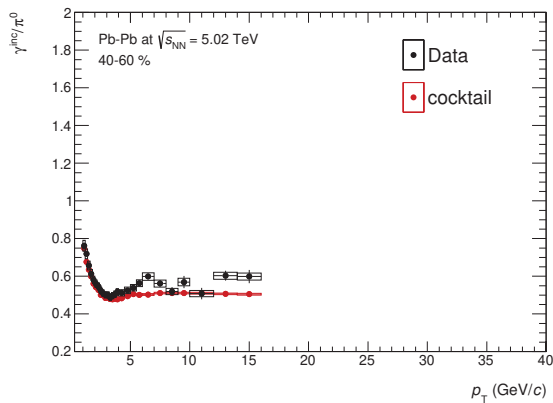
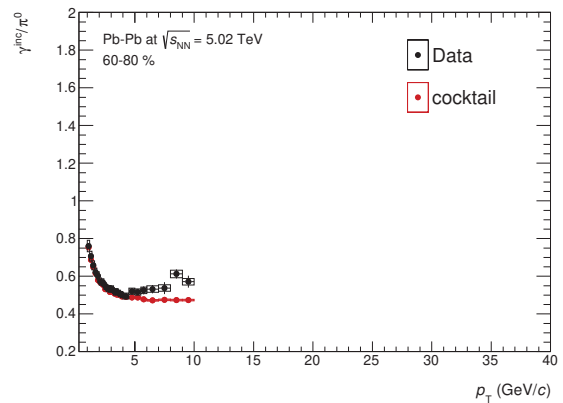
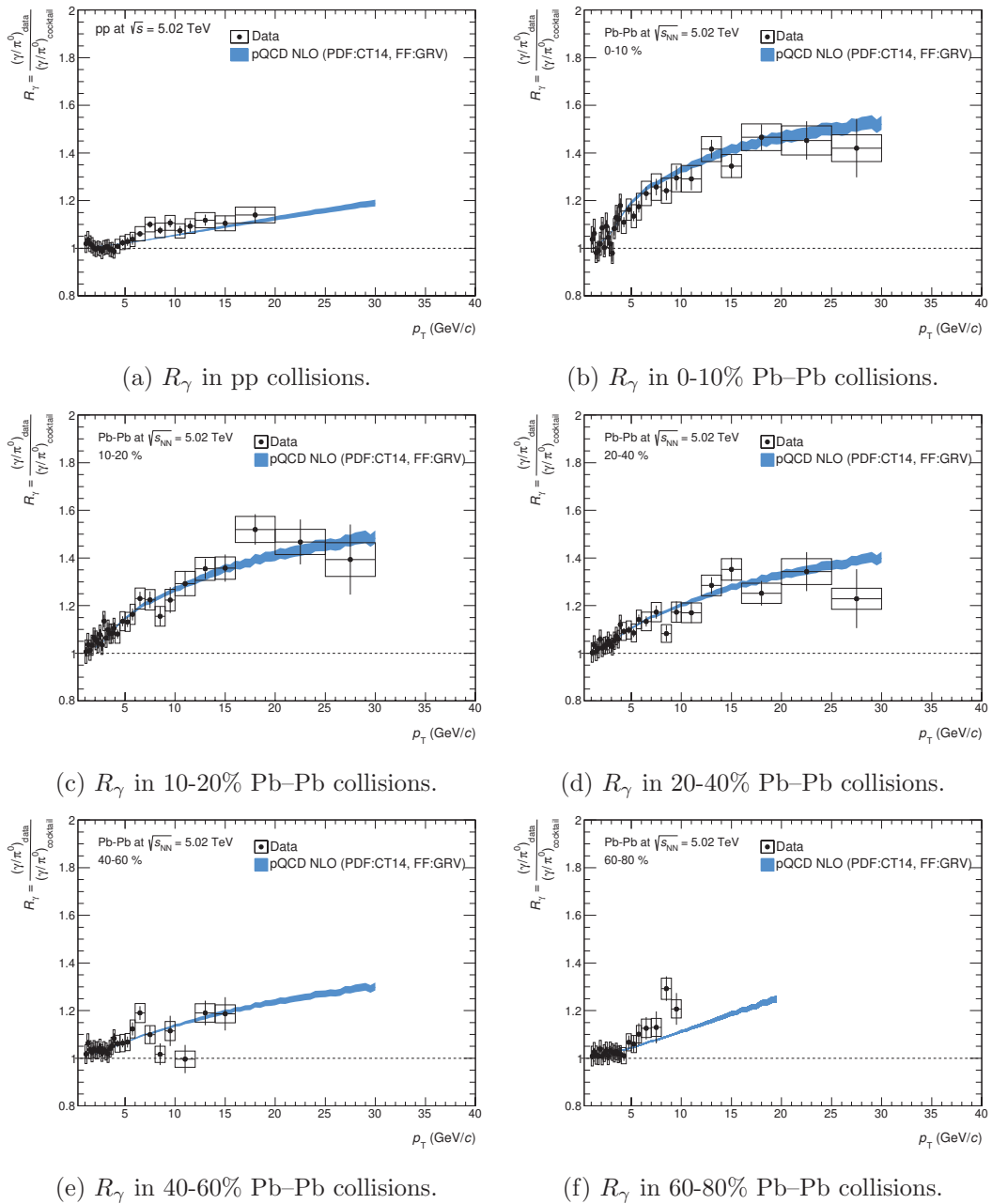

 (a) The $\gamma^{\text{inc}}/\pi^0$ ratio in pp collisions.

 (b) The $\gamma^{\text{inc}}/\pi^0$ ratio in 0-10% Pb-Pb collisions.

 (c) The $\gamma^{\text{inc}}/\pi^0$ ratio in 10-20% Pb-Pb collisions.

 (d) The $\gamma^{\text{inc}}/\pi^0$ ratio in 20-40% Pb-Pb collisions.

 (e) The $\gamma^{\text{inc}}/\pi^0$ ratio in 40-60% Pb-Pb collisions.

 (f) The $\gamma^{\text{inc}}/\pi^0$ ratio in 60-80% Pb-Pb collisions.

 Figure 137: $\gamma^{\text{inc}}/\pi^0$ ratios in pp and Pb-Pb collisions at $\sqrt{s_{\text{NN}}} = 5.02$ TeV.

1464 **9.2.2 Direct photon excess ratio R_γ**

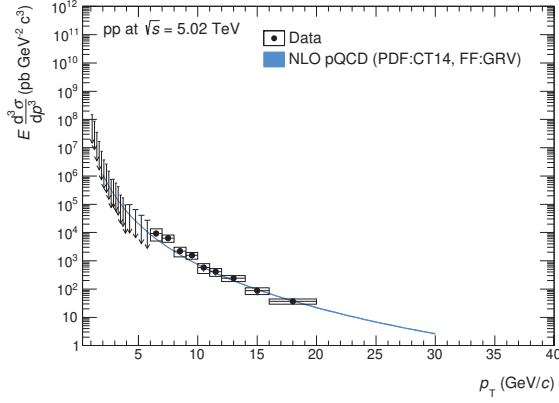
1465 As plotted on Figure 138, R_γ becomes larger with the event multiplicity (i.e. central collisions)
 1466 at high p_T . This is explained by the suppression of neutral mesons in central collisions, while
 1467 the direct photon is transparent probe for the QCD medium. Therefore, the excess of prompt
 1468 photons that are produced by initial hard scatterings between partons becomes significant at
 1469 higher p_T in central collisions. R_γ for the pQCD NLO calculation is defined as :

$$R_\gamma^{\text{NLO}} = 1 + N_{\text{coll}} \cdot \frac{\gamma_{\text{decay}}^{\text{dir}}}{\gamma_{\text{cocktail}}} \quad (38)$$

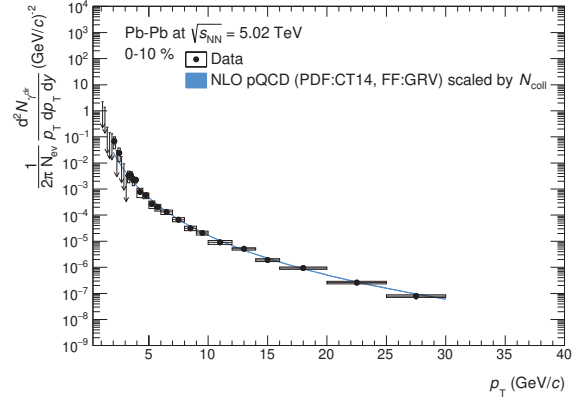

 Figure 138: R_γ in pp and Pb-Pb collisions at $\sqrt{s_{\text{NN}}} = 5.02$ TeV.

1471 **9.2.3 Direct photon spectra**

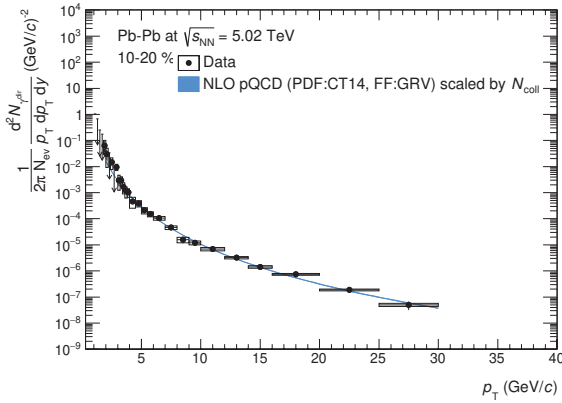
1472 Finally, direct photon spectra or upper limits at the 90% confidence level have been extracted as
 1473 shown by Figure 139. The pQCD calculation basically describes prompt photon yields at high
 p_T well in both pp and Pb–Pb collisions.



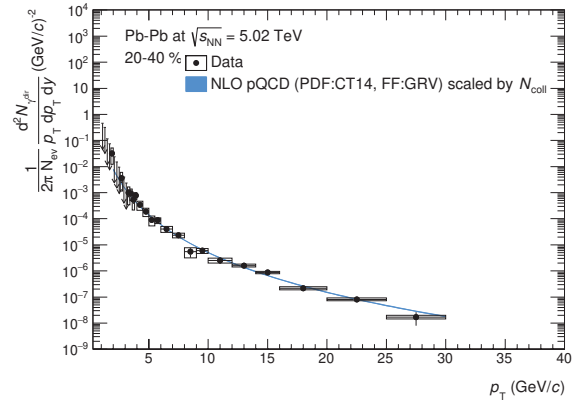
(a) The production cross section of direct photons in pp collisions.



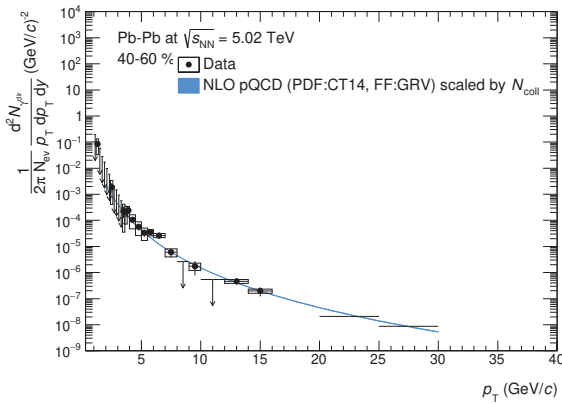
(b) The invariant yield of direct photons in 0-10% Pb–Pb collisions.



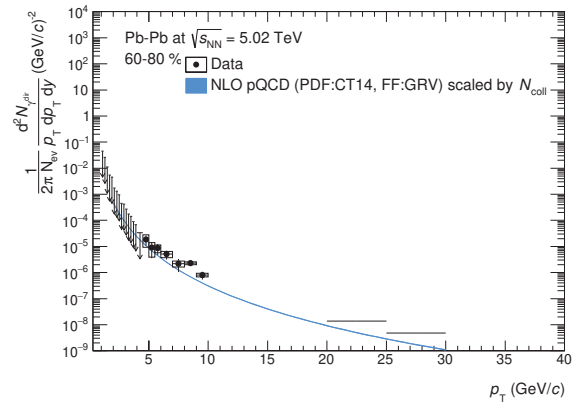
(c) The invariant yield of direct photons in 10-20% Pb–Pb collisions.



(d) The invariant yield of direct photons in 20-40% Pb–Pb collisions.



(e) The invariant yield of direct photons in 40-60% Pb–Pb collisions.



(f) The invariant yield of direct photons in 60-80% Pb–Pb collisions.

 Figure 139: Direct photon spectra in pp and Pb–Pb collisions at $\sqrt{s_{NN}} = 5.02$ TeV.

1474 **9.2.4 R_{AA} of direct photons**

1475 In this thesis, only upper limits on direct photon yields at the 90% confidence level have been set
 1476 at low p_T . Nevertheless, a few data points on R_γ (Figure 138b) and the invariant yield of direct
 1477 photons (Figure 139b) in central collisions show larger value than the pQCD calculation at low
 1478 p_T . Hence, it is interesting to see R_{AA} of direct photons. As shown by Figure 140, direct photon
 1479 yields beyond the pQCD calculation which can describe prompt photon yields by a factor of up
 1480 to about 4 is observed at $p_T < 4$ GeV/c. This can be interpreted as an indication of thermal
 1481 photon emissions from the hot and dense medium in central Pb–Pb collisions. Focusing on R_{AA}
 1482 at high p_T region, hadron yields are strongly suppressed, while it is consistent with unity for
 1483 direct photons. The resulting R_{AA} emphasizes the observed strong hadron suppression is related
 1484 to final state effects due to the formation of hot and dense colored medium. Additionally, the
 1485 experimental fact that R_{AA} of direct photons is consistent with unity at high p_T proves successful
 Glauber modeling in terms of the collision geometry.

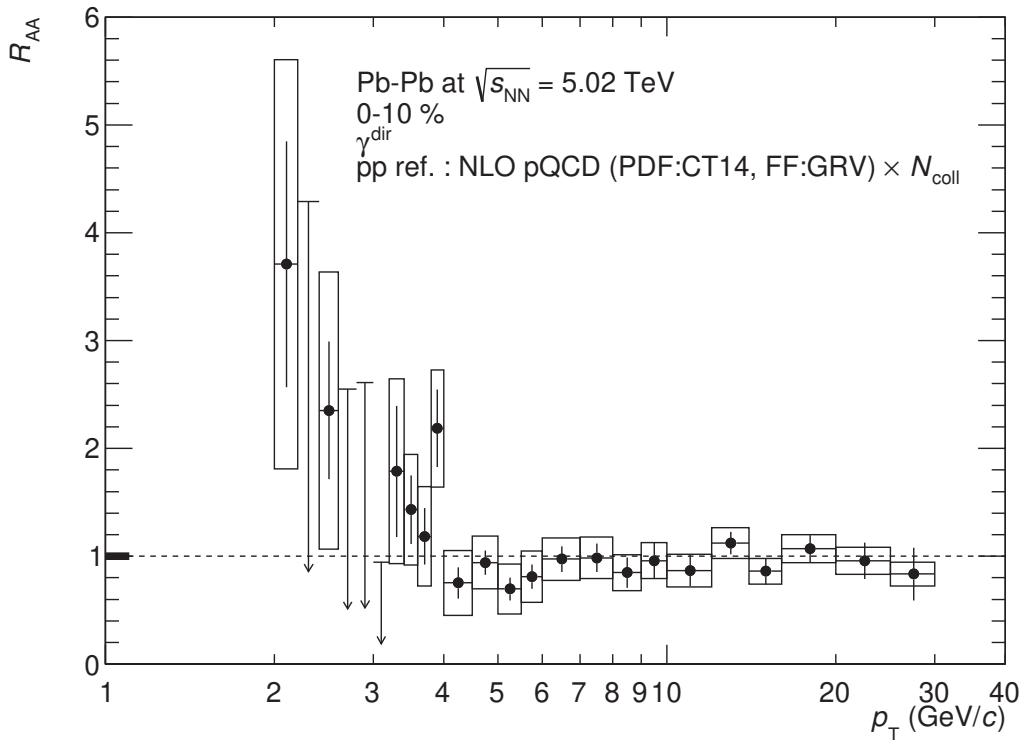


Figure 140: R_{AA} of direct photons in Pb–Pb collisions at $\sqrt{s_{NN}} = 5.02$ TeV for centrality 0-10%.

1486

1487 **9.2.5 Effective temperature T_{eff} extraction**

1488 The inverse slope of an exponential fit at low p_T regime is interpreted as the average temperature
 1489 over all the space-time evolution. As written in the previous section (9.2.4), p_T spectra of
 1490 prompt photons at high p_T agree with the pQCD calculation, which justifies these measurements.
 1491 Moreover, there is indication of excess due to thermal emissions from the QGP at low p_T beyond
 1492 the pQCD calculation in central Pb–Pb collisions (0-10%). Therefore, there is a possibility to
 1493 fit data points at low p_T by the exponential function $A \times \exp(-p_T/T_{\text{eff}})$ and modified Hagedorn
 1494 function. Namely, the global fitting function is :

$$\frac{1}{2\pi N_{\text{ev}}} \frac{d^2 N_{\gamma^{\text{dir}}}}{p_T dp_T dy} = A \times \exp(-p_T/T_{\text{eff}}) + B \times \left(1 + \frac{p_T^2}{p_0^2}\right)^{-n}, \quad (39)$$

1495 where parameters B , p_0 and n for prompt photons at high p_T are fixed by the pQCD calculation
 1496 to reduce the number of degrees of freedom. So, free parameters are A and T_{eff} . Both data points
 and upper limits at the 90% C.L. are included in the fitting. The obtained effective temperature

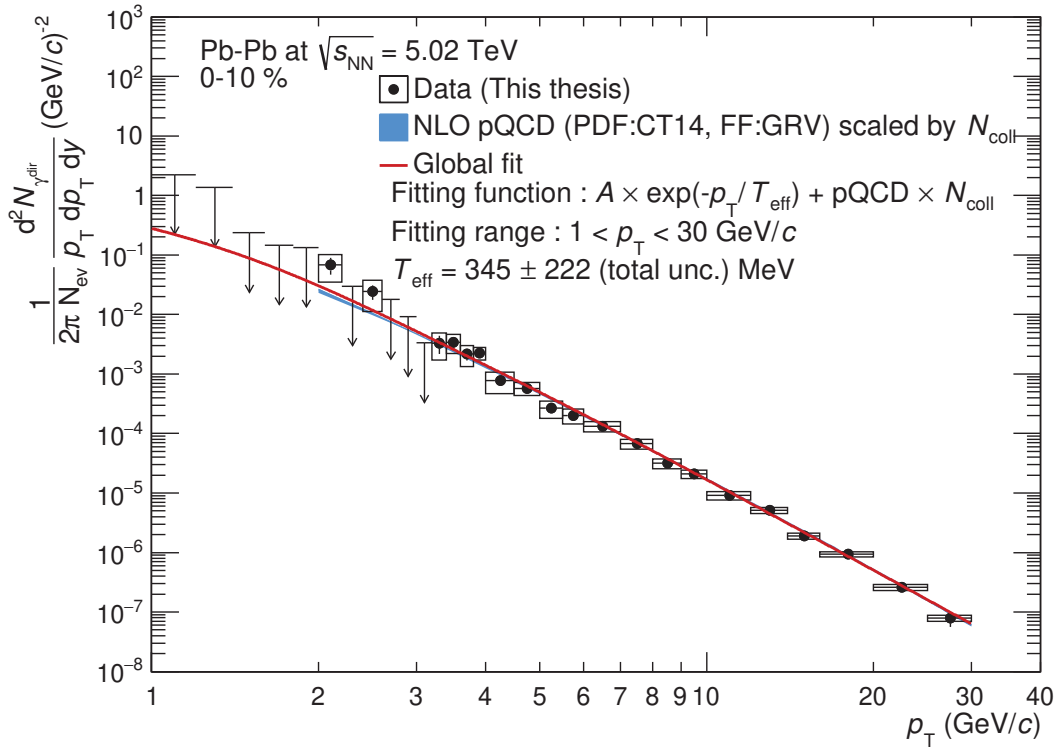


Figure 141: The p_T spectrum of direct photons in Pb–Pb collisions at $\sqrt{s_{\text{NN}}} = 5.02$ TeV for centrality 0-10% and the TCM fit to data.

1497 T_{eff} is 345 ± 222 (total unc.) MeV in Pb–Pb collisions at $\sqrt{s_{\text{NN}}} = 5.02$ TeV for centrality 0-
 1498 10%. The statistical and systematic uncertainty of the T_{eff} are not separated, because upper
 1499 limits on direct photon yields at the 90 % C.L. are set based on the quadratic sum of them.
 1500 For references, it has been reported that $T_{\text{eff}} = 239 \pm 25$ (stat.) ± 7 (syst.) MeV [30] via real
 1501 photons in 0-20 % central Au–Au collisions at $\sqrt{s_{\text{NN}}} = 0.2$ TeV at RHIC by PHENIX, and
 1502 $T_{\text{eff}} = 294 \pm 12$ (stat.) ± 47 (syst.) MeV [31] in 0-20 % central Pb–Pb collisions at $\sqrt{s_{\text{NN}}} = 2.76$
 1503 TeV with ALICE at the LHC.
 1504

10 Conclusion

The measurement of neutral mesons and direct photons in pp and Pb–Pb collisions at $\sqrt{s_{\text{NN}}} = 5.02$ TeV has been performed in ALICE with the PHOS detector. p_{T} spectra and nuclear modification factors R_{AA} of π^0 meson in $0.4 < p_{\text{T}} < 35$ GeV/ c and η meson in $2.0 < p_{\text{T}} < 16$ GeV/ c have been measured in pp and Pb–Pb collisions at $\sqrt{s_{\text{NN}}} = 5.02$ TeV. This is the first measurement of the suppression of π^0 at such high p_{T} regime. π^0 and η mesons show the same suppression pattern at $p_{\text{T}} > 4$ GeV/ c in all centrality classes. The suppression pattern between η and K^{\pm} mesons seems to be similar at low p_{T} , though the uncertainty for η meson is large. It is found that p_{T} spectrum of π^0 becomes harder than that at $\sqrt{s_{\text{NN}}} = 2.76$ TeV in both pp and Pb–Pb collisions. Nevertheless, the suppression of π^0 meson in Pb–Pb collisions compared to pp collisions is the same level between $\sqrt{s_{\text{NN}}} = 2.76$ and 5.02 TeV, which is by a factor of up to 8. This indicates the larger energy-loss at the higher collision energy. Comparing the light and heavy flavor hadrons, namely π^0 and D mesons, the suppression of D mesons at $p_{\text{T}} < 10$ GeV/ c is weaker than that of π^0 , which is interpreted as the smaller energy-loss for charm quarks than for up, down quarks. The suppression pattern of η meson seems to be similar to K^{\pm} meson consisting of a strange quark, though uncertainties for the η meson measurement is large. The direct photon measurement is complicated due to the huge background of decay photons from hadrons. By using measured p_{T} spectra of π^0 , η mesons and m_{T} -scaled $\omega(782)$, $\eta'(958)$ mesons as inputs to the cocktail simulation, decay photon yields have been estimated and statistically subtracted from inclusive photon spectra. Direct photon excess ratios R_{γ} show clear prompt photon signals originating from initial hard scatterings at high p_{T} . The prompt photon production is described by the pQCD NLO calculation well in both pp and Pb–Pb collisions at $\sqrt{s_{\text{NN}}} = 5.02$ TeV. Direct photon spectra or upper limits at the 90 % of C.L. have been extracted up to $p_{\text{T}} = 30$ GeV/ c in central Pb–Pb collisions. The resulting R_{AA} of direct photons which is consistent with unity at high p_{T} justifies the measurement and proves the successful Glauber modeling for the collision geometry. Focusing on R_{AA} of direct photon at low p_{T} in central collisions, a few data points show the excess beyond the pQCD calculation by a factor of up to 4. This indicates thermal photon emissions from the hot and dense QCD medium. The obtained effective temperature T_{eff} is 345 ± 222 (total unc.) MeV in Pb–Pb collisions at $\sqrt{s_{\text{NN}}} = 5.02$ TeV for centrality 0-10%. This is the first measurement and setting upper limits on the direct photons in pp and Pb–Pb collisions at $\sqrt{s_{\text{NN}}} = 5.02$ TeV.

1536 Acknowledgement

1537 First of all, I would like to express my greatest appreciation to Prof. Toru Sugitate who super-
1538 vised me in my master and Ph.D courses. He supported my long stay at CERN with his research
1539 grant and told me strategy how to survive in a large experiment. My deepest appreciation goes
1540 to Dr. Yuri Kharlov. He gave me a lot of appropriate help for not only analyses, but also
1541 PHOS commissioning at CERN during LS1 and operation during Run2. Successful data taking
1542 of PHOS in Run2 could not be done without his leadership, this thesis either. Dr. Dmitri Peres-
1543 soukho who is a coordinator in PHOS analyses group together with Dr. Yuri Kharlov helped me
1544 with calibration of data and simulation. I deeply thank Alexander Vinogradov, Iouri Sibiryak,
1545 Dmitri Alexandrov who are PHOS experts for repairing and checking PHOS quality everyday. I
1546 am grateful to Prof. Kenta Shigaki who allowed me to have dinner at excellent restaurants with
1547 him in Geneva, Frascati, Amsterdam, wherever he was. I also thank Prof. Kensuke Homma,
1548 Prof. Takahiro Miyoshi and Dr. Yorito Yamaguchi. They gave me a lot of important comments
1549 and discussion about laser experiments and the plasma simulation at our meeting. Especially,
1550 Dr. Yorito Yamaguchi taught me a lot of important physical topics in photon and dilepton
1551 as transparent probes in heavy-ion collisions. I would like to thank Dr. Yosuke Watanabe, Dr.
1552 Shinichi Hayashi, Dr. Satoshi Yano, Dr. Daisuke Watanabe, Dr. Tsubasa Okubo, Dr. Kazuya
1553 Nagashima, Yosuke Ueda, Kosei Yamakaya and Akihide Nobuhiro for fruitful discussions and a
1554 pleasant life with them in Hiroshima and CERN.

1555 A Zero Suppression study in Run2

1556 A new noise reduction system has been introduced in PHOS readout since Run2. This is based
1557 on minimum sequence of samples (MINSEQ) in ALTRO chip [93]. MINSEQ is set to 3 samples
1558 in PHOS readout in Run2. It means data is readout only if consecutive ALTRO sample is longer
1559 than 3 samples. This mechanism successfully reduces noise by a factor of $3 \sim 4$ compared to
1560 Run1. Data size of noise scan was $2 \sim 3$ kBytes in Run1, but it is 0.8 kBytes in Run2. ZS
1561 threshold is set to 3 ADC counts. However, ZS threshold is effectively increased due to MINSEQ.
1562 In order to test this effect, effective ZS threshold was varied in M.C. and tuned for reproducing
1563 standard cluster cut efficiency and PID cut efficiency. As shown by Fig.142, standard cluster
1564 cuts play rolls only at $E_\gamma < 1$ GeV where an electro-magnetic shower evolution is not well
1565 defined and ZS at 20 MeV can reproduce data very well (the best). Fig.143 shows that ZS at
20 MeV is the best again.

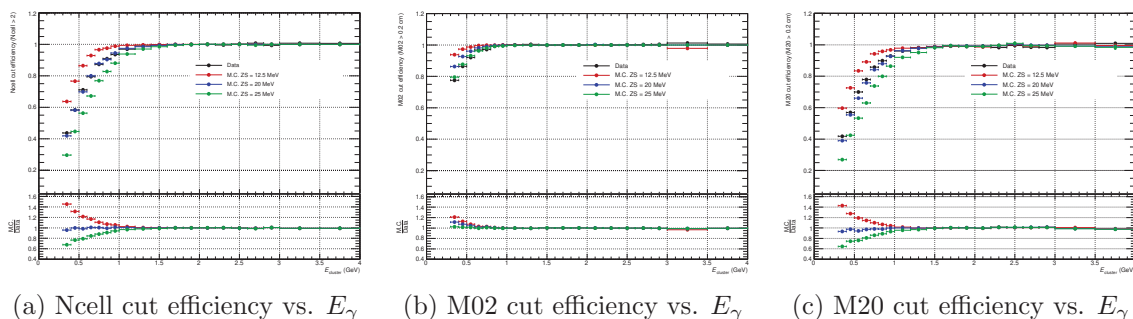


Figure 142: standard cluster cut efficiency as a function of photon energy. (12.5 MeV is default value in M.C.) Note these cuts are not apply in my analysis.

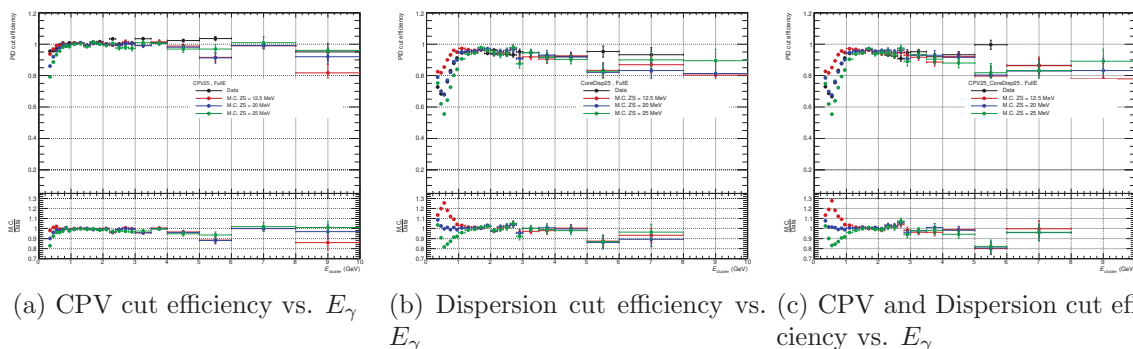


Figure 143: γ -ID cut efficiency as a function of photon energy. (12.5 MeV is default value in M.C.)

1566

1567 B pp collisions at $\sqrt{s} = 5.02$ TeV in 2015

1568 The LHC provided proton-proton collisions at $\sqrt{s} = 5.02$ TeV in 2015 and 2017. ALICE took 100
 1569 M events ($\sim 2 \text{ nb}^{-1}$) triggered by V0AND in November of 2015. On the other hand, as described
 1570 in section 3.1, ~ 10 times more V0AND events which corresponds to 19 nb^{-1} were recorded in
 1571 2017. Although data in 2015 have been also analyzed, it is just considered as a “guideline” for
 1572 this thesis. This small pp data recorded in early period gave me a great opportunity to estimate
 1573 systematic uncertainties at early stage and allowed me to save my time for 2017 data analyses.
 Hereafter, LHC15n represents pp data in 2015.

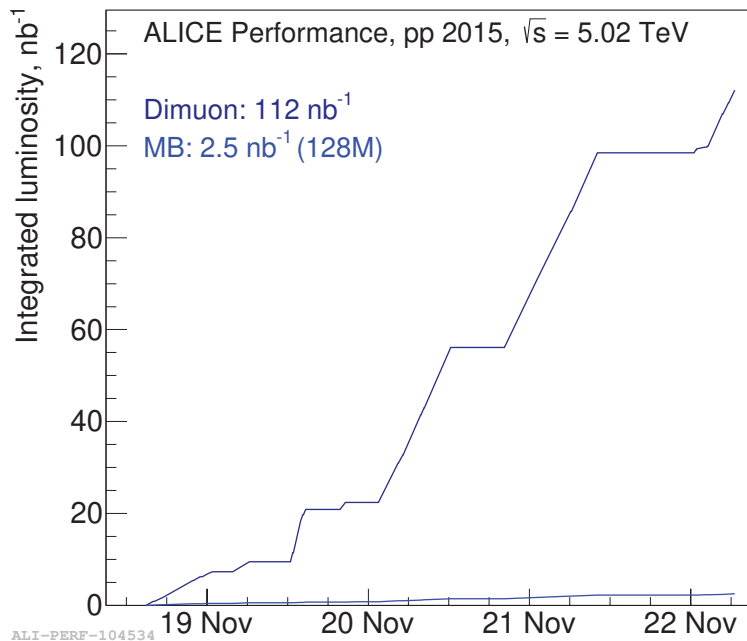


Figure 144: Integrated luminosity in pp collisions at $\sqrt{s} = 5.02$ TeV in 2015.

1574

1575 B.1 Date sets and QA

1576 B.1.1 Date sets in pp collisions at $\sqrt{s} = 5.02$ TeV

1577 run list in pp collisions at $\sqrt{s} = 5.02$ TeV in 2015 is following:

1578 LHC15n

1579 244628, 244627, 244618, 244617, 244542, 244540, 244531, 244484, 244483, 244482, 244481,
 1580 244480, 244453, 244421, 244418, 244416, 244411, 244377, 244364, 244359, 244355, 244351,
 1581 244343, 244340.

1582

1583 M.C. productions used in this analysis are following:

- 1584 • LHC16h8a + LHC16k5a PYTHIA8 for LHC15n
- 1585 • LHC16h8b + LHC16k5b PYTHIA6 for LHC15n
- 1586 • LHC16h3 PYTHIA8 jet-jet for LHC15n
- 1587 • LHC17i7 single particle (π^0 , η , γ) simulation for LHC15n/o

1588 **B.1.2 event selection**

1589 Following event cuts have been applied in order to select physics events both in data and M.C..

- 1590 • physics selection to reject beam-gas interaction
-
- 1591 • the number of charged track associated with primary vertex
- > 0
-
- 1592 • pileup rejection by SPD
-
- 1593 •
- $|Z_{\text{vtx}}| < 10$
- cm

 1594 **B.1.3 minimal cluster selection**

- 1595 •
- $E > 0.2$
- GeV (to extract photon signal as much as possible at low energy)
-
- 1596 •
- $M02 > 0.1$
- cm is applied only
- $E > 1$
- GeV (to extract photon signal as much as possible at
-
- 1597 low energy)
-
- 1598 •
- $|\text{TOF}| < 12.5$
- ns in pp

1599 As a first check of PHOS data, an average cluster energy and an average number of hits are plotted (Fig.145). Average values stay stable in all runs.

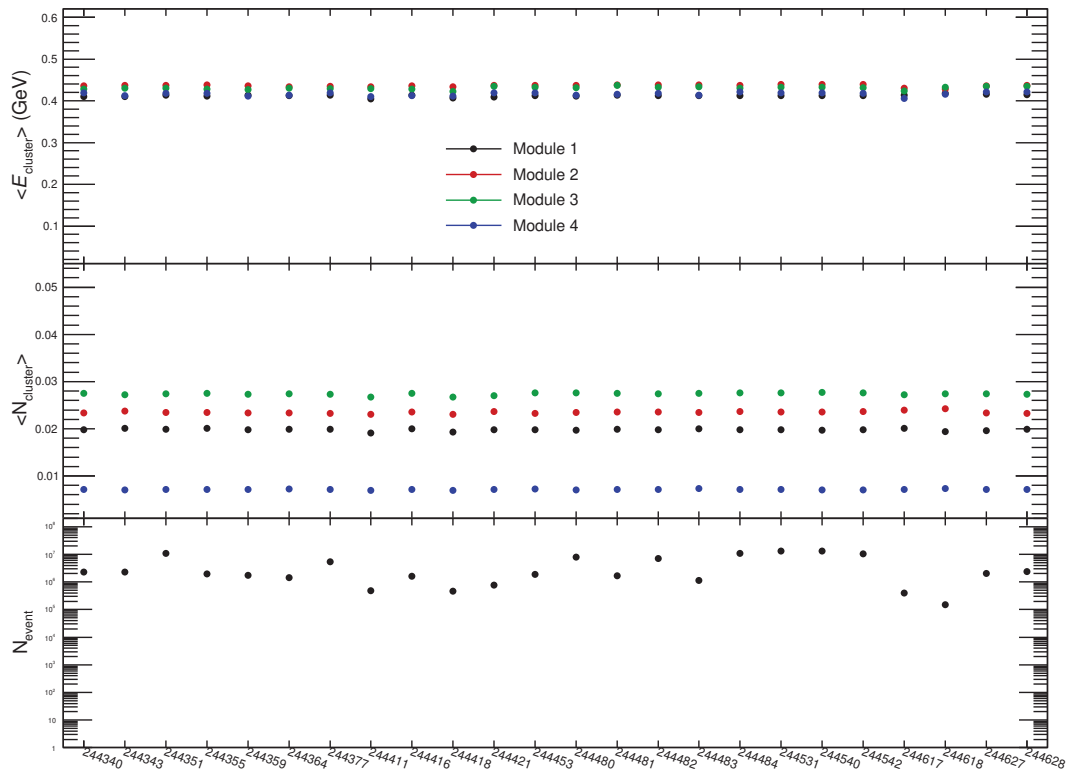


Figure 145: average cluster energy and number of hits in each run on PHOS in LHC15n.

1600

 1601 **B.1.4 π^0 peak parameters vs. run numbers**

 1602 π^0 peak parameters are plotted (Fig.146) run-by-run to verify that PHOS was stable in this
 1603 period. As a result, M1,2,3 are all stable. Especially, π^0 peak could not be seen well on M4,

1604 because M4 has limited detector acceptance. A peak position in M1,2,3 are consistent within
 1605 statistical error bar. There are poor statistics in some runs where π^0 peak is not so clear.
 1606 Note that M4 was excluded from the beginning because a systematic uncertainty of material
 1607 budget is large in front of M4 due to TOF + TRD, which is not suitable for the precise photon
 measurement.

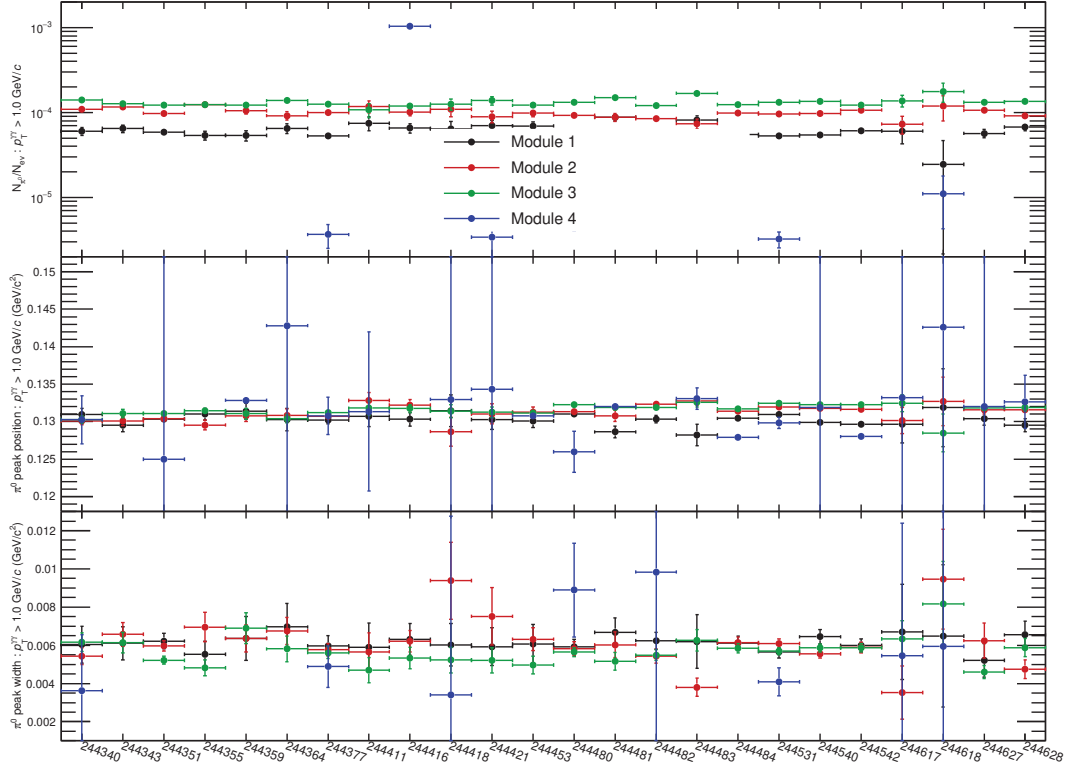


Figure 146: π^0 yield, peak position and sigma in each run in LHC15n.

1608

1609 B.2 Trigger QA

1610 B.2.1 Distance between fired TRU channels and clusters

1611 B.2.2 Energy distribution of matched clusters

1612 B.3 Raw yield extraction

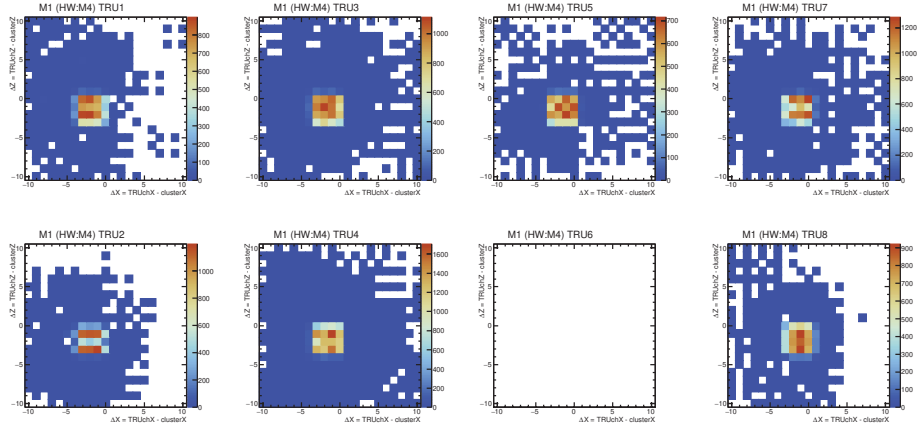
1613 Unfortunately, η measurement was not possible due to the small statistics in LHC15n.

1614 B.4 Acceptance \times reconstruction efficiency

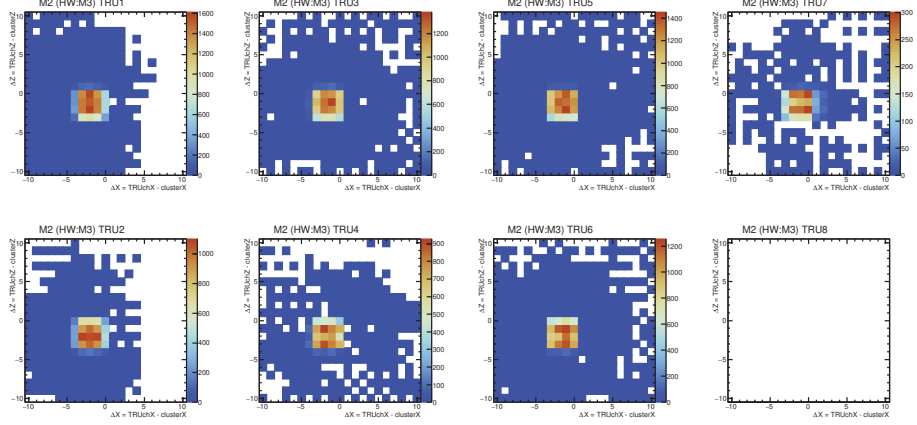
1615 At first, peak positions and peak widths have been compared between data and M.C..

1616 B.5 Trigger efficiency

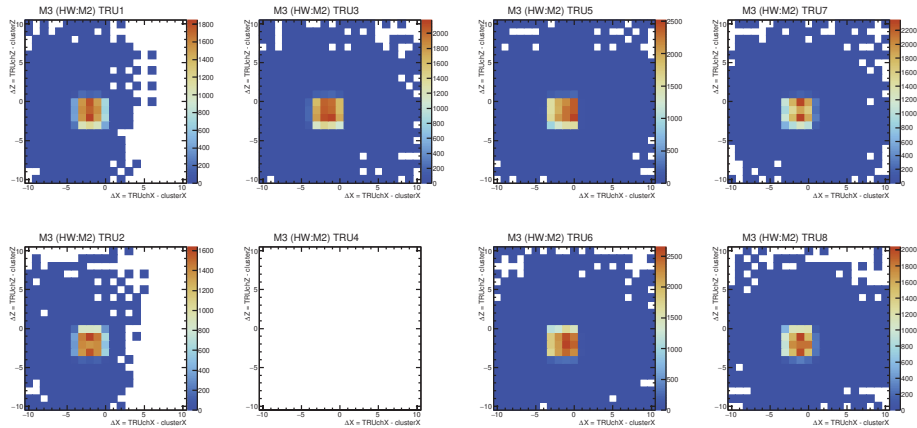
1617 PHOS trigger allows us to measure high energy photons/electrons efficiently in ALICE. An
 1618 energy threshold of PHOS L0 trigger in LHC15n period was set to 3 GeV in sum of 4x4 FastOR.
 1619 Due to the poor TRU acceptance in LHC15n period, trigger efficiency ϵ_{trg} is saturated at about
 1620 0.28 ± 0.02 at high p_T .



(a) The distance between fired TRU channels and cluster position on M1 in LHC15n.

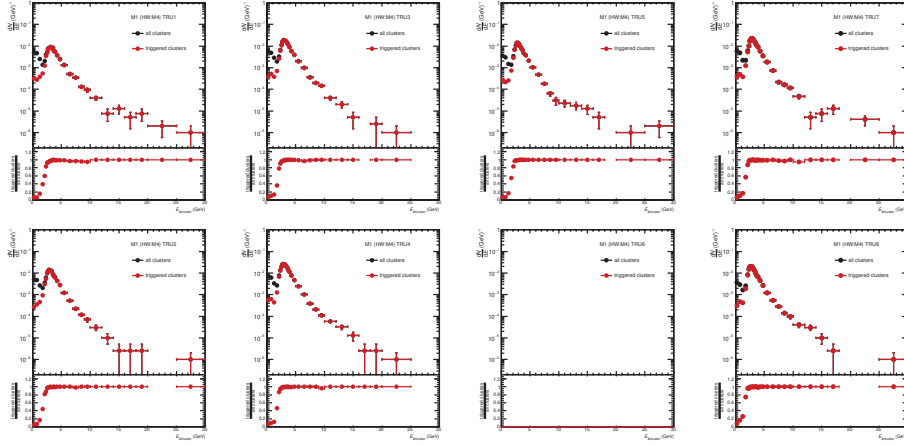


(b) The distance between fired TRU channels and cluster position on M2 in LHC15n.

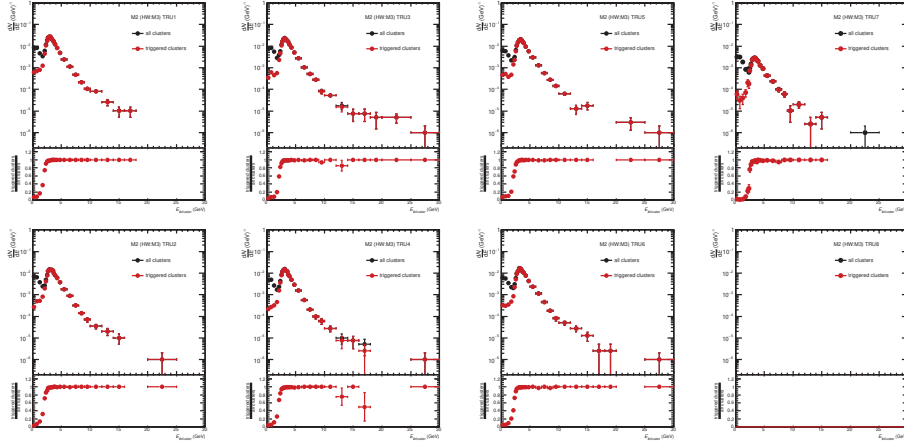


(c) The distance between fired TRU channels and cluster position on M3 in LHC15n.

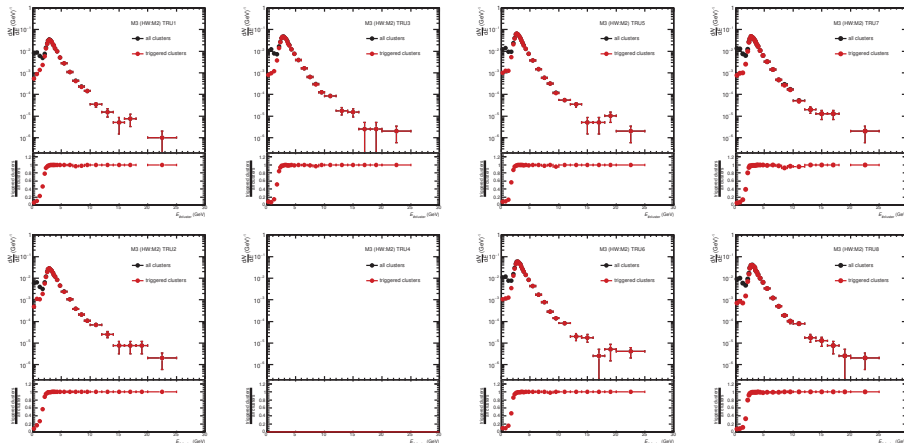
Figure 147: The distance between fired TRU channels and cluster position in different module for $E_{\text{cluster}} > 3$ GeV in LHC15n. Note that M4 is excluded from my analysis from the very beginning.



(a) Energy distribution on M1 in LHC15n.



(b) Energy distribution on M2 in LHC15n.



(c) Energy distribution on M3 in LHC15n.

Figure 148: Energy distribution of all clusters and triggered clusters and ratios in LHC15n. Note that M4 is excluded from my analysis from the very beginning.

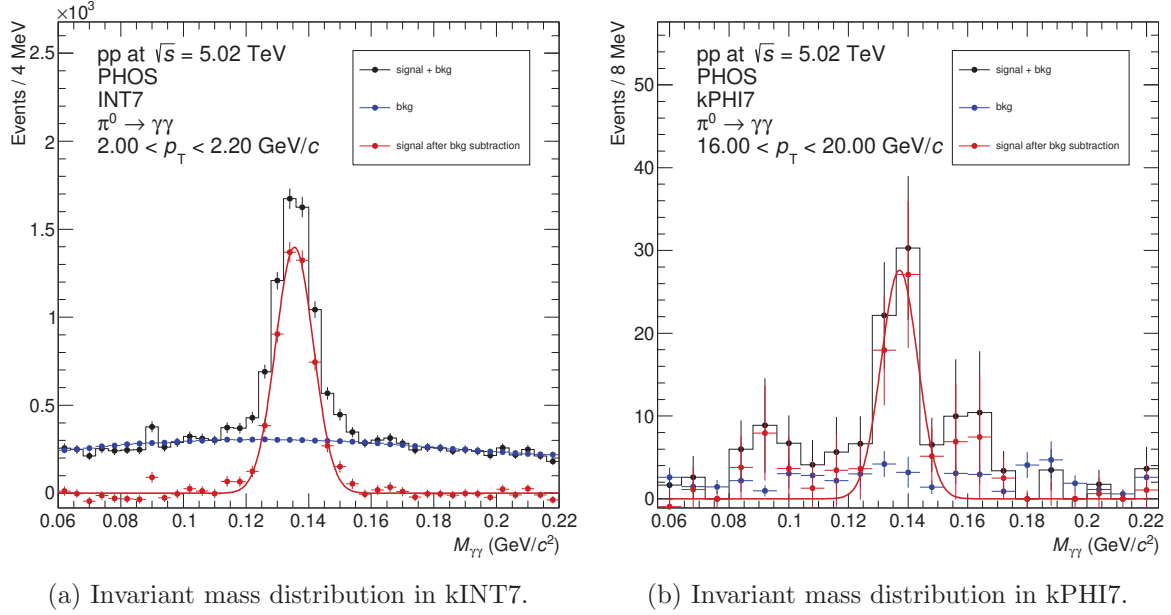


Figure 149: π^0 peak in kINT7 and kPHI7. An energy threshold of PHOS L0 trigger was 3 GeV in 2015

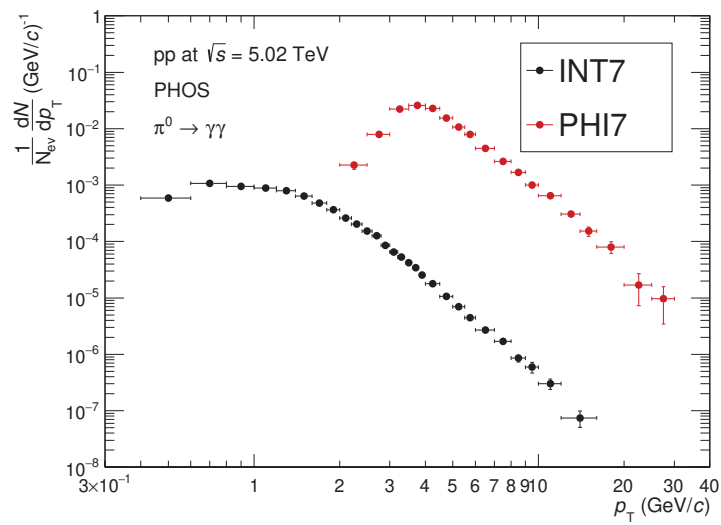


Figure 150: Raw yields of π^0 in LHC15n.

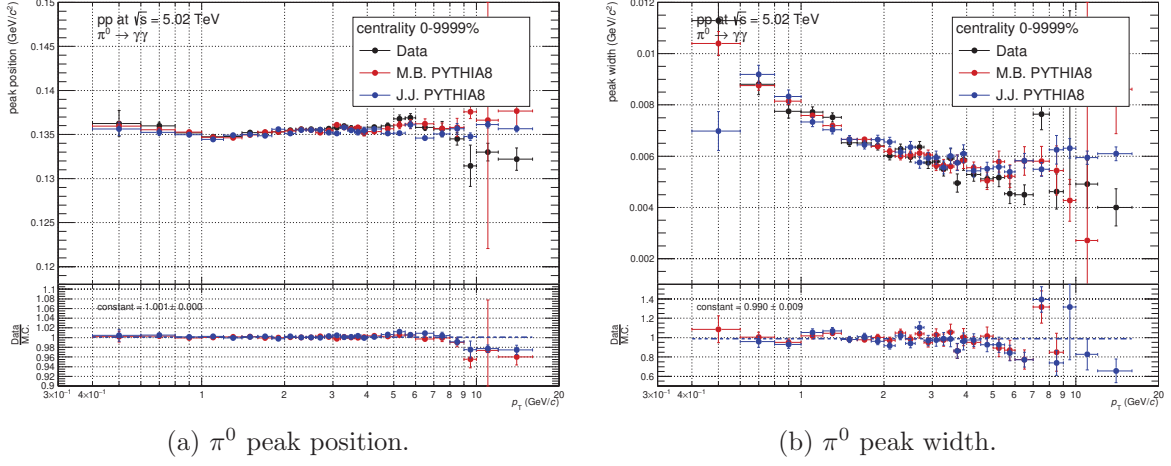
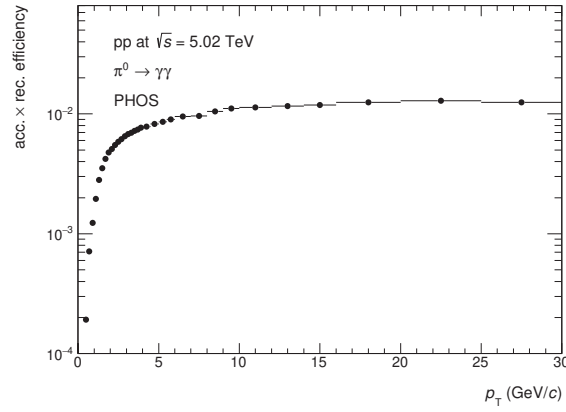
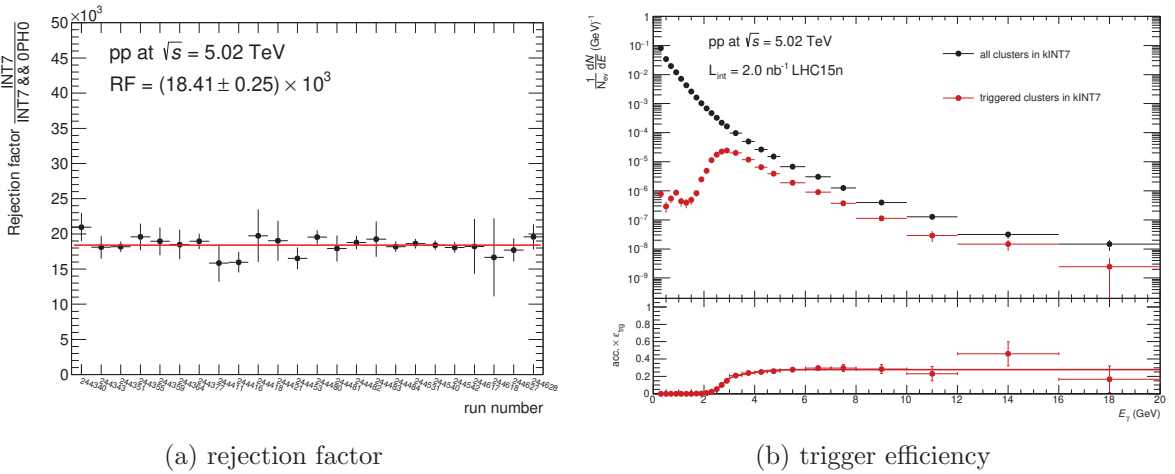

 Figure 151: peak parameters of π^0 in data and M.C. as a function of p_T .

 Figure 152: The acceptance \times reconstruction efficiency of π^0


Figure 153: The rejection factor and trigger efficiency of PHOS L0 trigger in LHC15n data.

1621 B.6 Timing cut

1622 Timing cut ($|\text{TOF}_{\text{cluster}}| < 12.5$ ns) was applied at cluster level to reject clusters from other BCs.
 1623 Thus, TOF cut efficiency (ε_{TOF}) as a function of photon energy has to be measured.
 1624 where, $N_{\text{TOF } \gamma}^{\text{triggered BC}}$ is the number of photons after TOF cut in the triggered BC and $N_{\text{all } \gamma}^{\text{triggered BC}}$
 1625 is the number of photons in the triggered BC respectively. Then, histograms are filled with the
 1626 number of photons weighted by the inverse of ε_{TOF} as a function of photon energy after TOF
 1627 cut. Since ε_{TOF} is measured as a function of photon energy, $\frac{1}{\varepsilon_{\text{TOF}}^1 \times \varepsilon_{\text{TOF}}^2}$ is necessary at neutral
 mesons level which are reconstructed from 2 photons.

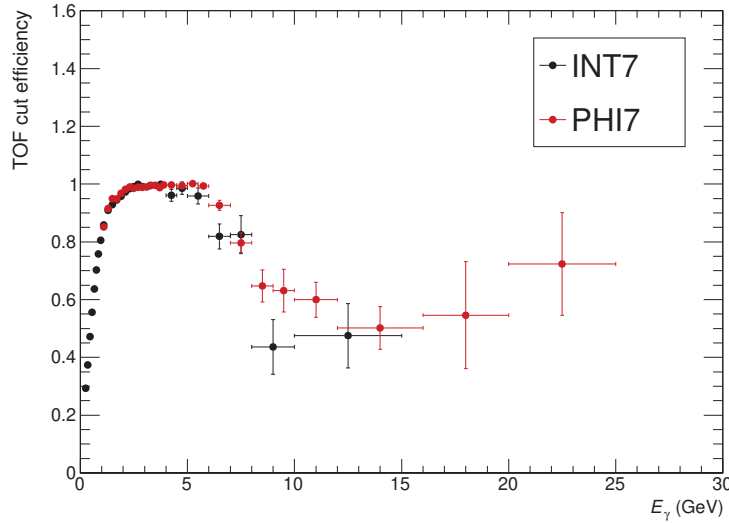


Figure 154: TOF cut efficiency as a function of photon energy in LHC15n data sample.

1628

1629 B.7 Feed down from strange hadrons

1630 The same approach as in 2017 data was applied.

1631 B.8 Systematic uncertainties in pp collisions at $\sqrt{s} = 5.02$ TeV in LHC15n

1632 B.8.1 Yield extraction of neutral mesons

1633 Fitting function, range and integration range were varied to estimate systematic uncertainty of
 1634 yield extraction. This estimation was performed by the fully corrected yields. R.M.S./mean
 1635 value in each p_T bin is considered as the uncertainty of yield extraction.

- 1636 • Fitting function [Gaussian,crystallball] for signal and [pol1,pol2] for background
- 1637 • Fitting range [0.06,0.22], [0.04,0.20], [0.08,0.24] GeV/ c^2 for π^0
- 1638 • Fitting range [0.40,0.70], [0.35,0.65], [0.45,0.75] GeV/ c^2 for η
- 1639 • Integration range $[\pm 3\sigma, \pm 2\sigma]$

1640 B.8.2 PID cut

1641 No PID cut was applied in pp analysis.

1642 **B.8.3 TOF cut**

1643 There were data taking period when a bunch space of each pp collision was 1000 ns which
 1644 was much wider than timing resolution of PHOS. These runs allow us to estimate systematic
 1645 uncertainty of TOF cut efficiency. The idea is defined by Eq.24. The deviation from unity in the
 1646 ratio is considered as a systematic uncertainty of TOF cut. It is found to be 4% from Fig.155
 in kINT7 events recorded in LHC15n period, not depending on p_T .

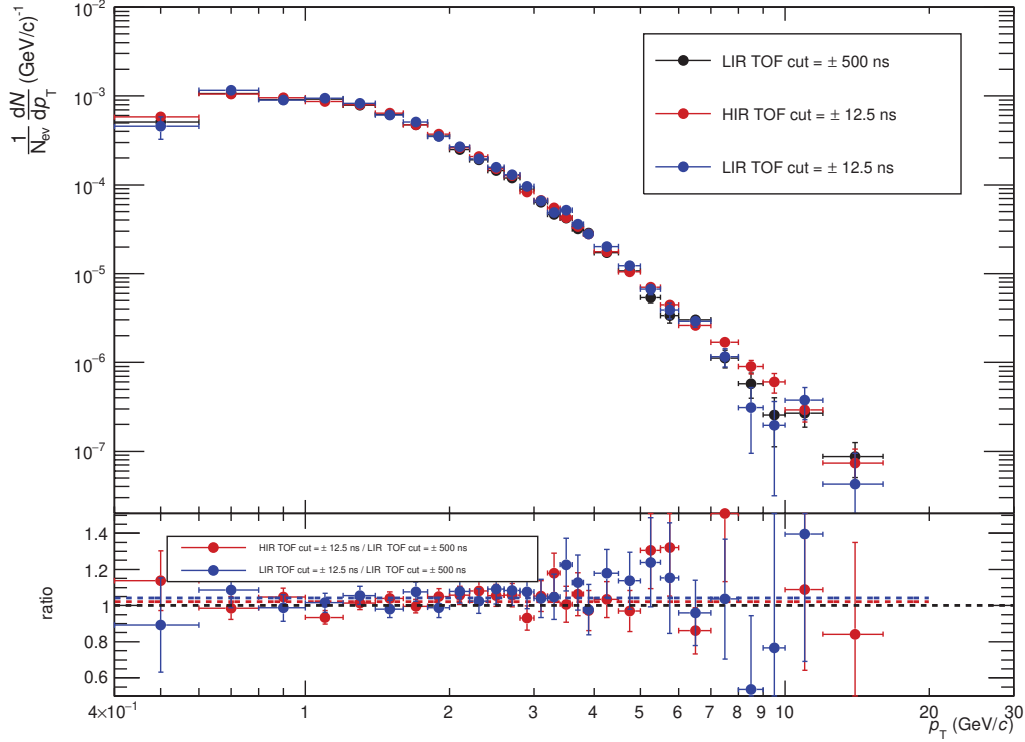


Figure 155: The ratio of π^0 yield in BS = 25 ns to one in BS = 1000 ns triggered by kINT7 in pp collisions at $\sqrt{s} = 5.02$ TeV.

1647

 1648 **B.8.4 Feed-down correction**

1649 The systematic uncertainty of K/π ratio in pp collisions at $\sqrt{s} = 2.76$ TeV is $\sim 10\%$ [61] at the
 1650 maximum. Therefore, the final systematic uncertainty of π^0 yields from feed down correction is
 1651 $0.3 \sim 0.6\%$, decreasing with p_T .

 1652 **B.8.5 Global energy scale**

1653 The same approach was performed as described in section 5.2.

 1654 **B.8.6 Non-linearity of energy response**

1655 The peak position measured by PHOS depends on p_T . This is due to p_T slope of particle
 1656 spectrum and finite energy resolution of the PHOS detector. The important effect is, so called,
 1657 non-linearity of energy response. One has to tune non-linearity and reproduce peak position in
 1658 M.C. for efficiency calculation. However, it is too difficult to understand non-linearity response
 1659 which may come from APD response and/or light yield of a crystal in simulation. A simple

1660 non-linearity model defined by Eq.40 to correct the measured energy was used in this analysis.

$$E_{\text{corr}} = E \cdot f(E), \quad f(E) = 1 + \frac{a}{1 + E^2/b^2} \quad (40)$$

1661 where, E_{corr} is corrected energy and E is energy before non-linearity correction. Parameters
 1662 a,b were varied in M.C. to find the best combination that can reproduce π^0 peak position. The
 1663 ratio of π^0 peak position in data to that in M.C. was fitted by a 0th-order polynomial function
 1664 and χ^2/ndf were obtained, shown on Fig.156. The best parameters are $a = -0.06$, $b = 0.7$.
 1665 Combinations (a,b) at $\chi^2/\text{ndf} < 2$ were taken into account to estimate uncertainty of non-
 1666 linearity. The systematic uncertainty of non-linearity was estimated by R.M.S./mean value with
 1667 different nonlinearity function shown by Fig.157. The systematic uncertainty of non-linearity is
 2% at low p_T and decreasing with p_T (Fig.156b).

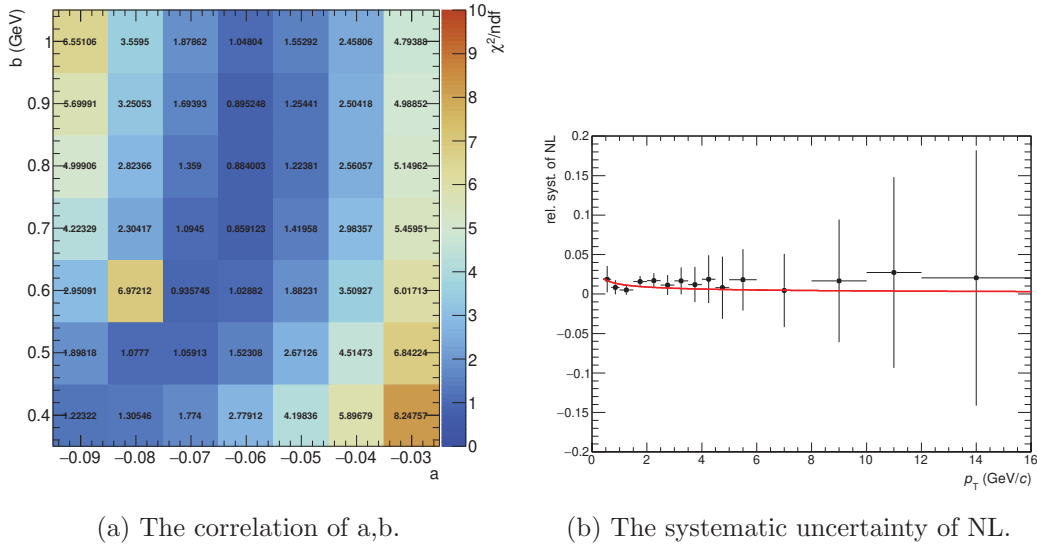


Figure 156: χ^2/ndf of fitting to the ratio of π^0 peak position in data to that in M.C. at different parameters a,b.

1668

1669 B.8.7 Acceptance of detector

1670 The systematic uncertainty of acceptance was estimated by varying the distance to the bad
 1671 channel (0 cell or 1cell). 0 cell is default value in my analysis. The deviation from unity in the
 1672 ratio of corrected yield of π^0 in different distance cut is considered as systematic uncertainty
 1673 of acceptance. The deviation from unity is 1.5% and this value is systematic uncertainty of
 1674 acceptance.

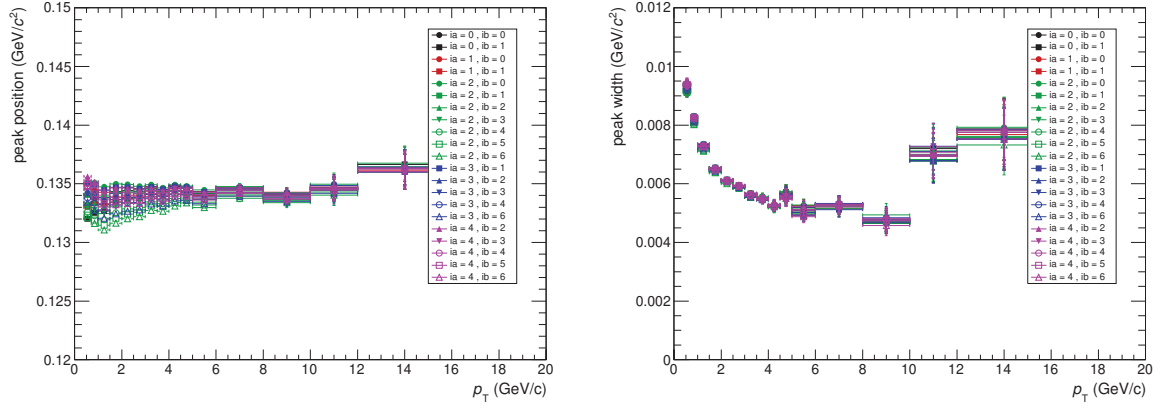
1675 B.8.8 Material budget

1676 This is common in all period and taken from section 5.9.

1677 B.8.9 Summary of systematic uncertainties

1678 Total systematic uncertainty is summarized on Fig.159.

1679 B.9 Invariant differential cross section of π^0


 (a) π^0 peak position in different NL.

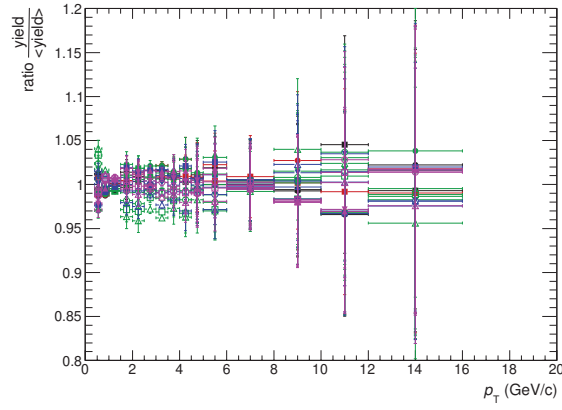
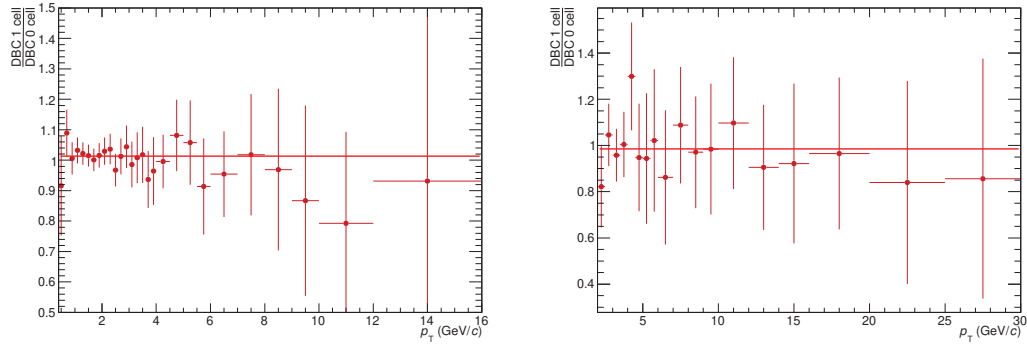
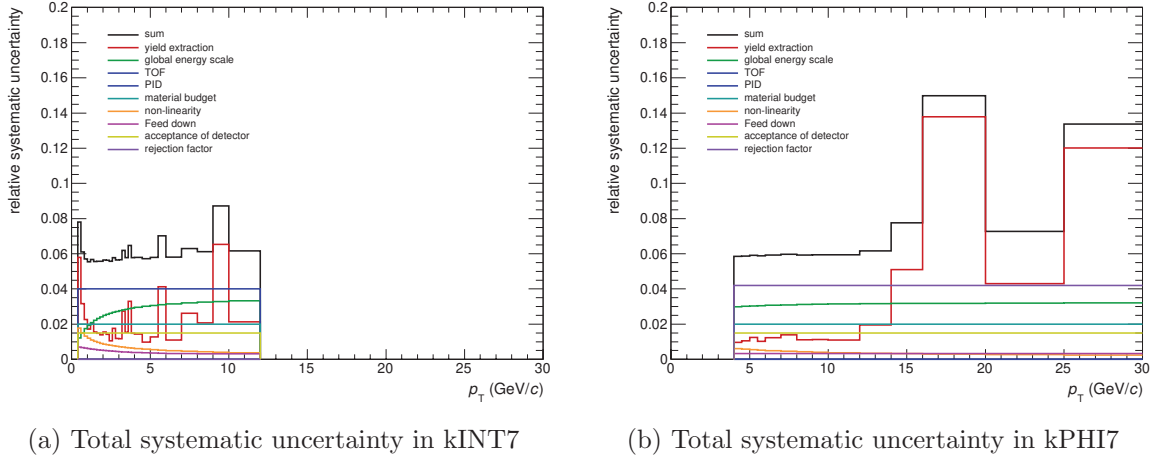
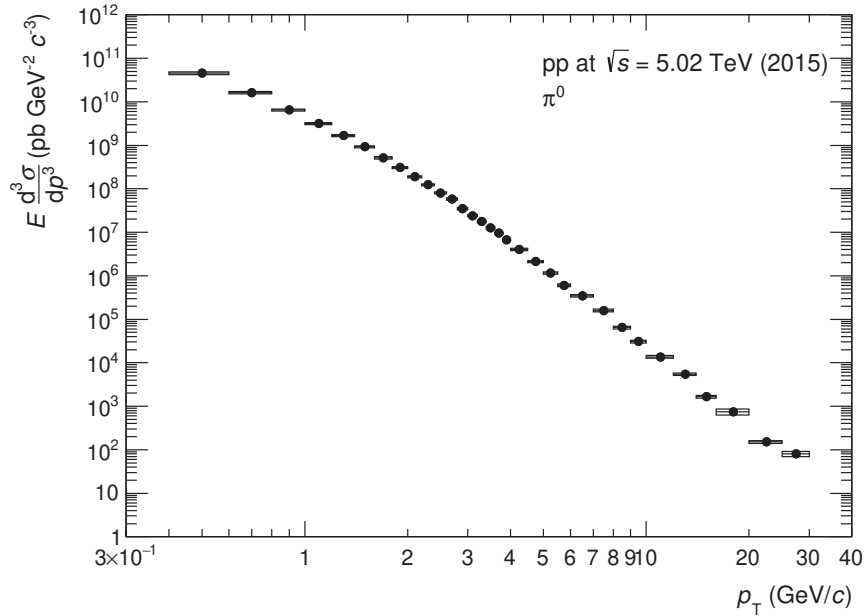
 (b) π^0 peak width in different NL.

 (c) The ratio of π^0 raw yield in different NL.

 Figure 157: π^0 peak parameters in different NL.


(a) The ratio of corrected yield in kINT7.

(b) The ratio of corrected yield in kPHI7.

Figure 158: The ratio of corrected yield in different distance cut.


 Figure 159: Summary of systematic uncertainties of π^0 measurement

 Figure 160: The invariant differential cross section of π^0 .

References

1680
1681
1682
1683
1684
1685
1686
1687
1688
1689
1690
1691
1692
1693
1694
1695
1696
1697
1698
1699
1700
1701
1702
1703
1704
1705
1706
1707
1708
1709
1710
1711
1712
1713
1714
1715
1716
1717

- [1] J. D. Bjorken. Energy Loss of Energetic Partons in Quark - Gluon Plasma: Possible Extinction of High $p(t)$ Jets in Hadron - Hadron Collisions. 1982.
- [2] Szabolcs Borsanyi, Zoltan Fodor, Christian Hoelbling, Sandor D. Katz, Stefan Krieg, and Kalman K. Szabo. Full result for the QCD equation of state with 2+1 flavors. *Phys. Lett.*, B730:99–104, 2014.
- [3] A. Bazavov et al. The chiral and deconfinement aspects of the QCD transition. *Phys. Rev.*, D85:054503, 2012.
- [4] Frithjof Karsch. Lattice results on QCD thermodynamics. *Nucl. Phys.*, A698:199–208, 2002.
- [5] Gert Aarts. Introductory lectures on lattice QCD at nonzero baryon number. *J. Phys. Conf. Ser.*, 706(2):022004, 2016.
- [6] Michael L. Miller, Klaus Reygers, Stephen J. Sanders, and Peter Steinberg. Glauber modeling in high energy nuclear collisions. *Ann. Rev. Nucl. Part. Sci.*, 57:205–243, 2007.
- [7] CERN. Participants and spectators at the heavy-ion fireball. April,26 2013. CERN COURIER.
- [8] S. S. Adler et al. High p_T charged hadron suppression in Au + Au collisions at $\sqrt{s_{NN}} = 200$ GeV. *Phys. Rev.*, C69:034910, 2004.
- [9] J. Adams et al. Transverse momentum and collision energy dependence of high $p(T)$ hadron suppression in Au+Au collisions at ultrarelativistic energies. *Phys. Rev. Lett.*, 91:172302, 2003.
- [10] K. Aamodt et al. Suppression of Charged Particle Production at Large Transverse Momentum in Central Pb-Pb Collisions at $\sqrt{s_{NN}} = 2.76$ TeV. *Phys. Lett.*, B696:30–39, 2011.
- [11] Serguei Chatrchyan et al. Study of high- p_T charged particle suppression in PbPb compared to pp collisions at $\sqrt{s_{NN}} = 2.76$ TeV. *Eur. Phys. J.*, C72:1945, 2012.
- [12] Georges Aad et al. Measurement of charged-particle spectra in Pb+Pb collisions at $\sqrt{s_{NN}} = 2.76$ TeV with the ATLAS detector at the LHC. *JHEP*, 09:050, 2015.
- [13] F. Abe et al. Transverse Momentum Distributions of Charged Particles Produced in $\bar{p}p$ Interactions at $\sqrt{s} = 630$ GeV and 1800 GeV. *Phys. Rev. Lett.*, 61:1819, 1988.
- [14] M. Jacob and P. Landshoff. THE INNER STRUCTURE OF THE PROTON. *Sci. Am.*, 242:46–55, 1980.
- [15] J. W. Cronin, Henry J. Frisch, M. J. Shochet, J. P. Boymond, R. Mermod, P. A. Piroue, and Richard L. Sumner. Production of hadrons with large transverse momentum at 200, 300, and 400 GeV. *Phys. Rev.*, D11:3105–3123, 1975.
- [16] M. Arneodo et al. The A dependence of the nuclear structure function ratios. *Nucl. Phys.*, B481:3–22, 1996.
- [17] J. J. Aubert et al. The ratio of the nucleon structure functions F_2^n for iron and deuterium. *Phys. Lett.*, 123B:275–278, 1983.

-
- 1718 [18] M. Gyulassy, P. Levai, and I. Vitev. NonAbelian energy loss at finite opacity. *Phys. Rev.*
1719 *Lett.*, 85:5535–5538, 2000.
- 1720 [19] Ivan Vitev. Testing the mechanism of QGP-induced energy loss. *Phys. Lett.*, B639:38–45,
1721 2006.
- 1722 [20] Magdalena Djordjevic and Miklos Gyulassy. Heavy quark radiative energy loss in QCD
1723 matter. *Nucl. Phys.*, A733:265–298, 2004.
- 1724 [21] R. Baier, Yuri L. Dokshitzer, Alfred H. Mueller, S. Peigne, and D. Schiff. Radiative energy
1725 loss and p(T) broadening of high-energy partons in nuclei. *Nucl. Phys.*, B484:265–282,
1726 1997.
- 1727 [22] R. Baier, Yuri L. Dokshitzer, Alfred H. Mueller, S. Peigne, and D. Schiff. Radiative energy
1728 loss of high-energy quarks and gluons in a finite volume quark - gluon plasma. *Nucl. Phys.*,
1729 B483:291–320, 1997.
- 1730 [23] Magdalena Djordjevic and Ulrich W. Heinz. Radiative energy loss in a finite dynamical
1731 QCD medium. *Phys. Rev. Lett.*, 101:022302, 2008.
- 1732 [24] Magdalena Djordjevic. Theoretical formalism of radiative jet energy loss in a finite size
1733 dynamical QCD medium. *Phys. Rev.*, C80:064909, 2009.
- 1734 [25] Dusan Zigic, Igor Salom, Jussi Auvinen, Marko Djordjevic, and Magdalena Djordjevic. Joint
1735 R_{AA} and v_2 predictions for $Pb + Pb$ collisions at the LHC within DREENA-C framework.
1736 2018.
- 1737 [26] Dusan Zigic, Igor Salom, Marko Djordjevic, and Magdalena Djordjevic. DREENA-B frame-
1738 work: first predictions of R_{AA} and v_2 within dynamical energy loss formalism in evolving
1739 QCD medium. 2018.
- 1740 [27] M. Gyulassy, P. Levai, and I. Vitev. Jet tomography of Au+Au reactions including
1741 multigluon fluctuations. *Phys. Lett.*, B538:282–288, 2002.
- 1742 [28] A. Adare et al. Enhanced production of direct photons in Au+Au collisions at $\sqrt{s_{NN}} = 200$
1743 GeV and implications for the initial temperature. *Phys. Rev. Lett.*, 104:132301, 2010.
- 1744 [29] A. Adare et al. Detailed measurement of the e^+e^- pair continuum in $p + p$ and Au+Au
1745 collisions at $\sqrt{s_{NN}} = 200$ GeV and implications for direct photon production. *Phys. Rev.*,
1746 C81:034911, 2010.
- 1747 [30] A. Adare et al. Centrality dependence of low-momentum direct-photon production in
1748 Au+Au collisions at $\sqrt{s_{NN}} = 200$ GeV. *Phys. Rev.*, C91(6):064904, 2015.
- 1749 [31] Jaroslav Adam et al. Direct photon production in Pb-Pb collisions at $\sqrt{s_{NN}} = 2.76$ TeV.
1750 *Phys. Lett.*, B754:235–248, 2016.
- 1751 [32] R. Albrecht et al. Transverse momentum distributions of neutral pions from nuclear col-
1752 lisions at 200 AGeV. *Eur. Phys. J. C*, 5(nucl-ex/9805007. IKP-MS-98-05-01. 2):255–267.
1753 13 p, May 1998. Accepted for publication in *Eur.Phys.J.C*, 13 pages including 16 figures
1754 Report-no: IKP-MS-980501.
- 1755 [33] R. Albrecht et al. Limits on the production of direct photons in 200-A/GeV S-32 + Au
1756 collisions. *Phys. Rev. Lett.*, 76:3506–3509, 1996.

- 1757 [34] D. K. Srivastava and B. Sinha. Single photons from S + Au collisions at the CERN Super
1758 Proton Synchrotron and the quark - hadron phase transition. *Phys. Rev. Lett.*, 73:2421–
1759 2424, 1994.
- 1760 [35] A. Dumitru, U. Katscher, J. A. Maruhn, Horst Stoecker, W. Greiner, and D. H. Rischke.
1761 Pion and thermal photon spectra as a possible signal for a phase transition. *Phys. Rev.*,
1762 C51:2166–2170, 1995.
- 1763 [36] M. M. Aggarwal et al. Centrality dependence of neutral pion production in 158-A-GeV
1764 Pb-208 + Pb-208 collisions. *Phys. Rev. Lett.*, 81:4087–4091, 1998. [Erratum: *Phys. Rev.*
1765 *Lett.*84,578(2000)].
- 1766 [37] M. M. Aggarwal et al. Observation of direct photons in central 158-A-GeV Pb-208 + Pb-208
1767 collisions. *Phys. Rev. Lett.*, 85:3595–3599, 2000.
- 1768 [38] A. Adare et al. Azimuthally anisotropic emission of low-momentum direct photons in
1769 Au+Au collisions at $\sqrt{s_{NN}} = 200$ GeV. *Phys. Rev.*, C94(6):064901, 2016.
- 1770 [39] Shreyasi Acharya et al. Direct photon elliptic flow in Pb-Pb collisions at $\sqrt{s_{NN}} = 2.76$ TeV.
1771 *Phys. Lett.*, B789:308–322, 2019.
- 1772 [40] Oliver S. Bruning, P. Collier, P. Lebrun, S. Myers, R. Ostojic, J. Poole, and P. Proudlock.
1773 LHC Design Report Vol.1: The LHC Main Ring. 2004. [https://cds.cern.ch/record/
1774 782076](https://cds.cern.ch/record/782076).
- 1775 [41] O. Buning, P. Collier, P. Lebrun, S. Myers, R. Ostojic, J. Poole, and P. Proudlock. LHC
1776 Design Report. 2. The LHC infrastructure and general services. 2004. [http://cds.cern.
1777 ch/record/815187](http://cds.cern.ch/record/815187).
- 1778 [42] M. Benedikt, P. Collier, V. Mertens, J. Poole, and K. Schindl. LHC Design Report. 3. The
1779 LHC injector chain. 2004. <https://cds.cern.ch/record/823808>.
- 1780 [43] by Cian O’Luanaigh. Heavy metal: Refilling the lead source for the LHC. Feb 2013.
- 1781 [44] Fabienne Marcastel. CERN’s Accelerator Complex. La chaîne des accélérateurs du CERN.
1782 Oct 2013. General Photo.
- 1783 [45] K. Aamodt et al. The ALICE experiment at the CERN LHC. *JINST*, 3:S08002, 2008.
- 1784 [46] Betty Bezverkhny Abelev et al. Performance of the ALICE Experiment at the CERN LHC.
1785 *Int. J. Mod. Phys.*, A29:1430044, 2014.
- 1786 [47] P.Cortese et al. *Technical Design Report of forward detectors FMD, T0 and V0*, CERN-
1787 LHCC-2004-025, 2004. <https://cds.cern.ch/record/781854>.
- 1788 [48] E. Abbas et al. Performance of the ALICE VZERO system. *JINST*, 8:P10016, 2013.
- 1789 [49] Jaroslav Adam et al. Determination of the event collision time with the ALICE detector
1790 at the LHC. *Eur. Phys. J. Plus*, 132(2):99, 2017.
- 1791 [50] K Aamodt et al. Alignment of the ALICE Inner Tracking System with cosmic-ray tracks.
1792 *JINST*, 5:P03003, 2010.
- 1793 [51] G.Dellecasa et al. *Technical Design Report of ITS*, CERN-LHCC-99-012, 1999. [http:
1794 //cds.cern.ch/record/391175](http://cds.cern.ch/record/391175).

- 1795 [52] Christian Lippmann. Upgrade of the ALICE Time Projection Chamber. 2014. <https://cds.cern.ch/record/1622286/>.
1796
- 1797 [53] The ALICE Collaboration. Addendum to the Technical Design Report for the Upgrade of
1798 the ALICE Time Projection Chamber. 2015. <http://cds.cern.ch/record/1984329/>.
- 1799 [54] G.Dellecasa et al. *Technical Design Report of TPC*, CERN-LHCC-2000-001, 2000. http://cds.cern.ch/record/451098.
1800
- 1801 [55] V.Manko et al. *Technical Design Report of PHOS*, CERN-LHCC-99-004, 1999. http://cds.cern.ch/record/381432.
1802
- 1803 [56] D. V. Aleksandrov et al. A high resolution electromagnetic calorimeter based on lead-
1804 tungstate crystals. *Nucl. Instrum. Meth.*, A550:169–184, 2005.
- 1805 [57] C. Zhao, L. Liu, K. Røed, D. Rohrlich, Y. Kharlov, L. Bratrud, J. Alme, and T. B. Skaali.
1806 Performance of the ALICE PHOS trigger and improvements for RUN 2. *JINST*, 8:C12028,
1807 2013.
- 1808 [58] T. C. Awes, F. E. Obenshain, F. Plasil, S. Saini, S. P. Sorensen, and G. R. Young. A Simple
1809 method of shower localization and identification in laterally segmented calorimeters. *Nucl.*
1810 *Instrum. Meth.*, A311:130–138, 1992.
- 1811 [59] Christian Wolfgang Fabjan et al. ALICE: Physics performance report, volume II. *J. Phys.*,
1812 G32:1295–2040, 2006.
- 1813 [60] Martino Gagliardi, Jesus Guillermo Contreras Nuno, Christoph Mayer, and Satoshi Yano.
1814 ALICE luminosity determination for pp collisions at $\sqrt{s} = 5, 8$ and 13 TeV. *ALICE public*
1815 *note*, 2016.
- 1816 [61] Betty Bezverkhny Abelev et al. Production of charged pions, kaons and protons at large
1817 transverse momenta in pp and Pb - Pb collisions at $\sqrt{s_{NN}} = 2.76$ TeV. *Phys. Lett.*,
1818 B736:196–207, 2014.
- 1819 [62] Betty Bezverkhny Abelev et al. K_S^0 and Λ production in Pb-Pb collisions at $\sqrt{s_{NN}} = 2.76$
1820 TeV. *Phys. Rev. Lett.*, 111:222301, 2013.
- 1821 [63] Jaroslav Adam et al. Measurement of pion, kaon and proton production in proton - proton
1822 collisions at $\sqrt{s} = 7$ TeV. *Eur. Phys. J.*, C75(5):226, 2015.
- 1823 [64] Jaroslav Adam et al. Centrality dependence of the pseudorapidity density distribution for
1824 charged particles in Pb-Pb collisions at $\sqrt{s_{NN}} = 5.02$ TeV. *Phys. Lett.*, B772:567–577, 2017.
- 1825 [65] Ehab Abbas et al. Centrality dependence of the pseudorapidity density distribution for
1826 charged particles in Pb-Pb collisions at $\sqrt{s_{NN}} = 2.76$ TeV. *Phys. Lett.*, B726:610–622,
1827 2013.
- 1828 [66] Particle Data Group. Statistics. [http://pdg.lbl.gov/2017/reviews/
1829 rpp2017-rev-statistics.pdf](http://pdg.lbl.gov/2017/reviews/rpp2017-rev-statistics.pdf).
- 1830 [67] M.J. Oreglia. A Study of the Reactions $\psi' \rightarrow \gamma\gamma\psi$. *PhD. thesis*. [http://www.slac.
1831 stanford.edu/pubs/slacreports/slac-r-236.html](http://www.slac.stanford.edu/pubs/slacreports/slac-r-236.html).
- 1832 [68] Jaroslav Adam et al. Pseudorapidity and transverse-momentum distributions of charged
1833 particles in proton-proton collisions at $\sqrt{s} = 13$ TeV. *Phys. Lett.*, B753:319–329, 2016.

- 1834 [69] A. A. Bylinkin and A. A. Rostovtsev. Role of quarks in hadroproduction in high energy
1835 collisions. *Nucl. Phys.*, B888:65–74, 2014.
- 1836 [70] A. A. Bylinkin and M. G. Ryskin. Secondary hadron distributions in two component model.
1837 *Phys. Rev.*, D90(1):017501, 2014.
- 1838 [71] Alexander Bylinkin, Nadezda S. Chernyavskaya, and Andrei A. Rostovtsev. Predictions on
1839 the transverse momentum spectra for charged particle production at LHC-energies from a
1840 two component model. *Eur. Phys. J.*, C75(4):166, 2015.
- 1841 [72] R. Hagedorn. Thermodynamics of strong interactions. 1971.
- 1842 [73] Betty Bezverkhny Abelev et al. Neutral pion production at midrapidity in pp and Pb-Pb
1843 collisions at $\sqrt{s_{NN}} = 2.76$ TeV. *Eur. Phys. J.*, C74(10):3108, 2014.
- 1844 [74] Shreyasi Acharya et al. Production of π^0 and η mesons up to high transverse mo-
1845 mentum in pp collisions at 2.76 TeV. *Eur. Phys. J.*, C77(5):339, 2017. [Eur. Phys.
1846 J.C77,no.9,586(2017)].
- 1847 [75] B. Abelev et al. Neutral pion and η meson production in proton-proton collisions at $\sqrt{s} =$
1848 0.9 TeV and $\sqrt{s} = 7$ TeV. *Phys. Lett.*, B717:162–172, 2012.
- 1849 [76] Shreyasi Acharya et al. Neutral pion and η meson production at mid-rapidity in Pb-Pb
1850 collisions at $\sqrt{s_{NN}} = 2.76$ TeV. *Phys. Rev.*, C98(4):044901, 2018.
- 1851 [77] Shreyasi Acharya et al. Neutral pion and η meson production in p-Pb collisions at $\sqrt{s_{NN}} =$
1852 5.02 TeV. *Eur. Phys. J.*, C78(8):624, 2018.
- 1853 [78] Shreyasi Acharya et al. π^0 and η meson production in proton-proton collisions at $\sqrt{s} = 8$
1854 TeV. *Eur. Phys. J.*, C78(3):263, 2018.
- 1855 [79] ALICE Collaboration. Centrality determination in heavy ion collisions. *ALICE public note*,
1856 2018. <http://cds.cern.ch/record/2636623/>.
- 1857 [80] Jaroslav Adam et al. Centrality dependence of the nuclear modification factor of charged pi-
1858 ons, kaons, and protons in Pb-Pb collisions at $\sqrt{s_{NN}} = 2.76$ TeV. *Phys. Rev.*, C93(3):034913,
1859 2016.
- 1860 [81] Nicolò Jacazio. Production of identified charged hadrons in Pb-Pb collisions at $\sqrt{s_{NN}} =$
1861 5.02 TeV. *Nucl. Phys.*, A967:421–424, 2017.
- 1862 [82] S. Acharya et al. Measurement of D^0 , D^+ , D^{*+} and D_s^+ production in Pb-Pb collisions at
1863 $\sqrt{s_{NN}} = 5.02$ TeV. *JHEP*, 10:174, 2018.
- 1864 [83] Albert M Sirunyan et al. Measurement of the B^\pm Meson Nuclear Modification Factor in
1865 Pb-Pb Collisions at $\sqrt{s_{NN}} = 5.02$ TeV. *Phys. Rev. Lett.*, 119(15):152301, 2017.
- 1866 [84] Simon Wicks, William Horowitz, Magdalena Djordjevic, and Miklos Gyulassy. Elastic,
1867 inelastic, and path length fluctuations in jet tomography. *Nucl. Phys.*, A784:426–442, 2007.
- 1868 [85] Magdalena Djordjevic, Bojana Blagojevic, and Lidija Zivkovic. Mass tomography at differ-
1869 ent momentum ranges in quark-gluon plasma. *Phys. Rev.*, C94(4):044908, 2016.
- 1870 [86] K. Aamodt et al. Midrapidity antiproton-to-proton ratio in pp collisions at $\sqrt{s} = 0.9$ and
1871 7 TeV measured by the ALICE experiment. *Phys. Rev. Lett.*, 105:072002, 2010.

-
- 1872 [87] Betty Abelev et al. Measurement of electrons from semileptonic heavy-flavour hadron
1873 decays in pp collisions at $\sqrt{s} = 7$ TeV. *Phys. Rev.*, D86:112007, 2012.
- 1874 [88] Torbjorn Sjostrand, Stephen Mrenna, and Peter Z. Skands. PYTHIA 6.4 Physics and
1875 Manual. *JHEP*, 05:026, 2006.
- 1876 [89] P. K. Khandai, P. Shukla, and V. Singh. Meson spectra and m_T scaling in $p + p$, $d + \text{Au}$,
1877 and $\text{Au} + \text{Au}$ collisions at $\sqrt{s_{NN}} = 200$ GeV. *Phys. Rev.*, C84:054904, 2011.
- 1878 [90] A. Adare et al. Production of ω mesons in $p + p$, $d + \text{Au}$, $\text{Cu} + \text{Cu}$, and $\text{Au} + \text{Au}$ collisions at
1879 $\sqrt{s_{NN}} = 200$ GeV. *Phys. Rev.*, C84:044902, 2011.
- 1880 [91] A. Adare et al. Measurement of neutral mesons in $p + p$ collisions at $\sqrt{s} = 200$ GeV and
1881 scaling properties of hadron production. *Phys. Rev.*, D83:052004, 2011.
- 1882 [92] A. Adare et al. Heavy Quark Production in $p + p$ and Energy Loss and Flow of Heavy
1883 Quarks in $\text{Au} + \text{Au}$ Collisions at $\sqrt{s_{NN}} = 200$ GeV. *Phys. Rev.*, C84:044905, 2011.
- 1884 [93] CERN. ALICE TPC readout chip user manual. *CERN EP/ED*, 2002.